Contract No:

This document was prepared in conjunction with work accomplished under Contract No. DE-AC09-08SR22470 with the U.S. Department of Energy (DOE) Office of Environmental Management (EM).

Disclaimer:

Savannah River National Laboratory™

OPERATED BY SAVANNAH RIVER NUCLEAR SOLUTIONS

Power hardware-in-the-loop testing of distribution solid state transformers

Mechanical Methods for Foam Control

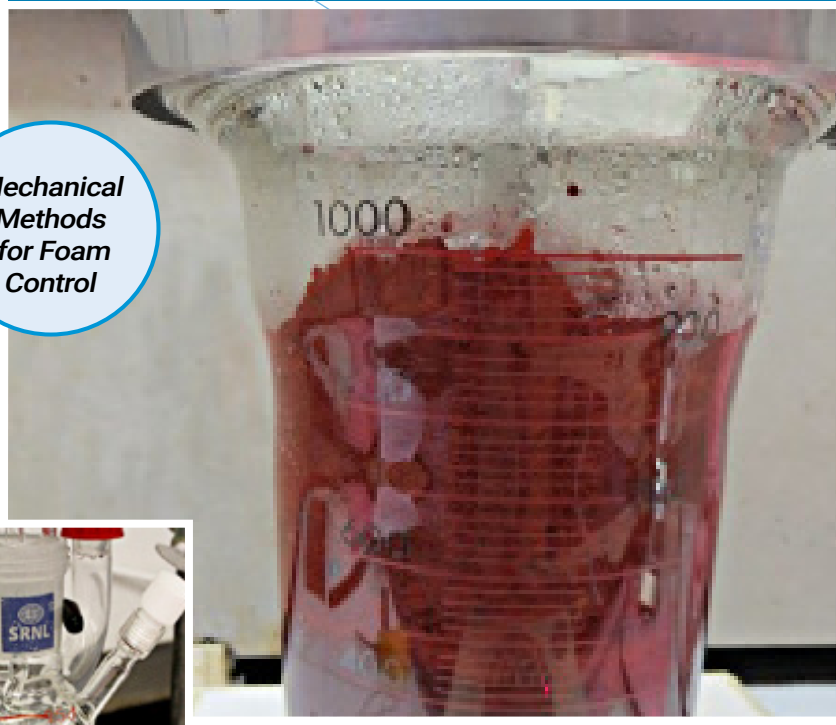

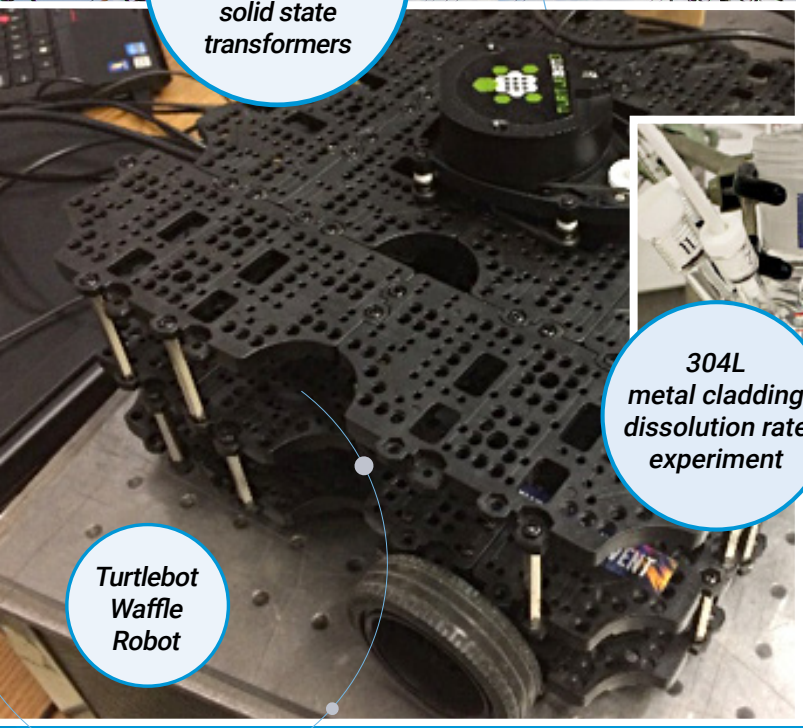

304L metal cladding dissolution rate experiment

Turtlebot Waffle Robot

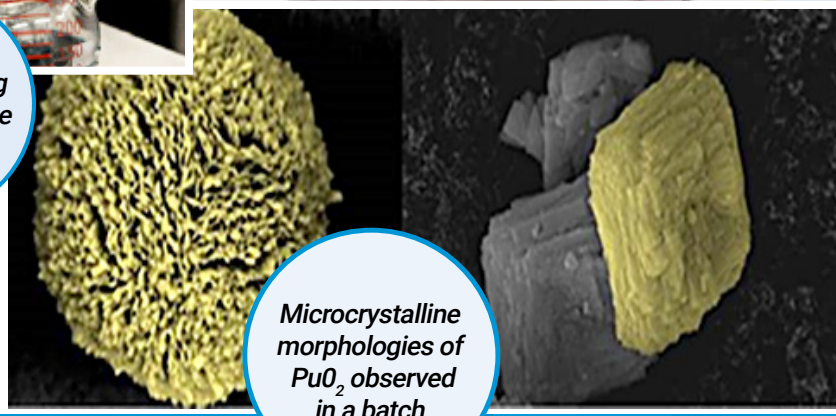

Microcrystalline morphologies of PuO_2 observed in a batch

2018 LDRD Annual Report

Savannah River National Laboratory

Laboratory Directed Research and Development Program

Environmental Stewardship

Nuclear Materials Management

National Security

Secure Energy Manufacturing

DISCLAIMER

SRNL-STI-2019-00170

CONTENTS

LAB DIRECTOR

Over the past 13 years, our Laboratory Directed Research and Development (LDRD) Program at Savannah River National Laboratory (SRNL) has served as a key driver incubating novel concepts and positioning the laboratory for future growth in key mission areas. The LDRD program delivers prospects for studying and advancing innovative ideas that will augment the ability of the lab to support the critical Department of Energy (DOE) missions in environmental stewardship, nuclear materials management, smart manufacturing, and national security. As the global manufacturing sector is undergoing a technological transformation not seen since the onset of the industrial revolution, a host of revolutionary technologies are allowing the industrial sector to re-think almost every aspect of how work is done. SRNL has taken a strategic direction focused on developing and adapting the best science and technology for the chemical and materials manufacturing needs of DOE and the National Nuclear Security Administration (NNSA). With this objective in mind, our FY18 LDRD program included a focus on innovative steps to obtain digital tools and data needed to fuel advances in manufacturing, including projects related to process intensification, process imaging, additive manufacturing, and cyber security.

LDRD also plays an impactful role cultivating staff excellence by providing the opportunity to further develop existing and growing emerging core competencies. In addition, the LDRD program builds the framework to create and strengthen strategic partnerships with other national labs, universities and commercial companies. SRNL's university partnerships are valuable as they not only allow for rewarding collaborative efforts, but also provide a direct connection with the next generation of scientists and engineers as students and post-doctoral researchers working on innovative R&D programs.

This report reflects the execution of our LDRD program within the objectives and guidelines outlined by the DOE through the DOE Order 413.2C. The projects described herein reflect the innovation required to fulfill SRNL's strategic vision and program plans, and they provide great value to the DOE and the nation. The diversity exhibited in the research and development projects underscores the DOE Office of Environmental Management (DOE-EM) and National Nuclear Security Administration (NNSA) missions and enhances these missions by developing the technical capabilities and human capital necessary to support future national needs.
On behalf of the SRNL Senior Management team, I would like to congratulate those members of the SRNL staff and their collaborators for their achievements and the excellence of their work. Their efforts reflect the importance of SRNL's creative ideas and competencies to our nation.

Dr. Vahid Majiidi
Laboratory Director
Savannah River National Laboratory

Savannah River National Laboratory's (SRNL)
Laboratory Directed Research and Development Program (LDRD)

Fiscal Year (FY) 2018 marked the thirteenth year of Savannah River National Laboratory's (SRNL's) Laboratory Directed Research and Development (LDRD) program and the largest year to date. When the program began in FY06, just two years after SRNL becoming the DOE's 17th national lab, it began with a modest authorized collection rate of just under 1.5%. It grew from there each year, reaching 5% in FY17. The authorized collection rate was maintained at 5% on FY18. The increase in collection rates experienced during the last years evidences the value placed on this important program, which provides the discretionary funding needed to develop ideas for future programmatic growth in our key business areas of environmental stewardship, national security, nuclear materials management, and secure energy manufacturing, as well as develop and maintain our core competencies. The LDRD program leverages the unique capabilities of SRNL to yield foundational scientific research and development (R&D) essential to our core business areas, while aligning optimally and continuously with SRNL's Strategic Plan and providing long-term benefits to DOE and the National Nuclear Security Administration (NNSA), other customers, and stakeholders. As can be seen in the "By the Numbers" summary, this program also plays an important role in sustaining staff excellence with high participation by students, post-docs, and early-career staff. Over 85% of the projects in FY18 included contributions from early-career or post-doctoral staff.

FY18 LDRD PROGRAM FOCUS AREAS:

The FY18 LDRD Program included focus areas in each of our three main business areas, as well as encouraging proposals supporting the themes of the Advanced Manufacturing Collaborative (AMC).

ENVIRONMENTAL STEWARDSHIP AND NUCLEAR MATERIALS MANAGEMENT

Unique concepts that lead to new approaches and options for critical EM risk reduction challenges and also reduce the life cycle in processing high activity liquid waste and nuclear materials, remediating contaminated soil, groundwater and facilities, as well as validating long-term remediation strategies.

NATIONAL SECURITY

Unique concepts that address national security mission area needs that are currently underserved by the DOE Lab system. Game-changing innovations and tools that advance the national security agenda for the United States Government, including monitoring, nonproliferation, and deterrence.

SECURE ENERGY MANUFACTURING

Advanced research in the development, demonstration, and deployment of secure energy manufacturing technologies and secure energy manufacturing; innovative technologies to assure the future utilization of clean, reliable energy or dramatically improve the energy efficiency of industrial, manufacturing, transportation, and building technologies, plus strengthen SRNL's Core Competencies.

FY18 MULTI-PROGRAMMATIC FOCUS AREA

- Environmental Stewardship
- Nuclear Materials Management
- National Security
- Secure Energy Manufacturing
- Advanced Imaging Technologies
- Process Intensification
- Cyber-Security

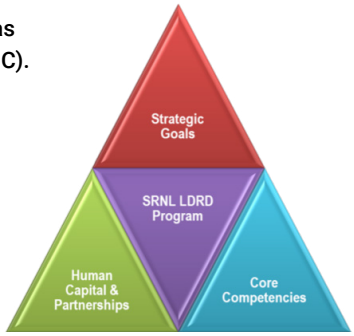

LDRD is the bridge to new capabilities and missions.

ADVANCED MANUFACTURING COLLABORATIVE (AMC)

Themes of the AMC include additive manufacturing, process intensification, virtual reality, process modeling, computational chemistry, smart manufacturing, robotics, and cyber security.

FY18 PORTFOLIO: 30 PROJECTS ($7.6 M UNBURDENED)

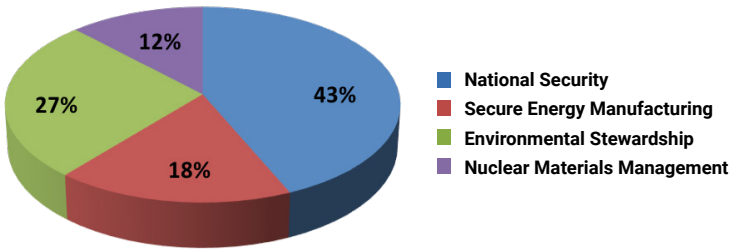

The pie chart shows the distribution of FY18 projects, both new starts and continuation projects, among the four program areas.

SRNL BY THE NUMBERS

TOTAL PROGRAM COST

$9.8 M

TOTAL NUMBER OF PROJECTS

41

AVERAGE PROJECT COST

$238 K

FY2018 LDRD Metrics

SCIENTIFIC PRODUCTIVITY

Research efforts supported by the LDRD program led to securing intellectual property and peer reviewed publications.

2 **invention disclosures submitted during FY18**

2 **patents granted related to prior year LDRD efforts**

8 **publications in peer reviewed journals**

TANGIBLE ACCOMPLISHMENTS RESULTING FROM PERSISTENT TECHNICAL EFFORTS IN FY18

14 **Post-Doc researchers were members of LDRD supported research team in FY18,**

8 **performed research at SRNL.**

SUSTAINING STAFF EXCELLENCE

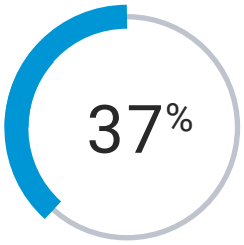

Percent of the FY18 projects were led by early career staff (terminal degree within past 10 years)

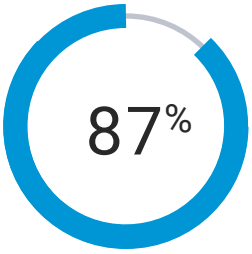

Percent of the FY18 projects involved Post-Docs or early career professionals

Forging Strategic Partnerships

2018 TOTAL COLLABORATION

UNIVERSITIES	COMPANIES	NATIONAL LABS
8	4	5

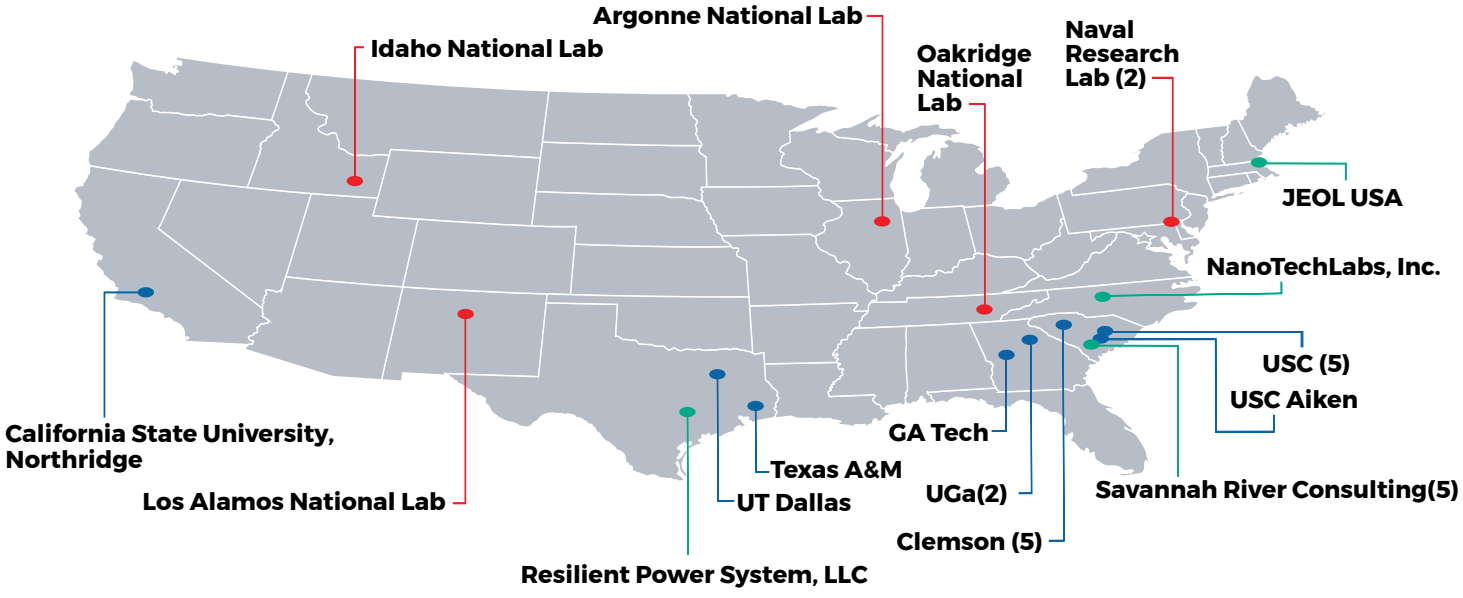

ENVIRONMENTAL STEWARDSHIP

SILVER-IODINE SECONDARY WASTE STABILIZATION: MULTI-SCALE EVALUATION

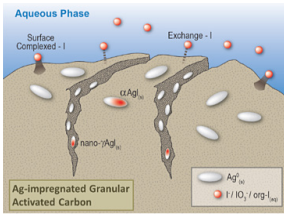

PROJECT TEAM:
D. I. Kaplan (Primary),
D. Li, D. Diprete

SUBCONTRATOR:
Texas A&M University

THRUST AREA:
Environmental Stewardship

PROJECT START DATE:
October 1, 2016

PROJECT END DATE:
September 30, 2018

Iodine-129 is a key risk driver in most low-level waste cementitious waste repositories. Rankings of iodine species by their tendency to bind to grout were: iodide << organo-iodine ≤ iodate. Similarly, ranking of grout formulations by their tendency to immobilize iodine were: Grout$_{+slag}$ < Grout$_{-slag.}$ A significant fraction of the iodide hydrated (cured) with the grout was converted to organo-iodine in the leachate. For the first time, these studies demonstrate that multiple iodine species can co-exist simultaneously in grout porewater, the iodine species initially added to the grout can greatly affect immobilization, a large fraction of the hydrated iodine was strongly bound into the structure of the grout, and that Ag-GAC can be safely disposed in grout formulation, but not in the presence of slag. These results help explain previous data and reduce uncertainty associated with the disposal of nuclear waste.

FY 2018

Objectives

- Determine iodine speciation in cementitious materials with slag (Grout$_{+slag}$) and without slag (Grout$_{-slag}$)
- Determine the impact of iodine speciation on immobilization by grout
- Determine if grout is compatibility as a waste form for the most common adsorbent used to remove aqueous and gaseous radioiodine, silver-impregnated granular activated carbon (Ag-GAC)

FY 2018

Accomplishments

- Developed a new analytical protocol that permits identifying iodine speciation in high salt environments.
- Demonstrated that multiple iodine species exist at the same time in grout leachate.
- Demonstrated that the iodine speciation of waste may influence cementitious waste form effectiveness.
- A fraction of iodine that is hydrated in grout cannot be readily released from the grout (data not shown here), suggesting that the single low distribution coefficient (K_d) approach to describing radioiodine release may not be appropriate for all cementitious iodine.

INTRODUCTION

Iodine-129 (^{129}I) is commonly the single greatest risk driver in high-level and low-level nuclear repositories.[1] This risk stems from several basic properties of ^{129}I, including that under many geochemical conditions, it can move as an anion at nearly the rate of water through the subsurface environment. ^{129}I is also extremely radiologically toxic because over 90% of body burden accumulates in the thyroid, which weighs only about 14g in an adult.[2] To illustrate how the properties of ^{129}I magnify its risk, ^{129}I accounts for only 0.00002% of the radiation released from the Savannah River Site in Aiken, South Carolina, but contributes 13% of the population dose, a six orders of magnitude magnification of risk with respect to its radioactivity.[3] There is also a large worldwide inventory of radioiodine as a result of its high fission yield and this inventory is rapidly increasing as a result of nuclear energy production.[1] Radioiodine is produced at a rate of 1 Ci per gigawatt of electricity produced by nuclear power.[4]

Low-level aqueous radionuclide waste is presently being disposed of as a cementitious waste form in the vadose zone of Savannah River Site[5] and is being evaluated at several other locations around the world.[6,7,8] The radioactive liquid waste is blended into the cementitious dry mix and then disposed of in the vadose zone. The resulting waste form binds the radionuclide through a wide range of mechanisms, while at the same time reducing water flux.[7,9] Slag is a common ingredient in cementitious waste forms because it reduces porosity, alters set time, and creates a strongly reducing environment that promotes the immobilization of several redox sensitive radionuclides, including Np, Pu, Se, Tc, and U. Slag is a glass-like by-product from smelting raw ore. Upon activation of the slag by the high pH of cement porewater, the redox condition decreases and is poised by sulfide species, mainly S^{2-}.[10,11] The reductive capacity of slag varies depending on its source, but is quite high and comparable to that of pyrite, in the range of 799 and 820 meq/kg.[12,13] The impact of the strongly reducing conditions created by slag-based cementitious waste forms on iodine immobilization has not been evaluated.

To the best of our knowledge, there have been no measurements of aqueous iodine speciation in cementitious systems. This can be in part attributed to the fact that the analytical methods of choice for speciation measurements, such as XANES and ion chromatography, require much higher iodine concentrations than commonly exists in these systems. Thermodynamic calculations predict that iodide (I^-) should be the dominant species, especially under subsurface repository conditions. Atkins and Glass10 concluded that iodine in cementitious systems will likely exist as I^- because I^- oxidation to iodate (IO_3^-) by molecular oxygen is extremely slow. In slag-containing cement blends, the strongly reducing environment would favor the I^- species.[11]

APPROACH

A series of batch adsorption and desorption experiments were conducted utilizing grout samples with slag ($Grout_{+slag}$) and without slag ($Grout_{-slag}$) and with and without silver impregnated granular activated carbon (Ag-GAC) that had been equilibrated with dissolved I^- (AgI-GAC) **(Table 1)**.

	Wt-% Dry Blend				
	Slag	Cement	Fly Ash	AgI-GAC[a]	Liquid:Dry Blend
$Grout_{-slag}$	0	25	75	0	0.29
$Grout_{+slag}$	45	8	47	0	0.45
$Grout_{-slag/AgI-GAC}$	0	25	55	20	0.29
$Grout_{+slag/AgI-GAC}$	45	8	27	20	0.49

[a] AgI-GAC = 10 wt% Ag impregnated on granular activated carbon. The Ag-GAC was loaded with ~9 mg/kg iodide.

Table 1. Grout Samples Formulations

Solutions used in the batch experiments were created to simulate grout porewater. These solutions were created by equilibrating a 1:10 grout:water suspension for 2 weeks, then pass the suspension through a 0.1-µm filter **(Table 2)**. All experiments involving the slag-free grout samples were conducted on the benchtop, whereas all the slag-containing grout samples were conducted in an inert glovebag (5%H_2/95% N_2).

Iodine speciation was conducted by the derivatization method described by Zhang et al.[14] The hydrated grout samples were characterized by standard methods, including XRF, XRD, and CHN analyses (to quantify organic and inorganic carbon). All measurements were conducted in duplicate.

K-edge XANES spectra of grout samples, together with several reference materials (i.e., KI, KIO_3 and 4-iodoaniline), were collected using the Materials Research Collaborative Access Team Sector 10-BM beamline at the Advanced Photon Source (Argonne National Lab, Argonne, IL). Statistical analyses were performed in the software R version 3.5.0 (2018-04-23),[15] using the Student's t-test or Tukey's Range Test in the STATS package (version 3.6.0).[16]

		$Grout_{-slag}$	$Grout_{+slag}$
Solid Phase[b]	Total I (mg/kg)	0.083	0.177
	Organic C (mg/kg)	1,200	1,300
	Inorg. C (mg/kg)	16,400	14,500
	Fe_2O_3 (wt-%)	4.47	3.04
	SO_3 (wt-%)	0.81	1.06
	LOI	12.79	11.43
Grout Leachate	Total I (µg/L)[c]	1.80	20.08
	pH	12.21	12.37
	Eh (mV)	+423	-307
	DOC (mg/L)	4.28	4.98
	Ca (mg/L)	8.31	38.48
	Fe (mg/L)	0.10	0.48
	K (mg/L)	314.7	235.0
	Na (mg/L)	1135	512
	Si (mg/L)	13.60	9.41
	Cl^- (mg/L)	5.44	23.60
	NO_3^- (mg/L)	7.87	5.02
	SO_4^- (mg/L)	323.4	41.67

[a] Average of duplicate analyses; Grout leachate data from a 1:10 grout-to-water suspension; $Grout_{-slag}$ suspension equilibrated for 14 days on a benchtop and $Grout_{+slag}$ suspension equilibrated for 14 days in an inert glovebox.

Table 2. Grout and Grout Leachate Characterization

RESULTS/DECISION

Kinetic Desorption Experiment with Iodide, Iodate, and 4-Iodoaniline Hydrated in Grout.

A ranking of the iodine amendments based on their tendency to release iodine into the aqueous phase was: I^- >> 4-iodoaniline (representative of an organo-iodine species) ≥ IO_3^- **(Figure 1).** For the I^- or 4-iodoaniline amended grout samples, there were no significant difference between the amount of total iodine released from the $Grout_{-slag}$ and $Grout_{+slag}$ suspensions. For the IO_3^- amended samples, total iodine concentrations leached from the $Grout_{-slag}$ were about twice that of the $Grout_{+slag.}$

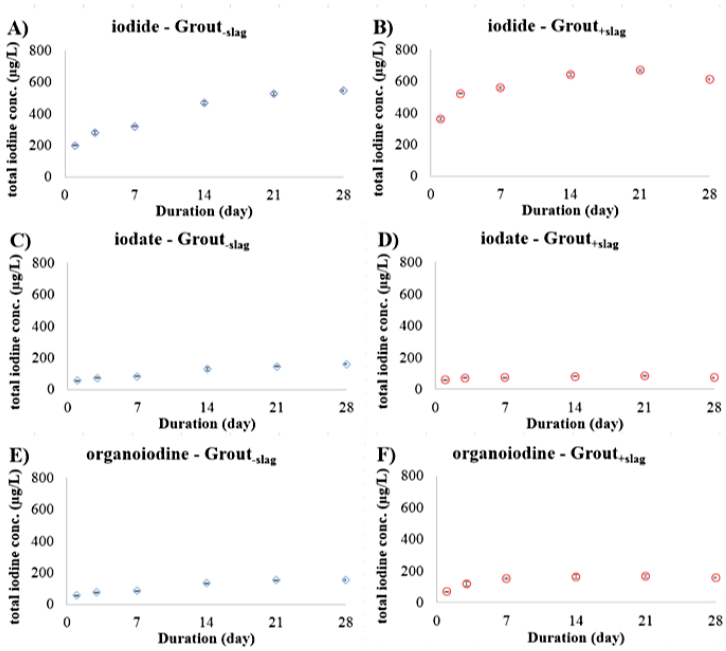

Figure 1. Total aqueous iodine concentrations desorbed from 6 grout treatments: (a) $Grout_{-slag}$ amended with I^-, (b) $Grout_{+slag}$ amended with I^-, (c) $Grout_{-slag}$ amended with IO_3^-, (d) $Grout_{+slag}$ amended with IO_3^-, (e) $Grout_{-slag}$ amended with 4-iodoanaline, and (f) $Grout_{+slag}$ amended with 4-iodoanaline. Error bars were calculated from duplicate samples and propagated error and may be hidden by symbol. Grout samples were hydrated with 190 µmol/L iodine as I^-, IO_3^- and 4-iodoaniline, cured for >3 months, and the solid:liquid ratio during the 28 day desorption period was 1:20. The aqueous phase was the grout leachate described in Table 1.

Apparent (non-steady state) desorption distribution coefficients (K_d; solid:liquid iodine concentration ratio) **(Table 3)** were between 3 and 40 times greater than the adsorption K_d values (on average ~ 3 L/kg). Furthermore, the I^-, IO_3^-, and 4-iodoanaline apparent desorption K_d values for $Grout_{-slag}$ were significantly less than corresponding K_d values for the $Grout_{+slag}$ suspensions (Student's t-test at $p \le 0.05$) **(Table 3).** Furthermore, I^- K_d values were less than IO_3^- or 4-iodoaniline K_d values. 4-iodoaniline K_d values were less than or equal to IO_3^- K_d values (Tukey's Range Test at $p \le 0.05$).

	iodide amended	iodate amended	4-iodoaniline amended
$Grout_{-slag}$	6.14 ± 0.07[a] bB[b]	30.62 ± 0.17 aB	32.28 ± 1.15 aB
$Grout_{+slag}$	7.50 ± 0.10 cA	121.78 ± 9.54 aA	42.07 ± 2.47 bA

[a] K_d values (C_{grout}/C_{aq}) were calculated using the 28-day data from Fig. 1 (C_{aq}) and the solid concentration at the end of the 28-day equilibration period (C_{grout}). Initially, the total iodine in $Grout_{-slag}$ was 9.077 ± 1.030 µg/g and in $Grout_{+slag}$ was 9.469 ± 1.981 µg/g.

[b] Different lowercase letters within a row represent significantly ($p \le 0.05$, $n = 2$) different values according to Tukey's HSD Range Test. Different uppercase letters within a column represent significantly ($p \le 0.05$, $n = 2$) different values according to Student's t-test.

Table 3. Desorption K_d values (L/kg) as a function of grout formulation and iodine species added to mix prior to curing.

Variable	$Grout_{+Slag/AgI-GAC}$	$Grout_{-Slag/AgI-GAC}$
Eh (mV)	-392 ± 37	439 ± 1*
pH	12.41 ± 0.04*	9.34 ± 0.08.
Ag (µg/L)	0.82 ± 0.96	92.11 ± 11.37*
DOC (mg/L)	7.66 ± 0.53	13.60 ± 1.56*
Tot I (µg/L)	19,269 ± 26263*	3.3 ± 1.1
I- (wt%)	80*	12
IO_3^- (wt%)	0	0
Org-I (wt%)	20	88*

* Indicates a significant greater value according to the Student t-test ($p \le 0.05$, n = 2).

Table 4. Comparison of Aqueous Chemistry after 60 days of the Suspensions Containing Grout with and without Slag that were Amended with AgI-GAC.

Iodine K-edge XANES Analysis. Iodine K-edge XANES analysis was conducted on $Grout_{-slag}$ and $Grout_{+slag}$ samples that had been hydrated with I^-, IO_3^-, or 4-iodoaniline **(Figure 2 below).** Potassium iodide (KI), potassium iodate (KIO_3), and 4-iodoaniline were included in the analyzes as reference materials. Irrespective of whether slag was or was not present, iodine speciation in the grout samples did not change between the time it was added and the time it was analyzed by XANES (about 1 month later). This lack of iodine transformations noted in the aqueous phase **(Table 2 on previous page and Figure 2**). Clearly, the solid and aqueous phases were not in equilibrium. Under these experimental conditions, measurement of the solid phase iodine speciation provided little insight into the aqueous iodine speciation.

Kinetic Desorption of Iodine from Ag-GAC imbedded in Grout. Much more iodine was released from the $Grout_{+slag/AgI-GAC}$ samples than from the $Grout_{-slag/AgI-GAC}$ sample **(Figure 3 and Table 4).** Geochemical modeling (Geochemist's Workbench) suggested that the release of iodine may be attributed to the strongly reducing conditions created by the slag **(Table 4),** which promoted the reduction of the Ag^+ in the AgI to Ag^0. This reduction process resulted in the dissolution of the AgI solid, thereby releasing the iodide. Furthermore, in the presence of slag, the concentration of Ag in the aqueous phase was <2 µg/L, XRD and geochemical modeling indicated the Ag had precipitated as nano-Ag^0 particles.

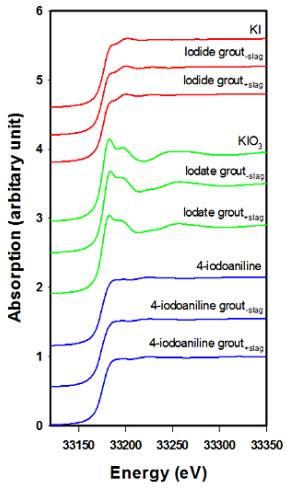

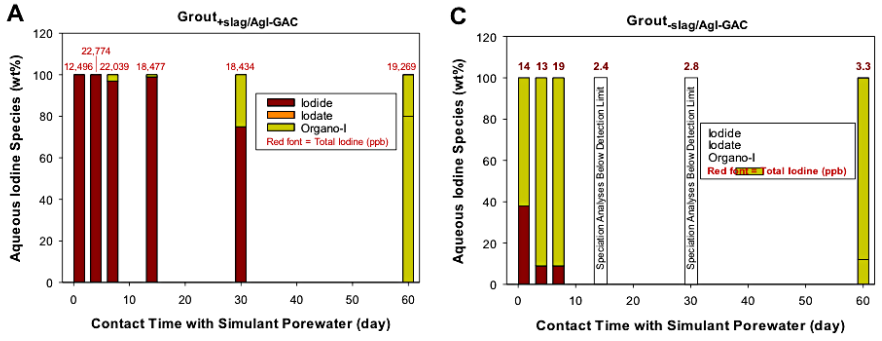

Figure 2. (Left) Iodine K-edge XANES spectra of grout with and without slag, that were hydreated with iodine, iodate, or 4 iodoaniline. Also presented are reference standards of KI, KIO_3 and 4-iodoaniline. *Figure 3. (Above) Percent aqueous iodine speciation in suspensions of grout with slag, $Grout_{-slag/AgI-GAC}$. The $grout_{+slag/AgI-GAC}$ experiments were conducted in an inert atmosphere, where as the $Grout_{-slag/AgI-GAC}$ experiments were conducted on a benchtop. Total aqueous iodine (µg/L, is noted in the above histogram. Results area averages of the duplicate measurements.*

FUTURE DIRECTIONS

Two Proposals Stemming from Seed Data Generated from this Study

1. Kaplan, D. I., and D. Li. 2018. Iodine and Ruthenium Removal from the Advanced Liquid Processing System (ALPS) Multi-nuclide Removal Facility. TEPCO. $270k for FY19
2. Nichols, R., D. I. Kaplan. and C. A. Langton. 2018. Response to Request for Information on HEPA Filter Waste Form Development and Testing Related to Radioiodine Immobilization to Support the IDF PA. Washington River Protection Services, Hanford. $700k for FY19.

PRESENTATIONS

1. Kaplan, D. I.; Santschi, P. H.; Ohnuki, T.; Li, D.; Nichols, R.; Price, K.; Xu, C.; Lin, P.; Xing, W.; Schwehr, K.; Tanaka, K.; Seaman, J. (2018) Radioiodine Speciation in Cementitious EnvironmWents. *In International Conference on Heavy Metals in the Environment,* Athens, GA, 2018.
2. Kaplan, D. I., Xu, C., Lin, P., Li, D., Schwehr, K., Tanaka, K., Ohnuki, T., and Santschi, P. H. (2018). Radioiodine Speciation in Cementitious Environments. *In* "Goldschmidt 2018". Geochemistry Society, Boston, MA.
3. Kaplan, D. I., Price, K. A., Seaman, J. C., Li, D., Lin, P., Xu, C., Schwehr, K., Tanaka, K., Ohnuki, T., and Santschi, P. H. (2018). Iodioiodine Speciation Impact on Ag-Activated Carbon Immobilization in Cementitious Environments. *In* "Goldschmidt 2018". Geochemistry Society, Boston, MA.
4. Qafoku, N. P., Kaplan, D. I., Lawter, A. R., Neeway, J. J., Szecsody, J. E., Bagwell, C. E., and Truex, M. J. (2018). Iodine conceptual models at the Hanford and Savannah River sites: Similarities and differences *In* "Goldschmidt 2018". Geochemistry Society, Boston, MA.
5. Ohnuki, T., Kozai, N., Tanaka, K., Tokunaga, K., Utsunomiya, S., Ikehara, R., Komiya, T., Takeda, A., Kaplan, D. I., and Santschi, P. H. (2018). Alkaline-activated metakaolin solidification of iodine sorbed by layered double hydroxides. *In* "Goldschmidt 2018". Geochemical Society, Boston, MA.
6. Kaplan, D. I., P. Santschi, T. Ohnuki, K. Roberts, D. Li, K. Price, C. Xu, P. Lin, K. Tanaka, J. Seaman. (2018). Influence of Aqueous Radioiodine Speciation on Uptake by Silver-Granulated Activated Carbon. 19th International Conference on Heavy Metals in the Environment – 2018, Athens, GA, July 21 – 25, 2018.
7. Ohnuki, T., N. Kozai, K. Tanaka, K. Tokunaga, S. Utsunomiya, D. I. Kaplan, P. Santschi. (2018) Sorption and Solidification of Iodate. RadChem 2018. Marianske Lazne, Czech Republic, May 13 – 18, 2018.
8. Kaplan, D. I.; Powell, B. A.; Um, W.; Seaman, J. M.; Kukkadapu, R.; Qafoku, O.; Du, Y.; Bowden, M. E.; Li, D.; Arai, Y. (2017) *Radionuclide Leaching and Mineral Characterization of Core Samples Recovered from the Saltstone Disposal Facility, Aiken, SC* USA, Migration 2017 - 16th International Conference on the Chemistry and Migration Behaviour of Actinides and Fission Products in the Geosphere, Barcelona, Spain, September 10-15, 2017, 2017; Barcelona, Spain, 2017.

PUBLICATIONS

1. Kaplan, D. I., Xu, C., Li, D., Lin, P., Xing, W., Nichols, R., Schwehr, K., and Santschi, P. H. (2018). Radioiodine Speciation in Cementitious Environments. *Environmental Science & Technology* (Submitted).
2. Kaplan, D. I., K. Price, C. Xu, D. Li, P. Liu, W. Xing, R. Nichols, K. Schwehr, J. C. Seaman, P. H. Santschi. (2018). Radioiodine Speciation in a Silver-Amended Cementitious Environments. *Environmental Science & Technology* (In Review).
3. Tanaka, K., Kaplan, D. I., and Ohnuki, T. (2017). Radionuclides in the Environment. Applied Geochemistry 85: 119-120.
4. Arai, Y.; Powell, B. A.; Kaplan, D. I., (2017) Sulfur Speciation in Untreated and Alkali Treated Ground-granulated Blast Furnace Slag. Sci. *Total Environ.* 589, 117-121.

REFERENCES

1. Kaplan, D. I.; Denham, M. E.; Zhang, S.; Yeager, C.; Xu, C.; Schwehr, K. A.; Li, H. P.; Ho, Y. F.; Wellman, D.; Santschi, P. H., Radioiodine biogeochemistry and prevalence in groundwater *Critical Reviews of Environmental Science and Technology* **2014,** *44,* (20), 2287-2337.
2. ICRP, Report of the *Task Group on Reference Man.* Pergamon Press: Oxford, 1975.
3. Kantelo, M. V.; Bauer, L. R.; Marter, W. L.; Murphy, C. E., Jr.; Zeigler, C. C. *Radioiodine in the Savannah River Site Environment;* WSRC-RP-90-424-2; Westinghouse Savannah River Company, Aiken, SC, 1990.
4. McKay, A., The Making of the Atomic Age. *Oxford University Press* 1984.
5. SRR FY2016 *Special Analysis for the Saltstone Disposal Facility at the Savanah River Site;* Savannah River Remediations: Aiken, SC, 2016.
6. Mann, F. M.; Puigh, R. J.; Finfrock, S. H.; Khaleel, R.; Wood, M. I. *Integrated Disposal Facility Risk Assessment;* RPP-15834; CH2M Hill Hanford Group, Inc., Richland, WA, 2003.
7. Ochs, M.; Mallants, D.; Wang, L., *Radionuclide and Metal Sorption on Cement and Concrete.* Springer: Heidelberg, 2016.
8. Li, J.; Wang, J., Advances in cement solidification technology for waste radioactive ion exchange resins: A review. *Journal of hazardous materials* **2006,** *135,* (1-3), 443-448.
9. Evans, N., Binding mechanisms of radionuclides to cement. *Cem. Concr. Res.* **2008,** *38,* (4), 543-553.
10. Atkins, M.; Glasser, F. P., Application of portland cement-based materials to radioactive waste immobilization. *Waste Management* **1992,** *12,* 105-131.
11. Angus, M. J.; Glasser, F. P., The Chemical Environment in Cement Matrices. *Mat. Res. Soc. Symp. Proc.* **1985,** *50,* 547-556.
12. Um, W.; Yang, J.-S.; Serne, R. J.; Westsik, J. H., Reductive Capacity Measurement of Waste Forms for Secondary Radioactive Wastes. *J. Nucl. Mater.* **2015,** *467,* 251-259.
13. Roberts, K. A.; Kaplan, D. I. *Reduction Capacity of Saltstone and Saltstone Components;* SRNL-STI-2009-00637, Rev 0; Savannah River National Laboratory, Aiken, SC, 2009.
14. Zhang, S.; Schwehr, K. A.; Ho, Y. F.; Xu, C.; Roberts, K. A.; Kaplan, D. I.; Brinkmeyer, R.; Yeager, C. M.; Santschi, P. H., A Novel Approach for the Simultaneous Determination of Iodide, Iodate and Organo-Iodide for I-127 and I-129 in Environmental Samples Using Gas Chromatography-Mass Spectrometry. *Environmental Science & Technology* **2010,** *44,* (23), 9042-9048.
15. R Core Team R: A Language and Environment for Statistical Computing. www.R-project.org/ (2Jun2018),
16. R Core Team and Contributors Worldwide The R Stats Package, Version 3.6.0. (2Jun2018),

ACRONYMS

Ag	Silver
Ag^0	Zero valent silver
AgI	Silver iodide
APS	Advanced Photon Source
CHN Analyzer	Carbon, Hydrogen, Nitrogen Analyzer
GAC	Granular activated carbon
$Grout_{+slag}$	Grout containing slag
$Grout_{-slag}$	Grout without slag
$Grout_{+slag/AgI-GAC}$	Grout with slag and silver impregnated activated carbon
$Grout_{-slag/AgI-GAC}$	Grout with slag and silver impregnated activated carbon
I^-	Iodide
IO_3^-	Iodate
K_d	Distribution coefficient
KI	Potassium iodide
KIO_3	Potassium iodate
XANES	X-ray Absorption Near-Edge Spectroscopy
XRF	X-ray Florescence
XRD	X-ray Diffraction

TOTAL NUMBER OF POST-DOCTORAL RESEARCHERS

2 Post-Doctoral Researchers were funded under this project: Dr. Chen Xu and Dr. Peng Liu from Texas A&M University

QUATERNARY AMINE-BASED SODALITE SORBENT FOR SELECTIVE REMOVAL OF TC-99 AND I-129

PROJECT TEAM:
J. O. Dickson (Primary), D. Li, D. I. Kaplan, J. C. Seaman, B. A. Powell

SUBCONTRATOR:
SREL, Clemson University

THRUST AREA:
Environmental Stewardship

PROJECT START DATE:
October 1, 2017

PROJECT END DATE:
September 30, 2018

Technetium-99 and Iodine-129 are risk-driven contaminants of high priority to DOE-EM office. Both radionuclides are prevalent at DOE nuclear waste sites. Because these radionuclides greatly affect the catalytic redox extraction process of uranium and plutonium in the fuel cycle, their removal from spent nuclear solution is highly desirable for efficient recovery of uranium and plutonium, and mitigation of potential releases of these radionuclides to the environment. The goals of this project were to develop advanced sorbents for simultaneous capture of Tc-99 and I-129 from contaminated groundwater and nuclear waste streams. This research examined modification of porous commercial and synthesized aluminosilicate minerals (zeolite) for enhanced retention of radionuclides. Herein we report the development of a sorbent that: (1) binds pertechnetate (TcO_4^-) with a sorption efficiency (K_d) greater than any other sorbent materials previously reported in literature, 2) exhibits fast sorption kinetics and (3) uptakes TcO_4^- under acidic and oxidizing conditions where Tc-99 retention is problematic. Thus, the use of quaternary-amine modified mesoporous zeolite as an amendment and/or permeable reactive barrier would be a robust strategy for Tc-99 remediation. Moreover, further modification of the evaluated zeolite materials with silver is envisioned to promote effective retention of both Tc-99 and I-129 and this study was slated for fiscal year 2019.

FY 2018

OBJECTIVES

The overarching objective the research was to develop an effective remediation technology for Tc-99 sequestration from contaminated aqueous media through syntheses, fine-tuning mineral structures and composition, and testing of several sequestering agents. Specifically, the objectives of this projects were as follows:

- Develop quaternary ammonium-functionalized zeolite sorbents (organo-zeolite) for enhanced removal of TcO_4^- from contaminated aqueous media.
- Compare sequestration of TcO_4^- by unmodified and modified zeolite.
- Demonstrate sorbents' performance characteristics and operational conditions for beneficial use in field conditions.
- Design modified sorbents for iodine sequestration during FY2019.

ACCOMPLISHMENTS

- Structural and chemical modification of zeolites significantly enhanced Tc-99 binding by several orders of magnitude, resulting in K_d values as high as 4 × 109 mL/g.
- Fast kinetic properties and high selectivity for Tc-99 were measured in the presence of competing anions.
- There was a steep increase in ReO_4^- (Tc-99 surrogate) uptake with increasing perrhenate concentration. Maximum loading capacity was over 100 mg/g and anticipated to be significantly higher with higher loading of the MSAV-15 sorbent with ReO_4^-.
- Follow-up work will focus on fine-tuning these sorbents for simultaneous capture of Tc-99 and I-129.

INTRODUCTION

Significance and Motivation: As contaminants of high priority to DOE-EM mission, technetium-99 and iodine-99 are key risk drivers at several DOE sites **[1].** Both are anionic radionuclides that pose potential long-term risks to public health and the environment due mainly to the burgeoning inventory, relatively long half-life, and high to extreme toxicity. Moreover, the predominant chemical speciation form of these radionuclides, i.e., pertechnetate (TcO_4^- and iodide (I–)/iodate (IO_3^-)), exhibit high environmental mobility that renders cleanup a technical challenge and costly endeavor **[2-5].**

Immobilization Technology: Among proposed remedial technologies are structural immobilization and stabilization of Tc-99 and I-129 in low-temperature waste forms, such as crystalline frameworks, carbon and clay/resin-based sorbents. The application of these remediation strategies has been largely hindered by the much higher concentrations, typically by several orders of magnitude, of competing anions commonly found in groundwater and nuclear waste streams. Because there are heightened needs for cost-effective technologies for Tc-99 and I-129 remediation, a proposed alternative approach is the use of quaternary ammonium-modified silver feldspathoids, specifically zeolite of the faujasite type to sequester both anions for long-term storage. Zeolite are porous aluminosilicate minerals comprised of alternating SiO_4 and AlO_4 tetrahedral units covalently joined by bridging O-atoms to form three-dimensional flexible frameworks with well-defined pores/cavities **(Figure 1) [6-8].** Due to the selective functionality of the 3-dimensional porous zeolite structure, removal of both Tc-99 and I-129 anions is feasible even in the presence of higher concentrations of competing ions (e.g., NO_3^- and CO_3^{2-}). Silver and quaternary ammonium-modified zeolites have been widely studied as potential hosts for I-129 and Tc-99; however, there is little published literature on bifunctional zeolite with silver and organic group, where both ligands are distributed on and within the zeolite structure for effective immobilization of Tc-99 and I-129.

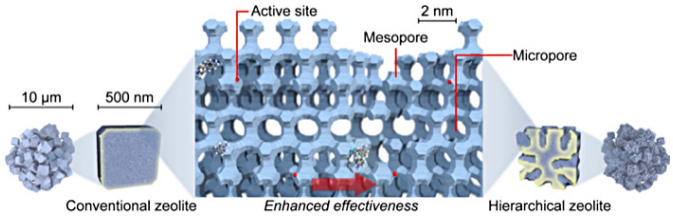

Figure 1. Creation of mesoporosity enhances the effectiveness of zeolite as a sequestering agent. Image adopted from Keller, 2015

APPROACH

Hydrophilic zeolites with Si/Al <10 (SAFE & SOTEF samples) were hydrothermally synthesized according to published literature while hydrophobic zeolite with Si/Al >10 (SAV-15) was acquired from Zeolyst International, Malvern PA. Commercial and synthesized zeolites were modified with quaternary ammonium, specifically hexadecyltrimethylammonium bromide ($C_{19}H_{42}NBr$), to enhance affinity for TcO_4^- **(Figure 2).** Benchtop batch studies were performed in SRS groundwater simulant and Tc-99 adsorbed to the zeolite sorbents were characterized by physicochemical techniques, such as powder X-ray diffraction, Brunauer-Emmett-Teller analysis, particle/zeta potential measurements, liquid scintillation counting, and ICP-MS. Factors such as effect of pH and counterions, and contact time were optimized for practical application of the sorbents. Rate equations and adsorption isotherms were employed to elucidate the adsorption mechanism.

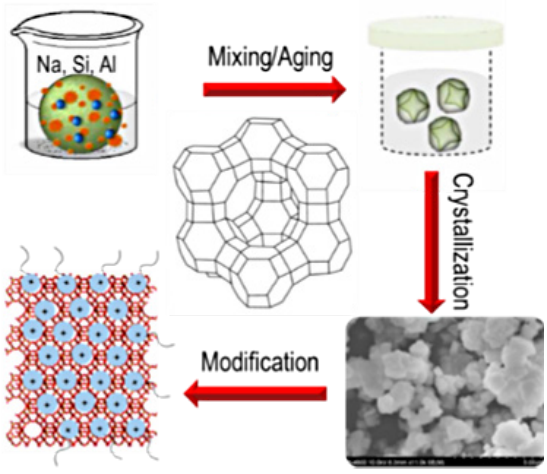

Figure 2. A generalized synthesis and modification procedure for zeolite.

Evaluation of the performance characteristics of the zeolites by batch adsorption tests were performed by adding 100 mg of unmodified and modified sorbents to 100 mL of SRS groundwater simulant. Then TcO_4^-/ReO_4^- activity/concentration, pH and reaction time were introduced into the solid-liquid mixtures as variables. The batch mixtures were spiked either with a known Tc-99 activity or rhenium (a Tc-99 surrogate) concentration and the pH and reaction time were varied from 3.5 – 10 and 5 - 1440 minutes, respectively. Upon completion of the reaction time the mixtures were passed through 0.2-µm polyestersulphone/polypropylene filters and the Tc-99 activity and/or rhenium concentration in each supernatant was either determined by LSC and/or ICP-MS, respectively. Sorption coefficient (K_d), kinetic and maximum adsorptive capacity values were then calculated from the supernatant concentrations using rate equations and adsorption isotherms.

RESULTS/DECISION

Morphology: The X-ray diffraction patterns of the unmodified and modified samples are displayed in **Figure 3.** The XRD patterns indicate that the samples were predominantly zeolite of the faujasite type framework (zeolite Y). However, the SAFE and MSAFE samples contained approximately less than 10% inclusions of another zeolite phase(s). Upon modification the zeolite characteristic peaks for the MSAV-15 sample compared to the SAV-15 shifted to a lower 2°θ value indicative of pore/cavity enlargement likely due to ingress of the organic ligand into the zeolite framework.

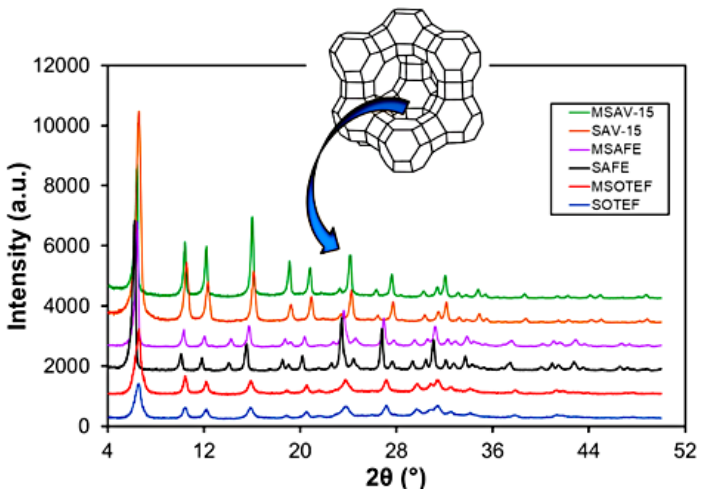

Figure 3: X-ray diffraction patterns of unmodified and modified zeolite Y.

The particle size characterization of the unmodified and modified samples is displayed in **Figure 4A.** The average particle size of the zeolite materials ranged from 0.5 – 4 μm with the SOTEF samples having the smallest particle size. The **zeta potential** measurements, indicative of point of net zero charge (PZC) on the structure is shown in **Figure 4B.** In general, all zeolite samples exhibited PZC at approximately pH of 5. At pH ≤ 5 the structure is expected to have a net positive charge whereas at pH ≥ 5 net negative charge.

Batch Sorption: Adsoption isotherms are important in understanding interaction of Tc-99 with the zeolites and optimizing the use of zeolites as a sorbent. Adsorption experiments at ambient pH indicate HDTMA-modified zeolites bound significant higher concentrations of Tc-99 compared to the unmodified zeolites. The distribution coefficient, K_d, which is the solids-to-liquid concentration ratio of the radionuclide (in units of mL/g) is used to describe the degree of sorption. High K_d values are indicative of greater extent of sorption. As shown in **Figure 5,** the K_d value after 24 hours of contact time at ambient pH of 5 – 8.5 for the zeolite samples were as high as approximately 5 to $>10^9$ mL/g. For purposes of comparison, typical K_d values for SRS and Hanford soils are between 0.1 and 2 mL/g [9]. The modification of the SAV-15 zeolite with HDTMA significantly increased Tc-99 sorption to the MSAV-15 material by a factor of approximately 10^7. It is worth noting that the high K_d value was calculated based on measurements near to the method detection limit. The K_d increases for MSAFE and MSOTEF samples were more moderate, approximately a factor of two and three, respectively.

Adsorption kinetics of Tc-99 on unmodified and modified zeolites exhibited initial steep increase in the adsorbed Tc-99 concentration with about 90–100% of the equilibrium concentration adsorbed within 60 minutes (data not shown). Tc-99 was adsorbed quickly by MSAV-15 zeolite during the first 30 minutes of solid–liquid contact time, rapidly progressing towards equilibrium within 5 to 10 minutes. Overall Tc-99 adsorbed best to MSAV-15 zeolite.

Technetium-99 sorption to zeolite materials as a function of pH is presented in **Figure 6A on following page.** The batch experiments were conducted in a 1:1000 solid-to-SRS groundwater simulant ratio. Overall modification enhanced Tc-99 sorption to the modified sorbent materials generally decreased with increasing pH values. Sorption of Tc-99 to MSOTEF and MSAV-15 materials varied from 27 – 66% and 61-99%, respectively. Among evaluated zeolites the MSAV-15 performed best at pH values of 3 – 5.

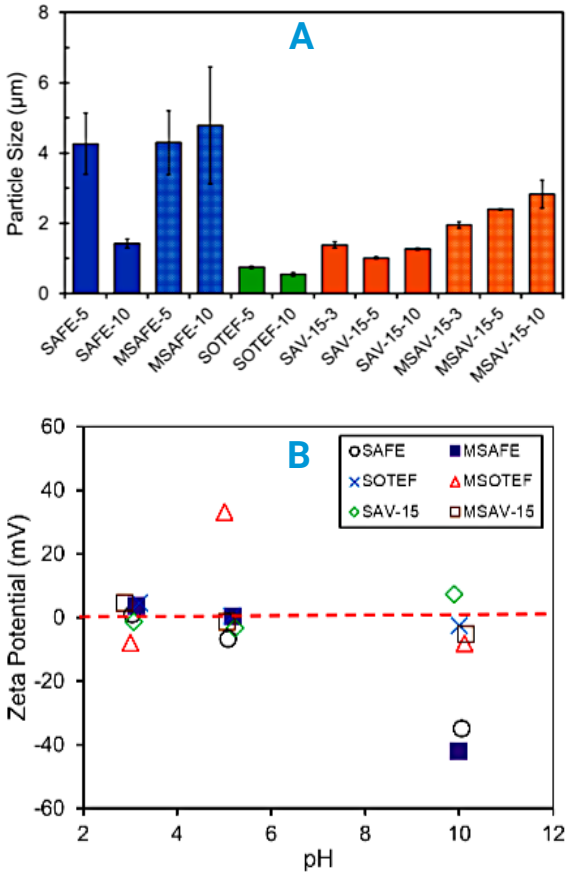

Figure 4. ***(Above)*** *Particle size distribution (A) and PZC (B) of unmodified and modified zeolite Y.* *Figure 5.* ***(Below)*** *TcO_4^- sorption (K_d) to unmodified and modified zeolite Y.*

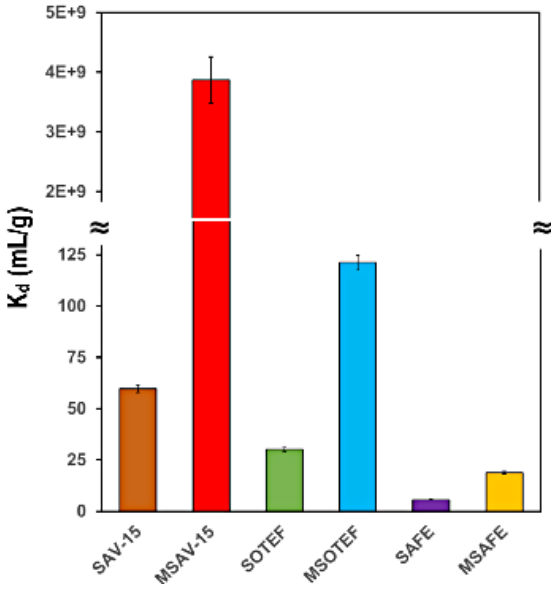

The maximum sorption of rhenium (Tc-99 surrogate) to MSAV-15 with increasing rhenium concentration is presented in **Figure 6B.**

The Type II adsorption isotherms (BET model identified as the Green Line in **Figure 6b**) satisfactorily describe this observed adsorption on MSAV-15 zeolites. The adsorption is considered a multilayer physical adsorption of ReO_4^- in the mesopores and macropores of the zeolite sorbent consistent with observed X-ray data. It is worth noting that a plateau of ReO_4^- sorption had not been reached and it is highly likely that higher loadings of ReO_4^- on the MSAV-15 sorbent could be achieved.

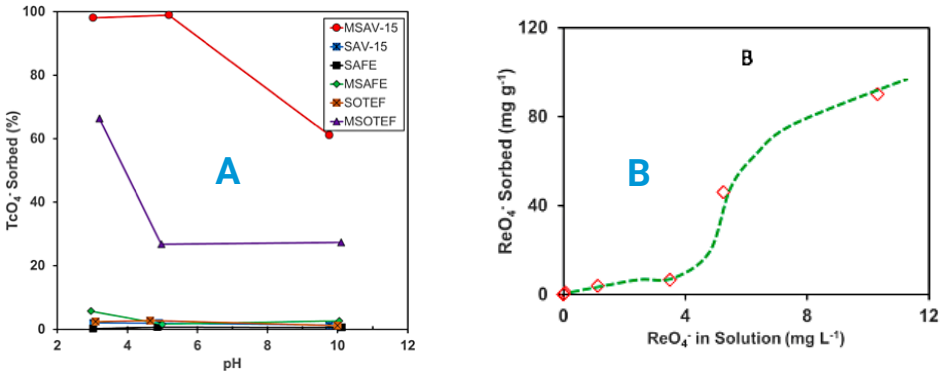

Figure 6. pH-dependent TcO_4^- sorption (A) to unmodified & modified zeolite and ReO_4^- sorption isotherm (B) of MSAV-15.

FUTURE DIRECTIONS

- Seed data from this study will be leveraged to solicit external funding from the following agencies: DOE Environmental Management (EM-12 Soil and Groundwater Remediation; EM-20 Tank Waste and Nuclear Materials disposition), DOE Office of Science (SC-22.2 Materials Sciences), and DOE Office of Nuclear Energy (NE-University Programs (NEUP)).
- Additionally, study results will find application for: (1) DOE-EM Technology Development's initiative on technetium, (2) DOE-SC Basic Energy Sciences annual call in Geosciences, and (3) DOE-SC Basic Energy Sciences annual call in Separation Science.

PUBLICATIONS

1. Dickson J. O., Li D., Kaplan D. I., Seaman J. C., Conroy N. A., and Powell B. A., (2018). Structural Organo-Modified Feldspathoid for Selective Removal of Anionic Radionuclides. The 28th Goldschmidt conference, August 2018, Boston, Massachusetts, USA.
2. Dickson J. O., Li D., Kaplan D. I., Seaman J. C., Conroy N. A., and Powell B. A., (2018). Structural Organo-Modified Feldspathoid For Selective Removal of Technetium-99 and Iodine-129. The 19th International Conference on Heavy Metals in the Environment (ICHMET). July 2018, Athens, Georgia, USA.

REFERENCES

1. Kaplan D.I., et al., Radioiodine biogeochemistry and prevalence in groundwater Critical Reviews of Environmental Science and Technology, 2014. 44(20): p. 2287-2337
2. Jaisi D. P., Dong H., Plymale A. E. Fredrickson J. K., Zachara J. M., Heald S., and Liu C., 2009. Reduction and Long-Term Immobilization of Technetium by Fe(II) associated with Clay Mineral Nontronite, Chemical Geology, 264 (2009), pp. 127-138, doi:10.1016/j. chemgeo.209.02.018.
3. Marshall T. A., Morris K., Law G. T. W., Mosselmans J. F., Bots P., Parry S. A., and Shaw S., 2014. Incorporation and Retention of 99-Tc(IV) in Magnetite under High pH Conditions, Environmental Science and Technology, 48 (2014), pp. 11853-11862, dx.doi.org/10.1021/es503438e.
4. Hou X., Hansen V., Aldahan A., Possnert G., Lind O. C., and Lujaniene G., 2009. A Review on Speciation of Iodine-129 in the Environmental and Biological Samples, Analytica Chimica Acta, 632 (2009), pp. 181-196, doi:10.1016/ j.aca.2008.11.013.
5. Zhang S., Fo Y., Creeley D., Roberts K., Xu C., Li H., Schwehr K., Kaplan, D., Yeager, C., and Santschi P, 2014. Temporal Variation of Iodine Concentration and Speciation (127I and 129I) in Wetland Groundwater from the Savannah River Site, USA, Environmental Science & Technology, 2014, 48 (19), pp. 11218-11226, doi:10.1021/es502003q.
6. Depmeier W., The sodalite family - A simple but versatile framework structure, in: G. Ferraris, S. Merlino (Eds.) Micro- and Mesoporous Mineral Phases2005, pp. 203-240.
7. Keller T., Arras J., Stefan Wershofen S., and Javier Pérez-Ramírez J., 2015. Design of Hierarchical Zeolite Catalysts for the Manufacture of Polyurethane Intermediates, ACS catalysis, 2015, 5, pp. 734–743, doi: 10.1021/cs5017694.
8. Smedt C., Ferrer F., Leus K., and Spanoghe P., 2015. Removal of Pesticides from Aqueous Solutions by Adsorption on Zeolites as Solid Adsorbents, Adsorption Science & Technology, 2015, 33, pp. 457-484.
9. Kaplan, Daniel I. Geochemical Data Package for Performance Assessment Calculations Related to the Savannah River Site. United States: N. p., 2016. Web. doi:10.2172/1281771.

ACRONYMS

Al	Aluminum
DOE	Department of Energy
CO_3^{2-}	Carbonate
EM	Environmental Management
HDTMA	Hexadecyltrimethylammonium
ICP-MS	Inductively coupled plasma mass spectroscopy
I^-	Iodide
IO_3^-	Iodate
NO_3^-	Nitrate
PZC	Point of net zero charge
TcO_4^-	Pertechnetate
ReO_4^-	Perrhenate
Si	Silica
SRS	Savannah River Site
K_d	Sorption coefficient
SAVE-15	Commercial zeolite Y with Si/Al ≈ 80
MSAVE-15	HDTMA-modified zeolite Y with Si/Al ≈ 80
SOTEF	Organic-template free zeolite Y synthesized according to Tang et al, 2016
MSOTEF	HDTMA-modified organic-template free zeolite Y synthesized according to Tang et al, 2016
SAFE	Zeolite Y synthesized according to Ferdov et al, 2017
MSAFE	HDTMA-modified zeolite Y synthesized according to Ferdov et al, 2017

TOTAL NUMBER OF POST-DOCTORAL RESEARCHERS

Dr. Nathan Conroy, Clemson University
Dr. Yuyu Xie, Clemson University
Dr. Fanny Coutelot, SRwEL, University of Georgia

METAL-ORGANIC-FRAMEWORK GLASSES AS RAD CONTAMINANT SEQUESTERS AND NUCLEAR WASTE FORMS

PROJECT TEAM: Dien Li (Primary), Natalia Shustova (U of South Carolina), Kathryn Taylor-Pashow, Daniel I. Kaplan, Jake Amoroso, Tom Bennett (U of Cambridge, UK)

SUBCONTRATOR:
University of South Carolina

THRUST AREA:
Environmental Stewardship

PROJECT START DATE:
October 1, 2017

PROJECT END DATE:
September 30, 2018

Remediation of Tc remains an unresolved challenge at SRS and other DOE sites. The objective of this project was to develop novel metal organic framework (MOF) glasses for radioactive contaminant sequestration and stabilization from aqueous media. We synthesized, characterized and evaluated ten MOFs of known crystal structure and chemistry for screening MOFs for TcO_4^- and ReO_4^- sequestration. MIL-101(Cr) was most effective for TcO_4^- and ReO_4^- sequestration from artificial groundwater at equilibration pH values with the removal capacity of 0.076 mg/g for Tc and 0.197 mg/g for Re. MIL-101(Fe), SLUG-22 and UiO-66-NO2 were moderately effective under similar conditions (pH < 8). These results established a solid foundation for further development of MIL-101(Cr) and new MOFs to increase TcO_4^- removal capacity and improve MOF structural stability in FY19. This research may provide a highly applicable platform for solving critical DOE and industrial problems related to nuclear environmental stewardship and nuclear power production.

FY 2018

OBJECTIVES

- Synthesize and characterize ten MOFs of known crystal structure and chemistry.
- Evaluate the MOFs for TcO_4^- and ReO_4^- removal from artificial groundwater.
- Develop methods for vitrifying the crystalline MOFs.

ACCOMPLISHMENTS

- Ten MOFs of known crystal structure and chemistry were synthesized, characterized and evaluated for TcO_4^- and ReO_4^- sequestration from artificial groundwater.
- UiO-66-NO_2 was effective for sequestering TcO_4^- from groundwater at pH 3 and 7.5.
- MIL-101(Cr) was most effective for TcO_4^- and ReO_4^- sequestration from artificial groundwater at equilibration pHs with the removal capacity of 0.076 mg/g for Tc and 0.19 7 mg/g for Re. MIL-101(Fe) and SLUG-22 were moderately effective for TcO_4^- and ReO_4^- sequestration under similar conditions.
- MIL-101(Cr) is targeted as a top candidate for developing new MOFs with higher TcO_4^- removal capacity and improved stability during FY19. MIL-101-Fe, UiO-66-NO_2 and SLUG-22 are potentially candidates.

INTRODUCTION

^{99}Tc is a major long-lived fission product created during nuclear power generation. Over the years, Tc has been inadvertently introduced into the environment from leaks at waste storage facilities. ^{99}Tc currently is one of the key risk drivers at the Savannah River Site (SRS) and other DOE environmental management sites (most notably the Hanford Site, Paducah Gaseous Diffusion Plant, and Oak Ridge National Laboratory). The most common chemical form of Tc in liquid nuclear wastes and in the environment is anionic pertechnetate (TcO_4-). TcO_4- displays limited adsorption onto common sediment minerals and is highly mobile making it difficult to capture or to be immobilized **[1]**. As the stockpile of ^{99}Tc-bearing nuclear waste continues to increase rapidly, novel sequestration technologies are needed to reduce its potential contamination of the environmental and living organisms.

With current technologies, quaternary amine-based resins have been used to remove aqueous Tc **[2**]. However, these resins are expensive and have only modest TcO_4- loading capacities from the raffinate waste streams. Chemical reductants (e.g., Fe_3S_4, soluble or structural Fe(II)) **[3]** and some bacteria **[4]** can reduce Tc(VII) to the sparingly soluble Tc(IV). However, the resulting $Tc(IV)O_2 \cdot 1.6H_2O$ has a solubility of 1.5×10^{-8} M in groundwater **[5]**, which greatly exceeds the EPA's maximum contaminant level of 5×10^{-10} M, and is readily re-oxidized and re-mobilized under most environmental conditions **[6].** Tc reduction to form sulfides (e.g., Tc2S7) **[7]** or embedding into other sulfide phases **[8]** or iron oxide waste forms **[9]** have also been investigated. However, these methods are not practical for many applications. There are currently no demonstrated technologies that are highly efficient and cost-effective for separation of Tc-containing nuclear waste streams and remediation of aqueous Tc in the contaminated sites.

The overarching objective of this project was to develop novel metal organic framework (MOF) glasses as radioactive contaminant sequesters and nuclear waste forms. During FY18, we synthesized and characterized ten MOFs of known crystal structure and chemistry, evaluated them for TcO_4- and ReO_4- sequestration from artificial groundwater, and investigated their thermal properties that would help in developing vitrification technology. Based on the selected types of MOFs, we will develop new MOFs that are expected to have higher capacity, improved selectivity and stability for TcO_4- and other anionic contaminant sequestration from aqueous media.

APPROACH

A general two-step approach is adopted in the implementation of this project. First, during FY18, we synthesized, characterized and evaluated MOFs of known crystal structure and chemistry to screen out the types of MOFs that might show high capacity and high stability for TcO_4- sequestration from groundwater. As this project has been renewed for FY19, we will focus on selected types of MOFs to develop new MOFs through ion exchange, functionalization, or scissor / insert methods. The new MOFs are expected to have higher Tc capacity and improved stability. Powder X-ray diffraction (XRD), BET surface area measurement and thermogravimetric analysis were used for MOF characterization, while synchrotron radiation X-ray absorption spectroscopy will be applied to studying Tc or Re speciation after the sequestration by MOFs.

RESULTS/DECISION

Synthesis of MOFs

We set three criteria in the screening of MOFs for FY18: (i) high stability in aqueous media, including high pH solutions similar to nuclear waste streams, (ii) high capability for removing anions like TcO_4-, I-, IO_3-, and organo-I-, and (iii) potential for economical vitrification. As such, ten MOFs have been selected and prepared at the University of South Carolina (Dr. Natalia Shustova) to determine which types of MOFs are best fitted to these criteria.

1.1. ZIF-8 ($Zn(mIM)_2$; mIM = 2-methylimidazolate, ZIF = Zeolitic Imidazolate Framework). Zinc nitrate hexahydrate ($Zn(NO_3)_2 \cdot 6H_2O$) (0.239 g, 8.03×10^{-4} mol) and 2-methylimidazole (0.060 g, 7.31×10^{-4} mol) was dissolved in 18 mL DMF in a 40 mL vial. The vial was capped and heated at a rate of 5 °C/min to 140 °C in a programmable oven, held at this temperature for 24 h, then cooled at a rate of 0.4 °C/min to room temperature. The mother liquor was then decanted and replaced with 20 mL of chloroform. Colorless crystals were collected from the upper layer (floating on the chloroform layer) and washed with DMF (10 mL x 3) and dried under high-vacuum for 1 hour **[10]**.

1.2. ZIF-67 ($Co(mIM)_2$; mIM = 2-methylimidazolate). Two separate mixtures of cobalt nitrate hexahydrate ($Co(NO_3)_2)\cdot 6H_2O$) (0.225 g, 7.73 x 10^{-4} mol) dissolved in 6 mL of deionized H_2O, and 2-methylimidazole (2.75 g, 3.34 x 10^{-2} mol) dissolved in 40 mL of H_2O were combined in a round-bottom flask equipped with a condenser and heated with stirring at 60 °C for 12 minutes. Stirring was halted after 12 minutes and the solution was left at 60 °C for 20 hours, and then cooled to room temperature. The suspension was then filtered and washed with methanol (10 mL x 3) and dried under high-vacuum for 1 hour **[11].**

1.3. ZIF-70 ($Zn(IM)_{1.13}(nIM)_{0.87}$; IM = imidazolate, nIM = 2-nitroimidazolate). In a 20 mL glass vial, 5 mL from a 2-nitroimidazole stock solution (0.20 M, 1.0 × 10^{-3} mol) and 5 mL imidazole stock solution (0.20 M, 1.0 × 10^{-3} mol) were mixed together. Subsequently, 4 mL of a zinc nitrate hexahydrate stock solution (0.20 M, 8.0 × 10^{-4} mol) was added and stirred. The resulting solution was capped and heated at 110 °C for 4 days, followed by natural cooling to room temperature. Upon cooling, the resulting yellow-orange crystals were filtered and washed with DMF (3 x 15 mL) **[12].**

1.4. UiO-66-NO_2 ($Zr_6O_4(OH)_4(BDC\text{-}NO_2)_6$; BDC-$NO_2^{2-}$ = 2-nitrobenzene-1,4-dicarboxylate, UiO = University of Oslo). Zirconium chloride (ZrCl4) (0.923 g, 3.96 x 10^{-3} mol) and 2-nitroterephthalic acid (0.845 g, 4.00 x 10^{-3} mol) were placed in a 40 mL vial and then dissolved in 10 mL of DMF, followed by the addition of 0.67 mL of concentrated hydrochloric acid. The vial was capped and heated at a rate of 1 °C/min to 120 °C in a programmable oven, held at this temperature for 16 h, then cooled at a rate of 0.4 °C/min to room temperature. The powder was then filtered, washed with DMF (10 mL x 3) then placed back in a DMF solution **[13].**

1.5. ZIF-71 ($Zn(dcIM)_2$; dcIM = 4,5-dichloroimidazolate). A solution of zinc acetate dihydrate ($Zn(O_2CCH_3)\cdot 2H_2O$ (0.088 g, 4.0 x 10^{-4} mol) in 15 mL of methanol and a solution of 4,5-dichloroimidazole (0.219 g, 1.6 x 10^{-3} mol) in 15 mL of methanol were combined in a 40 mL vial. The vial was then sealed and let to stand at room temperature for 24 h. The methanol was then removed by pipet and 20 mL of fresh chloroform was added every day for three days. The crystalline powder was then filtered and dried under high-vacuum for 1 hour **[14].**

1.6. ZIF-82 (Zn(nIM)(cIM); nIM = 2-nitroimidazolate, cIM = 5-cyanoimidazolate). In a 20 mL glass vial, 5 mL of a 2-nitroimidazole stock solution (0.20 M, 1.0 × 10^{-3} mol) and 5 mL of a 5-cyanoimidazole stock solution (0.20 M, 1.0 × 10^{-3} mol) were mixed together. Subsequently, 4 mL of a zinc nitrate hexahydrate stock solution (0.20 M, 8.0 × 10^{-4} mol) was added and stirred. The resulting solution was capped and heated at 100 °C for 4 days, followed by natural cooling to room temperature. Upon cooling, the resulting yellow-orange crystals were filtered and washed with DMF (3 x 15 mL) **[12].**

1.7. MIL-101-Cr ($Cr_3F(H_2O)_2O(BDC)_3$; BDC = 1,4-benzenedicarboxylate, MIL = Materials Institute Lavoisier). Chromium(III) nitrate nonahydrate (0.400 g, 1.00 × 10^{-3} mol) was dissolved in 4.8 mL of deionized water, then placed in a Teflon-lined autoclave. Terepthalic acid (0.164 g, 9.87 × 10^{-4} mol) was then added followed by the addition of 0.2 mL of HF (5.0 M, 1.0 × 10^{-3} mol). The autoclave was then sealed and placed in an oven at 220 °C for 8 hours. Upon cooling, the resulting green solid was centrifuged to collect the precipitate and solvent exchanged with DMF (3 × 10 mL) with centrifugation between each exchange. The product was then heated in DMF (120 °C, 12 h), filtered, and then boiling ethanol (80 °C, 12 h) and filtered off **[15].**

1.8. MIL-101-Fe ($Fe_3Cl(C_3H_7NO)O(BDC)_3$; BDC = 1,4-benzenedicarboxylate). Iron(III) chloride hexahydrate (0.325 g, 1.20 × 10^{-3} mol) and terepthalic acid (0.103 g, 6.20 × 10^{-4} mol) were dissolved in 10 mL DMF by sonication, followed by stirring for 20 minutes. The resulting solution was then loaded into a Teflon-lined autoclave. The autoclave was then sealed and placed in an oven at 110 °C for 24 hours. Upon cooling, the resulting brown solid was centrifuged to collect the precipitate and solvent exchanged with DMF (3 × 10 mL) with centrifugation between each exchange. The product was then heated in DMF (120 °C, 12 h), filtered, and then boiling ethanol (80 °C, 12 h) and filtered off **[15].**

1.9. SLUG-21 ($Ag_2(bpy)_2(O_3SCH_3CH_2SO_3)$; bpy = 4,4-bipyridine, SLUG = University of California, Santa Cruz). Silver nitrate ($AgNO_3$, 0.236 g, 1.40 x 10^{-3} mol), 1,3-ethanedisulfonic acid dehydrate (0.314 g, 1.39 x 10^{-3} mol) and 4,4-bipyridine (0.217 g, 1.39 x 10^{-3} mol) were suspended in 10 mL of deionized water and stirred for 3 minutes. The resulting mixture was loaded into a Teflon-lined autoclave, sealed, and then heated in an oven at 150 °C for 3 days, followed by natural cooling to room temperature. Upon cooling, the resulting colorless plate crystals were filtered, washed with deionized water (3 x 15 mL) and washed with acetone (3 x 15 mL) **[16].**

1.10. SLUG-22 ($Cu_2(bpy)_2(O_3SCH_3CH_2SO_3)$; bpy = 4,4-bipyridine). Copper acetate monohydrate (0.054 g, 2.70 x 10^{-4} mol), 1,2-ethanedisulfonic acid dihydrate (0.073 g, 3.23x 10^{-4} mol) and 4,4'-bipyridine (0.042 g, 2.70 x 10^{-4} mol) were suspended in 2 mL of deionized water and stirred for 30 minutes. The resulting mixture was loaded into a Teflon-lined autoclave, sealed, and then heated in an oven at 175 °C for 4 days, followed by cooling at a rate of 7 °C/hour. Upon cooling, the resulting yellow-green needle-like crystals were filtered, washed with deionized water (3 x 15 mL) and washed with acetone (3 x 15 mL) **[17].**

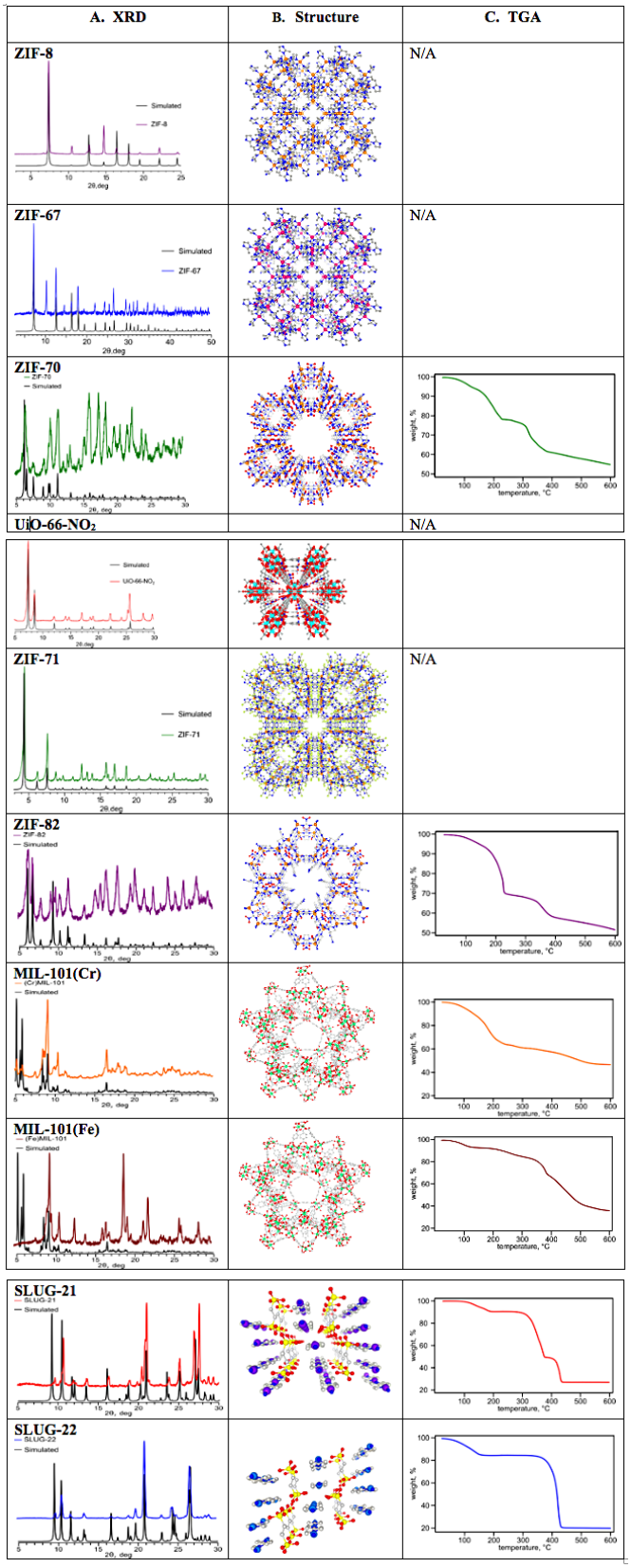

Figure 1. XRD (A), crystal structure (B) and TGA (C) of MOFs

Characterization of MOFs

The MOFs were characterized by powder X-ray diffraction (XRD) and thermogravimetric analysis (TGA) to confirm their known crystal structure **(Figure 1).**

Effectiveness of MOFs for TcO_4^- and ReO_4^- sequestration from artificial groundwater

The ten MOFs were evaluated for TcO_4^- and its non-radioactive surrogate, ReO_4^-, sequestration from artificial groundwater under atmospheric ($PCO2 = 10^{-3.5}$ atm) conditions. Sorption coefficient (K_d, mL/g) and the equilibrium sorption capacity (q_e, mg/g) were calculated using formula 1 and 2, respectively:

$$K_d = \frac{C_0 - C_e}{C_e} \times \frac{V}{M} \quad (1)$$

$$q_e = \frac{(C_0 - C_e) \times V}{M} \quad (2)$$

where C_0 and C_e were Tc or Re concentrations before and after adsorption, respectively, V was the total volume of liquid phase (i.e., groundwater), and M was the mass of the solid material.

The adsorption coefficients of ZIF-8, ZIF-67, ZIF-70 and UiO-66-NO_2 from the first-round sample preparation are summarized in **Table 1 on following page.** The results demonstrated that UiO-66-NO_2 was effective for sequestering TcO_4^- from groundwater at pH 3 and 7.5. Some MOFs were not stable under acid conditions. New MOFs need to be developed for Tc uptake under alkaline conditions.

MOFs	K_d (mL/g)		
	pH 3	pH 7.5	pH 12
ZIF-8	unstable	72	0
ZIF-67	unstable	9	0
ZIF-70	12	0	0
UiO-66-NO_2	750	156	0

Table 1. Adsorption coefficient (K_d, mL/g) of ZIF-8, ZIF-67, ZIF-70 and UiO-66-NO2 for TcO_4^- removal from artificial groundwater of different pH values

The adsorption quantities of ZIF-70, ZIF-82, MIL-101(Cr), MIL-101(Fe), SLUG-21 and SLUG-22 for TcO_4^- sequestration from artificial groundwater at equilibration pH values were determined using batch experiments. The results **(Figure 2)** demonstrated that MIL-101(Cr) was most effective for TcO_4^- and ReO_4^- sequestration from artificial groundwater at equilibration pH values with the removal capacity of 0.076 mg/g for Tc and 0.197 mg/g for Re. MIL-101(Fe) and SLUG-22 were moderately effective for TcO_4^- and ReO_4^- sequestration under similar conditions.

Potential for Economical Vitrification

Thermogravimetric analyses of selected MOFs were conducted **(Figure 1 on previous page).** The results indicated that these MOFs may be vitrified using economic methods, like heating under 400 °C. The actual vitrification technology will be developed for the eventually selected MOFs that are demonstrated to have high capacity for TcO_4^- removal and improved stability in aqueous media.

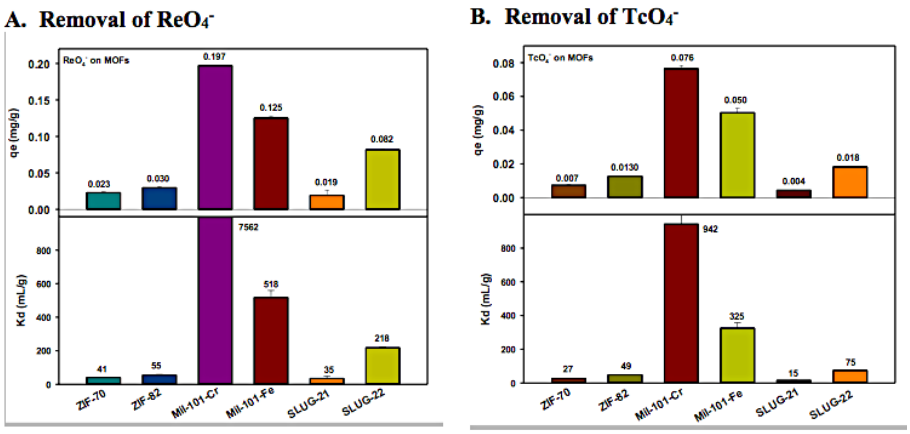

Figure 2. Removal capacity of MOFs for ReO_4^- (A) and TcO_4^- (B) sequestration from artificial groundwater.

FUTURE DIRECTIONS

- Develop new MOFs for higher TcO_4^- removal capacity and improved stability, especially under alkaline conditions.
- Evaluate MOFs for TcO_4^- removal under different environmental and geochemical. conditions (i.e., pH, Eh, solution chemistry) and for TcO_4^- separation from liquid nuclear wastes.
- Prepare proposals to DOE EM Soil & Groundwater Remediation Program, International Program, and DOE Nuclear Energy program.

PUBLICATIONS/PRESENTATIONS

1. Dien Li, Natalia B. Shustova, Kathryn M. Taylor-Pashow, Daniel I. Kaplan, Jake W. Amoroso, Thomas D. Bennett, Metal-Organic-Frameworks (MOFs) for Sequestration and Stabilization of Pertechnetate (TcO_4-) from Groundwater and Liquid Nuclear Wastes, *International Conference of Heavy Metals in the Environment* 2018, Athens, USA, July 21-25, **2018.**

REFERENCES

[1] J.P. Icenhower, N.P. Qafoku, J.M. Zachara, W.J. Martin, The biogeochemistry of technetium: A review of the behavior of an artifical element in the natural environment, Am. J. Sci., 310 (2010) 721-752.

[2 L.Y. Liang, B.H. Gu, X.P. Yin, Removal of technetium-99 from contaminated groundwater with sorbents and reductive materials, Sep. Technol. 6 (1996) 111-122.

[3] T. Peretyazhko, J.M. Zachara, S.M. Heald, B.H. Jeon, R.K. Kukkadapu, C. Liu, D. Moore, C.T. Resch, Heterogeneous reduction of Tc(VII) by Fe(II) at the solid-water interface, Geochim. Cosmochim. Acta, 72 (2008) 1521-1539.

[4] A.E. Plymale, J.K. Fredrickson, J.M. Zachara, A.C. Dohnalkova, S.M. Heald, D.A. Moore, D.W. Kennedy, M.J. Marshall, C.M. Wang, C.T. Resch, P. Nachimuthu, Competitive reduction of pertechnetate ((TcO_4-)-Tc-99) by dissimilatory metal reducing bacteria and biogenic Fe(II), Environ. Sci. Technol. 45 (2011) 951-957.

[5] D. Li, D.I. Kaplan, Solubility of Technetium Dioxides (TcO_2-c, TcO_2·1.6H_2O and TcO_2·2H_2O) in Reducing Cementitious Material Leachates: A Thermodynamic Calculation, Savannah River National Laboratory, Aiken, SC 20908, 2013.

[6] J.K. Fredrickson, J.M. Zachara, A.E. Plymale, S.M. Heald, J.P. McKinley, D.W. Kennedy, C.X. Liu, P. Nachimuthu, Oxidative dissolution potential of biogenic and abiogenic TcO2 in subsurface sediments, Geochim. Cosmochim. Acta, 73 (2009) 2299-2313.

[7] Y. Liu, J. Terry, S. Jurisson, Pertechnetate immobilization in aqueous media with hydrogen sulfide under anaerobic and aerobic environments, Radiochim. Acta, 95 (2007) 717-725.

[8] D.M. Fan, R.P. Anitori, B.M. Tebo, P.G. Tratnyek, J.S.L. Pacheco, R.K. Kukkadapu, M.H. Engelhard, M.E. Bowden, L. Kovarik, B.W. Arey, Reductive sequestration of pertechnetate ((TcO_4-)-Tc-99) by nano zerovalent iron (nZVI) transformed by abiotic sulfide, Environ. Sci. Technol., 47 (2013) 5302-5310.

[9] W. Um, H.S. Chang, J.P. Icenhower, W.W. Lukens, R.J. Serne, N.P. Qafoku, J.H. Westsik, E.C. Buck, S.C. Smith, Immobilization of 99-technetium (VII) by Fe(II)-goethite and limited reoxidation, Environ. Sci. Technol. 45 (2011) 4904-4913.

[10] K.S. Park, Z. Ni, A.P. Cote, J.Y. Choi, R.D. Huang, F.J. Uribe-Romo, H.K. Chae, M. O'Keeffe, O.M. Yaghi, Exceptional chemical and thermal stability of zeolitic imidazolate frameworks, Proc. Nat. Acad. Sci. U.S. America, 103 (2006) 10186-10191.

[11] J.F. Qian, F.A. Sun, L.Z. Qin, Hydrothermal synthesis of zeolitic imidazolate framework-67 (ZIF-67) nanocrystals, Mater. Lett. 82 (2012) 220-223.

[12] R. Banerjee, Control of pore size and functionality in isoreticular zeolitic imidazolate frameworks and their carbon dioxide selective capture properties, J. Am. Chem. Soc., 131 (2009) 3875-3877.

[13] Z.H. Rada, H.R. Abid, H.Q. Sun, S.B. Wang, Bifunctionalized metal organic frameworks, UiO-66-NO_2-N (N = -NH_2, -$(OH)_2$, -$(COOH)_2$), for enhanced adsorption and selectivity of CO2 and N2, J. Chem. Eng. Data, 60 (2015) 2152-2161.

[14] R.P. Lively, M.E. Dose, J.A. Thompson, B.A. McCool, R.R. Chance, W.J. Koros, Ethanol and water adsorption in methanol-derived ZIF-71, Chem. Commun., 47 (2011) 8667-8669.

[15] I.Y. Skobelev, A.B. Sorokin, K.A. Kovalenko, V.P. Fedin, O.A. Kholdeeva, Solvent-free allylic oxidation of alkenes with O_2 mediated by Fe- and Cr-MIL-101, J. Catal., 298 (2013) 61-69.

[16] H.H. Fei, M.R. Bresler, S.R.J. Oliver, A New paradigm for anion trapping in high capacity and selectivity: Crystal-to-crystal transformation of cationic materials, J. Am. Chem. Soc., 133 (2011) 11110-11113.

[17] H.H. Fei, D.L. Rogow, S.R.J. Oliver, Reversible anion exchange and catalytic properties of two cationic metal-organic frameworks based on Cu(I) and Ag(I), J. Am. Chem. Soc., 132 (2010) 7202-7209.

ACRONYMS

DOE	Department of Energy
MIL	Materials Institute Lavoisier
SLUG	University of California, Santa **Cruz**
SRS.09	Savannah River Site
TGA	Thermogravimetric analysis
UiO	University of Oslo
XRD	X-ray diffraction
ZIF	Zeolitic Imidazolate Framework

TOTAL NUMBER OF POST-DOCTORAL RESEARCHERS

0.5 of post-doctoral researcher involved through the subcontractor with the University of South Carolina.

IN-SITU METHOD DEVELOPMENT TO IDENTIFY RADIOLOGICAL CONTAMINATION IN SOILS

PROJECT TEAM:
T. S. Whiteside (Primary), K. M. Fenker, A. D. Brand, T. Aucott

THRUST AREA:
Environmental Stewardship

PROJECT START DATE:
October 1, 2017

PROJECT END DATE:
September 30, 2018

Rapid in-situ analysis of soil contamination could eliminate the need for 90% of laboratory analyses, reduce waste, and decrease cost. Increasing the number of sites analyzed per dollar spent would allow for more precisely defined contamination areas. The proposed work fits in well with DOE-EM and DOE-NNSA missions to monitor the environment during clean-up or post-detonation analysis. It fits with SRNL business-unit program plans for (SRNL-ES) advancing techniques for characterizing contaminants in-situ and (SRNL-NS) advancing sampling and analytical capabilities for detection.

This project has developed an in-situ method to characterize radiological contamination in soils using commercial-off-the-shelf detectors coupled with nuclear physics models so that it is inexpensive, fast, and can be done by minimally trained personnel.

FY 2018

Objectives

- Develop a method to measure any type of soil (clay, sand, loam) for contamination of ^{137}Cs, in the field, at accuracies equivalent to those obtained by laboratory measurements.
- Determine if different soil composition and soil moisture content significantly impact radiation measurements.
- Determine quality of portable USB-based instrumentation
- Determine if the depth of contamination can be calculated from measured radiation energies

Accomplishments

- Developed a simple-to-use method that with minimal further development could be deployed for use in the field.
- Demonstrated that this method is appropriate for determining the footprint of a contaminated area (> 1 pCi/g), it is not appropriate for measuring global-background levels of contamination (0.1 pCi/g).
- Soil composition is not a major source of error in reporting overall concentration of contamination.
- The performance of all USB-based instrumentation is nearly equal. The primary difference between them is the ease of setup (Digibase), simplicity of custom programming (TB-5), and cost (Digibase).
- Depth to contamination can be determined with prior knowledge of a site, however it may not be necessary for practical cleanup purposes.

INTRODUCTION

Currently, when sampling soils for radiological contamination, technicians dig holes, remove samples, transport the samples to a laboratory, analyze the samples in the laboratory, and then return the sample to the site or dispose of the sample. Rapid in-situ analysis could eliminate the need for 90% of laboratory analyses, reduce waste, and decrease cost. Increasing the number of sites analyzed per dollar spent would allow for more precisely defined contamination areas. This work builds on a method developed for the Savannah River Nuclear Solutions' Environmental Compliance group to determine ^{137}Cs in fauna and technology developed for DOE's Office of Nuclear Incident Response. The ^{137}Cs method previously developed is as accurate as the laboratory measurements and provides results in minimal time. We extended this method to other media (soils) and were able to report possible contamination levels within the measured volume.

The method developed can be used to rapidly delineate the footprint of a contamination area and report the possible contamination in a specific volume of soil. In addition, this work has examined the performance of different pieces of hardware used during the measurement process which has led to a better understanding of when to select a specific instrument. Furthermore, this work has explored the possibilities of measuring contamination that is buried and using the spectra to report the depth.

APPROACH

To develop a rapid, portable method for measuring ^{137}Cs in soils we started with the method developed for measuring ^{137}Cs in animals hunted at the Savannah River Site. We determined the impact different soil types (sandy, clayey, loamy) and compositions (wet, dry, porous, solid) would have on the measurements by creating several models using nuclear physics code. To determine the minimum count time, we considered the SCDHEC and EPA regulations to determine the cleanup standards for ^{137}Cs at SRS, which is 28 pCi/g [DHEC2016], desired uncertainty, which is an order of magnitude [EPA2000]. To accurately measure the soil volume, we developed a method for configuring the detector, shielding, and calibration source such that the detector could be held in a consistent position. To determine the concentration in a specified volume of soil (1 cm, 5 cm, 15 cm, and infinite from the surface) we measured the volume "seen" by the detector and used nuclear physics code to distribute a standard quantity of ^{137}Cs throughout these volumes and created scaling factors to relate actual to modeled measurements. We validated these factors on certified phantoms and tested the method in the field.

To make this system more portable (controllable from smartphone or tablet), we evaluated several commercially available USB-based multi-channel analyzers on the basis of ease-of-use, performance, programmability, and price.

To determine the depth of a buried contamination layer, we used the peak-to-valley ratio of a ^{137}Cs spectra obtained at different depths to create a calibration curve. To use this curve with confidence requires knowledge of a site's history.

RESULTS/DECISION

Due to the (relative) low molecular weight of soil minerals, there were no differences in the modeled detector response for soil composed of different types of solids. Different soil saturation levels do impact the detector response, due to the different densities. However, an error of 13% in estimating the density (completely saturated or complete dry soil) results in less than a 7% error in reported concentration at "infinite" depth. Using the cleanup standards, we calculated a minimum count time of 10 minutes. This time will enable detection of contamination as low as 1 pCi/g, but this system will not see global-fallout levels of ^{137}Cs, 0.1 pCi/g.

The soil volume "seen" by the shielded detector was experimentally measured and determined to be equivalent to a right cylinder with a radius of 10 cm and a height of 20 cm. We used the nuclear physics models to provide scaling factors to convert counts to pCi per gram at different depths and densities. We then confirmed the model by measuring certified phantoms, which had a range of concentrations, and converting the counts into concentration.

Different soil saturation levels do impact the detector response, due to the different densitites.

We took measurements in several locations near monitoring site PSC-002-D1, beside Steel Creek in SRS P-area, which is a known contamination area. At this location, we determined the contamination was within 27 feet of the center of the stream, in contrast to gamma-overflight data showing it to be within 400 feet (93% smaller). As shown in **Figure 1,** we calculated the soil concentration to be between 1 and 6 pCi/g 18 feet from the center of the creek, between 0.7 and 4 pCi/g 6 feet south-west of that location (24' from center of the creek) and not measurable beyond at 27' from the center of the creek. Approximately 150' upstream, in the middle of the creek-bed, in an area covered in rip-rap, we calculated the soil concentration to be between 12 and 63 pCi/g. We used the peak-to-valley relationship as reported in SRNL-MS-2018-00120 to see if the contamination was under the rip-rap. We estimated the depth of contamination to be between 1 and 3 inches, which corresponds to a concentration between 12 and 57 pCi/g.

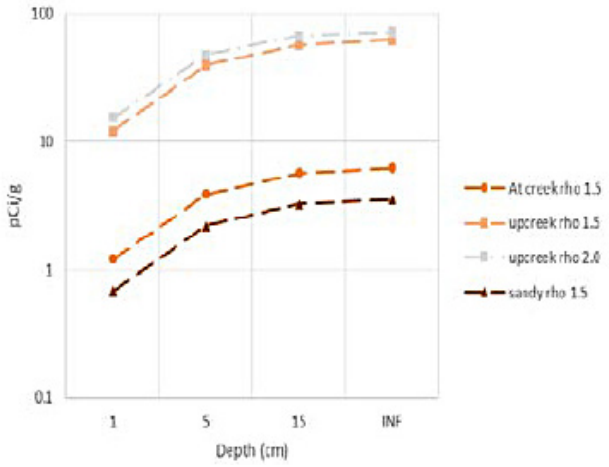

Figure 1. Calculated soil contamination at depth at Steel Creek

The ease-of-use, performance, programmability, and price was evaluated for the Ortec Digibase, Canberra Osprey, Amptek TB-5, and the Bridgeport usbBase. The Digibase is the easiest to setup and use on conventional systems, for use with Android-based operating systems, the easiest is either the TB5 or usbBase. For programmability, the usbBase or TB5 is easiest, followed by the Digibase and Osprey. Price scales with analog-to-digital converter (ADC) size: the Digibase (10-bit), usbBase (12-bit), TB5 (13-bit), and Osprey (14-bit ADC). The performance of these systems was similar, but mainly driven by the ADC "bitness". This was assessed by comparing measurements of a standard source, 166mHo. 166mHo was selected because it has many intense peaks across the range of 80 – 1000 keV. In addition to each other, we compared the performance to the Canberra DSA-LX and the XIA PIXIE-4. Several figures-of-merit were analyzed to compare the data-acquisition systems, including the resolution of the peaks, and the integral and differential linearity of the ADC.

FUTURE DIRECTIONS

- Explore the applicability of this work to other radionuclides, specifically Uranium-235/238
  - Backwater Basin, OH (DOE-LM)
  - Tim's Branch at SRS (Clemson University)
- Develop common control software and integrate with driver software for the various USB-based detector hardware. This will enable rapid instrumentation development using the most appropriate equipment for the application.

PUBLICATIONS/PRESENTATIONS

1. SRNL-STI-2018-00510: Calculating Cs-137 concentration in soil using nuclear modeling and laboratory standards
2. SRNL-STI-2018-00524: Evaluation of multichannel analyzers for gamma-radiation measurements
3. SRNL-MS-2018-00120: Improving the Field Portability of Neutron and Gamma Counting Techniques
4. SRNL-L4120-2018-00023: Uranium measurements in upper Tim's Branch

REFERENCES

1. DHEC2016 Environmental Surveillance and Oversight Program 2016 Data Report.
2. EPA2000 Environmental Protection Agency Soil Screening Guidance for Radionuclides: User's Guide EPA/540-R-00-0071

ACRONYMS

DOE-EM	Department of Energy Environmental Management
DOE-NNSA	Department of Energy National Nuclear Security Administration
EPA	Environmental Protection Agency
MCA	Multi-Channel Analyzer
SCDHEC	South Carolina Department of Health and Environmental Control
SRS	Savannah River Site
SRNL	Savannah River National Laboratory
USB	Universal Serial Bus

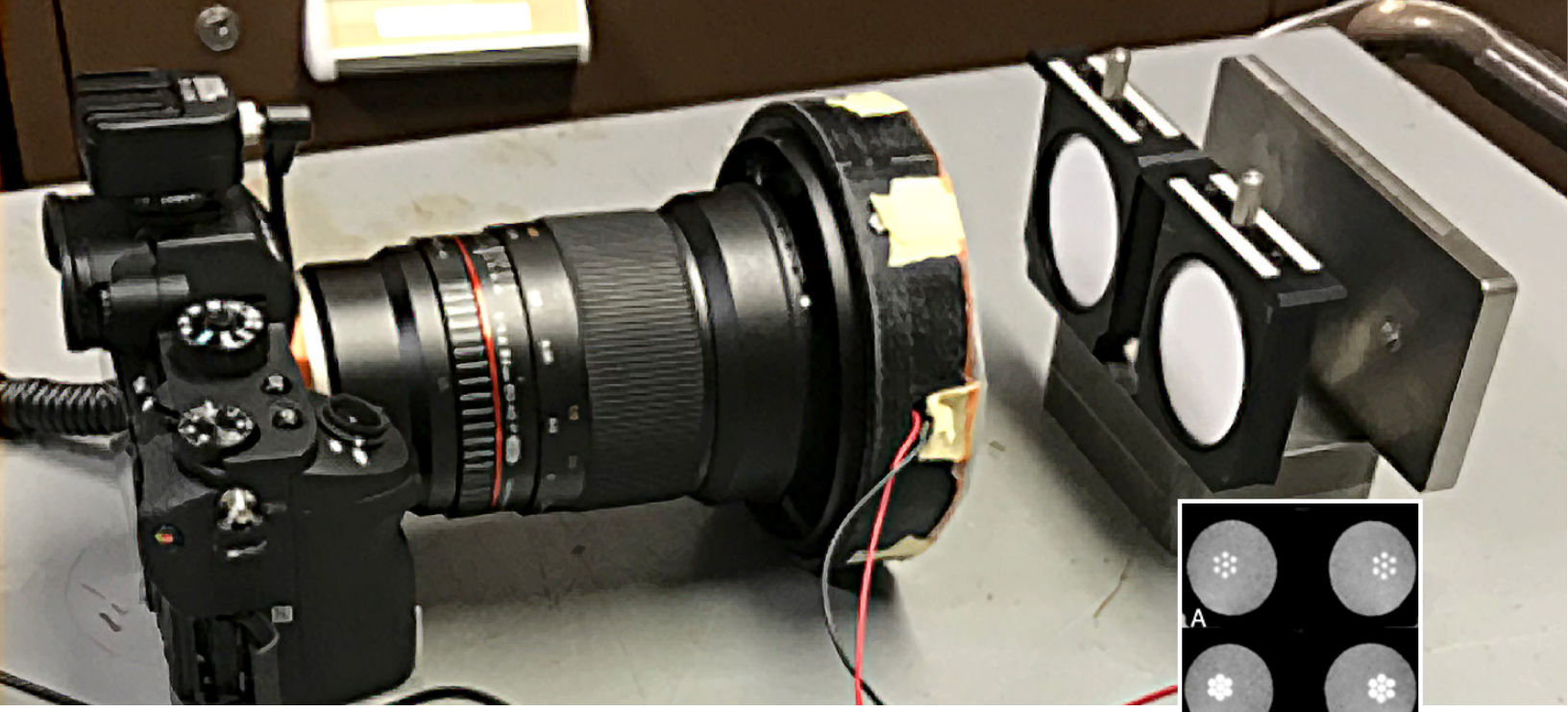

Inset: *In-situ GrayQb™ test system (left) dual pinhole Am-241 20mR radiation images digitally captured with in-situ GrayQb™ using different pinhole sizes (right)*

GAMMA IMAGING AND MAPPING ADVANCEMENTS

PROJECT TEAM:
Jean Plummer (PI), Donald Benza (Co-PI), Kalee Fenker, David Immel, Catherine Mancuso, Daniel Garon (SULI Intern)

COLLABORATORS:
Scott Watson, Nicola Winch (LANL)

THRUST AREA:
Environmental Stewardship

PROJECT START DATE:
October 1, 2017

PROJECT END DATE:
September 30, 2018

The Savannah River National Lab (SRNL) collaborated with Los Alamos National Lab to develop an in-situ GrayQb™ radiation mapping device eliminating the need to remove the radiation sensitive phosphor storage plate (PSP) from the device for scanning between exposures. This was accomplished by developing a variant of the LANL patented MiniMax camera-based system capable of reading x-ray images from Phosphor Storage Plates (PSP) and incorporating it into the GrayQb housing. Digital images captured in-situ can be readily uploaded and analyzed on a remote computer. Additionally, testing identified a new PSP material 4 times more sensitive than the previous PSP film for use as the GrayQb™ detection medium. Lastly, test mockups indicated that the field of view of the camera-based reader would support a multiple pinhole collimator without increasing the dimensions of the system, therefore a dual pinhole collimator was developed to acquire stereoscopic gamma images rendering this new device physically capable of obtaining 3D images.

FY 2018

Objectives

- Develop an in-situ gamma mapping device by combining the technologies employed in the SRNL patented GrayQb™ radiation mapping device with the LANL patented MiniMax camera-based PSP reader.
- Increase GrayQb™ detection sensitivity by identifying more sensitive detection mediums and collimating configurations.
- Maintain GrayQb™ advantages of small size, affordability and deployability.

FY 2018

Accomplishments

- Successfully tested MiniMax system to read a radiation source exposed PSP during SRNL visit to LANL
- Developed PSP Image Simulator
- Verified that new PSP material from Carestream Medical is 4 times more sensitive than previous PSP films
- Performance tested selected cameras against MiniMax custom camera to identify smaller less expensive alternatives
- Developed physical capability to acquire stereoscopic radiation images for 3D mapping by incorporating a dual pinhole collimator
- Characterized Sony and MiniMax cameras with radiation sources
- Characterized dual pinhole and various pinhole sizes with radiation sources
- Housing redesign first iteration complete

INTRODUCTION

The SRNL developed GrayQb™ device has successfully accomplished objectives to identify and map radiological conditions to increase efficiencies and promote worker safety for DOE-EM D&D activities, **Figures 1 & 2**. Deployments, while successful, have demonstrated opportunities for additional high value features to include in-situ mapping and increased detection sensitivity. The ability to read the radiation image from the exposed PSP in-situ would negate the need to remove the PSP for processing by an external scanner after exposure, **Figure 3.** This provides significant deployment cost savings in radiation areas by removing the need to retrieve GrayQb™ for scanning between each image acquisition. Additionally, in-situ processing removes the human handling of the PSP which reduces potential human error in the processing and promotes ease of use. Identifying more sensitive detection mediums and better performing collimating configurations can increase detection sensitivity leading to faster results which may make the device more attractive for time sensitive missions.

LANL patented MiniMax (Miniature, Mobile, Agile X-ray) was developed as a mobile compact lightweight device capable of reading x-ray images captured in the field on photostimulable material. A main objective of this LDRD was to explore the ability to employ this technology for radiation imaging and include it into the GrayQb™ housing to obtain in-situ results. Based on previous x-ray and radiological testing with PSPs, it was thought that this would be feasible. The MiniMax is a camera-based system capable of capturing a photostimulable image using a single flash from a bright red LED source filtered through a blue dichroic filter, **Figure 4.** It was desired to customize this method for GrayQb™ where the PSP is much smaller than x-ray applications and where it was desired preserve the small size and affordability of the GrayQb™.

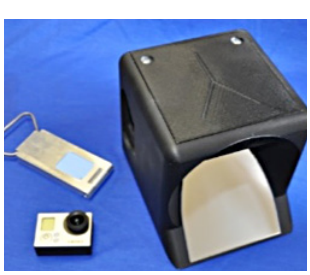

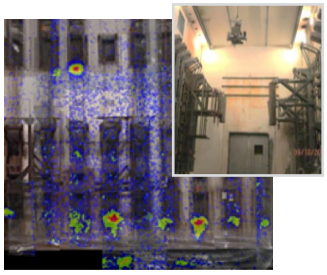

Figure 1. ***(Above Left)*** *GrayQb™ device with PSP imaging cartridge & camera.*
Figure 2. ***(Above Right)*** *GrayQb™ Hanford PRF Canyon Results.* ***Inset:*** *GrayQb™ crane deployment*

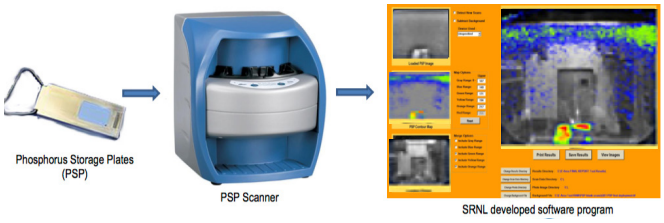

Figure 3. ***(Above)*** *Current Gamma Image results processing requires PSP to be removed from device and externally scanned.* *Figure 4.* ***(Below)*** *Proposed gamma image results processing method will incorporate a camera-based PSP reader based on the LANL developed MiniMax into the GrayQb™ housing for in-situ results.*

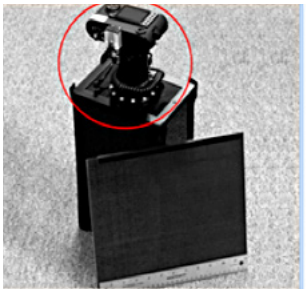

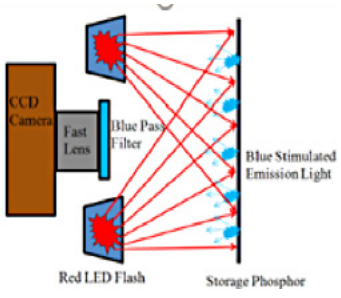

APPROACH

SRNL partnered with LANL to develop a customized version of their patented MiniMax camera-based PSP reader system for use in the GrayQb™ device to perform gamma imaging in-situ. Component alternatives and configurations were explored and tested to minimize the cost and size increase to the GrayQb™. Of interest was identifying COTS components to replace high end custom components found in the MiniMax. One area of greatest potential for savings in both cost and footprint was the camera selection for GrayQb™. Identification of cameras with high sensitivity photodetectors representing small, medium and large footprints and respective costs were identified for test.

A PSP gamma image simulator was designed, built and validated, **Figure 5.** The simulator provided repeatable PSP test samples simulating radiation exposures to easily perform camera testing and comparisons without rad sources. The test cameras as well as the MiniMax were performance tested in the R&DE lab using the simulator. Two days of testing were performed with radiation sources at the SRNL Calibration Facility. The first visit in June focused on testing alternate PSP materials which were thicker and potentially more sensitive and various collimator and PSP configurations. The second visit in September focused on characterizing the Sony as7II camera, considered the most promising of the candidate cameras, and the MiniMax system with radiation sources. Additionally, tested during the second visit was the dual pinhole collimator.

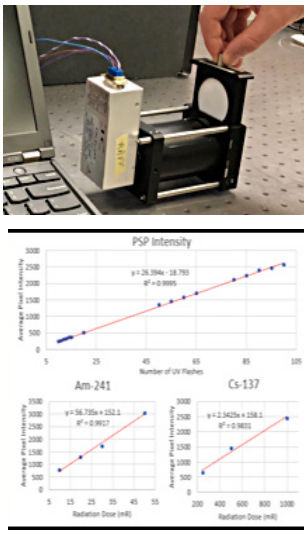

*Figure 5. PSP Image Simulator **(Top)** validation and correlation to radiation dose **(Bottom)***

RESULTS/DECISION

A new PSP material purchased from Carestream medical was selected as the new imaging medium for the GrayQB™. Laboratory testing with sources showed the new PSP to be up to four times more sensitive than the currently used dental PSP. The new PSP is much thicker which increases the likelihood that radiation will be absorbed by the film. Testing also demonstrated the higher sensitivity significantly reduced the necessary exposure times as expected, especially for higher energy isotopes such as Cs-137.

The PSP image simulator was verified to be a viable method for simulating gamma images onto a PSP. The simulator produced a programmable number of UV flashes and the PSP response to the number of flashes was related to the PSP response of a radiation dose using data collected at the HPICL facility, **Figure 5.**

Several cameras were selected to be tested as candidates for the GrayQb™ PSP reader system; the Sony αs7 II, the Mightex CXE-B013-U, and the Allied Vision Guppy. Test mockups were developed for these camera systems, **Figure 6.** Camera evaluation metrics included footprint, cost, resolution, sensitivity, and noise. PSPs were exposed with various amounts of "dose" using the image simulator and then imaged with each camera system, **Figure 7.** The Sony

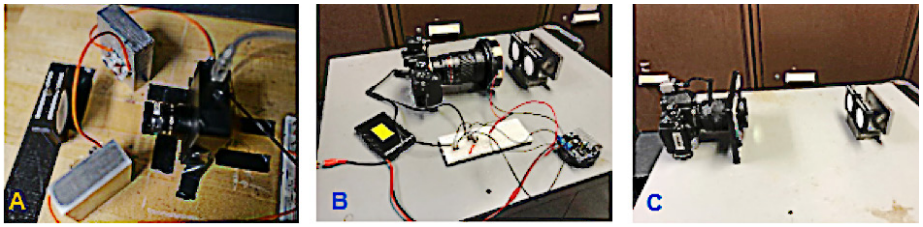

*Figure 6. Camera test setups used with PSP image simulator - **A: Mightex CXE-B013U, B: Sony as7 II, C: MiniMax.***

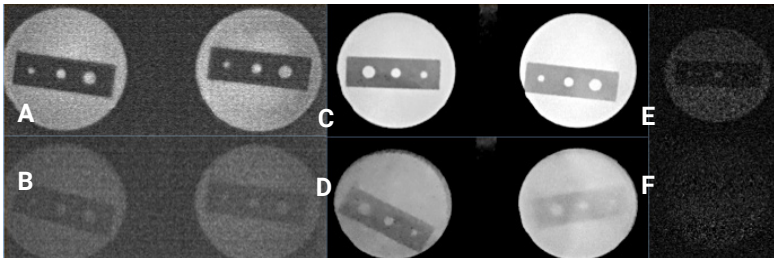

Figure 7. Test images from the Camera test setups used with PSP image simulator.

camera was selected as the best overall camera due to having very high sensitivity and low noise, **Figure 7.** The Mightex camera was small in footprint and had high sensitivity but suffered from high noise which degraded the images. Its small size makes it attractive for a possible high dose GrayQB™ when signal would not be in short supply. The Guppy has the smallest footprint but relatively poor sensitivity which makes it useful only for high dose situations. The cost of the Sony and Mightex cameras plus the lenses (~$2500) keeps the GrayQB™ in an attractive price range.

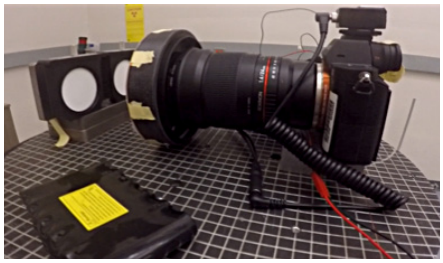

Figure 8. ***(Top Left)*** *Sony test mock up at calibration facility.* *Figure 9* ***(Top Right)*** *Dual pinhole collimator with removable pinholes.* *Figure 10.* ***(Bottom Left)*** *Am-241 multi source used.* *Figure 11* ***(Bottom Right)*** *Results for 20mR Am-241 dose except where noted.* ***A:*** *1mm Pinhole @ 28 cm* ***B:*** *2mm Pinhole 28 cm* ***C:*** *17mmPinhole @ 28 cm* ***D:*** *1mmPinhole (Left) and 2mm Pinhole (Right) @ 50cm* ***E:*** *1mmPinhole @ 100cm* ***F:*** *1mmPinhole @ 28cm 1.5mR.*

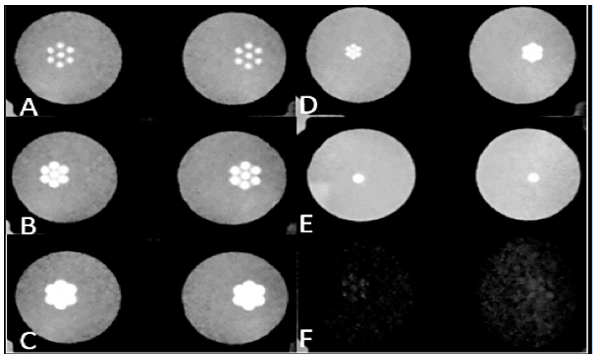

The Sony based PSP reader mockup system and the MiniMax were characterized at the SRS Calibration Facility using Am-241 and Cs-137 button sources, **Figure 8.** The wide field of view of the Sony and Mightex camera made it possible to add pinholes to the collimator without requiring an increase in GrayQb™ size; a dual pinhole tungsten collimator with removeable 1mm and 2mm pinholes was manufactured and used, **Figure 9.** Capturing images with the dual collimator allows for stereoscopy to be performed in the future and different pinhole sizes to be tested. The pinholes performed as expected with the 1mm pinhole showing better resolving power compared to the 2mm pinhole, but less overall intensity captured on the PSP, an Am-241 multisource configuration was used to help determine resolution, **Figures 10 & 11**. Resolution drops off considerably as distance increases, but this was expected. The removable pinholes give the GrayQb™ excellent flexibility moving forward.

FUTURE DIRECTIONS

- **3D In-Situ Radiation Mapping.** Incorporation of the dual pinhole collimator in the in-situ device facilitates future development to locate hot spots in 3D space using stereoscopic techniques; additional software development is required for image processing to produce a user-friendly result.
- **Mini In-Situ GrayQb™.** The Mightex camera is much smaller than the Sony but not as sensitive; for applications with higher dose rates, i.e. 100mR and above, a very small (6" x 8") Mini in-situ GrayQb™ could be developed for use.

PRESENTATIONS

An abstract has been submitted to the Waste Management 2019 Symposia titled "In-Situ Radiation Mapping Device"

PUBLICATIONS

1. "GrayQb™ Single-Faced Version 2 (SF2) Hanford Plutonium Reclamation Facility (PRF) Deployment Report" SRNL-STI-2015-00673, November 2015.
2. "GrayQb™ Single-Faced Version 2 (SF2) Open Environment Test Plan," SRNL-TR-2014-00196, August 2014.
3. Immel, D., Bobbitt, J., Plummer J.; "Radiation Imaging System". U.S. Patent 9,291,719 issued 2016 March 22.
4. Immel, D., Bobbitt, J., Plummer J.; "Radiation Imaging System". U.S. Patent 9,377,536 issued 2016 June 28.

ACRONYMS

COTS Commercial off the Shelf
PSP Phosphor Storage Plate

INTELLECTUAL PROPERTY

An invention disclosure will be submitted.

DEVELOPMENT OF NOVEL FOAMING SOLUTIONS FOR HIGH LEVEL WASTE (HLW) PROCESSING

PROJECT TEAM:
D.P. Lambert, A.M. Howe, W.H Woodham, D.J. Newell, D.J. Adamson, M.E. Kinard, T.L. Earls, V.B. Timmerman, G.R. Golcar, A.A. Ramsey

THRUST AREA:
Environmental Stewardship

PROJECT START DATE:
October 1, 2017

PROJECT END DATE:
September 30, 2018

Foaming of high-level waste (HLW) slurries is an issue at the Defense Waste Processing Facility (DWPF) Chemical Process Cell (CPC) which is currently mitigated with a chemical antifoam agent. However, alternatives are being evaluated to potentially improve operations in support of the Salt Waste Processing Facility (SWPF) startup. The efficiency of alternative antifoams and the effectiveness of non-chemical methods for foam control were examined to improve HLW treatment at DWPF and to eliminate the flammability hazards associated with the Antifoam 747 currently in use. Initial results indicate that Y-17112, a superspreader developed by Momentive Performance Materials, may be more suitable for use at DWPF. Non-chemical foam control strategies were also evaluated; however, they were found less effective than chemical methods and would be impractical to implement. Alternative chemical antifoams and process changes, e.g. sequencing, to mitigate foam generation during HLW treatment at DWPF will be further investigated in the future.

FY 2018

Objectives

- Identify alternative antifoam agents and non-chemical solutions for foam control
- Determine efficiency of alternative antifoam agents
- Determine effectiveness of non-chemical methods

Accomplishments

- Meeting with antifoam experts at Illinois Institute of Technology (IIT) led to identification of hydrolysis resistant superspreaders.
- Tested the efficiency of superspreaders Y-17309, Y-17581, Y-17112 against Silwet L-77 across broad pH range; Y-17112 was identified as a possible replacement for Antifoam 747 currently used in DWPF.
- Collaborated with Savannah River Remediation (SRR) to identify possible non-chemical foam control strategies; Liquid spray/mist, headspace agitators, and ultrasonic energy, were selected and tested.

INTRODUCTION

Foaming occurs during treatment of high level waste (HLW) at (DWPF) in the Chemical Process Cell (CPC) due to high gas generation from process steam and chemical off gas products[1]. The presence of amphiphilic particles in the waste slurry stabilizes the foam. Efficient processing of HLW requires foam control, as foamovers lead to lower productivity and potential radioactive contamination of condensate streams. DWPF currently employs Antifoam 747, a surfactant produced by Momentive Performance Materials, as an antifoaming agent during waste treatment[2]. While it controls foam, processing issues have arisen from its use. During DWPF chemical processing, antifoam must be effective up to 103°C and between a pH range of 3-13. Antifoam 747 is efficient at pH 6-8 but degrades outside that optimal pH range[3]. Savannah River National Laboratory (SRNL) has identified multiple flammable antifoam degradation products during laboratory scale experiments.

The efficiency of alternative antifoam agents and the effectiveness of non-chemical methods for foam control were evaluated as part of an effort to improve HLW treatment operations at DWPF and to eliminate, or reduce, the flammability hazards associated with Antifoam 747 currently in use.

APPROACH

Chemical Antifoam Testing: Through collaboration with antifoam experts at the Illinois Institute of Technology (ITT) the following hydrolysis resistant superspreaders, produced by Momentive Performance Materials, were identified and selected for further testing: Y-17112, Y-17309, Y-17581. The efficiency of these superspreaders along with Silwet L-77 (the main component of Antifoam 747) were tested across a wide pH range (1 – 13) at varying concentrations (100 ppm – 5000 ppm). A 50 µL drop of antifoam solution was placed on a backlit Petri dish. Utilizing a specialized camera and software, the coverage area was measured over a 60 second time interval as each solution spread as shown in **Figure 1** and **Figure 2.**

Chemical Antifoam Testing - Hydrolysis Resistant Superspreaders

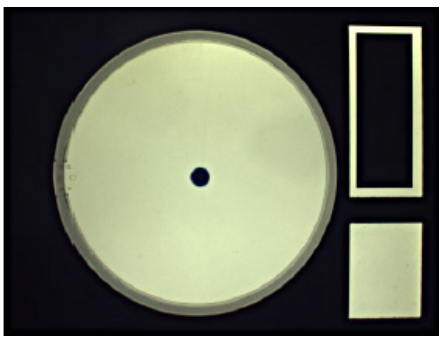

Figure 1. Silwet L-77 pH 13, 1000 ppm

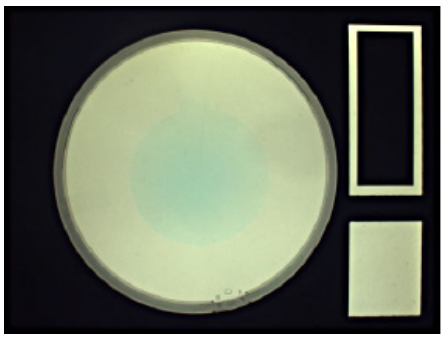

Figure 2. Y-17122 pH 13, 1000 ppm

Mechanical Methods for Foam Control: In addition, several non-chemical foam control strategies were proposed, discussed, and evaluated by a multi-disciplinary team, including DWPF process control engineers[4,5]. The strategies that were ranked most likely to be effective for foam control were identified for further evaluation, including: the use of liquid spray/mist, agitators in the headspace, and ultrasonic energy **(see Figures 3 & 4).** These alternative methods were tested in laboratory scale experiments using physical and chemical simulants. The simulant was heated to boiling (~100°C) and agitated, simulating DWPF processing. Foam generation was carefully monitored while the potential mechanical methods for foam control were tested. Process changes, particularly with respect to operations sequencing, (addition of acid while boiling, processing more dilute/concentrated slurries, delay boiling until chemical reactions are complete, etc.) were also identified as a feasible foam control strategy.

Mechanical Methods for Foam Control - Agitation

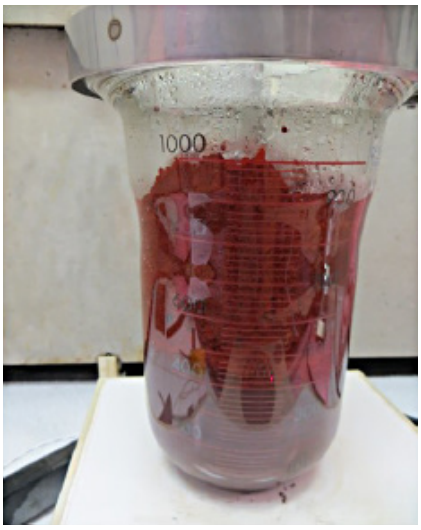

Figure 3. No Foam Control During Mixing/Boiling

Figure 4. Headspace Agitators During Mixing/Boiling

RESULTS/DECISION

Chemical Antifoam Testing: Initial spread rate (cm^2/s) across a pH range of 1 to 13 and degradation time were utilized to determine the efficiency of each superspreader as an antifoam agent during DWPF chemical processing. Silwet L-77 and Y-17112 outperformed Y-17309 and Y-17581, achieving greater spread rates and sustaining chemical stability. Silwet L-77 attained the highest spread rates of 2.7 cm^2/s and 2.0 cm^2/s at pH 8.5 and 10 respectively. In extreme acidic and alkaline conditions, however, Silwet L-77 solutions failed to spread at all. Y-17112 achieved consistent spread rates between 1.0 cm^2/s and 1.5 cm^2/s across the entire pH range, even at lower concentrations.

These initial results indicate that Y-17112 may be a more suitable antifoam agent for HLW waste treatment in DWPF. The efficiency of Y-17112 must first be confirmed in laboratory scale boil tests, which will replicate actual waste treatment.

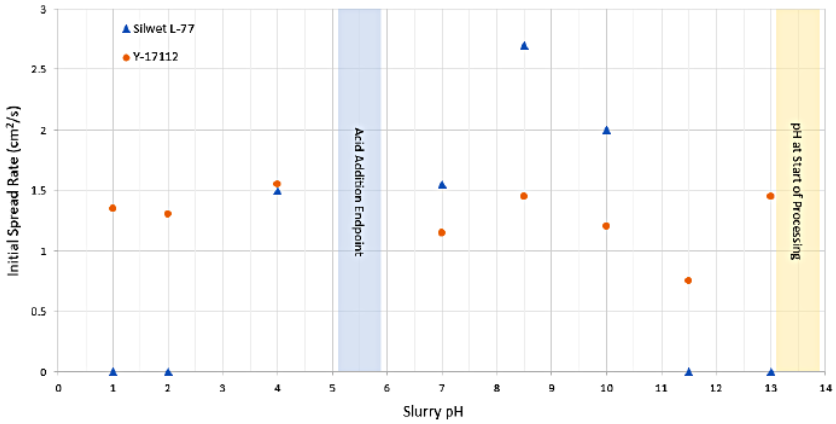

Figure 5. Initial Spread Rate (cm^2/s) of Silwet L-77 and Y-17112 Solutions (1000 ppm) Across pH Range

Mechanical Methods for Foam Control: During the initial test, where no method

for foam control was implemented, the liquid level increased from 500 mL to 980 during boil up. **Table 1** sumarizes the results from non-chemical foam controls tests. The liquid level nearly doubled, resulting in foam generation of 96%. Ultra-sonication did not reduce foam production. Agitation through ultrasonic energy thickened the foam, stabilizing it further. Spraying the generating foam with fine water particles (at a rate of 380 mL/hr) reduced the foam level to 8%, but once the water mist was discontinued the foam level again increased to 96%. While spraying appeared promising, the quantity of water required to control foaming during HLW processing in DWPF would likely be inviable.

Non-chemical Method	Liquid Level Prior to Boiling (mL)	Liquid Level During Boiling (mL)	Foam Level (%)
No Foam Control	500	980	96
Water Spray/Mist (~380 mL/hr)	500	540	8[1]
Headspace Agitators	450	750	67
Ultrasonic Energy (750 Watts; 20 kHz)	400	>1000	>100[2]

[1]During spraying/misting; Foam level increased to 96% once spay/mist was stopped
[2]Ultra-sonication led to a thicker more stable foam

Table 1. Results of Non-chemical Foam Control Tests

The use of agitators in the headspace reduced the rate of foam generation and a maximum foam level of 67% was achieved. Space in DWPF processing tanks, however, is limited due to the presence of existing equipment and instrumentation, making the installation and use of additional agitators in the headspace impractical[6]. These results suggest that the implementation of effective non-chemical foam control strategies in DWPF are not feasible. Alternative chemical antifoams and process changes to mitigate foam generation during HLW treatment at DWPF will be further investigated in the future.

FUTURE DIRECTIONS

- Test superspreaders Y-17309, Y-17581, and Y-17112 in laboratory scale SRAT/SME cycles, simulating DWPF chemical processing.
- Perform SRAT/SME cycles with process changes: Addition of acid while boiling, processing more dilute/concentrated slurries, delay boiling until chemical reactions are complete, etc.

REFERENCES

1. Calloway, J. T. B.; Martino, C. J.; Jantzen, C. M.; Wilmarth, W. R.; Stone, M. E.; Pierce, R. A.; Josephs, J. E.; Barnes, C. D.; Daniel, W. E.; Eibling, R. E.; Choi, A. S.; White, T. L.; Crowley, D. A.; Baich, M. A.; Johnson, J. D.; Vijayaraghavan, K.; Nikolov, A. P.; Wasan, D. T., Radioactive Waste Evaporation: Current Methodologies Employed for the Development, Design and Operation of Waste Evaporators at the Savannah River Site and Hanford Waste Treatment Plant. 2003, (37327), 157-170.
2. Koopman, D. C. *Comparison of Dow Corning 544 Antifoam to IIT747 Antifoam in the 1/240 SRAT;* WSRC-TR-99-00377; Savannah River Technology Center: Aiken, SC, 2000.
3. Lambert, D. P.; Koopman, D. C.; Newell, J. D.; Wasan, D. T.; Nikolov, A. P.; Weinheimer, E. K., Improved Antifoam Agent Study End of Year Report, EM Project 3.2.3. 2011.
4. Ramsey, A. A.; Golcar G., *Meeting Minutes from 12/05/2017 Brainstorming Session for Developing Non-chemical Foaming Solutions for Control of Foam in the DWPF Chemical Process Cell;* SRNL-L3100-2017-00066; Savannah River National Laboratory: Aiken, SC, 2018.
5. Ramsey, A. A., *Meeting Minutes from 02/08/2018 Follow-up Meeting Regarding Task 2A –Identification of Non-chemical Solutions for Foam Control;* SRNL-L3100-2018-00017; Savannah River National Laboratory: Aiken, SC, 2018.
6. Hansen, E. K., *Determination of the 1/6th Scale SERT Agitator Speeds;* SRNL-ITS-2005-00202, Rev. 0; Savannah River National Laboratory: Aiken, SC, 2005.

ACRONYMS

CPC	Chemical Process Cell
DWPF	Defense Waste Processing Facility
HLW	High Level Waste
ITT	Illinois Institute of Technology
SME	Slurry Mix Evaporator
SRAT	Sludge Receipt and Adjustment Tank
SRNL	Savannah River National Laboratory
SRR	Savannah River Remediation
SWPF	Salt Waste Processing Facility

INTELLECTUAL PROPERTY

Non-disclosure agreement between Savannah River National Laboratory (SRNL), Savannah River Remediation (SRR), and Momentive Performance Materials regarding the exact composition of Silwet L-77, Y-17581, Y-17309, and Y-17112.

HYPERSPECTRAL RAMAN IMAGING USING A SPATIAL HETERODYNE SPECTROMETER (SHS)

PROJECT TEAM:
K.A.S. Fessler, R. Lascola, P. O'Rourke, S. Serkiz.

PROJECT TEAM:
S.M. Angel
(University of South Carolina)

THRUST AREA:
Environmental Stewardship

PROJECT START DATE:
October 1, 2018

PROJECT END DATE:
September 30, 2019

SRNL, and the larger community, has limited chemical-specific imaging (CHI) capabilities, which would be beneficial for remote detection of threat chemicals or use in inaccessible/harsh environments, as well as in-line process monitoring. CHI is underdeveloped due to issues of sensitivity, stable alignment and calibration, and ease of operation associated with most optical instruments. The project objective is to develop a novel, rugged, highly sensitive spectrometer to support real-time, CHI using hyperspectral Raman spectroscopy. Raman spectroscopic analysis will provide chemical specificity and using a spatial heterodyne spectrometer (SHS) will increase the sensitivity due to the high light throughput design. The SHS design does not require moving parts allowing for a very stable system, reducing alignment and calibration issues. The instrument will be assembled and initially applied to Raman gas detection of the Saltstone disposal unit headspace gas concentrations. Raman gas analysis is the most impacted by sensitivity issues and will be used to demonstrate the increased light collection capability of the SHS over a conventional dispersive spectrometer. The system will be later modified to image spectral information in a spatial domain to provide information on the spatial distribution of a sample scene.

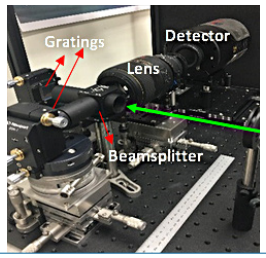

Figure 1. Image of SHRS built at SRNL. Green arrow indicates incoming light.

FY 2018

Objectives

- Instrumentation assembly and demonstration for Raman gas analysis
  - Determine and procure (as necessary) components needed to analyze Saltstone-relevant compounds (H_2, NH_3).
  - Design and build a gas sample cell.
  - Demonstrate ability to measure gas samples with a SHS and compare results to a conventional Raman spectrometer.

Accomplishments

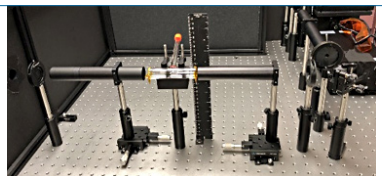

Figure 5. Raman gas sampling assembly.

- Purchased and received all major instrument components and assembled the instrument **(Figure 1).** Completing the instrument assembly has established the SHS instrument as an optical spectroscopic capability in the SRNL analytical portfolio.
- Identified a focused application for initia demonstration of the SHS. Gas analysis of the headspace above the Saltstone in the SDU6 is the intended application.
- Gas cell assembly was designed and assembled—provides a sampling system for the Raman gas measurements with the ability to increase the size of the laser beam illuminating the system **(Figure 5).** The larger beam diameters will allow more analyte molecules to be excited and potentially increase the sensitivity using the SHS to collect and analyze the Raman scattered light, unlike a conventional dispersive spectrometer.
- Hg measurements were demonstrated using the SHS and are being used to finalize the alignment of the system **(Figure 4)**. The measurements are also being used to begin data analysis procedures.

INTRODUCTION

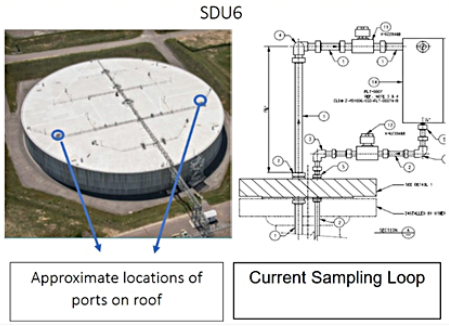

Figure 2. Saltstone Disposal Unit 6 and Sampling Loop

The Spatial Heterodyne Spectrometer (SHS) is a recently developed technology for optical spectroscopy that promises enhanced sensitivity and new opportunities for process and field measurements compared to conventional spectrometers. Sensitivity gains of 10-100x are obtained through light collection over a wide field-of-view and measurement across a two-dimensional detector array. The SHS may provide a faster response time to facilitate process controls and reactions to emerging off-normal conditions, as might be used when monitoring dissolver headspaces for flammability concerns. With no moving parts, a SHS can support the use of typically delicate laboratory instrumentation in a field environment. More novel measurement applications take advantage of the 2D nature of the detection for obtaining images of the scene. One dimension can be used to provide spatial information at the sample, permitting chemically sensitive imaging that can provide real-time determination of chemical distributions. Examples where such information would be valuable include imaging chemical concentration gradients in a process vessel and rapid detection of "residues of interest" across a wide area. With sufficient development, temporal information may also be obtained, permitting tracking of rapidly evolving chemical reactions.

Saltstone disposal Unit 6 (SDU6) **(Figure 2)** requires controls to ensure the flammable gas concentration limit for a list of chemicals is not exceeded. Calculated estimates of gas concentrations are very conservative and experimental measurements are needed to provide accurate gas concentrations to fill the tank with the appropriate amount of waste without exceeding the concentration limits. *In-situ* measurements are ideal to provide real-time analysis of the conditions within the tank. However, the current tests require pulling a sample and the sampling loop does not work as intended.

APPROACH

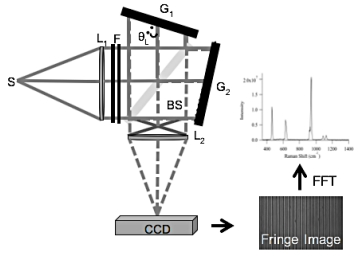

Figure 3. SHRS schematic; fringe image, and Raman spectrum from fast Fourier transform of fringe image.

Raman spectroscopy is an optical scattering technique which provides a molecular "fingerprint" of compounds in the solid, liquid, or gas phase. Raman scattering is an inherently weak technique with only 1 in 10^8 photons Raman scattered, and increasing the irradiance, the number of molecules excited, or the collection efficiency are ways to improve signal strength. Of these methods, irradiance is often limited by sample photodegradation, and gases have the lowest molecular density of all sample phases which cannot be improved without pre-concentration. Increasing collection efficiency has historically had several challenges. Conventional dispersive spectrometers typically exchange spectral resolution for higher collection efficiency due to the slit-based spectrometer design. Michelson interferometeric spectrometers offer large collection efficiency, yet wavelength separation is achieved via a moving mirror which must travel large distances (ultraviolet) or in an extremely stable environment (mid-infrared) for high resolution. Both conditions provide challenges for operation in a process or field environment.

A new type of interferometric spectrometer, the spatial heterodyne spectrometer (SHS), has recently been adapted for Raman spectroscopic analysis.[1-6] The instrument **(Figure 3**) offers large collection efficiency and high resolution in a system with no moving parts. With no moving parts, the SHS design promises the ruggedness and stability required for instrumentation being placed in a facility or used in the field. The spectrometer design also allows for monolithic units to be engineered for specific wavelength ranges. As stated above, increasing the collection efficiency is an approach to improve the sensitivity of a Raman measurement technique, and the SHS is a spectrometer that offers large collection efficiencies without compromising resolution or instrument size and stability. We propose to investigate the collection efficiency improvements for gas samples in a backscattering (180°) or perpendicular (90°) sampling arrangement when using an SHS. Depending on the optical set up, we expect to achieve a collection efficiency 10-100 times larger when using a SHS. The corresponding increases in sensitivity would make Raman spectroscopy a more attractive option for gas monitoring

applications such as the SDU headspace analysis for flammable species. Sensitivity improvements could be used to lower detection limits, increase the speed of detection and response, or a combination of the two. The first year of the project will focus on building an SHS, designing and assembling a gas sample cell, and measuring the collection efficiency of the SHS in comparison to a conventional dispersive spectrometer. The majority of the first year budget will be dedicated to purchasing the necessary materials to build the SHS, and the remainder will go towards labor for assembling the system and performing the experiments.

RESULTS/DECISION

The SHS specifications were determined based on the SDU application. The flammable gases of concern for the Saltstone off-gassing are H_2 and NH_3. With no known fluorescent compounds present in the samples, the laser wavelength was chosen to be in the visible where commercially of the shelf (COTS) small, powerful lasers and high-quality optics are available and Raman efficiency is better than at longer wavelengths. A spectral resolution of 10 cm^{-1} is more than adequate for discriminating the Raman bands of H_2 (540, 655, and 4160 cm^{-1}) and NH_3 (934, 967, 3340, and 3659 cm^{-1}).[7-9] Gratings with a groove density of 150 mm gr/mm gratings will produce a resolution of ~2.5 cm^{-1} with a spectral range of ~2200 cm^{-1}. A larger spectral range and less resolution would be more ideal in the future to observe all Raman bands listed using gratings with a lower groove density, but the current arrangement will work well for discriminating the compounds using the Raman bands in the spectral region where both species show a signal. The system components have been procured, received, and assembled **(Figure 4).**

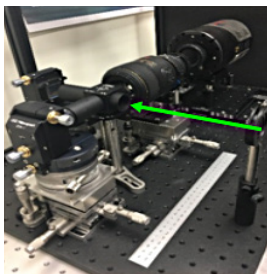

Figure 4. Image of SHRS built at SRNL. Green arrow indicates incoming light.

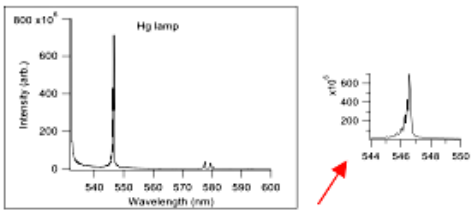

Figure 5. Hg lamp source used for optical alignment and system characterization. Inset shows data processing artifacts.

In the process of assembling and aligning the spectrometer, the spectrum of the emission from a mercury (Hg) lamp was measured. The spectrum to the right is a representative emission spectrum of Hg measured with the SHS constructed at SRNL **(Figure 5).** The inset in **Figure 5** shows artifacts on the left side of the 546 nm band. The band artifacts have been determined to be a product of data processing and highlights the importance of developing data processing techniques to produce high-quality data (FY19).

FUTURE DIRECTIONS

- Optimization of SHS system for Saltstone headspace application and demonstrate lab-scale measurements
  - Lab measurements to demonstrate Raman as a useful technique for Saltstone samples at relevant concentrations (~100s ppm) and to identify potential implementation issues and solutions.
  - Streamlining data acquisition and developing data processing.
- Adaptation of system for hyperspectral measurements and optimization
  - Determine the components and arrangement needed to allow for hyperspectral measurements
  - Demonstrate ability to collect hyperspectral Raman images with a SHS

PUBLICATIONS/PRESENTATION

1. Scix Conference oral presentation; October 22, 2018; Atlanta, GA.
2. SERMACS Conference oral presentation; November 1, 2018; Augusta, GA.

REFERENCES

1. Gomer, N.R.; Gordon, C.M.; Lucey, P.; Sharma, S.K.; Carter, J.C.; Angel, S.M. "Raman Spectroscopy using a Spatial Heterodyne Spectrometer: Proof of Concept." Appl. Spectrosc. 2011. 65(8):849-857.
2. Lamsal, N.; Angel, S.M. "Deep-Ultraviolet Raman Measurements using a Spatial Heterodyne Raman Spectrometer (SHS)." Appl. Spectrosc. 2015. 69(5):525-534.
3. Barnett, P.D.; Angel, S.M. "Miniature Spatial Heterodyne Raman Spectrometer with a Cell Phone Camera Detector." Appl. Spectrosc. 2017. 71(5):988-995.
4. Barnett, P.D.; Strange, K.A.; Angel, S.M. "Improving Spectral Results through Row-by-Row Fourier Transform of Spatial Heterodyne Raman Spectrometer Interferogram." Appl. Spectrosc. 2017. 71(6):1380-1386.
5. Strange, K.A.; Angel, S.M. "Characterization of a Visible Spatial Heterodyne Raman Spectrometer for Standoff Detection" Appl. Spectrosc. In preparation.
6. Strange, K.A.; Paul, K.C.; Angel, S.M. "Transmission Raman Measurements using a Spatial Heterodyne Raman Spectrometer." Appl. Spectrosc. 2017. 71(2):250-257.
7. Tuschel, D. "Headspace Raman Spectroscopy." Spectrosc. 2014. 29(9):1-6.
8. Teal, G.K.; MacWood, G.E. "The Raman Spectra of the Isotopic Molecules H_2, HD, and D_2." J. Chem. Phys. 1935. 3(12):760-764.
9. De Groot, W.A. "The Use of Spontaneous Raman Scattering for Hydrogen Leak Detection." 30th Joint Propulsion Conference, Indianapolis, IN. 1994. Pg.1-11.

ACRONYMS

CHI	Chemical-Specific Imaging
Scix	The Great Scientific Exchange
SDU	Saltstone Disposal Unit
SERMACS	Southeastern Regional Meeting for American Chemical Society
SHS	Spatial Heterodyne Spectrometer
SRNL	Savannah River National Laboratory

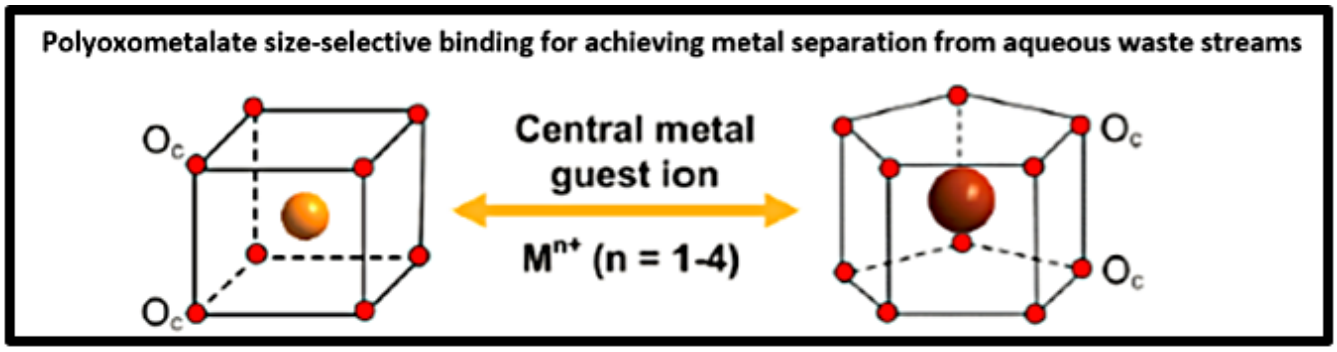

SYNTHESIS AND CHARACTERIZATION OF NOVEL ACTINIDE COMPOUNDS FOR DEVELOPMENT OF REMEDIATION TACTICS

PROJECT TEAM:
J. H. Christia (Primary),
T. C. Shehee, U. Kortz,
C. McMillen, N. S. Dalal, J. Ling

THRUST AREA:
Environmental Stewardship

PROJECT START DATE:
October 1, 2018

PROJECT END DATE:
September 30, 2018

It is important to improve our understanding of actinides in order to improve our understanding of the factors that contribute to extraction selectivity. Detailed structural, magnetic, and electronic studies of novel actinide compounds can provide useful information on bonding behavior to guide the development of novel separation and environmental remediation strategies. To date, about 95% of known chemical structures containing actinide metals contain either uranium or thorium. The lack of structures containing other actinides is largely driven by limitations placed on most researchers (e.g. limited access to radiological equipment, radioactive materials, and government licensing). Thus, actinide chemistry and novel actinide compound development remains a relatively open area to study. In this LDRD, we sought to synthesize and characterize single crystals of novel polyoxometalates (POMs) that can encapsulate plutonium and uranium.

FY 2018

Objectives

- Purify a plutonium precursor to be used in subsequent chemical reactions
- Equip our lab with the necessary equipment and chemicals for performing a variety of POM syntheses
- Complete successful single-crystal syntheses of POM lanthanide analogues.
- Complete successful single-crystal syntheses of POM uranium and plutonium analogues.
- Use single-crystal x-ray diffractometry to elucidate the structures of newly synthesized actinide compounds
- Perform magnetic characterization of newly synthesized actinide compounds.

Accomplishments

- Successfully purified a plutonium salt for synthesis from plutonium metal
- Equipped our lab with the necessary equipment and chemicals for performing a variety of POM syntheses
- Completed successful single-crystal syntheses of POM lanthanide analogues.
- Completed successful single-crystal syntheses of POM uranium and plutonium analogues.
- Acquired $50 k in funding related to actinide peroxide cluster synthesis

INTRODUCTION

A crucial challenge in achieving efficient separation of metals in aqueous waste streams and nuclear fuel processes is the difficulty in separating trivalent actinides from lanthanides due to similarities in oxidation state, ionic radii, and some chemical properties.[1] Therefore, it is critical to improve our understanding of the coordination chemistry of actinide complexes and the chemical differences between lanthanides and actinides in order to improve our understanding of the factors that contribute to extraction selectivity.

The goal of this LDRD was to develop and characterize the structure and magnetic properties of novel actinide compounds to strengthen SRNL's actinide chemistry competency, boost SRNL's external visibility via high-quality publications, and improve our understanding of the factors that contribute to lanthanide-actinide extraction and separation selectivity.

We focused our synthetic efforts on polyoxometalates, a family of metal oxide nanoclusters that have been studied for decades because they provide an opportunity to study nanoscale materials with well-defined structures that can be used in a diverse range of emerging applications.[2,3] In fact, lacunary polytungstates, especially $\alpha 2\text{-}\{P_2W_{17}O_{61}\}^{10-}$, have been used to facilitate the solvent extraction of trivalent actinides with primary amines.[4,5] In FY 18, we equipped our laboratory for handling new syntheses, and we successfully synthesized several single crystals of polyoxopalladates using plutonium and uranium precursor compounds. As we conclude FY 18, we plan to perform detailed structural characterization of our newly created materials.

APPROACH

We utilized existing POM synthetic templates but substituted Pu and U as the host metal cations. Our focus for FY 18 was on heteropolyoxopalladates that were recently shown to be very effective at incorporating small, medium, and also large lanthanide(III) ions into the center of the palladate ligand.[6] These results suggested that the $PdIII_{12}O_{32}$ shell can adjust to the coordination requirements of the encapsulated guest cation, which we postulated would prove very useful at stabilizing U and Pu. Typical synthesis involves a simple one-pot self-assembly reaction of $Pd(CH_3COO)_2$, phenylarsonic acid, and the respective metal(III) cation in 0.5 M aqueous sodium acetate solution with strict control over solution pH.

Figure 1. Photographed inside of a radiological glovebox, crystalline product is shown from a Plutonium-Palladium POM reaction

RESULTS/DECISION

In FY 18 we were able to set up our lab for performing POM actinide synthesis work, and we were successful in growing crystals from U and Pu-based syntheses using one-pot solvothermal methods. We plan to characterize these samples in the upcoming months. We also learned several important lessons regarding the chemical and environmental factors that impact crystal formation inside of a radiological glovebox. We plan to use these lessons for improving our throughput in FY 19, and we expect to be able to form several new actinide compounds in FY19.

FUTURE DIRECTIONS

- Synthesize new Pu starting materials (e.g. PuCl3)
- Explore several new POM syntheses using PuCl3
- Continue to obtain MSI funding and search for new funding sources to continue this work
- Determine whether newly synthesized structures have a binding preference for U or Pu
- Analyze the magnetic properties of newly synthesized compounds

REFERENCES

1. A. E. V. Gorden, M. A. DeVore and B. A. Maynard, Inorganic Chemistry, **2012,** 52, 3445-3458
2. M. T. Pope and A. Muller, Angew. Chem. Int. Ed., **1991,** 30, 34-48.
3. D. E. Katsoulis, Chem. Rev., **1998,** 98, 359-387.
4. M. S. Milyukova, N. S. Varezhkina and B. F. Nyasoedov, J. Radioanal. Nucl. Chem., **1986,** 105, 249-256.
5. M. S. Milyukova, N. S. Varezhkina and B. F. Myasoedov, Sov. Radiochem., **1990,** 32, 361-367.
6. M. Barsukova, N. V. Izarova, R. N. Biboum, B. Keita, L. Nadjo, V. Ramachandran, N. S. Dalal, N. S. Antonova, J. J. Carbó, J. M. Poblet and U. Kortz, Chemistry – A European Journal, **2010,** 16, 9076-9085.

ACRONYMS

MSIPP Minority Serving Institution Partnership Program
POM Polyoxometalate

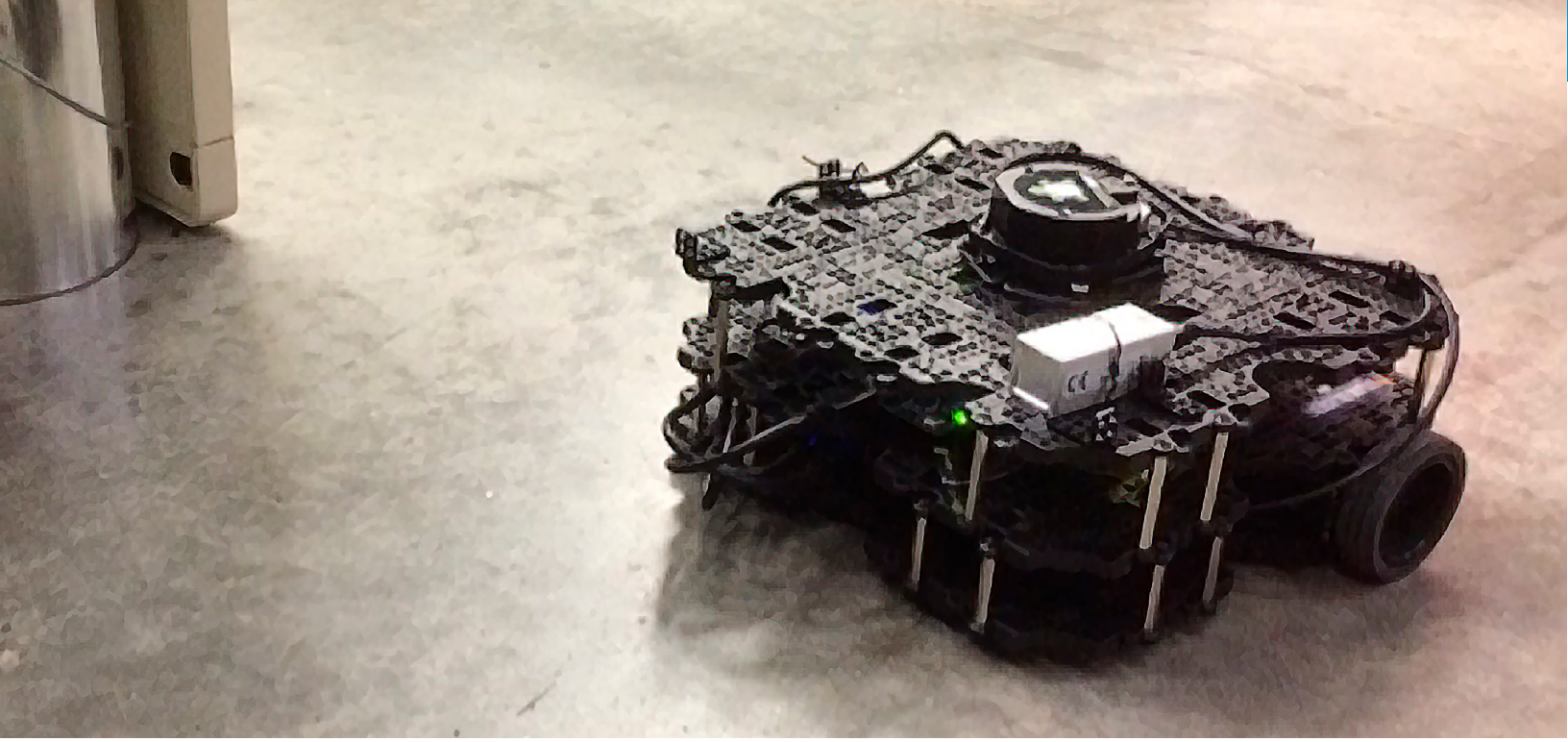

GAMMA-RAY RASTER IMAGING WITH ROBOTIC DATA COLLECTION

PROJECT TEAM:
Tim Aucott, Tad Whiteside, Willie Wells, Sebastián Zanlongo

THRUST AREA:
Environmental Stewardship

PROJECT START DATE:
October 1, 2017

PROJECT END DATE:
September 30, 2019

This project has developed an alternative imaging capability for measuring radioactive materials in situ. This approach uses a robotic-mounted gamma-ray detector which can move around an area of interest, sampling the space at a high frequency. By rastering across the area, an image can be created with no collimation and a high efficiency. A regression model was developed to map out material distribution as the robot moves through the environment. An informative path planning algorithm was also developed to maximize the information collected throughout the movement path.

The use of a robotic mount allows data collection for long periods of time unattended, and it will also eliminate uncertainties in positioning typically introduced by personnel. This approach will be particularly relevant for gloveboxes, shielded cells, or process piping which may have complex, non-uniform distributions of material.

FY 2018

Objectives

- Assemble data acquisition
- Calibrate and demonstrate
- Test data acquisition
- Evaluate performance

Accomplishments

- Assembled Turtlebot, including camera, LIDAR, and CZT detector
- Developed software interface for operating robot in conjunction with CZT detector
- Demonstrated ability to take CZT data in conjunction with contextual data
- Developed and tested GPR algorithms for reconstructing gamma ray source distributions
- Developed IPP algorithms for optimizing robot travel path

INTRODUCTION

Gamma-ray assays and images are a key tool for holdup characterization in a facility. Images can be used to create radiation maps, which can be used for establishing procedures, assist decontamination and aid radiological control. This project uses a small gamma-ray detector on a robotic platform to sample an area at high frequency in order to create an imaging. This approach is lightweight (requiring little to no lead shielding), autonomous (requiring minimal operator time and input) and precise (relying on cameral, LIDAR, and software to map out the space.

In addition, this work integrates state-of-the-art robotics developments to improve the acquisition of gamma-ray data. Informative Path Planning (IPP) is used to design a path for a robotic sensor platform to gather the most information about the radiation distribution while operating under the set of constraints given by the dynamics of the robot and other requirements such as minimizing the overall mission time.

The key challenge for IPP is the tight coupling in multiple layers of decisions such as selecting location where a robot should take samples, producing paths for the robot to use when travelling from one location to the next and generatating a radiation map using a Gaussian process regression (GPR) framework.

Given a robot equipped with a basic gamma detector and LIDAR sensor, how can we efficiently explore an unknown environment in such a way that we can satisfy the robot's constraints while simultaneously maximizing the accuracy of the map and minimizing the total runtime?

There are existing approaches which use directional sensors **[2]** to gain further information about where a radiation source might be. In this work, an omnidirectional gamma sensor is utilized, meaning that the origination of the radiation when measuring at a location is not known. This greatly lowers the cost of the equipment needed but increases the complexity of localization. The use of Gaussian process regression (GPR) and an associated utility function has been proposed by several authors **[3, 4];** however, the added difficulties of navigation in an unknown environment and the rapid drop-off of the radiation signal provide additional challenges.

APPROACH

A gamma-ray detection system, in this case a cadmium zinc telluride (CZT) semiconductor detector from Kromek, is mounted to a remote-controlled platform). The CZT provides excellent energy resolution in an extremely small package, keeping the payload light. The detector is controlled by an Intel Joule single-board computer, which in turn talks wirelessly to a laptop. Experiments were also carried out on a Turtlebot Waffle, which comes equipped with a laser detection system (LDS) and a light detection and ranging (LIDAR) system **(Figure 1).** Gamma-ray spectra are saved along LIDAR scans and positioning information.

Regression algorithms were analyzed using various weighting schemes which leverage exploitation (gathering more information on known locations) versus exploration (gathering information on unknown locations). Quantitative evaluations often favored exploitation-heavy weighting schemes, whereas qualitative comparisons would favor exploration-biased schemes. Given a set of possible sampling locations, the next sampling location can be iteratively selected by maximizing the appropriate utility function.

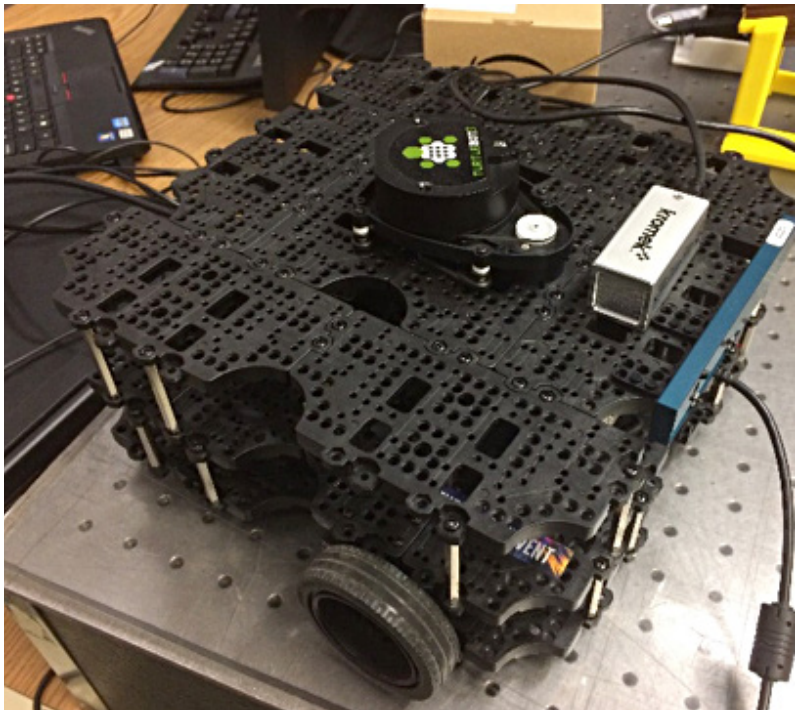

Figure 1. The Turtlebot Waffle robot, with important components and sensors

RESULTS/DECISION

A number of weighting schemes were tested and scored against the root mean square error (RMSE) both locally (for the region immediately surrounding a point source) and globally. With an exploration weight of 1.5, a good balance is found as the environment is explored, leading to low overall uncertainty and a later focus on exploring the local maxima. Interestingly, the weighting scheme of evenly balanced exploitation, exploration, and distance travelled gives the most rapid minimization of RMSE.

Experiments were then conducted with the robotic system. Data was gathered by the robot following a random trajectory **(Figure 2),** which was then used as a ground-truth to both reconstruct the radiation distribution and provide a simulated environment for a virtual robot. The reconstructed distribution **(Figure 3)** closely aligned with the truth, where the peak of the reconstruction aligned with the actual position of the point source.

Results for the path planning algorithm were tested in software models, using the ground-truth data collected by the system. The robot was able to localize the point sources with few samples, while further samples were used to provide further detail to the overall map. In the future, the robot's LIDAR could be used to perform simultaneous localization and mapping (SLAM) in conjunction with the radiation mapping, and to finalize integrating online IPP with the robot platform.

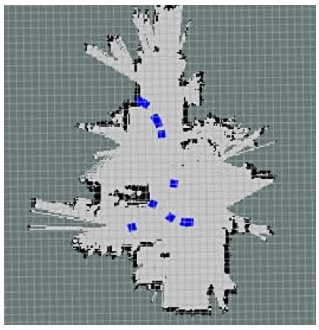

Figure 2. LIDAR scan of the room (black points) and spectrum acquisition locations (blue points).

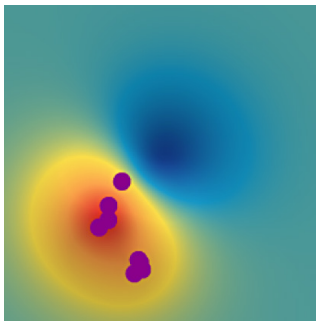

Figure 3. Reconstructed radiation distribution after seven spectra. Purple points correspond to locations where samples were taken. Red areas indicate higher expected radiation, and blue indicates a lower expectation.

FUTURE DIRECTIONS

- Implement SLAM in real time while robotic platform is travelling, to combine with reconstructed gamma-ray image.
- Integrate IPP algorithms onto the platform, including real-time communication with the robotic operating system (ROS)
- Take data in facilities, in order to test algorithms on complex, real-world distributions.

PRESENTATIONS

1. S. Zanlongo, Y. Tan, T. Aucott, "Informative Path Planning for Mapping Radiation," ANS Winter 2018 Meeting, Scheduled November 2018.
Partnerships: Florida International University

PUBLICATIONS

1. L. Ocampo Giraldo, A. E. Bolotnikov, G. S. Camarda, S. Cheng, G. De Geronimo, A. McGilloway, J. Fried, D. Hodges, A. Hossain, K. Ünlü, M. Petryk, V. Vidal, E. Vernon, G. Yang, and R. B. James, "Arrays of Position-Sensitive Virtual Frisch-Grid CdZnTe Detectors: Results from a 4x4 array prototype", IEEE Trans. on Nucl. Science 64, No. 10, 2698-2705 (2017). Digital Object Identifier: 10.1109/TNS.2017.2743160. Published November 2017.
Partnerships: Brookhaven National Lab, University of Texas, North Carolina State University

2. Alexander Moiseeva, Alexey Bolotnikov, Gian Luigi DeGeronimo, Elizabeth Hays, Ralph James, David Thompson, and Emerson Vernon, "High-energy 3D calorimeter for use in gamma-ray imaging based on position-sensitive virtual Frisch-grid CdZnTe detectors", Journal of Instrumentation, accepted December 2017.
Partnerships: NASA GSFC, University of Maryland, Brookhaven National Lab

3. L. Ocampo Giraldo, A.E. Bolotnikov, G.S. Camarda, G. De Geronimo, J. Fried, R. Gul, D. Hodges, A. Hossain, K. Ünlü, E. Vernon, G. Yang, R.B. James, "Study of sub-pixel position resolution with time-correlated transient signals in 3D pixelated CdZnTe detectors with varying pixel sizes", Nuclear Instruments and Methods in Physics Research Section A: Accelerators, Spectrometers, Detectors and Associated Equipment, Volume 884, 11 March 2018, Pages 136-139, ISSN 0168-9002, https://doi.org/10.1016/j.nima.2017.12.024.
Partnerships: Pennsylvania State University, Brookhaven National Lab, University of Texas

4. A. E. Bolotnikov, G. S. Camarda, G. De Geronimo, J. Fried, D. Hodges, A. Hossain, K. Kim, G. Mahler, L. Ocampo Giraldo, E. Vernon, G. Yang, R. B. James, "A 4x4 array module of position-sensitive virtual Frisch-grid CdZnTe detectors for gamma-ray imaging spectrometers", Nuclear Instruments and Methods in Physics Research A, accepted, August 2018.
Partnerships: Brookhaven National Lab, University of Texas, Korea University, North Carolina State University

5. L. Ocampo Giraldo, A. E. Bolotnikov, G. S. Camarda, G. De Geronimo, J. Fried, D. Hodges, A. Hossain, K. Ünlü, E. Vernon, and R. B. James, "Using A Linear Array of Position-Sensitive Virtual Frisch-Grid CdZnTe Detectors for Uranium Enrichment Measurements", Nuclear Instruments and Methods in Physics Research A, submitted April 2018.
Partnerships: Pennsylvania State University, Brookhaven National Lab, University of Texas

REFERENCES

1. K. Vetter, R. Barnowksi, A. Haefner, T. H. Y. Joshi, R. Pavlovsky, and B. J. Quiter, "A Gamma-Ray imaging for nuclear security and safety : Towards 3-D gamma-ray vision," Nucl. Inst. Methods Phys. Res. A, vol. 878, pp. 159–168, 2018.
2. M. Lee, M. Hanczor, J. Chu, Z. He, N. Michael, R. Whittaker, "3-D Volumetric Gamma-ray Imaging and Source Localization with a Mobile Robot," Waste Management Symposia 2018.
3. R. Marchant and F. Ramos, "Bayesian Optimisation for informative continuous path planning," Proc. - IEEE Int. Conf. Robot. Autom., pp. 6136–6143, 2014.
4. G. Hitz, A. Gotovos, F. Pomerleau, M. É. Garneau, C. Pradalier, A. Krause, and R. Y. Siegwart, "Fully autonomous focused exploration for robotic environmental monitoring," Proc. - IEEE Int. Conf. Robot. Autom., pp. 2658–2664, 2014.

ACRONYMS

CZT Cadmium Zinc Telluride
IPP Informative Path Planning
GPR Gaussian Process Regression
LDS Laser Detection System
LIDAR LIght Detection And Ranging
RMSE Root Mean Square Error
SLAM Simultaneous Localization and Mapping

TOTAL NUMBER OF POST-DOCTORAL RESEARCHERS

This project employed one post-doctoral intern (Sebastian Zanlongo) and one graduate student intern (Aimee Gonzalez) through the MSIPP program.

USE OF PROCESS IMAGING TO IMPROVE THE PERFORMANCE OF A FILTER

PROJECT TEAM: M. R. Poirier (PI), F. F. Fondeur, A. L. Houk, S. D. Fink

THRUST AREA:
Environmental Stewardship, Imaging

PROJECT START DATE:
February 1, 2018

PROJECT END DATE:
September 30, 2018

Solid-liquid separation is the rate limiting step for many waste treatment processes in the DOE complex, as well as in industry. Understanding the fouling process, the properties of the fouling material, and the change in the fouling structure and foulant properties with time will improve our understanding of filtration processes. Feed slurries containing gibbsite or hematite in water were prepared and fed to the stirred cell filter. Images were collected of the feed slurry and filter cake during the filtration process. After the images were collected, AutoQuantX3 was used to improve the image quality, and ImagePro3D was used to quantify the properties of the particles and filter cake.

FY 2018

Objectives

- Select and procure commercial off the shelf software to process collected video
- Capture video of solid particle movement and filter cake formation on surface of filters.
- Quantify filter cake properties
- Demonstrate feasibility of data collection and tools

Accomplishments

- Collected images of filter cake during filtration of gibbsite/water and hematite/water slurries
- Used AutoQuantX3 software to improve image quality.
- Used ImagePro3D software to determine particle size distribution of particles at filter cake-liquid interface and to determine filter cake thickness.

INTRODUCTION

This project employed process imaging technologies to better understand solid particle movement and filter cake formation on the surface of filters. The overall objective is to identify means to reduce filter fouling, thereby increasing filtrate throughput.

APPROACH

Testing used an existing stirred cell apparatus **(Figure 1)** to conduct the tests. The Millipore stirred cell is an ~100 mL glass vessel that receives a feed slurry through the top, uses pressure to force the liquid through a filter media, and has an exit through the bottom of the cell. The apparatus contains a stir bar to provide agitation of the feed slurry, but the stir bar was removed to improve image collection.

Feed slurries containing ~ 10 g/L of gibbsite or hematite in water were prepared and fed to the stirred cell. Images were collected of the feed slurry and filter cake during the filtration process.

Commercial off the shelf imaging software was identified and evaluated to improve the quality of the collected images and to quantify the properties of the filter cake and solid particles.

Figure 1. Stirred Cell Filtration Apparatus

RESULTS/DECISION

Images were collected during the filtration of gibbsite/water and hematite/water slurries, as well as during the cleaning of the filters with 0.5 M oxalic and nitric acid. **Figure 2** shows the filtration of a hematite/water slurry and the chemical cleaning of a gibbsite/water slurry with nitric acid.

After the images were collected, AutoQuantX3 was used to improve the image quality, and ImagePro3D was used to quantify the properties of the particles and filter cake. **Figure 3** shows an image of a hematite/water slurry and a filter cake before and after using the AutoQuantX3 software. **Figure 4** shows the particle size distribution of the solid particles at the filter cake-liquid interface, along with measurements of the filter cake thickness as a function of position.

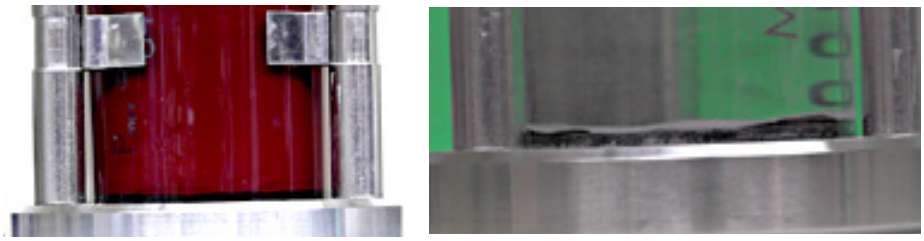

Figure 2. Filtration of hematite/water slurry and chemical cleaning of gibbsite/water slurry with nitric acid

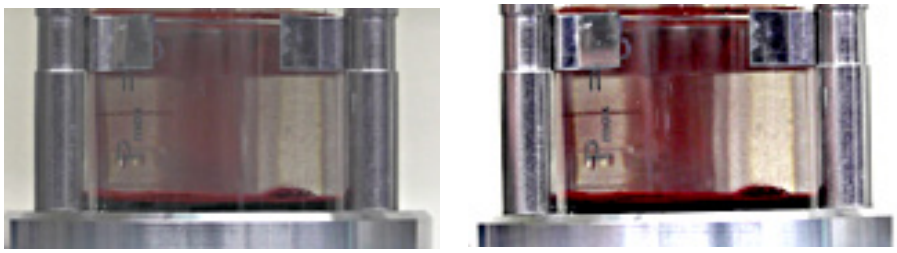

Figure 3. Image of hematite filter cake before and after using the AutoQuantX3 software

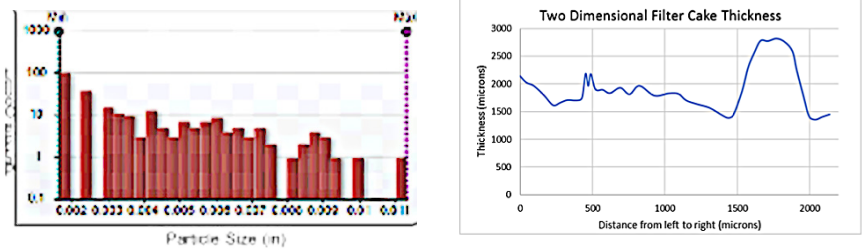

Figure 4. Particle Size Distribution and Filter Cake Thickness from Hematite/Water Slurry Filtration

FUTURE DIRECTIONS

- Extend testing to cross-flow filter configurations
- Investigate approaches for imaging of particles within filter pores
- Develop software tools to rapidly process large amounts of data and convert the data to a form that can be used by the end user

PRESENTATIONS/PUBLICATIONS

No reports or presentation were given in FY2018.

A presentation at the 2019 AIChE Spring meeting is planned.

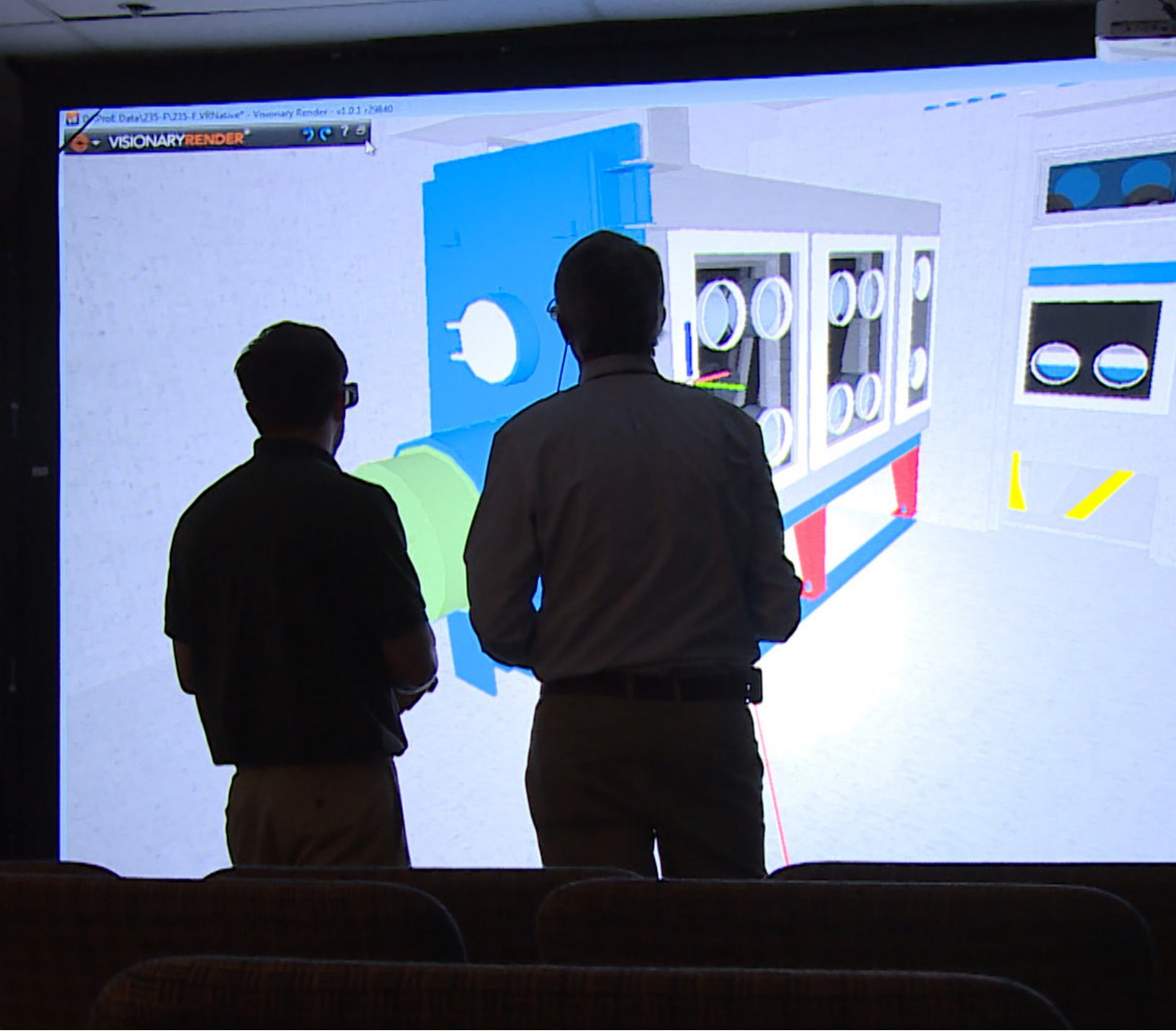

NUCLEAR MATERIALS MANAGEMENT

DISSOLUTION OF USED NUCLEAR FUEL USING A TBP/N-PARAFFIN SOLVENT

PROJECT TEAM: T. S. Rudisill (Primary)
T. C. Shehee, D. H. Jones

UNFUNDED COLLABORATORS:
G. D. DelCul
(Oak Ridge National Laboratory)

THRUST AREA:
Nuclear Materials Management
Environmental Stewardship
Secure Energy Manufacturing

PROJECT START DATE:
October 1, 2017

PROJECT END DATE:
September 30, 2018

The complete recycle of used nuclear fuel (UNF) is desirable to recover the energy value from the remaining U and the higher actinides; however, construction of a large-scale facility is prohibitively expensive. To address this issue, we evaluated a hybrid process combining the dissolution of UNF pretreated (oxidized) for tritium removal in tributyl phosphate (TBP) with solvent extraction cycles required for recovery of actinide and lanthanide elements. We prepared actinide solid solutions containing selected fission product elements as surrogates for pretreated, irradiated reactor fuel. The distribution of the actinide and fission product elements was measured between the solvent and residual solids to determine dissolution efficiencies. Dissolution of solid solutions in the TBP solvent was effective for the recovery of both the actinide and lanthanide elements. Our data indicate that most of the fission products generated during fuel irradiation except for the lanthanides and Re(Tc) would remain in the undissolved solids.

FY 2018

Objectives

- Demonstrate the feasibility of dissolving and purifying the actinide materials in UNF using a TBP/n-paraffin solvent following pretreatment with nitrogen dioxide gas (NO2) to remove tritium
  - Evaluate the dissolution of irradiated Dresden reactor fuel in a 30 vol % TBP/n-paraffin solvent and characterize the distribution between the solvent and residual solids; pretreated irradiated Dresden fuel was not available from ORNL due to the termination of the tritium removal project by the DOE-NE Fuel Cycle Program
  - Prepare actinide solid solutions as materials which are representative of pretreated UNF and evaluate their dissolution efficiency in a TBP/n paraffin solvent

Accomplishments

- Dissolution of solid solutions in a TBP/n-paraffin solvent was effective for the recovery of the actinide and lanthanide elements
  - A majority of the Re(Tc) also dissolved in the TBP solvent
  - An increase in the TBP concentration results in an increased dissolution efficiency for the elements of interest
- Near complete dissolution of U was obtained in experiments performed at both 24 and 50 ℃
  - Dissolution efficiency of TRU actinides and lanthanide fission products increased with increasing temperature
  - Current work indicates that kinetics may control the extent of dissolution of the solid solutions
- A two-stage dissolution process was successful for recovery of the actinides and lanthanide fission products
  - Lanthanide fission products and Am/Cm are easily stripped from the TBP solvent with dilute HNO3
  - Additional cycles of solvent extraction can be used to provide additional purification and separate the U, Np, and Pu and Am/Cm

INTRODUCTION

When UNF is removed from a reactor, approximately 95% of the initial U is still present in the fuel. The fuel also contains higher actinides (e.g., Np, Pu, Am, and Cm) which can be recovered, fabricated into fuels or targets, and used to generate additional energy. However, construction of a large-scale reprocessing facility with the capability to completely recycle UNF is prohibitively expensive. Simplified flowsheets which reduced the equipment footprint and facility size are needed to improve the economic viability of complete recycle. To address this issue, we have performed a demonstration of a hybrid process which combines the dissolution of pretreated UNF in a TBP-containing solvent with two cycles of solvent extraction required for the recovery of the actinide and lanthanide elements. A conceptual flowsheet for the headend facilities including the hybrid process is shown in **Figure 1.**

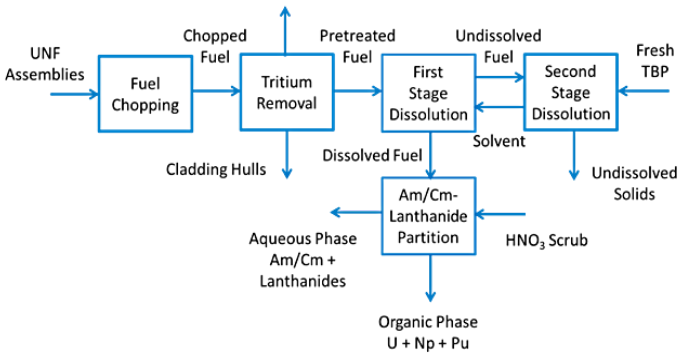

Figure 1. Conceptual Headend Process for the Recycle of UNF

A dry pretreatment process based on the oxidation of UNF was demonstrated at the ORNL for the removal of tritium (and I_2) in the headend portion of a fuel reprocessing facility. In this process, contact with a NO_2/O_2 mixture converts the fuel into a fine UO_3 powder, and with further reaction time and temperature adjustment, the UO_3 can be converted to $UO_2NO(NO_3)_2$ **[1].** In the nitrate form, U can be dissolved (extracted) directly into TBP. The direct dissolution of the UO_3 product into TBP can also be achieved by using TBP pre-equilibrated with nitric acid **[2].** Although, the direct dissolution of both UO_3 and $UO_2NO(NO_3)2$ into TBP has been demonstrated **[3]**, the extent of dissolution of other components of UNF into a TBP solvent has not been investigated.

To demonstrate the feasibility of the hybrid process, we prepared actinide solid solutions containing nonradioactive fission product elements as representative surrogates for light water reactor fuel pretreated for tritium removal. The surrogate UNF's were subsequently used in dissolution experiments to evaluate the distribution of the actinides and fission product elements between the solid and liquid phases. The feasibility of dissolving the solids solutions was investigated using 30 and 50 vol % TBP, at ambient (24-28 °C) and 50 °C, and using a two-stage dissolution process in which the initial volume of TBP was decanted from the undissolved solids and fresh TBP added for a second stage of dissolution.

APPROACH

Based on our previous work to demonstrate the dissolution of simulated UNF into a TBP/n-paraffin solvent **[4]**, we chose to prepare solid solutions from a uranyl nitrate solution containing transuranics (Np, Pu, and Am), Cs and Sr, lanthanides (Ce, Nd, and Er), and Re whose chemical behavior should mimic the behavior of Tc. Other major fission product elements (e.g., Mo, Zr, Ru, and Pd) which did not dissolve in the TBP dissolution experiments performed during the previous work were eliminated from the experimental design. The nominal masses of U and nonradioactive fission product elements used in the experiments were 1.25 and 0.2 g, respectively. Only trace quantities (< 0.02 g) of the transuranic actinides were used in the experiments. The solid solution was prepared by initially combining the nitrate solutions of the elements of interest. The actinides and nonradioactive fission products were then precipitated by adding ammonium hydroxide (NH_4OH) to the nitrate solution **(Figure 2a).** The hydroxide precipitates were filtered and transferred to an alumina crucible and dried in a muffle furnace at 110 °C for 30 min. The dry powder was subsequently calcined at 600 °C for 2 h to prepare the solid solution (Figure 2b). Prior to use in a dissolution experiment, the solid solutions were ground to

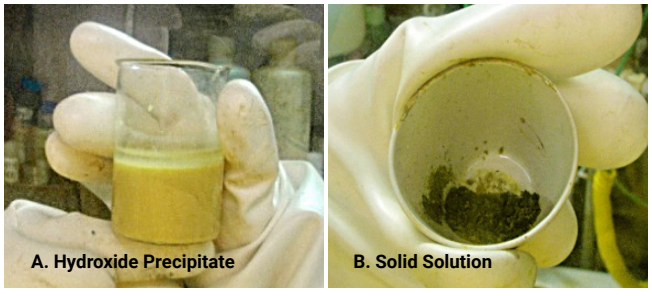

Figure 2. Preparation of Actinide Solid Solution Containing Nonradioactive Fission Product Elements ***(Left)*** *Hydroxide Precipitate* ***(Right)*** *Solid State*

a fine, free-flowing powder using a mortar and pestle to simulate the morphology of the UNF powder following pretreatment by the tritium removal process.

The solid solution dissolution experiments were performed in a 100-mL beaker using a hot plate/stirrer to provide heating (when necessary) and mixing with a magnetic stir bar. A 50-mL aliquot of solvent was used in all experiments. Experiments were performed using 30 and 50 vol % TBP in dodecane and at the ambient glovebox temperature and 50 °C. An external thermocouple controlled by the hot plate/stirrer was used to maintain the dissolving temperature at 50 °C. The ambient temperature in the glovebox ranged between 24 and 28 °C. The dissolution time was maintained consistently at 4 h. Once the dissolution was complete, the residual solids were separated from the solvent by filtration. A small aliquot of dodecane (8 mL) was used to wash residual solvent from the solids. The solids were then dissolved using a 50 mL aliquot of 8 M HNO_3 containing 0.05 M KF at 60 to 80 °C. Two-stage dissolution experiments were performed using 30 and 50 vol % TBP. Following the first-stage dissolution, a majority of the solvent was decanted from the beaker and an additional 50-mL aliquot of fresh TBP was added to perform the second stage of the dissolution. The organic (TBP solvent) and aqueous (HNO_3/KF) solutions generated during the dissolution experiments were sampled and analyzed for the elements of interest by inductively-couple plasma mass spectroscopy (ICPMS). Recovery efficiencies for each element were calculated from the ICPMS analyses and the measured volumes of the aqueous and organic solutions recovered following completion of the experiments.

RESULTS/DECISION

The dissolution of the U oxide began almost immediately upon combining the solid solution and the TBP solvent as evident from the yellow color of the solvent. The residual solids remaining from the dissolution were sticky and tended to coat the wall of the beaker. To address the incomplete transfer to the filter, the recovered solids were returned to the beaker where the acid dissolution was performed. Complete dissolution of the solids was obtained in all experiments. The dissolution efficiencies for experiments performed using 30 and 50 vol % TBP are compared in **Table 1.** Comparable data from previous work are also provided in the table for dissolutions performed using surrogate UNF prepared by adding nonradioactive fission product elements or transuranic actinides to UO_3 produced by treating unirradiated, depleted UO_2 pellets for tritium removal **[4].** Inspection of the data show that the dissolution efficiencies for the actinides from the solid solutions are much improved compared to the dissolution efficiencies from the mixture of oxides measured in the previous work. Increased dissolution efficiencies were also observed for Ce and Re. The dissolution efficiencies of the actinides (U(VI), Np(IV), Pu(IV), and Am(III)) and lanthanides (Ln(III)) from the solid solution are consistent with the expected extraction behavior in TBP with high nitrate salting **[5-7].** The dissolution behavior of the actinides, lanthanides, and Re from the solid solutions prepared in this work are likely more consistent with the dissolution behavior of solid solutions formed in reactor fuels during irradiation than the dissolution behavior observed from mixtures of oxides prepared in the previous work. The present work also shows that the dissolution efficiencies for the actinides, lanthanides, and Re are improved when the TBP concentration was increased from 30 to 50 vol %.

Exp	Solid-1	Solid-2	UO-9	UO-10	UO-11	UO-12	UO-21	UO-22
TBP (vol %)	30	50	30	30	30	30	30	30
Temp (°C)	24	24	22	22	50	50	23	25
Element	Dissolution Efficiency							
Sr	0.17	0.12	0.0	0.0	0.1	0.0	-	-
Cs	0.04	0.02	0.0	0.0	0.0	0.0	-	-
Ce	21.5	49.4	0.0	0.0	2.2	0.2	-	-
Nd	55.0	77.5	71.2	65.1	66.4	46.0	-	-
Eu	83.8	93.3	83.1	82.7	83.6	60.4	-	-
Re(Tc)	49.1	61.6	11.2	9.2	11.1	3.3	-	-
U	99.8	99.7	98.3	99.5	94.1	88.3	113	106
Np0	99.1	99.6	-	-	-	-	0.3	0.3
Pu	81.8	94.9	-	-	-	-	< 0.4	< 0.6
Am	57.6	81.2	-	-	-	-	0.1	0.1

Table 1. Elemental Efficiencies for Dissolution of Surrogate UNF in a TBP/n-paraffine Solvent

The elemental dissolution efficiencies for experiments performed at 24 and 50 °C are shown in Table 2. Near complete dissolution of U was obtained in both experiments. However, the dissolution efficiencies for the transuranic actinides and lanthanides improved in the experiment performed at 50 °C. In the previous work, the highest U recovery efficiencies were obtained at nominally 25 °C compared to experiments performed at 50 °C **[4].** This observation is consistent with U distribution coefficients between TBP and HNO_3 decreasing with increasing temperature **[6]**. A temperature effect was not discernable in the previous work for the

transuranic actinides and fission product elements which were mixed with the UO_3 from the tritium pretreatment process. The high solubility of the U from the solid solution in the TBP solvent probably obscured any noticeable temperature effect. The improvement of the dissolution efficiencies of other elements of interest in the present work **(Table 2)** suggest there may be a kinetic effect that may control the extent of dissolution. The effect of temperature may be more pronounced with actual LWR fuel which has been pretreated for tritium removal.

Two-stage dissolutions were effective for the recovery of nearly all the actinide elements and most of the lanthanides from the solid solutions. The elemental dissolution efficiencies for the first and second stages of dissolution and the overall efficiencies are shown in **Table 3.** Based on the previous **[4]** and current work, most of the fission products generated during fuel irradiation except for the lanthanides and Re(Tc) would remain in the undissolved solids. The loaded TBP solvent exiting a two-stage process would contain the actinides, a majority of the lanthanides, and small amounts of other extractable fission products such as Re(Tc). The Am/Cm, lanthanides, and other fission products could be scrubbed from the solvent using dilute HNO3. A higher concentration of HNO_3 would be necessary to strip Tc from the TBP solvent **[8].** An additional solvent extraction process would be required to separate the Am/Cm from the lanthanide fission products. A second cycle of solvent extraction could be used to provide additional purification and partition the U, Np, and Pu into the desired product streams.

Exp	Solid-1	Solid-2
TBP (vol %)	30	30
Temp (˚C)	24	50
Element	Dissolution Efficiency	
Sr	0.17	0.02
Cs	0.04	0.07
Ce	21.5	69.0
Nd	55.0	88.0
Eu	83.8	96.5
Re	49.1	29.0
U	99.8	99.8
Np	99.1	99.7
Pu	81.8	94.2
Am	57.6	86.2

Table 2. Elemental Dissolution Efficiencies at 24 and 50˚C in 30 vol % TBP

Exp	Solid-3			Solid-4		
TBP (vol %)	30			50		
Temp (˚C)	27			28		
Element	Dissolution Efficiency					
	Stage 1	Stage 2	Overall	Stage 1	Stage 2	Overall
Sr	0.024	0.024	0.048	0.019	0.016	0.035
Cs	0.068	0.161	0.229	0.080	0.028	0.108
Ce	63.5	24.8	88.3	52.3	16.3	68.6
Nd	76.4	20.6	96.9	72.9	17.3	90.2
Eu	87.4	12.1	99.5	84.1	13.8	97.9
Re(Tc)	70.3	18.7	89.0	55.9	12.4	68.3
U	96.5	3.48	99.9	93.7	6.21	99.9
Np	95.4	4.44	99.8	89.6	10.2	99.8
Pu	78.5	19.3	97.9	81.7	9.83	91.5
Am	19.4	79.6	99.0	63.6	21.8	85.3

Table 3. Elemental Recoveries Measured in Two-Stage Dissolutions using 30 and 50 vol % TBP

FUTURE DIRECTIONS

- Demonstrate the dissolution of irradiated UNF pretreated for tritium removal in a TBP/n paraffin solvent
  - Pretreat irradiated fuel samples to prepare UO3 and potentially $UO_2NO(NO_3)_3$ for dissolution tests (work no discontinued by the DOE-NE Fuel Cycle Program)
  - Perform laboratory-scale dissolution experiments to demonstrate the efficacy of the TBP dissolution process
  - Perform experiments to address differences in observed behavior of irradiated and unirradiated fuel and supplement results from experiments performed with UNF surrogates prepared from solid solutions
- Pretreated fuel may be available from the DOE-NE Fuel Cycle Program CoDCon demonstration at Pacific Northwest National Laboratory if the tritium pretreatment process is performed as part of the continuing demonstration

PUBLICATIONS/PRESENTATIONS

1. T. S. Rudisill, T. C. Shehee, D. H. Jones, G. D. DelCul, *Dissolution of Used Nuclear Fuel using a TBP/n-Paraffin Solvent,* SRNL-MS-2018-00055, 42nd Annual Actinide Separations Conference, Charleston, SC, May 22, 2018.
2. T. S. Rudisill, T. C. Shehee, D. H. Jones, G. D. DelCul, *Dissolution of Used Nuclear Fuel using a TBP/n-Paraffin Solvent,* SRNL-MS-2018-00154, Briefing for the Southern Company, Aiken, SC, August 30, 2018.
3. Presentation of a poster at the 20th Symposium on Separation Science for Energy Applications in Gatlinburg, TN on October 21-24, 2018.
4. Publication of a manuscript in the proceedings from the 20th Symposium on Separation Science for Energy Applications in a special edition of the journal *Separation Science and Technology.*

REFERENCES

1. G. D. DelCul, R. D. Hunt, B. B. Spencer, and R. T. Jubin, *Demonstrate Complete NO2-based Tritium-Pre-Treatment Process with Simulated Fission Products at Kilogram Scale,* FCRD-MR-WFD-2015-000397, Oak Ridge National Laboratory, Oak Ridge, TN (September 2015).
2. F. A. Dorda, V. V. Lazarchuk, V. A. Matyukha, M. V. Sirotkina, and V. V. Tinin, *Kinetics of UO_3 dissolution in nitric acid saturated 30% TBP in a hydrocarbon diluent, Radiokhimiya,* Vol. 52, No. 5, p. 397-398 (2010).
3. Hiroshi Tomijima, Totsuka-ku, Yokohama, Kazushige Tsukui, Direct Dissolution of Water-insoluble Uranium Compounds by Contact with Neutral Organic Solvents Pretreated with Nitric Acid, Patent 3,288,568 (November 29, 1966).
4. T. S. Rudisill, T. C. Shehee, D. H. Jones, and G. D. DelCul, *Dissolution of Nuclear Fuel using a TBP/n-paraffin Solvent,* SRNL-STI-2017-00662, Savannah River National Laboratory (October 2017).
5. M. C. Thompson, *Distribution of Selected Lanthanides and Actinides Between 30% TBP in n-Paraffin and Various Metal Nitrate Solutions,* DP-1336, E. I. du Pont de Nemours & Co., Aiken, SC (November 1973).
6. M. L. Hyder , W. C. Perkins, M. C. Thompson, G. A. Burney, E. R. Russell, H. P. Holcomb, and L. F. Landon, *Processing of Irradiated, Enriched Uranium Fuels at the Savannah River Plant,* DP-1500, E. I. du Pont de Nemours & Co. (1979).
7. T. J. Colven, C. W. Cline, and A. E. Wible, *Processing of Irradiated Natural Uranium at Savannah River,* DP-500, E. I. du Pont de Nemours & Co., Aiken, SC (August 1960).
8. M. C. Thompson, M. A. Norato, G. F. Kessinger, R. A. Pierce, T. S. Rudisill, and J. D. Johnson, WSRC-TR-2002-00444, Demonstration of the UREX Solvent Extraction Process with Dresden Reactor Fuel Solution, Westinghouse Savannah River Company, Aiken, SC (September 2002).

ACRONYMS

HNO_3	nitric acid
ICPMS	inductively-coupled plasma mass spectroscopy
KF	potassium fluoride
Ln	lanthanide
NH_4OH	ammonium hydroxide
NO_2	nitrogen dioxide
ORNL	Oak Ridge National Laboratory
SRNL	Savannah River National Laboratory
TBP	tributyl phosphate
UNF	used nuclear fuel
UO_2	uranium dioxide
$UO_2NO(NO_3)_3$	uranyl nitrate
UO_3	uranium trioxide

OXYHYDROXIDES ON ALUMINUM SPENT NUCLEAR FUEL:

FORMATION STUDIES AND REMOVAL PRACTICES TO PREVENT RADIOLYTIC GAS PRODUCTION

PROJECT TEAM:
R. E. Fuentes (co-PI),
A. L. d'Entremont (co-PI), C. Verst,
C. Crawford, L. C. Olson,
B. L. García-Díaz, and R. L. Sindelar

COLLABORATORS:
T. Knight, M. Shalloo
University of South Carolina

THRUST AREA:
Nuclear Materials Management

PROJECT START DATE:
October 1, 2017

PROJECT END DATE:
September 30, 2018

Aluminum-clad Spent Nuclear Fuel (ASNF) has chemically-bound water in the form of hydrated oxides or hydroxides (oxyhydroxides) on the cladding surface due to water exposure during irradiation and storage. This presents a challenge to sealed (road-ready) dry storage. To assess the risks associated with oxyhydroxides on ASNF for dry storage, it is necessary to understand their growth/formation and morphology as the precursor state for drying and their gas generation from radiolysis. This will help determine safe oxyhydroxide loadings on dry-stored fuel as well as methods of removal. In this work, oxyhydroxides were grown on aluminum substrates and the resulting layers were studied for morphology and thickness. Radiolysis studies were performed on powders to establish a correlation between morphology and particle size on gas generated. These experiments, along with literature data, will be used to develop models and drying methods for use in establishing safe dry storage conditions.

FY 2018

Objectives

- Integrate literature models for oxyhydroxide formation and growth into a composite model and perform heat flux immersion experiments for oxyhydroxide formation to validate the model.
- Establish irradiation and gas sampling apparatus with test protocols for a range of material system and irradiation conditions and measure radiolytic gas generated from materials.
- Investigate thermal treatments and parameters to determine conditions required for adsorbed water removal and chemically-bound water removal.

Accomplishments

- The growth of oxyhydroxide layers and their response to irradiation and drying strategies is being investigated to facilitate long-term, sealed dry storage of Al-clad spent nuclear fuel.
- Literature review on Al aqueous corrosion has been conducted to guide experimental efforts and develop a predictive model for oxide content on ASNF.
- Oxyhydroxide films have been successfully grown and characterized using a "hot-wall" setup designed to simulate heat flux through fuel cladding, for several Al alloys at different temperatures.
  - Improves understanding of oxide growth under well-controlled conditions
  - Non-radioactive specimens for drying and/or radiolysis tests
- A radiolysis test apparatus has been established and used to obtain G-values for H2 release from oxyhydroxides. This capability has been successfully demonstrated on powders.
- A drying chamber has been constructed at USC and is expected to perform testing on lab-grown oxyhydroxides in FY 2019.

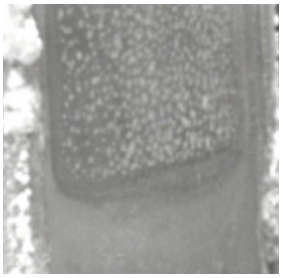

*(**Above**) Aluminum-clad fuel assembly with intact, protective oxyhydroxide film after long-term wet storage in good-quality water; (**Below**) trihydroxide deposits due additional corrosion during wet storage in poor water quality (SRNL photographs)*

INTRODUCTION

Safe storage with end-state disposition of Aluminum-clad Spent Nuclear Fuel (ASNF) is a major mission for Nuclear Material Management Programs (NMMP), with National Nuclear Safety Administration (NNSA), Department of Energy – Office of Environmental Management (DOE-EM) and Office of Science (DOE-SC), and Commerce Department customers. Water chemically-bound in the form of hydrated oxides or oxyhydroxides on aluminum cladding is prevalent on ASNF. This presents a challenge to sealed (road-ready) storage because oxyhydroxides can decompose and generate gases (e.g., oxygen, hydrogen) due to radiolysis that may cause pressurization, flammability conditions and corrosion within the storage container. The technical and engineering gaps that need to be addressed for safe storage and transportation were compiled in a recent report[1].

The formation and growth of oxyhydroxides on aluminum is dependent on temperature, heat flux and water quality; the formation and growth can occur both in reactor and while the ASNF is in wet storage in water basins for an extended period. A single model to predict the cumulative growth of oxyhydroxide from in-reactor use through long-term pool and dry storage is lacking in the literature. This LDRD was established to **(1)** investigate a unified model to predict oxyhydroxide formation on ASNF using thorough literature research and experimental results, **(2)** investigate radiolytic gas production dependence on oxyhydroxide form (e.g., gibbsite, bayerite, boehmite) by developing an irradiator and gas sampling apparatus, and **(3)** establish thermal processes for removal of oxyhydroxide films/layers. Experimentally grown oxyhydroxide layers will be characterized for morphology, thickness and surface conditions to facilitate both the modeling and drying efforts.

During FY18, oxyhydroxides were grown on Al substrates using hot wall tests. The resulting layers were characterized using X-ray Diffraction (XRD) to evaluate the resulting composition/chemical structure (e.g., gibbsite, bayerite, boehmite) and using Scanning Electron Microscopy (SEM) to examine surface morphologies and measure layer thickness. Improved understanding of surface structure coupled with literature review will help us to develop a composite model (currently in progress). Radiolysis and simultaneous thermal analysis (STA) was performed on oxyhydroxide powders with known composition and defined particle size to determine the dependence of hydrogen generation on oxyhydroxide type and morphology/particle size and to identify parameters and temperatures for the removal of residual water. The work encompasses routes for growth, radiolysis and drying to advance the understanding of the aluminum oxyhydroxides on ASNF to estimate the layers that exist on actual fuel and to establish processes for removal prior to (extended) dry storage with ultimate permanent disposal in a repository.

APPROACH

Oxyhydroxides were grown on aluminum substrates primarily using a hot-wall immersion method in the experimental setup shown in **Figure 1.** This setup heats the water bath through the aluminum sample, providing a heat flux across the surface exposed to water. This is suitable for replicating conditions in which heat flows in a prescribed direction (e.g., heat transferred to Al fuel cladding in reactor as well as during spent fuel pool storage due to attendant decay heat). Growth tests spanned a temperature range from 25°C to 100°C at times to evaluate growth kinetics. Characterizations including XRD and SEM were used to analyze the resulting oxyhydroxide.

Radiolytic gas generation from oxyhydroxides was measured using oxyhydroxide powder. Glass ampoules to hold the powder were made in the glass shop and were vacuum purged, helium filled, and flame sealed. The ampoules were placed in the SRNL Co-60 irradiator for a given time and the gas generated was removed using a purged collection tool by sealing the sample inside and cracking the glass to release the gas. The gas was analyzed using gas chromatography (GC). A picture of the collection tool is shown in **Figure 2** with an inset showing a flame-sealed glass ampoule containing powder before and after irradiation. STA of oxyhydroxide powders was also used to understand morphology transition and establish parameters for drying.

Figure 1. Hot-wall setup showing the location of the Al alloy disc specimen.

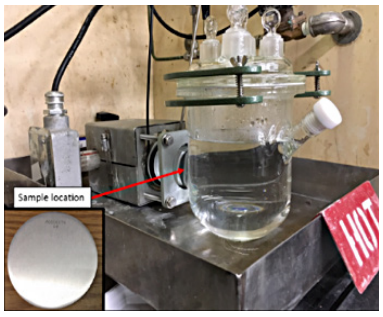

Figure 2. Gas collection tool for radiolytic gas generation tests. The inset picture shows a glass ampoule pf oxyhydroxide powder before (left) and after (right) irradiation.

RESULTS/DECISION

Hot wall immersion was used to grow oxyhydroxide films on specimens of three different aluminum alloys at various temperatures and durations. For example, Figure 3 shows SEM images of the surface of Al 1100 after 100°C hot-wall exposure for 7 days (left) and 41 days (right). XRD analysis indicated that the film was predominantly boehmite with no evidence of trihydroxides. For 100°C, either pseudoboehmite or crystalline boehmite is the expected phase[2]. SEM images of the surface morphology (Figure 3) showed a predominantly "needle-like" appearance of the oxide structure, which appears to correspond to platelets roughly perpendicular to the substrate and with random rotation, so that the edges of the platelets are seen from this angle. This morphology is consistent with oxyhydroxide morphologies described in the literature after immersion in 100°C water (studies were short-term, up to 2 h)[3,4]. There are also scattered "scale-like" features **(Figure 3)** that appear to be overlaid over the "needle-like" morphology after longer-duration exposure (41 days). Cross-section of the samples showed a total film thickness ranging from about 0.5 to 2 µm with appearance of a single-layer film. In parallel, a literature review was conducted to identify existing models and data for oxyhydroxide growth, to determine what environmental conditions have been observed to significantly impact the growth, and to gain insight into the physical mechanisms involved.

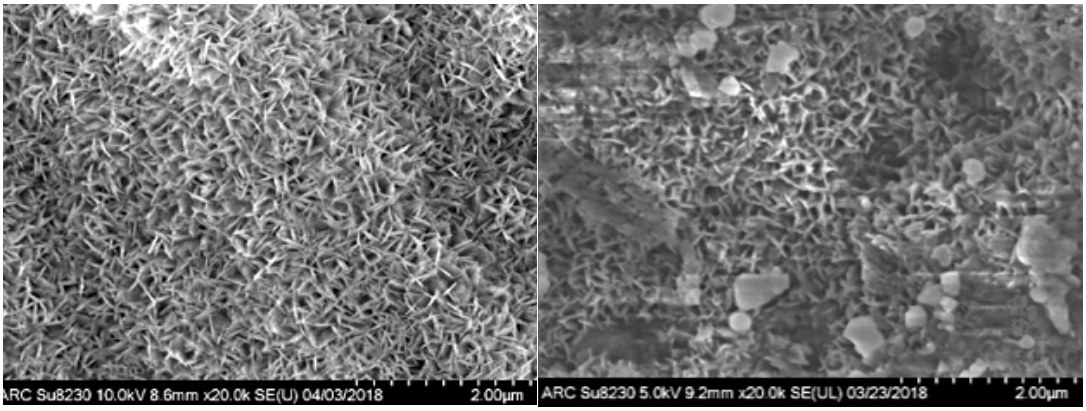

Figure 3. SEM images of Aluminum 1100 in hot-wall test at 100°C for 7 days (left) and 41 days (right).

Radiolysis tests were performed on oxyhydroxide powders to measure the radiolytic gas yield and the impact of grain size and adherence and provide gas generation differentiation depending on oxyhydroxide morphology. The powders used consisted of gibbsite with particle size ~15 µm, coarse boehmite with particle size ~77 µm and fine boehmite with particle size ~0.7 µm and were used as a first step prior to use of specimens with oxide films developed on aluminum coupon substrates. Measured G values were compared with literature data to validate of the experimental setup. The powders, contained in glass ampoules, were irradiated, and the concentration of released hydrogen was measured to compute G values. **Table 1** shows the hydrogen concentrations obtained for each powder in ppm and the calculated hydrogen G values, along with corresponding literature G values. As listed in the table, the boehmite powders yielded significantly more radiolytically produced hydrogen than the gibbsite powder: over two times more for the fine particle size and over seven times more for the coarse particle size. This is consistent with previous studies that found greater radiolytic hydrogen production for boehmite than for gibbsite[5]. While the initial powder results do fall in line with literature trends and ranges, the current results do not represent a statistically significant sample size.

Sample	Sample Dose (Rad)	H_2 Concentration (ppm)	H_2 G Value (mols/J x 10^{-7})	Derived G Values from literature[6] (mols/J x 10^{-7})
Gibbsite	16.67	502	0.0331	0.021
Boehmite (coarse)	16.67	3612	0.1911	0.057 - 0.13
Boehmite (fine)	16.67	1337	0.0783	

Table 1. Hydrogen concentration and hydrogen G-values obtained from three powders.

STA tests combining Thermogravimetric Analysis (TGA) and Differential Scanning Calorimetry (DSC) were performed on oxyhydroxide powders to explore their dehydration behavior. **Figure 4** shows results for gibbsite powder. The sample was heated to 350°C at a rate of 5°C/min and held for 1 hour, followed by cooling at the same rate down to 20°C. The points of importance are where the DSC curve turns sharply upward and when the TG curve begins to turn downward. These represent changes in energy transfer and the remaining percentage of starting mass, respectively. The most notable event is at 215°C where the DSC's upward turn (blue line) corresponds directly to the TG's downward turn (green line) indicating water evaporation. The total mass loss was approximately 30%. There was also a small change in slope of the DSC curve at about 239°C which could be indicative of an initial phase change to boehmite. A small vacuum chamber for drying tests has been constructed at the University of South Carolina (USC) for oxyhydroxide removal. **Figure 5** shows a schematic diagram of the chamber and a picture of the inside showing the two heater rods. The chamber will be used for oxyhydroxides grown on Al substrates using parameters and conditions determined from the STA analysis.

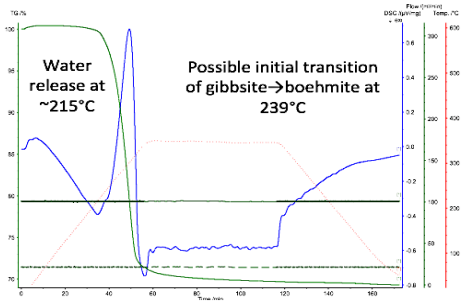

Figure 4. (Above) STA results using gibbsite powder.

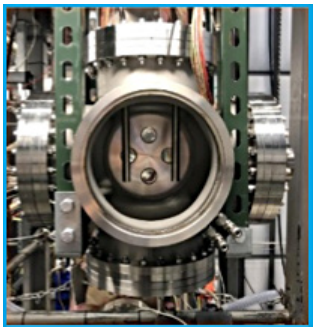

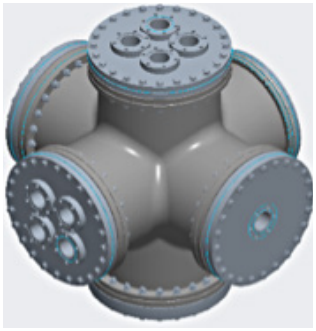

*Figure 5. Vacuum gas chamber schematic **(Left)** with a picture of the inside of chamber showing two heater rods **(Right)**.*

FUTURE DIRECTIONS

- Refine modeling using additional experimental results.
- Validate model with information from L-basin fuel of known power history and storage conditions and/or coupons with prescribed thermal profile for typical oxyhydroxide formation.
- Continue growing oxyhydroxides under varying well-controlled temperature and water conditions. Leverage knowledge from previous experiments and literature to accelerate growth of thicker and/or denser films.
- Investigate thermal treatments to determine temperatures required for water removal (i.e., physiosorbed and chemisorbed) using vacuum drying chamber at University of South Carolina.
- Explore drying technologies for ASNF using heated gas and forced gas dehydration with drying chamber and with scaled-up demonstration.

REFERENCES

1. DOE Spent Nuclear Fuel Working Group, "Aluminum-Clad Spent Nuclear Fuel: Technical Considerations and Challenges for Extended (>50 years) Dry Storage", DOE/ID RPT-1575, June 2017.
2. B. Rabin, M. Meyer, J. Cole, I. Glagolenko, G. Hofman, W. Jones, et al., "Preliminary Report on U-Mo Monolithic Fuel for Research Reactors," Idaho National Laboratory INL/EXT-17-40975, 2017.
3. A. N. Rider and D. R. Arnott, "Boiling water and silane pre-treatment of aluminium alloys for durable adhesive bonding," Int. J. Adhes. Adhes., 20, 209-220, 2000.
4. W. Vedder and D. A. Vermilyea, "Aluminum+water reaction," Trans. Faraday Soc., 65, 561-584, 1969.
5. M. L. Westbrook, R. L. Sindelar and D. L. Fisher, "Radiolytic hydrogen generation from aluminum oxyhydroxides solids: theory and experiment", J. Radioanal. Nucl. Chem, 303, 81-86, 2015.
6. J. A. Kaddissy, S. Esnouf, D. Durand, D. Saffre, E.Foy, and J.-P. Renault, "Radiolytic Events in Nanostructured Aluminum Hydroxides", J. Phys. Chem. C, 121(11), 6365-6373, 2017.

ACRONYMS

ASNF	Aluminum Spent Nuclear Fuel
DOE-EM	Department of Energy - Office of Environmental Management
DOE-SC	Department of Energy - Office of Science
DSC	Differential Scanning Calorimetry
GC	Gas Chromatography
NMMP	Nuclear Materials Management Programs
NNSA	National Nuclear Security Administration
SEM	Scanning Electron Microscopy
STA	Simultaneous Thermal Analyzer
TGA	Thermogravimetric Analysis
XRD	X-ray Diffraction

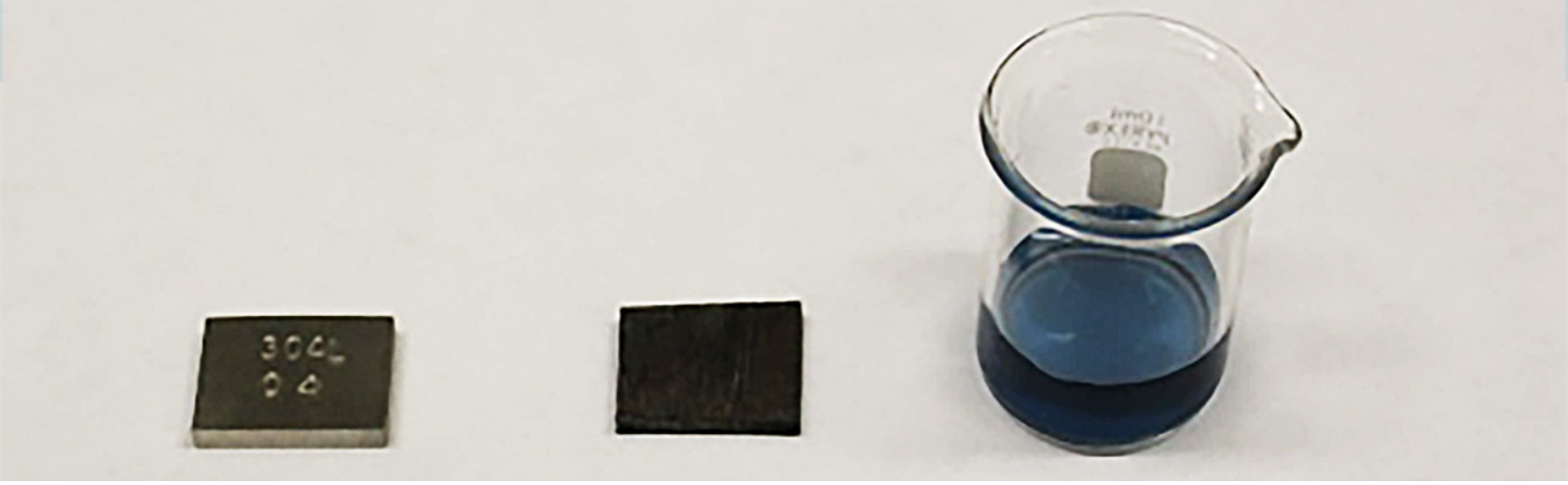

Dissolved Stainless Steel Cladding

DEMONSTRATION OF CHEMICAL DECLADDING AND DISPOSITION OPTIONS FOR NON-AL CLAD FUELS IN H-CANYON

PROJECT TEAM: M.G. Bronikowski, T.S. Rudisil, A.B. Thompson, D.D. Dick, M.A. DeVore II, W. Daniel, J.W. Amoroso, G.F. Kessinger

SUBCONTRACTOR:
(SRNL)

THRUST AREA:
Nuclear Materials Management

PROJECT START DATE:
October 1, 2017

PROJECT END DATE:
September 30, 2018

Aqueous disposition of non-Al clad fuels was studied in order to determine if H-Canyon would be a viable disposition option for this type of L-Basin fuel. A review of the L-Basin fuel types and its condition was done suggesting two major cladding types, Zircaloy and 304L stainless steel needed to be studied. Dissolution flowsheets options were reviewed. Sulfex and Zirflex processes were chosen as best for H-Canyon integration. Both process flowsheets were demonstrated on a lab scale to determine decladding rate, and off-gas and waste production. The resulting data suggested decladding in H-Canyon was an option but dissolver corrosion as well as off-gas and waste generation needed to be addressed. Small scale dissolution in a hot cell of smaller damaged fuel is a viable option with the flowsheets tested.

FY 2018

Objectives

- Review of L-Basin non-Al clad fuels
- Review of aqueous decladding flowsheets
- Scoping experiments to evaluate flowsheets identified as promising for SRS use, include dissolution rate, off-gas, and waste produced
- Training of new scientists on process chemistry

Accomplishments

- Discovered the majority of non-Al clad L-Basin Fuels is clad in Zircaloy 2 and 304 L stainless steel
- Sulfex and Zirflex dissolutions are consistent with earlier data allowing for this older data to be used for dissolution system design
- Sulfex and Zirflex dissolutions produce substantial waste so large-scale processing in H-Canyon would need to address this in the SRS waste disposition processes.
- Sulfex and Zirflex dissolutions worked well which adds an aqueous decladding too to small-scale dissolutions in Hot cells viable
- Two newer scientists were trained in experimentation needed for process chemistry

INTRODUCTION

L-Basin inventory includes stainless steel and Zircaloy clad fuels that need to be dispositioned. A disposition path of these fuels is uncertain or "TBD" with some being corroded, damaged, or at risk of degrading with time. A possible path, utilizing H-Canyon would need development as H-Canyon flowsheets do not address non-Al clad fuels. Technologies exist to declad stainless steel and Zircoly-clad fuels such as Darex, Sulfex, and Zirflex[1, 2]. These technologies are decades old and will likely result in effective decladding allowing fissile material recovery or disposal. However, the question of whether they can utilized at SRS in H-Canyon processing equipment or hot cells, with the resulting waste streams dispositioned needs study.

The project was significant for SRS in that it identified decladding technologies that with future work would be most useful for disposition of non -AL clad L-Basin fuels. The review of the L-Basin fuel cladding and its condition suggested the fuels most in need of disposition. The scoping dissolution rate tests run for this project pointed out that on a small scale both Sulfex and Zirflex were viable technologies for SRS, but on a larger H-Canyon scale Sulfex was the one that would be easiest to implement but waste streams and equipment corrosion need to be addressed. Dissolution of small "boutique" fuels in the SRNL hot cells now has options.

APPROACH

The objectives of the project were achieved through running lab scale dissolution experiments on non-Al cladding at typical H-Canyon temperatures for the dissolution technologies that were identified. Initial beaker tests were run prior to testing in the reaction vessel. Waste output and off-gas produced during dissolution were also monitored. The results would be used determine applicability for running at larger scale in H-Canyon. Lab scale results could also be used for smaller scale dissolution in hot cells. If our tests fit the older test data we assumed all of the older data could be used for assessing dissolutions in H-Canyon.

Figure 1. Reaction vessel showing 304L metal cladding dissolution rate experiment.

RESULTS/DECISION

The non-Al clad L-Basin fuel inventory was reviewed and binned for undamaged verses damaged cladding and fuel type. Three cladding types, Zircaloy 2, Zircaloy 4, and 304L stainless steel were found to be the majority in the Basin. Our dissolution technologies were thus constrained to stainless steel and Zircaloy cladding. A literature search for flowsheets was completed with three (Sulfex, Zirflex and Darex) flowsheets selected for study. The initial check of downstream effects for H Canyon disqualified Darex as it contained 3M HCl which would be problematic to fully remove. Chloride is well known cause crevice corrosion and produce pinholes in stainless steel. Only Sulfex and Zirflex would be tested.

Figure 2. Na_2SO_4 crystals produced from Sulfex waste solutions.

Two Sulfex dissolution solution concentrations 4M and 6M H_2SO_4 were tested on stainless steel. Dissolution rates of matched earlier work. The dissolution gives off only H_2 in a 1:1, stainless steel: H_2 molar ratio. Thus air sparging will need to be run with this process in H-Canyon as well as using a dissolver insert or corrosion resistant dissolver. Considerable sulfate solids are produced so waste issues may be a problem with large scale processing.

Two Zirflex dissolution solution concentrations 4M NH_4F + 0.5M NH_4NO_3 and 6M NH_4F + 1M NH_4NO_3 were tested on Zircaloy cladding. Dissolution rates were matched those of earlier work. The dissolution gave off a substantial amount of gas. Both H_2 and NH_3 are given off with the majority being NH_3. Dealing with the large amount of NH_3 gas with the nitric acid used in H – Canyon is an issue that would need to be addressed. The solubility of the waste product $(NH_4)_2ZrF_6$ would also have to be dealt with.

FUTURE DIRECTIONS

- Apply for DOE funding for dissolution of small damaged fuels in hot cells
- Corrosion testing to determine ideal dissolver material

PUBLICATIONS/PRESENTATIONS

1. "Demonstration of Sulfex and Zirflex Dissolution Processes" D.D. Dick, A.B. Thompson, W.E. Daniel, M.G. Bronikowski. and T.S. Rudisill, SRNL-STI-2018-00509, Sept. 2018.
2. "Application of Chemical Decladding to Non - aluminum Clad fuels in L-Area Basin", T.S.Rudisill
3. "Demonstration of chemical decladding and disposition options for non-Al clad nuclear fuels at the Savannah River Site" A. Thompson, D. Dick, G. Daniel, T. Rudisill, M. DeVore, and M. Bronikowski, Poster presentation, 70th SERMACS2018, Nov.1, 2018

TOTAL NUMBER OF POST-DOCTORAL RESEARCHERS

1. DeWayne Dick

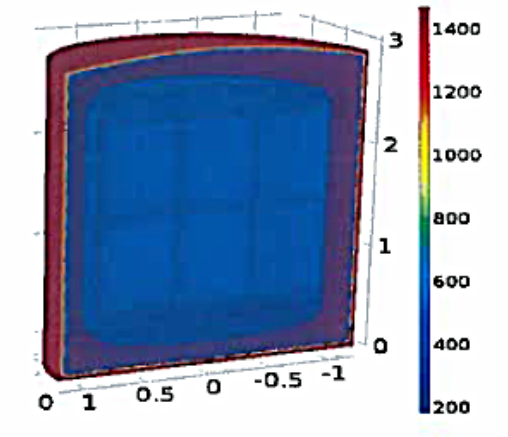

Surface temperature profile, in ° F, of a TRUPACT-tl with 14 55-gallon drums, each with 19 watts, fully engulfed in a pool fire.

INNOVATIVE PLUTONIUM WASTE FORMS: ACCEPTABILITY TO SHIP TO WIPP

PROJECT TEAM:
M. J. Brisson, M.A. Bernard, T. L. Danielson, B. M. Loftin, M. R. Kesterson, Z. M. Weis

THRUST AREA:
Nuclear Materials Management

PROJECT START DATE:
October 1, 2017

PROJECT END DATE:
September 30, 2018

Plutonium disposition is a high-profile issue gathering state and national attention. The State of South Carolina is in litigation against DOE due to a lack of plutonium disposition on the legislativelyagreed schedule. Disposal options are needed that can minimize the length and cost of the life cycle for dispositio11 of plutonium materials. Regardless of the waste form utilized, it must be acceptable for disposition at WIPP.

The project objective is to pe1form advanced modeling studies involving heat loading of waste forms with higher levels of plutonium loading. and studies to optimize plutonium levels and shipping packages that would be acceptable for shipment to WIPP. This project is integral to the overall evaluation of the technical and programmatic issues involved with the acceptability of shipping innovative plutonium waste forms for shipment to WIPP. This is a key objective for the Nuclear Material Management Focus Area to accelerate EM plutonium disposition.

FY 2018

Objectives

- Model criticality with respect to waste form and packaging assembly geometry
- Model waste form heat generation and dose rate
- Examine gas generation characteristics
- Evaluate possibility of Attractiveness Level E designation for waste form
- Evaluate suitability with respect to WIPP acceptance criteria and other regulatory standards

Accomplishments

- Thermal modeling of the packaging assembly of stainless steel - plutonium alloy-filled 5S-gallon drums, in a 7x2 array, was performed for two scenarios to calculate surface temperature profile based on a 19-watt heat source per drum, and to calculate the drum temperature profile in an accident scenario involving a fully engulfing pool fire at 1475° F for 30 minutes.

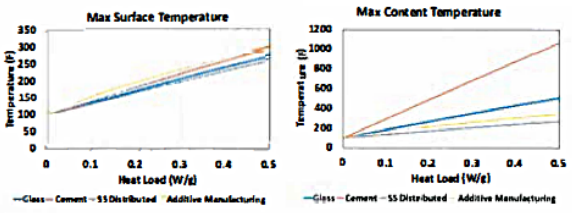

- Criticality assessments were performed on four ingot geometries. Dry cases resulted in a keff of less than 0.6. Including water increased keff, but subcriticality for the analyzed configurations was maintained.

INTRODUCTION

WIPP is a deep geologic repository located 26 miles east of Carlsbad, New Mexico. Its mission is the safe and permanent disposition of transuranic radioactive waste from atomic energy defense activities of the United States. The WIPP repository is located approximately 2150 feet underground in a salt formation that is part of the Delaware Basin. This salt formation that is free of flowing water, easily mined, impermeable and geologically stable. The salt rock naturally seals fractures and closes openings over time. Disposal of TRU waste began in 1999 and continues today with waste acceptance assisting in the cleanup of 22 generator sites nationwide.

The repository is now anticipated to receive a greater amount of plutonium materials than originally envisioned. An engineered waste form for safe and efficient transport and long-term disposal of plutonium materials is an urgent need. An optimal waste form could also reduce the disposition life-cycle and its associated costs to the taxpayer. In particular, if an engineered waste form could qualify as Attractiveness Level E under DOE-STD-1194-2011, significant cost savings could be realized. Such a waste form could also be used for plutonium disposition at non-DOE facilities outside the U.S.

In the current work, the feasibility of an innovative disposition method of a stainless steel - plutonium waste form, transported in a TRUPACT-11 shipping canister and designated as contact handled waste (i.e., dose rate ≤ 200 mrem per hour), is investigated. Through criticality assessment and thermal modeling, the stainless steel - plutonium waste form is shown to be a viable option worthy of further investigation.

APPROACH

Potential alternative waste forms were examined based on past and current studies at SRNL. For the selected form(s), advanced studies concerning heat loading and packaging optimization were conducted.

Radioactive material package design involves many aspects for which SRNL has expertise. The project utilized the advanced modeling expertise at SRNL to potentially eliminate the need to perform physical testing. Since new materials are available and can be accurately modeled, the selected waste disposition method can be incorporated into the computer models and a series of parametric studies can determine if a packaging is capable of providing the necessary level of containment to allow the package to be approved for storage at WIPP and transportation within commerce. Factors that must be considered in a new, innovative design include, but are not limited to, weight of the contents and packaging, thermal load within the contents, distribution of the contents within the waste form, total mass of the nuclear material within the waste form, and the dispersal of the contents when impacted in accident scenarios.

RESULTS/DECISION

A waste form consisting of stainless steel alloyed with plutonium was selected for detailed study. This waste form is engineered to be stable, uniform, and self-shielding. The proposed packaging assembly consists of placing stainless steel ingots, or pucks, in 55-gallon drums inside a TRUPACT-11 canister to be managed as contact handled waste. The TRUPACT-I1 canister is welt insulated so that heat does not readily reach the surface from the inside, or reach the contents from the outside.

COMSOL Multiphysics® was used to model the thermal properties of the proposed waste forms to be sent to WIPP. An initial scoping study was performed to compare different materials within a single 55-gallon drum. The wattage was varied so that the maximum surface temperature of the drum, and the maximum temperature of the contents of the drum could be calculated. Of the forms examined, stainless steel was shown to have the most favorable thermal characteristics with the lowest temperature of the drum surface and contents.

Example of criticality modeling using an infinite array of spheres.

FUTURE DIRECTIONS

- Optimization of waste form composition
- Modeling of gas generation, dose rate, and additional criticality studies
- Evaluation of feasibility of designation of the waste form as Attractiveness Level E per DOE-STD-1194-2011
- Obtaining approvals for shipping to WIPP.

REFERENCES

1. DOE-STD-1194-2011, DOE Standard: Nuclear Materials Control and Accountability, June 2011

ACRONYMS

TRU Transuranic
WIPP Waste Isolation Pilot Plant

NATIONAL SECURITY

Reduced graphene oxide filament as-prepared ***(Left)*** *and heated to 1400°C* ***(Right)***

REDUCED GRAPHENE OXIDE AS A FILAMENT MATERIAL FOR THERMAL MASS SPECTROMETRY

PROJECT TEAM:
J. M. Mannion, R. M. Achey, J. H. Hewitt, C. R. Shick Jr., M. J. Siegfried

THRUST AREA:
National Security

PROJECT START DATE:
October 1, 2017

PROJECT END DATE:
September 30, 2018

Isotopic information can be informative as to the intended use and/or production history of special nuclear material. For uranium and plutonium samples, thermal ionization mass spectrometry is the benchmark technique for determining isotope ratio data. Sample utilization in thermal ionization is, however, quite low with ionization efficiencies typically between 0.1% and 0.5%. One barrier to improving the ionization efficiency is thermodynamic limits related to the work function of the ionizing filament. Graphene oxide, having a tunable work function, has the potential to greatly improve ionization efficiencies over Re- or W-based filaments. The work function of RGO can be tuned through doping or incorporation of metal particulates. Work this year produced ultra-low background RGO and RGO-composite filaments that remained stable at high temperature under high vacuum conditions. Preliminary results using a commercial instrument demonstrate a 500% ionization enhancement for Uranium using Re-RGO composite-based filaments over traditional Re filaments when direct loading sample solutions onto filaments.

FY 2018

Objectives

- Improve RGO filament stability
- TIMS analysis of U/Pu on RGO filaments
- Operate RGO-based filaments in source chamber of commercial TIMS instrument
- Reduce RGO off-gassing
- Investigate RGO filament doping strategies

Accomplishments

- Furthered the development of RGO and hybrid RGO-based filaments
- Doped RGO filaments with Re, Pt, and F
- Demonstrated RGO filaments are stable at high temperature and high-vacuum conditions
- RGO filaments capable of withstanding 8 A of current (vs. ~5 A with Re)
- Utilized RGO-based filaments in a commercial TIMS instrument
- Re-RGO filaments improved ionization efficiency by 500% over Re direct loading
- Provided evidence that actinide-carbides are intermediates in thermal ionization

INTRODUCTION

Thermal Ionization Mass Spectrometry (TIMS) is an analytical technique that still sees widespread use in the fields of nuclear safeguards,[1,2] nuclear forensics,[3,4] and environmental monitoring[5,6] for the measurement and characterization of actinide species. TIMS is currently considered the benchmark technique for determining uranium and plutonium isotopic information.[2] Sample utilization in TIMS is, however, typically quite low due to poor ionization efficiencies – normally in the range of 0.1% - 0.5% for Pu and U. Research to try and increase ionization efficiencies has focused on geometry modifications of the typical rhenium filament material.[7-9] Because of thermodynamic limits related to work function of the analyte and the ionizing filament, entirely new materials (i.e., not Re or W) are needed in order to greatly improve ionization efficiency. Additionally, it has been theorized that carbonaceous filament additives may improve ionization efficiencies by promoting the creation of actinide carbides which stabilize the sample on the filament surface **(Figure 1).**[15] Thermal decomposition of actinide carbides at elevated temperatures (compared to in the absence of carbon) results in greater thermal ionization efficiency, as described by the Saha-Langmuir equation. Creating a carbon-based filament may further promote the creation of actinide-carbides by providing an abundant excess of carbon.

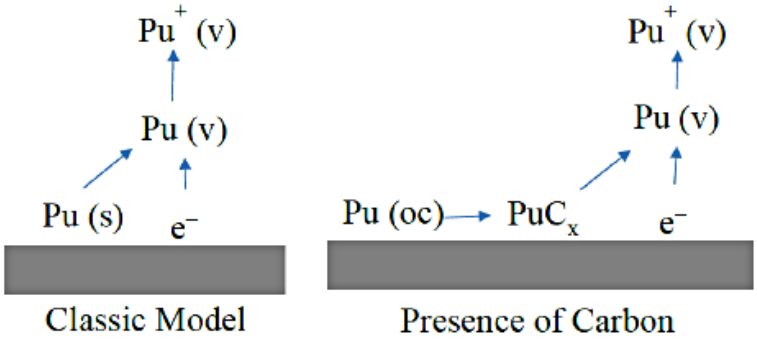

Figure 1. The presence of carbon is believed to benefit thermal ionization through the creation of actinide carbides which stabilize the sample on the ionization surface to higher temperatures, resulting in greater ionization efficiencies due to decomposition of the carbide.[15]

Developing new materials to be used as TIMS filaments is non-trivial. In a typical Pu or U analysis, filaments can reach temperatures greater than 1500 °C , requiring high-temperature stable materials. Recent work has shown that graphene-based materials can be 3D printed into small form factors that can be resistively heated to more than 2000 K (1727 °C).[10] This suggests a graphene-based TIMS filament is possible and could represent an entirely new substrate material for TIMS analyses. Moreover, because the work function of graphene is tunable,[11,12] the thermodynamic constraints that lead to poor ionization efficiency in Re- and W-based filaments could be overcome (orders of magnitude increases in ionization efficiency could be realized). Such improvements would be directly translated into reduced sample size requirements and/or enhanced analytical capabilities which would support the nonproliferation, safeguards, and forensics communities.

The first year of this LDRD project focused on developing the technical knowhow to reproducibly manufacture graphene-based filaments, testing different methods to mate RGO filaments to commercial TIMS filament assemblies, and initial durability studies of heated filaments under high vacuum conditions. Efforts this year focused on producing ultra-low background RGO and RGO-composite filaments that remained stable at high temperature under high vacuum conditions and characterizing Pu and U ionization. RGO and RGO-composite filaments were heated in the source chamber of a commercial TIMS instrument to temperatures greater than 1500 °C. Preliminary results demonstrate a 500% ionization enhancement for direct-loaded Uranium when using Re-RGO composite-based filaments over standard Re filaments and provide evidence for actinide-carbide intermediates in thermal ionization.

APPROACH

Efforts in FY18 focused on iteratively improving RGO-based filament design, developing reduction strategies to reduce/eliminate organic background and off-gassing, demonstrating viability for U and Pu ionization in a commercial TIMS instrument, and preliminary investigation into RGO doping strategies. Initial filament testing was performed in a custom-built "mock-TIMS" system with a vacuum chamber, a thermal ionization source, and a residual gas analyzer. Experiments with refined RGO-based filaments progressed to a commercial TIMS instrument where U and Pu ionization performance was characterized.

RESULTS/DECISION

The RGO filament design was iteratively improved to obtain robust filaments ultimately capable of withstanding greater than 8 A of current (vs. ~5 A for Re) in ultra-high vacuum. Specifically, strips of RGO were cut from thin sheets of graphene oxide fashioned from dried GO paste. GO strips were them mounted on a commercial TIMS post assembly using GO paste and welded Re metal strips. To generate hybrid or doped filaments, a similar procedure was followed with dopant precursors (e.g., Teflon, Re, ReO, Pt) mixed with the initial GO paste. A combination of thermal annealing and joule heating was used to reduce the GO filaments to a robust, usable form. Scanning Electron Microscope (SEM) images shown in **Figure 2** reveal the distribution of dopant materials on the surface of RGO filaments.

Initial studies to produce RGO filaments led to significant off-gassing and organic background signals during filament heating. Published graphene oxide reduction strategies were not adequate to eliminate organic backgrounds below the detection limits of high sensitivity TIMS. A reduction strategy was developed to analyze RGO reduction products in situ utilizing a custom-built mock thermal ionization source with a residual gas analyzer. This equipment enabled analysis of off-gassed species as a function of filament current and time **(Figure 3).** Optimal reducing conditions were found to be heating in air at 115 °C for 48 hours (higher temperatures resulted in exfoliation from entrapped water), followed by heating in a tube furnace with an inert atmosphere at 700 °C for 30 minutes and joule heating to greater than 5 A of filament current for at least 2 h.

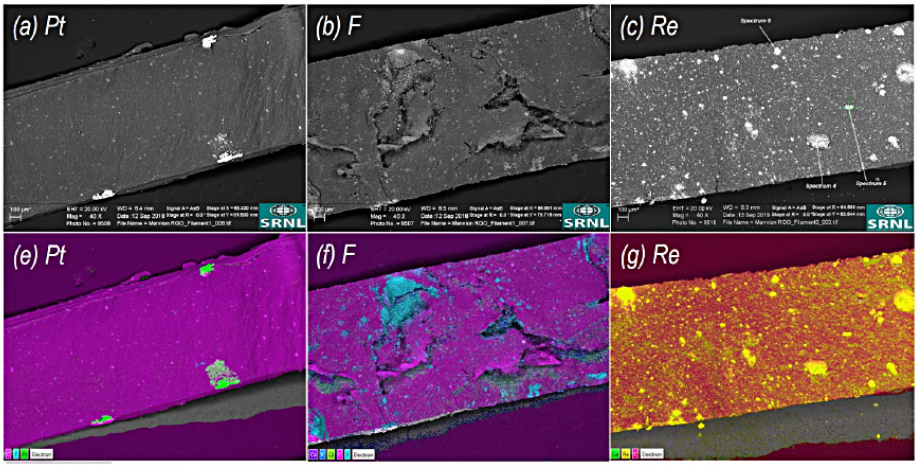

*Figure 2. **(a-c)** Scanning Electron Micrographs and **(e-g)** Energy dispersive X-ray spectral maps of **(a,e)** Platinum, **(b,f)** Fluorine, and **(c,g)** Rhenium hybrid GO filaments showing the distribution of selected elements on the surface.*

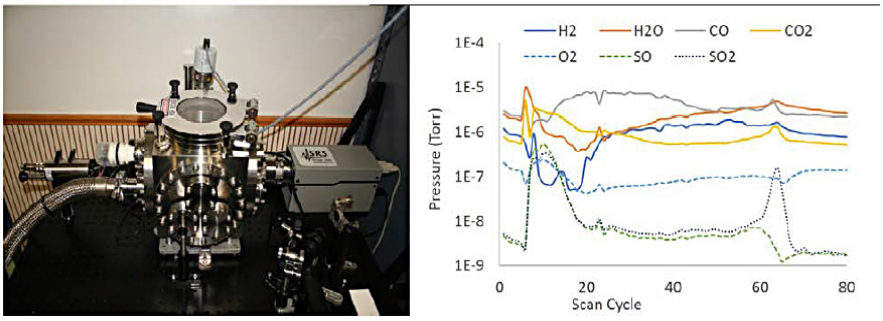

*Figure 3. **(Left)** Photograph of vacuum chamber with residual gas analyzer and power supply for TIMS filament, and **(Right)** a plot of intensity of select off-gas species as a function of time and filament heating.*

U and Pu samples deposited on RGO filaments were analyzed utilizing an IsotopX commercial single stage magnetic sector TIMS. Bead loading was initially investigated; however, beads were found to not adhere to the hot RGO surface. Direct loading was used for all subsequent sample analyses, involving simply drop-drying a sample on the RGO filament surface. After adequate reduction, non-doped RGO was found to perform well in terms of ion beam stability and low background, however, the lower work function of non-doped RGO resulted in poor ionization efficiencies compared to Re direct loading and Re bead loading. Surface fluorination was investigated as a means of improving ionization efficiency and was found to produce a two-fold improvement, however, ionization efficiencies were still lower than that of Re, suggesting low fluorine conversion utilizing this method. Achieving higher levels of doping was then attempted by mixing relatively large quantities of dopants into RGO paste prior to filament construction. Teflon and platinum were difficult to disperse in aqueous RGO paste and led to filament failure as these

large deposits melted/sublimed at high temperature. In contrast, RGO/Re hybrid filaments were found to perform comparably to the bead loading method and surpassed Re direct loading by ~500% in terms of ionization efficiency **(Figure 4).** The improvement (with RGO/Re hybrid filaments) over Re direct loading, and similar performance to Re bead loading, supports the theory that actinide carbides are beneficial intermediates in the thermal ionization of actinides, as the work function of RGO/Re filaments is not expected to exceed that of metallic rhenium.

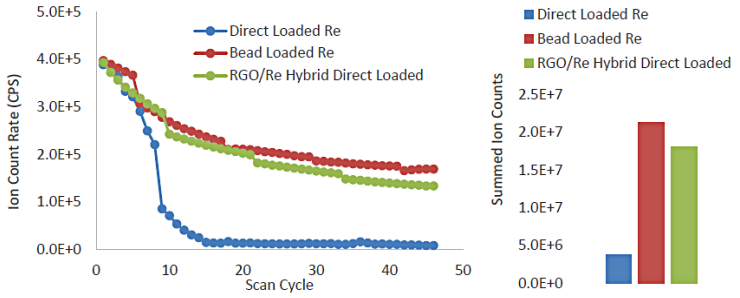

*Figure 4. **(Left)** Comparison of ion count rate decay for 100 ng U sample monitoring the 238U ion signal; filaments with various loading strategies were heated until a count rate of 400 counts per second was achieved and allowed to decay without modification of the filament current to determine sample stability. **(Right)** Comparison of total summed counts detected after sample decay.*

FUTURE DIRECTIONS

Results from this study are promising and warrant further investigation into RGO-based TIMS filaments. Potential future experiments include:

- Investigate alternative methods to increase fluorine conversion in RGO filaments. Possible pathways are improved Teflon dispersion, modification with gaseous fluorination reagents, or pre-assembly fluorination of RGO paste.
- Filament geometries, such as cavity sources, have shown improved ionization efficiency. RGO paste and 3D printing facilitate the creation of unique geometries.
- Further characterize Re/RGO hybrid filaments. Investigate the influence of rhenium dispersion, particle size, loading, and presence of other metals such as platinum.

PRESENTATIONS/PUBLICATIONS

1. J. M. Mannion, R. M. Achey, J. H. Hewitt, C. R. Shick Jr., M. J. Siegfried, "Reduced graphene oxide as a filament material for thermal ionization mass spectrometry". Expected: Communication in Talanta, Fall 2018.
2. J. M. Mannion, R. M. Achey, J. H. Hewitt, C. R. Shick Jr., M. J. Siegfried, "In Situ analysis of graphene oxide reduction products by residual gas analysis". Expected: Communication in Talanta, Fall 2018.

REFERENCES

1. Kraiem, M.; Richter, S.; Kuhn, H.; Stefaniak, E. A.; Kerckhove, G.; Truyens, J.; Aregbe, Y. Investigation of uranium isotopic signatures in real-life particles from a nuclear facility by thermal ionization mass spectrometry. *Anal Chem* **2011,** 83, 3011-3016.
2. Boulyga, S.; Konegger-Kappel, S.; Richter, S.; Sangely, L. Mass spectrometric analysis for nuclear safeguards. *Journal of Analytical Atomic Spectrometry* **2015,** 30, 1469-1489.
3. Mayer, K.; Wallenius, M.; Varga, Z. Interviewing a Silent (Radioactive) Witness through Nuclear Forensic Analysis. *Anal Chem* **2015,** 87, 11605-11610.
4. Richter, S.; Alonso, A.; De Bolle, W.; Wellum, R.; Taylor, P. D. P. Isotopic "fingerprints" for natural uranium ore samples. *Int J Mass Spectrom* **1999,** 193, 9-14.
5. LaMont, S. P.; Shick, C. R.; Cable-Dunlap, P.; Fauth, D. J.; LaBone, T. R. Plutonium determination in bioassay samples using radiochemical thermal ionization mass spectrometry. *Journal of Radioanalytical and Nuclear Chemistry* **2005,** 263, 477-481.
6. Armstrong, C. R.; Nuessle, P. R.; Brant, H. A.; Hall, G.; Halverson, J. E.; Cadieux, J. R. Plutonium Isotopes in the Terrestrial Environment at the Savannah River Site, USA: A Long-Term Study. *Environ Sci Technol* **2015,** 49, 1286-1293.
7. Bürger, S.; Riciputi, L. R.; Turgeon, S.; Bostick, D.; McBay, E.; Lavelle, M. A high efficiency cavity ion source using TIMS for nuclear forensic analysis. *Journal of Alloys and Compounds* **2007,** 444, 660-662.
8. Duan, Y.; Danen, R. E.; Yan, X.; Steiner, R.; Cuadrado, J.; Wayne, D.; Majidi, V.; Olivares, J. A. Characterization of an improved thermal ionization cavity source for mass spectrometry. *Journal of the American Society for Mass Spectrometry* **1999,** 10, 1008-1015.
9. Baruzzini, M. L.; Hall, H. L.; Watrous, M. G.; Spencer, K. J.; Stanley, F. E. Enhanced ionization efficiency in TIMS analyses of plutonium and americium using porous ion emitters. *Int J Mass Spectrom* **2017,** 412, 8-13.
10. Yao, Y.; Fu, K. K.; Yan, C.; Dai, J.; Chen, Y.; Wang, Y.; Zhang, B.; Hitz, E.; Hu, L. Three-Dimensional Printable High-Temperature and High-Rate Heaters. *ACS Nano* **2016,** 10, 5272-5279.
11. Kumar, P. V.; Bernardi, M.; Grossman, J. C. The Impact of Functionalization on the Stability, Work Function, and Photoluminescence of Reduced Graphene Oxide. *ACS Nano* **2013,** 7, 1638-1645.
12. Sygellou, L.; Paterakis, G.; Galiotis, C.; Tasis, D. Work Function Tuning of Reduced Graphene Oxide Thin Films. *The Journal of Physical Chemistry C* **2016,** 120, 281-290.
13. Hummers, W. S.; Offeman, R. E. Preparation of Graphitic Oxide. Journal of the American Chemical Society **1958,** 80, 1339-1339.
14. Yu, H.; Zhang, B.; Bulin, C.; Li, R.; Xing, R. High-efficient Synthesis of Graphene Oxide Based on Improved Hummers Method. **2016,** 6, 36143.
15. Mannion, J. M.; Improved Sample Loading for Plutonium Analysis by Thermal Ionization Mass Spectrometry and Alpha Spectroscopy. **2017,** All Dissertations 1969.

ACRONYMS

EDX	Energy Dispersive X-Ray Spectroscopy
GO	Graphene Oxide
RGA	Residual Gas Analyzer
RGO	Reduced Graphene Oxide
SEM	Scanning Electron Microscope
TIMS	Thermal Ionization Mass Spectrometry

INTELLECTUAL PROPERTY

1. Invention Disclosure - SRS-16-019 – *"Graphene Based Filaments for Thermal Ionization"*
2. Patent application - 15/435,976 - *"Graphene/Graphite-Based Filament for Thermal Ionization"*
3. Invention Disclosure – SRS-18-022 – *"Fluorine Doping of Graphene Based Heaters/ Thermal Ionization Filaments"*
4. Patent application - SRS-18-022 – *"Fluorine Doping of Graphene Based Heaters/ Thermal Ionization Filaments"*

TOTAL NUMBER OF POST-DOCTORAL RESEARCHERS

1

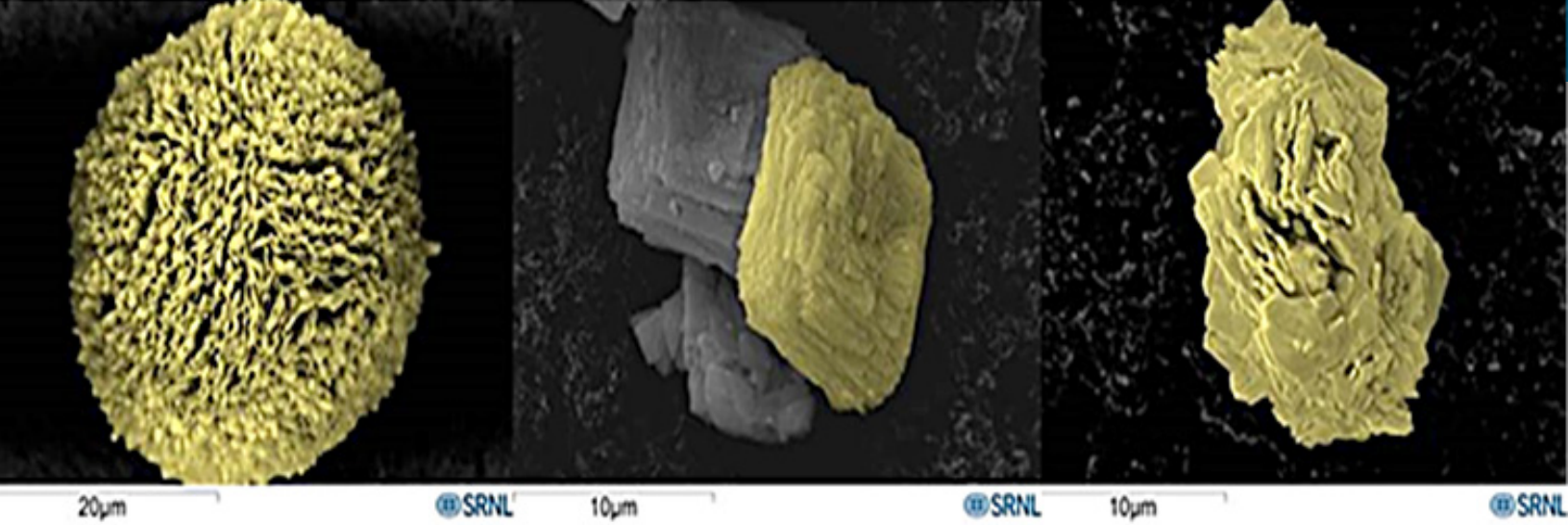

Figure 1. Three microcrystalline morphologies of PuO2 observed in a single production batch.

SYNCHROTRON-BASED MICRO-STRUCTURAL CHARACTERIZATION METHOD DEVELOPMENT FOR PU OXIDES

PROJECT TEAM:
J. Venzie (Primary),
M.A. DeVore II,
T.S. Shehee

COLLABORATORS:
J. Fortner (ANL), B. Powell
L. Schuller-Nickels (Clemson)

THRUST AREA:
National Security

PROJECT START DATE:
October 1, 2016

PROJECT END DATE:
September 30, 2018

Advanced microstructural analysis techniques were used to probe the internal structure of plutonium oxide particles as part of the development of new forensic signatures. Samples of Pu(III)O_2 and Pu(IV)O_2 with and without metal contaminants were prepared and shipped to Clemson University for SEM/EDS analysis, and to the Advanced Photon Source (APS) at Argonne National Laboratory (ANL) for X-ray fluorescence, X-ray diffraction, and X-ray Absorption Near Edge Spectroscopy (XANES) measurements. These techniques can probe samples at sub-micron spectral resolution to provide information on local crystallographic orientation, gradients, and strains.

SRNL was able to create unique sample ladders for containment of PuO_2 particles that met the APS safety standards for radioactive materials. X-ray fluorescence maps were created to find particles of interest and revealed that AFS 2 material also contains iron dispersed throughout the sample. Full XANES analysis has not been scrutinized; however, there seems to be a mixture of oxidation states of Pu(III) and Pu(IV) in the samples. Further analysis of all beamline data will take place in FY19.

FY 2018

Objectives

Efforts within FY18 concentrated on the shipping and sample preparation aspects, before performing experiments towards the end of FY18 at the Advanced Photon Source.

- Contracts placed with Clemson and ANL
- ANL sample preparation and holder approval
- Beam line experiments
- Shipment of samples to Clemson and ANL
- Successful APS general user proposal (GUP)

Accomplishments

- Successful shipments of plutonium particles to both Argonne and Clemson
- Successful beam line proposal originally scheduled for April 18.
- Successful beam line experiments in August 2018
- Sample preparation and analysis by electron microscopy

INTRODUCTION

The pre-detonation technical nuclear forensic (TNF) community is investing in the research, development, and exploitation of new non-isotopic forensic signatures of plutonium oxide. The community is interested in it as an intermediate form in the fuel and weapons cycle, and as the most common storage form for plutonium. Isotopic signatures, while useful, only provide limited information about the provenance of plutonium oxide. The TNF community is interested in exploring chemical and morphological characteristics to better understand the type of flowsheet used, scale of facilities, expertise of operators, etc. Detailed material science studies of plutonium oxide are needed to advance the understanding of the crystalline properties and their relationships to macro-scale signatures.

The process to which particles grow is dependent on their crystal structures, grain size, and orientation of grains within a particle. Variations in density and microstructure of PuO_2 powder have led to differing particle sizes and morphologies **(Figure 1 on previous page).** The microstructure is controlled by calcination temperature and the physiochemical conditions of precipitation, including shape of mixing tank, valance of plutonium, mixing sequence of plutonium and oxalic acid, precipitation temperature, and molar concentrations of oxalic acid, plutonium, and nitrate. Calcination has little effect on overall size of particle, but a great effect on surface roughness and particle morphology.

Nondestructive analysis of individual PuO_2 particles requires the use of bright sources of X-rays produced by synchrotron sources such as those produce at the Advance Photon Source at Argonne National Laboratory. The light source can reveal higher resolution crystallographic mapping, more sensitive chemical analysis, and higher fidelity morphological information than any methods currently available to SRNL. APS will allow the ability to simultaneously map XRD and XRF grains on a particle. These allow the measure of grain sizes, shapes, and orientations for investigation. Further analysis of the data includes interrogation of oxidation states via XANES, X-ray diffraction pattern matching, and analyzing particle morphology to XANES spectra.

APPROACH

Due to the complexity of working with plutonium samples, the administrative and procedural aspects of sending samples to APS are directly addressed and explicitly outline in the project. The largest risk is the development of procedures, processes, and agreements necessary to prepare, package, and ship radiological plutonium samples and are addressed in the first year of the project.

Specific activities included:

- Shipment of PuO_2 solids to Clemson and prepared samples on ladders to ANL in Type A containers
- Prepare samples with double containment for final ladder preparation at ANL
- GUP approval for beam line experiments
- Execution of beam line experiments

The third year will cover analysis of the ANL data for future publications.

- Verification of oxidation state of Pu in various samples
- Changes in diffraction or XANES due to contamination by other metals

RESULTS/DECISION

Figure 2 shows the elaborate process for creating samples of PuO_2 particles for analysis at the APS beamline. Approximately 1 inch by 1 inch squares of Kapton tape were cut out and placed on an SEM stub as a base. Three fiducial wires (Cu, Ni, Ti) were cut and placed in a triangle pattern. PuO_2 was sprinkled on the Kapton tape by a lint-free cotton-swab. A layer of epoxy was deposited and then a layer of Kapton film was placed on top and waited for the epoxy to harden. After hardening, another layer of

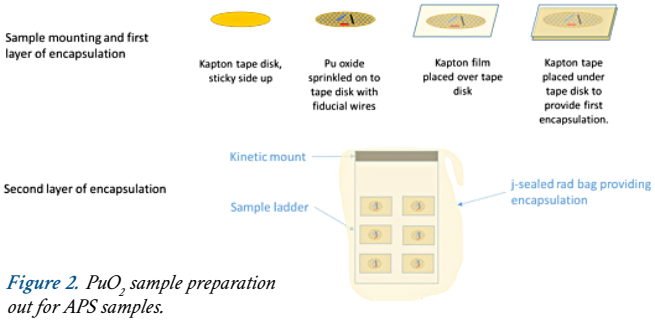

Figure 2. PuO_2 sample preparation out for APS samples.

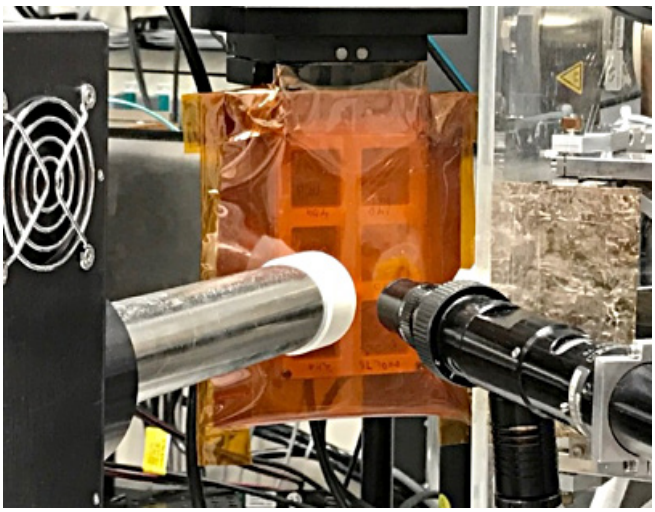

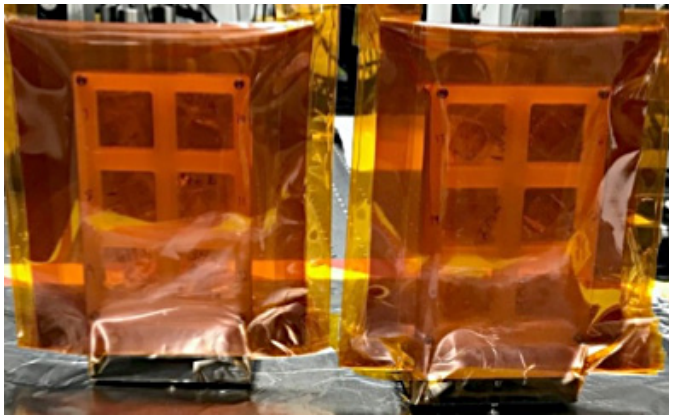

Figure 3. ***(Above)*** *Final assembly of PuO2 samples on ladder, and final encapsulation.*
Figure 4. ***(Left)*** *Sample ladder attached to kinematic mount. The black tube is from the beam line, and the silver is the fluorescence detector.*

Kapton tape was placed on the bottom in a clean hood to avoid contamination. The small coupons were shipped in separate petri dishes to ANL for final assembly. The samples were placed in the ladders connected to kinematic mounts and another layer of Kapton film as a bag was wrapped around each ladder **(Figure 3).** A ladder mounted in front of the beam is shown in **Figure 4.** The fluorescence detector is indicated by the white tip and the diffraction detector is not seen in the photo.

The kinematic mounts move on a X and Y translational stage allowing for complete control and location of mapping. Four maps are presented below in **Figure 5** that shows the XRF map for lab synthesized PuO_2, AFS 2 production material, lab synthesized PuO_2 with uranium contaminant, and lab synthesized PuO_2 with Fe contaminant. The map was used to locate the fiducial wires and the regions of particles that were subject to further analysis by X-ray diffraction and X-ray Absorption Near Edge Spectroscopy (XANES). The Pu containing particles show as blue, while the Fe containing particles show as green. Typical XRF spectrum of each sample is shown in **Figure 6** and the elements are determined by the major X-ray lines (Pu La1, U La1, Fe Ka1 and Ka2). Only two of the samples show significant quantities of Fe (AFS2 and Pu/Fe). The XRF of AFS 2 material is mostly plutonium without Fe, but the Fe indicated portions also contain Pu. The Fe contaminant in AFS 2 could be caused by several reasons, the simplest

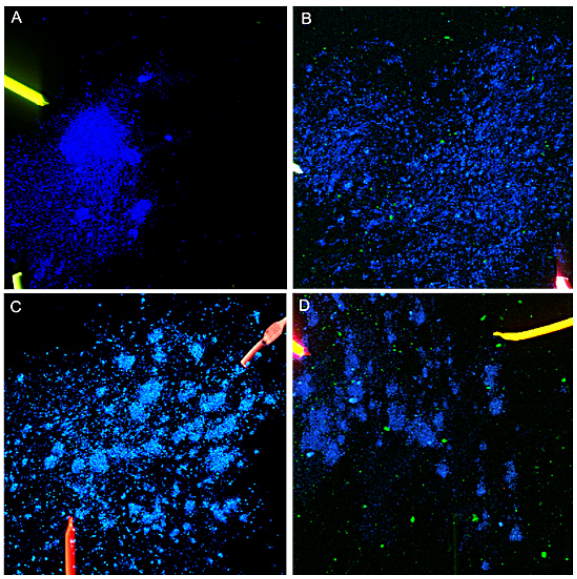

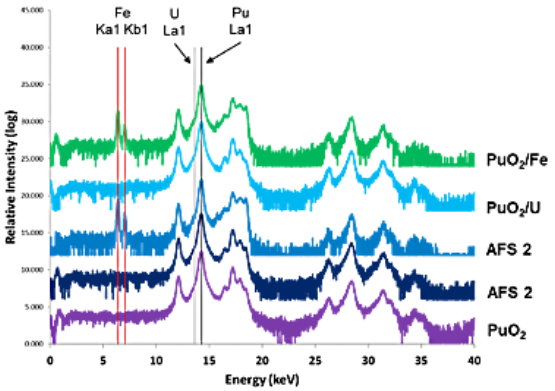

Figure 5. ***(Left)*** *XRF maps of individual samples A) Lab synthesized clean PuO_2 B) AFS 2 production PuO_2 C) Lab synthesized PuO_2 with U Contaminant D) Lab synthesized PuO_2 with Fe contaminant. Blue – plutonium particles, green – Fe containing particles.* *Figure 6.* *(Above) X-ray fluorescence of various samples from the beam line. Lines indicate elements present.*

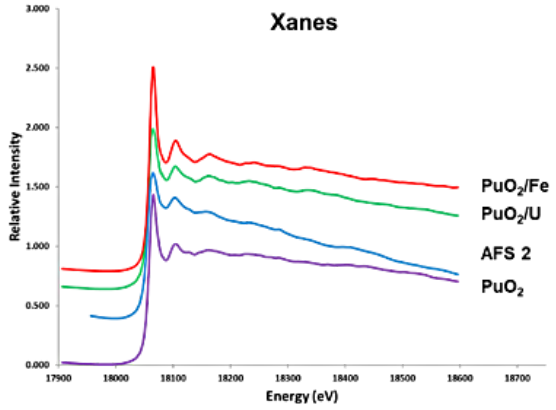

Figure 7. XANES spectra of samples from APS beam line. Further analysis is needed to fully dissect the spectra.

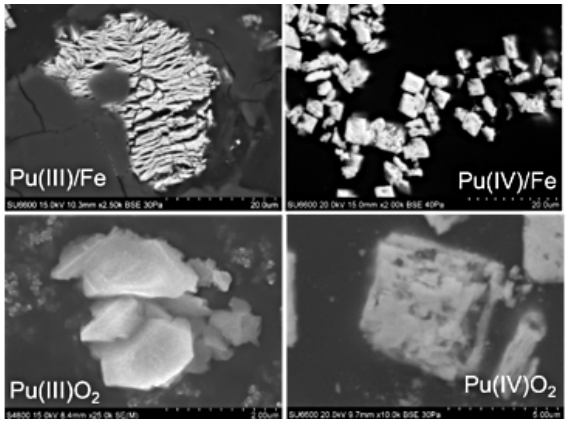

Figure 8. SEM images of PuO_2 particles after polishing revealing their internal structures.

is the stainless-steel B-vial the material is stored and transported. The most complex is from the production processes used in the plant that produced the material.

The typical XANES spectrum for each sample is shown in **Figure 7.** The XANES has not been fully scrutinized but the first two peaks are typical for an actinide oxide as would be expected for PuO_2. There appear to be slight differences in the location of the troughs between the first two peaks which could lead to other information about the particles and their makeup. Further analysis may show that there are different oxidation states for the samples as Pu(IV) and Pu(V) are very close in energy.

Clemson University was able to prepare dilute plutonium oxide particulates on SEM stubs and successfully polish them revealing their internal microstructures **(Figure 8).** Unfortunately, it appears that the grain size is too small to detect Kikuchi bands associated with EBSD. Clemson was also able to take samples to the Tender Energy X-ray Absorption Spectroscopy (TES) beamline at Brookhaven National Laboratory and perform XANES on the M5 edge of Pu. Unfortunately, all samples exhibited similar absorption peaks at the 3755 eV edge. Comparison with a Pu(VI) standard indicates that the SRNL samples have a different oxidation state **(Figure 9)** as would be expected when precipitating from Pu(III) and Pu(IV). Further analysis is needed to determine the exact oxidation state of SRNL samples.

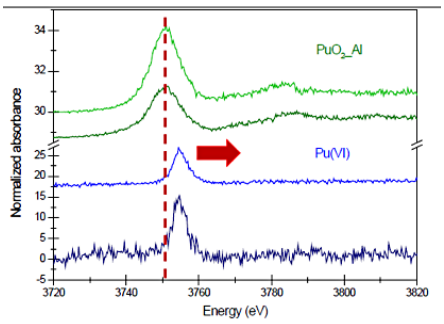

Figure 9. XANES M_5 edge of PuO_2 with standard Pu(VI) material to show differences in oxidation state

FUTURE DIRECTIONS

The future direction of his project is solely focused on analysis of the gigabytes of data accumulated at the Advanced Photon Source. Data analysis will include interpretation and matching of X-ray diffraction patterns, oxidation state analysis of XANES spectrum, and interactions of other elements such as Fe on XANES spectra. Efforts will also be made to match XANES, XRD, and XRF to morphology of PuO_2 particulates.

A technical document of steps that need to be completed to achieve success and provide a road map for other scientists to perform experiments at the Advanced Photon Source with less pushback of safety concerns.

ACRONYMS

ANL	Argonne National Laboratory
APS	Advanced Photon Source
GUP	General User Proposal
XANES	X-ray Absorption Near Edge Spectroscopy
XR	X-ray Diffraction
XRF	X-ray Fluorescence

DEVELOPMENT OF DIRECT INJECTION/ IONIZATION MASS SPECTROMETRY METHODS FOR WHOLE MOLECULE CHARACTERIZATION

PROJECT TEAM: M. Wellons (Primary), J. Mannion, C. Shick, J. Hewitt, K. Lawrence, A. Swindle, S. Koby, W. Kuhne

COLLABORATORS: C. Cody (JEOL USA Inc.)

THRUST AREA:
National Security

PROJECT START DATE:
October 1, 2017

PROJECT END DATE:
September 30, 2019

Paper spray ionization mass spectrometry (PSI-MS) was utilized for rapid chemical and isotopic characterization of trace uranium samples. Soft ionization facilitates the detection of whole molecule uranyl complexes including uranyl acetate, uranyl nitrate, and uranyl-tributylphosphate complex. Cotton swipe samples doped with a multi-element standard containing µg levels of U, Bi, Pb, Cd, Fe, and Zn were directly analyzed without purification or concentration. All elements doped on the cotton substrate were detected and demonstrated strong signal to noise from collection periods of approximately 1 min. Uranium quantitation is demonstrated through the use of internal standards to obtain linear calibration curves. Limits of detection were determined to be approximately 100 ng for UO_2 and uranyl acetate through measurement of ppb level solutions. The development and qualification of PSI-MS techniques could lead to significant safeguards-related cost reduction and timeliness by facilitating the triage and queueing of swipe samples for more sensitive and time-consuming analyses.

FY 2018

Objectives

- Perform scoping trials at vendor facility to develop a proof-of-concept data set
- Procure and install the instrument at SRNL
- Disseminate SRNL developments in the form of manuscripts and seminar presentations

Accomplishments

Primarily focused on method development for the JEOL AccuTOF mass spectrometer and the logistics associated with the instrument procurement, delivery, and installation.

- Visited the JEOL USA demonstration facility in Peabody MA—JEOLexperts ran numerous experiments at SRNL direction. In addition to general instrument operation the team demonstrated several key capabilities including:
  - Direct analysis (i.e. no sample preparation) of uranyl containing swipes.
  - Quantification of uranyl via an internal standard demonstrated.
  - Direct analysis of inorganic multi-element containing swipes.
  - Successful analysis of intact organo-uranyl complexes.

Team members being trained on the JEOL AccuTOF at SRNL after successful vendor installation; the JEOL AccuTOF can be seen in the back left of the image.

- The generated data has been utilized to develop a data analysis pipeline written in R language and has also been incorporated into a draft manuscript to be submitted to Envi. Sci. & Tech. Lett.
- Successfully coordinated a JEOL/SRNL nondisclosure agreement to enable better technical communication and data sharing between the two organizations. An instrument purchase order was placed in early February and was delivered May 15th, 2018; installation was completed in early September 2018.

INTRODUCTION

Determining uranium isotopic and concentration information from environmental samples typically involves extensive chemical and physical processing prior to analysis. Harsh sample preparation results in the loss of the original uranium chemical speciation (i.e. what the uranium was bonded to/with when found in the environment) as well as the mixing of anthropogenic uranium with background material contained within the collection media (e.g. a swipe or soil). The objective of this work is to adapt a bioanalytical mass spectrometry technology called paper spray ionization mass spectrometry (PSI-MS) for the rapid analysis of intact uranium complexes. PSI-MS is a recently developed atmospheric pressure mass spectrometry technique which allows for rapid (<5 min) sample analysis with no sample preparation **(Figure 1).** PSI-MS has been utilized for the direct analysis of blood, **[2-4]** urine, **[5, 6]** and environmentally collected chemical warfare agent simulants. **[7]** Paper spray ionization sources consist of a small triangle of paper (or other fibrous material such as cotton swipes) containing chemicals of interest to which a drop of solvent is added. High voltage is applied to this wedge which induces transport and "electrospray-like" ionization of chemicals present on the fibrous material **(Figure 1).** In the case of swipe samples, particulate on the swipe is extracted or solvated by the solvent, ionized via electrospray ionization mechanisms, and guided into the mass spectrometer by electric fields, resulting in a mass spectrum representative of species present on the swipe. Despite the promising nature of PSI-MS, no studies have previously been reported regarding U analysis by PSI-MS.

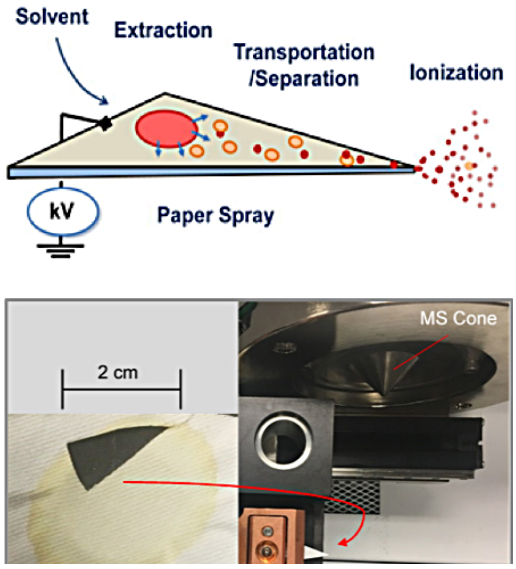

Figure 1. (Top) Diagram of paper Spray analysis from Ren et al.[1] (Bottom) cotton Texwipe with uranyl doping that has been sectioned and loaded into a paper spray ionization source by SRNL.

APPROACH

The overall project goal is to develop SRNL technical expertise in the arena of PSI-MS for uranium detection and characterization. This will be accomplished via a logical series of tasks which begin with training, reproduction of vendor scoping measurements, method development for various uranium species detection, and preliminary exploration of advanced PSI-MS techniques. These efforts are planned for FY18/19 with technical efforts beginning in FY18, post instrument installation, and continuing in-depth within the subsequent FY19. Work products from the effort will include peer-review publications on uranium analytical developments and exploration of advanced customer-relevant analytical concepts.

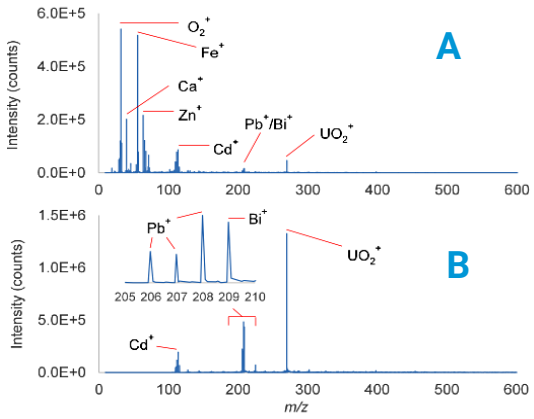

*Figure 2. Positive ion mass spectra of a directly analyzed cotton Texwipe with mixed element doping in **a)** low mass and **b)** high mass operation modes and extracted via MeOH/H_2O. High mass mode can be used to increase sensitivity for species with mass-to-charge ratios >100 through modulation of the ion guide voltage; sensitivity for UO_2 increased by approximately one order of magnitude in high mass mode.*

RESULTS/DECISION

Proof-of-concept research was conducted under the guidance of experts at the JEOL facility in Peabody, MA. **Figure 2** shows mass spectra collected from the direct analysis of swipe samples containing U in a heavy metal matrix with no sample preparation. All species deposited on the swipe were detected (U, Bi, Pb, Cd, Fe, and Zn) with strong signal-to-noise ratios (µg levels of mass loading) when extracted via solvent (80/20 MeOH and H_2O).

The measured isotope abundances were in good agreement with natural abundances for most of the major isotopes characterized. Minor background constituents were observed from the cotton swipes and the cotton swipes were found to produce stronger and more stable ion beams than the classic filter paper substrates. No major interfering species for U analysis was detected, and UO_2^+ was observed rather than atomic U^+.

U quantitation via the use of an internal standard was investigated. The ratio of the measured $^{238}U^{16}O_2$ to $^{160}Gd^{16}O$ intensity can be plotted against the deposited uranyl concentration to construct a calibration curve (Figure 3). The linear relationship between the $^{238}U^{16}O_2$ / $^{160}Gd^{16}O$ intensity ratio and the deposited uranyl concentration demonstrates that uranyl quantitation with PSI-MS is possible using an internal standard. Nanogram-level limits of detection were determined for uranyl through evaluation of serial dilutions of ppm (~7 µL deposition volumes) level solutions. In practice, internal standard would be contained in the solvent and metered solvent flow would be used to determine the mass quantities of internal applied to the swipe sample. 235/238 U isotope ratio measurements were also investigated **(Figure 3).** Initial results from scoping work indicates that low isotope ratio errors (<1% error) can be achieved with PSI-MS through adequate count rates (similarly to other mass spectrometry based analytical methods). Additionally, swipe limit of blank (LOB) for U is suspected to be lower for PSI-MS than other analytical methods as the swipe material is not digested for analysis by PSI-MS, preventing U within the natural fibers from contributing to the background and distorting measured isotope ratio values.

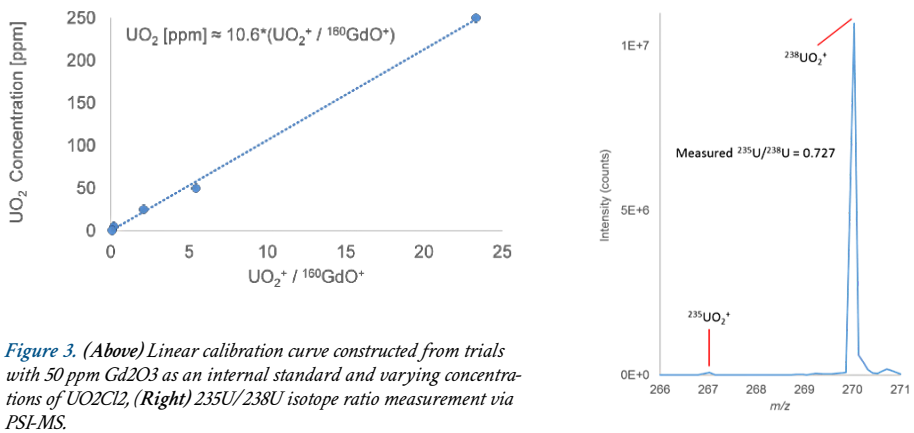

Figure 3. ***(Above)*** *Linear calibration curve constructed from trials with 50 ppm Gd2O3 as an internal standard and varying concentrations of UO2Cl2,* ***(Right)*** *235U/238U isotope ratio measurement via PSI-MS.*

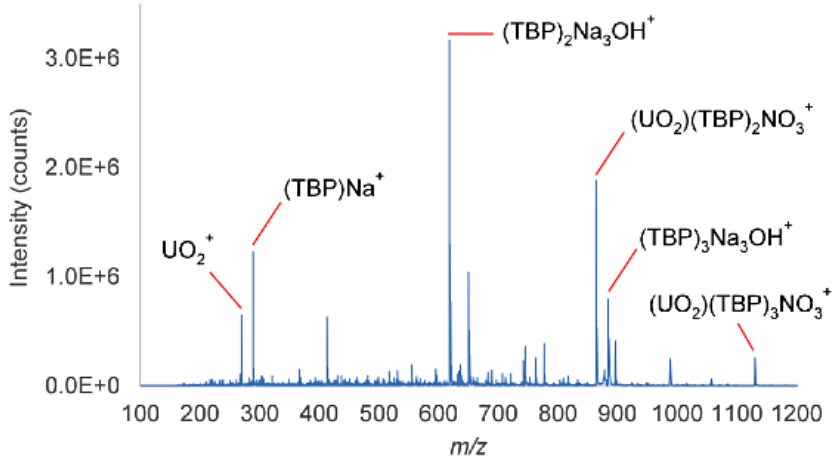

Figure 4. Positive ion mass spectrum of 0.2 µM uranyl nitrate and 0.5 µM TBP deposited on (7 µL) on cellulosic filter paper. Complete identification of the observed species was tabulated separately.

Uranyl tributylphosphate (TBP) complexes were prepared with a mixture of ligand and uranyl nitrate, briefly stirred, and then small volumes were directly injected on the paper substrate. The 1:2 and 1:3 uranyl-TBP complexes were detected in positive ion mode alongside TBP-Na adducts and the uranyl cation **(Figure 4).** These finding are similar to those reported by PNNL for ESI-MS characterization of aqueous uranyl-TBP mixtures, however, several differences were observed which warrant further investigation. **[8]** Soft-ionization, resulting from electrospray-like mechanisms, allows for the ionization of uranyl complexes while preventing ion fragmentation. In addition to uranyl-TBP complexes, uranyl acetate was also successfully analyzed via PSI-MS.

FUTURE DIRECTIONS

- Rigorous determination of limits of detection (LOD) and limits of quantitation (LOQ) from direct analysis of reference materials.
- Rigorous characterization of isotope ratio measurement accuracy.
- Analysis of biota (e.g. leaves) contaminated with U and other species of interest from SRS.
- Development of method protocols for various uranyl complexes of national security interest.
- Proof-of-concept experiments for nanoparticle characterization for industrial hygiene related applications.
- Engineering stabilization modifications for the analyte injection apparatus.
- Proof-of-concept experiments for other organic species relevant to national security interest.

PRESENTATIONS/PUBLICATIONS

1. *Paper spray mass spectrometry applications for uranium ion and molecular detection.* Expected: Communication in Envi. Sci. & Tech. Lett. in fall 2018.
2. *Paper spray ionization mass spectrometry for rapid chemical and isotopic characterization of trace uranium samples.* Upcoming presentation at SERMACS.

REFERENCES

1. Y. Ren, H. Wang, J. Liu, Z. Zhang, M.N. McLuckey, Z. Ouyang, Analysis of Biological Samples Using Paper Spray Mass Spectrometry: An Investigation of Impacts by the Substrates, Solvents and Elution Methods, Chromatographia 76(19) (2013) 1339-1346.
2. R.D. Espy, S.F. Teunissen, N.E. Manicke, Y. Ren, Z. Ouyang, A. van Asten, R.G. Cooks, Paper Spray and Extraction Spray Mass Spectrometry for the Direct and Simultaneous Quantification of Eight Drugs of Abuse in Whole Blood, Anal. Chem. 86(15) (2014) 7712-7718.
3. R.-Z. Shi, E.T.M. El Gierari, N.E. Manicke, J.D. Faix, Rapid measurement of tacrolimus in whole blood by paper spray-tandem mass spectrometry (PS-MS/MS), Clinica Chimica Acta 441 (2015) 99-104.
4. R. Jett, C. Skaggs, N.E. Manicke, Drug screening method development for paper spray coupled to a triple quadrupole mass spectrometer, Anal. Methods 9(34) (2017) 5037-5043.
5. J.A. Michely, M.R. Meyer, H.H. Maurer, Paper Spray Ionization Coupled to High Resolution Tandem Mass Spectrometry for Comprehensive Urine Drug Testing in Comparison to Liquid Chromatography-Coupled Techniques after Urine Precipitation or Dried Urine Spot Workup, Anal. Chem. 89(21) (2017) 11779-11786.
6. E.S. Jeong, K.H. Kim, E. Cha, O.-S. Kwon, S. Cha, J. Lee, Direct and rapid quantitation of ephedrines in human urine by paper spray ionization/high resolution mass spectrometry, Journal of Chromatography B 1028 (2016) 237-241.
7. E.S. Dhummakupt, P.M. Mach, D. Carmany, P.S. Demond, T.S. Moran, T. Connell, H.S. Wylie, N.E. Manicke, J.M. Nilles, T. Glaros, Direct Analysis of Aerosolized Chemical Warfare Simulants Captured on a Modified Glass-Based Substrate by "Paper-Spray" Ionization, Anal. Chem. 89(20) (2017) 10866-10872.
8. L.W. McDonald, J.A. Campbell, T. Vercouter, S.B. Clark, Characterization of Actinides Complexed to Nuclear Fuel Constituents Using ESI-MS, Anal. Chem. 88(5) (2016) 2614-2621.

ACRONYMS

PSI-MS Paper Spray Ionization Mass Spectrometry
TBP Tributylphosphate

TOTAL NUMBER OF POST-DOCTORAL RESEARCHERS

1. Joseph Mannion

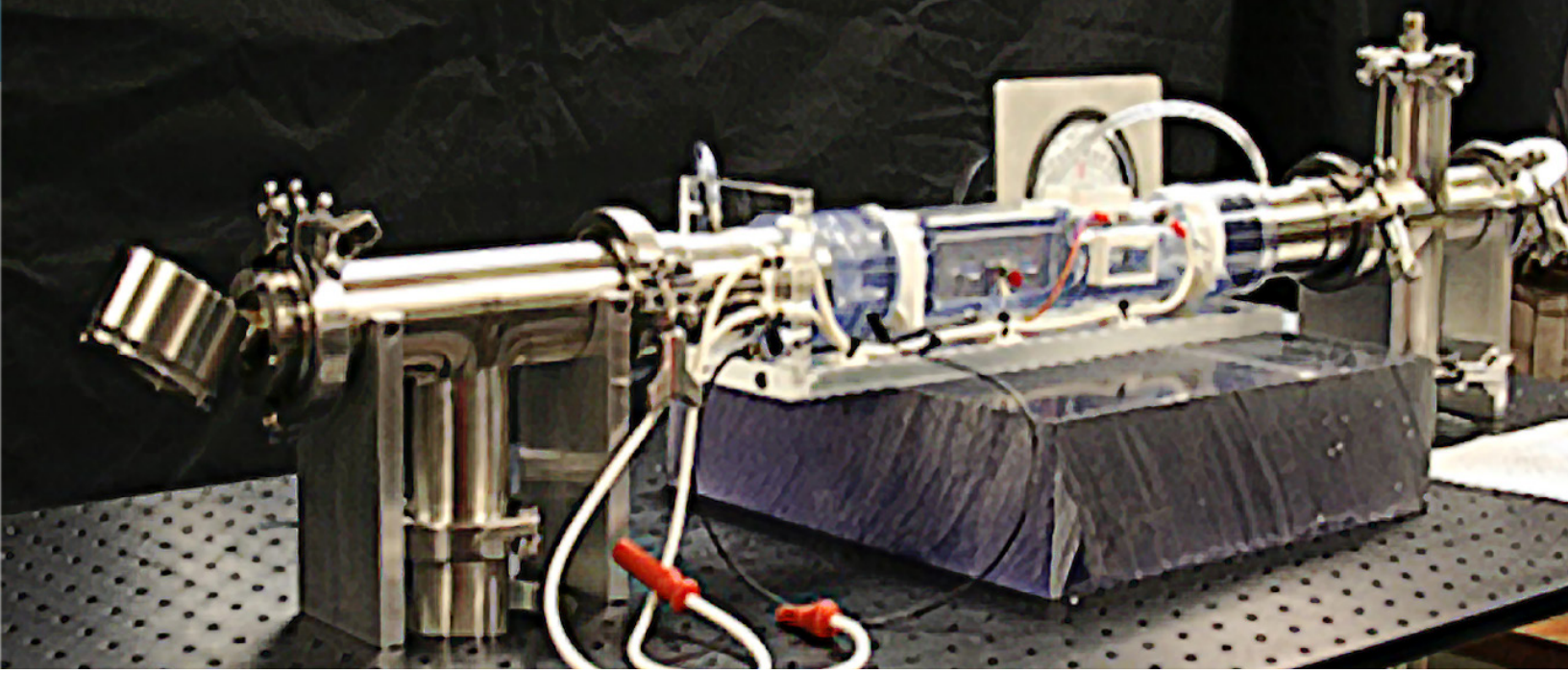

Racetrack experimental breadboard for collection studies.

SMART PARTICLE COLLECTOR WITH REAL TIME SPECTROSCOPIC ANALYSIS

PROJECT TEAM:
E. Villa-Aleman, J.J. DeGange, R.K. Huffman, A.L. Houk

THRUST AREA:
National Security

PROJECT START DATE:
October 1, 2017

PROJECT END DATE:
September 30, 2018

Facilities manufacturing materials for nuclear weapons programs release particulate matter to the environment. Particle collections from suspected facilities can help assess proliferation programs. SRNL designs and manufactures unique particle collectors for a variety of applications. The goal of this project is to develop new technologies to develop and manufacture smart particle collectors. Significant engineering advances to the collector were made using the Racetrack, an experimental breadboard setup based on the ACE 1.0 collector. Preliminary experimental results suggest significant improvement in the particle collection efficiency. This project also developed new tools for spectroscopic validation of a sample and unique smart features for the collection system.

FY 2018

Objectives

Original project consisted of 6 objectives (M1 – M6) spread over a two-year period (FY18 and FY19). Some objectives in the FY18 and FY19 were exchanged due to delays in the construction of the Racetrack (M1).

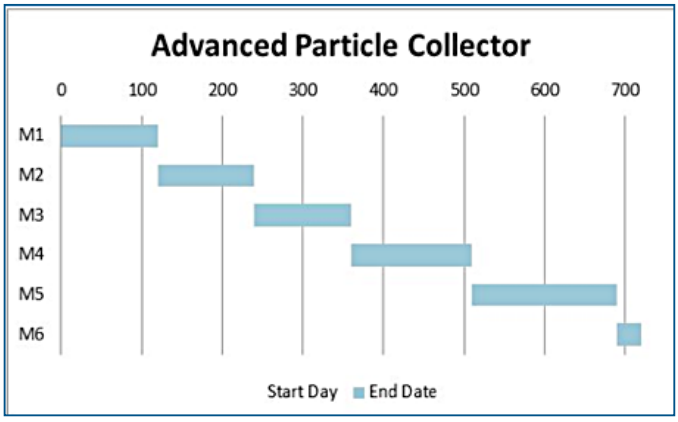

	Milestones, Deliverables, or Go/No-Go Decision	Progress Notes	% Complete
FY18	M1 – Design and construction of Racetrack for gas and particle characterization.		100%
FY18	M2 – Measure emission corona for various gaseous effluents and particulates	• Delays in the M1 milestone led to research	65%
FY18	M3 – Characterize particulates under laser illumination.		20%
FY19	M4 –Build an experimental breadboard with photosensors for particulate collection.		60%
FY19	M5 – Improve and modify existing collectors with smart attributes.	Preliminary results suggest that the new ESP-EV1 collector can perform significantly better (~ one order of magnitude) to current technologies.	60%
FY19	M6 – Write report on work conducted in this project.		100%

Objectives

- **FY18 Objectives Completed:** Construction of the Racetrack (M1) and testing gas and particle emissions in a plasma (M2).
- **FY19 Objectives Completed:** Designed and constructed a new collector; completed smart current monitoring, data loggers and collector triggering mechanisms using light, sound, and motion (M4 and M5 were partly completed).
- **FY19 Objectives Completed:** Designed and constructed a new collector; completed smart current monitoring, data loggers and collector triggering mechanisms using light, sound, and motion (M4 and M5 were partly completed).

Accomplishments

- **Racetrack Design:** Experimental breadboard for particle collection and analysis testing was designed and built. A clear-through, 3D printed particle collector tube was designed, built and tested specifically for the Racetrack with special electrical properties.
- **Corona Wire Current/Voltage Monitoring:** A circuitry board design was completed to measure current and voltage of corona discharge directly from the power supply. This information was useful to identify operational parameters of the collector.
- **Collector Event Triggering:** Sound, motion or light burst triggers were procured and integrated in the circuitry of the particle collector to detect unusual events. Tests were conducted and modifications to the system will be required prior to deployment.
- **Plasma Generation:** A new design for the collector tube with electrodes for plasma generation to produce emission from different gases and particles was completed. Preliminary studies indicate a positive outcome in the identification of particle material composition using optical spectroscopy.
- **Advanced Collection System:** First prototype design of collector "ESP-EV1" incorporating smart advanced concepts operating at one order of magnitude better collection than previous systems.

INTRODUCTION

The nonproliferation technology section at SRNL develops particle collectors for use in the characterization of facilities dedicated to the production of nuclear material. The particle collectors are based on electrostatic precipitation technology. Although the particle collectors have been shown to work through the years, our preliminary analysis suggest that there is significant room for improvement. In addition to the particle collector performance, very little information is available on the operational conditions, the type of particulate collected, etc.

In order to characterize the performance of the particle collectors, a benchtop electrostatic precipitator system (ESP-EV1) similar to the ACE 1.0 was designed and built to test different parameters affecting the collection. The preliminary data measured in the first year indicates that the performance of the collector can be improved by at least one order to magnitude.

APPROACH

The original project was funded as a two-year project. The work concentrated on a parallel approach of tests where systems were designed and built to test plasma generation and optical characterization and other systems to test particle collection efficiency, particle separation and performance drives, such as air flow, current, voltage, etc. The development of the Racetrack breadboard system, based on the ACE 1.0 particle collector with pulsed particle injection, provided a testing platform for optical laser characterization and imaging capabilities.

Engineering delays in the construction and delivery of the Racetrack, resulted in the shuffling of tasks from the 2nd year to the 1st year and vice-versa. The premature first year technical assessment of the project resulted in the cancellation of the 2nd year of the project and affected the final deliveries. Even then, significant advances were made in the 1st year to understand the variables affecting the performance of the particle collectors. The 1st year experimental approach resulted in the design and construction of a two-stage particle collector (ESP-EV1) with significant enhancement in the collection efficiency and particle size separation.

RESULTS/DECISION

The development of the Racetrack using additive manufacturing and new materials enabled us to visualize the injection of particulates into the system. The Racetrack helped us develop new methods to measure ionization current and its effect on the particle collection. Preliminary results suggest at least an order of magnitude improvement in particle collection after modifications have been made. At the end of the year, two variants of the new ESP-EV1 collector were built incorporating most advanced features for future deployment next to the current particle collector.

New optical concepts were also developed and tested in the 1st year program. Preliminary plasma generation with optical characterization provided successful results. Although further testing will be needed to incorporate the advanced features in the collectors, this approach will help provide timely information during a collection by providing information on the material collected. Similarly, new circuitry was designed to incorporate activation of the collectors based on light, sound and motion.

FUTURE DIRECTIONS

- Complete collection efficiency studies for particulates of different sizes.
- Design a particle sorting collector to separate particulates based on the mass/charge ratio across the collection substrate.
- Incorporate a miniaturized picoammeter in the particle collector to study relationship between particles collected and charge measured.
- Incorporate smart features, such as data loggers and optical analysis of particle elemental composition during a collection.
- Continue optical signatures development for system characterization.
- Write patents on new concepts.

ACRONYMS

ACE	Airborne Contaminant Extractor
ESP	Electrostatic Precipitator

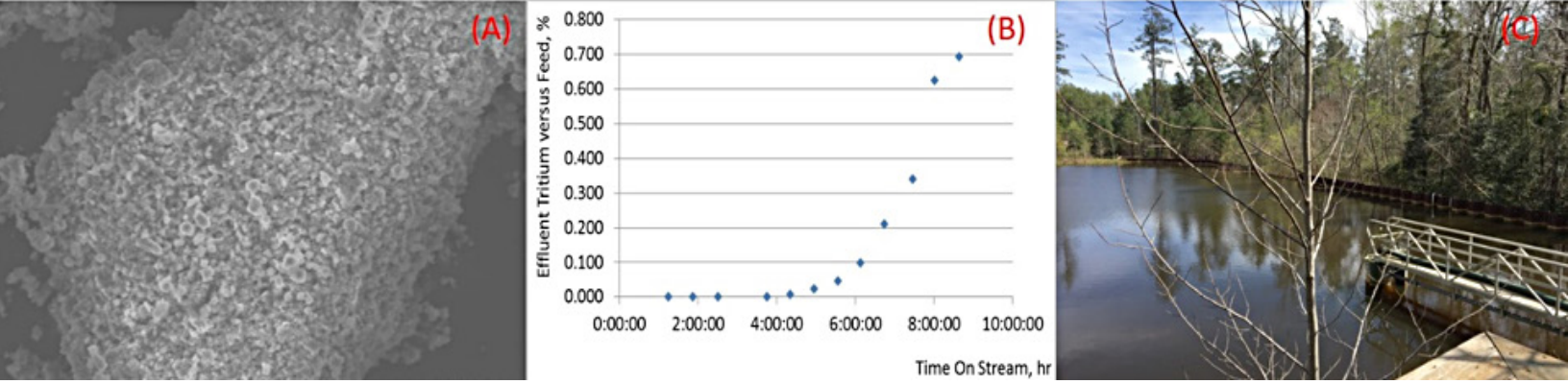

(A) SEM image of the catalytic exchange zeolite used as column packing; (B) delayed tritiated water breakthrough on a chromatographic column – Defense Programs Technology (DPT) previous data results; (C) MWMF Pond at SRS (water samples collection and initial field testing location)

ATMOSPHERIC TRITIUM SIGNATURE COLLECTION AND CONCENTRATION BY CATALYTIC EXCHANGE COLUMN

PROJECT TEAM:
Omar Rivera, Lucas Angelette, Ashlee Swindle, Douglas Hunter, Steve Xiao, Robert Rabun

THRUST AREA:
National Security

PROJECT START DATE:
October 1, 2017

PROJECT END DATE:
September 30, 2018

The primary goal of this project was to develop a methodology to collect and isotopically enrich tritiated water from bulk water in air. We pursued a reversible and continuous methodology based on fixed bed chromatographic columns and development of the parameters to achieve reduction in bulk volume of water stripped from air by selective enrichment of HTO over bulk H_2O. Defense Programs Technology teamed with Nonproliferation Technologies to combine capabilities and expertise developed for tritium processes and extend these processes to trace level collections and analyses. We demonstrated the elution profile of tritiated water from an optimized column in-order to down select the appropriate material and operating conditions. We evaluated collection and concentration of tritium from air which includes quantitative analyses methodology and assessment of enrichment capabilities. These parameters enabled us to go forward and test the column setup with the catalytic material for three initial in-field collections of HTO fragments at the Mixed Waste Management Facility (MWMF) located at SRS.

FY 2018

Objectives

- Demonstrate elution profile.
- Demonstrate tritium analysis.
- Demonstrate collectionof tritium from air.
- Verify column reuse cycles.
- Field testing of the column's ability to capture environmental tritium.

Accomplishments

- E-HAP Completion
- "Proof of Concept" Experiments
  - Air sampling H-D experiments, demonstrated we could obtain enriched deuterium.
  - Conducted HTO Experiments: Exposed column to head space of pond water with varying activities of tritium and over different durations of time (initial investigation of time effects).
  - Demonstrated the ability to successfully collect tritium in the air and elution from the "regenerated" column.
- Established/demonstrated routine analytical analysis capability for ultra-low-level tritium analysis.
- Demonstrated benchtop capability in environments of varying humidity: standard used for readiness of field testing.
- Collected preliminary temperature and humidity parameters for further optimization studies.
- Conducted field testing studies at the MWMF pond to monitor the column's capability to capture environmental tritium.

INTRODUCTION

Historically, there has been very little (if any) cross-sectional collaboration of capabilities between Defense Programs Technology (DPT) and Nonproliferation Technologies (NTS). Both Directorates are world experts in tritium handling and measurements. NTS collects and analyzes trace levels of tritium (T) under environmental conditions, while DPT works with highly purified tritium with process perspectives. This project aims to look at common problems between the two sections in the hopes that a better scientific understanding of tritium exchange dynamics will yield powerful insights for both groups.

The NTS significance: Environmental tritium levels in water is less than 0.027 pCi/g. The detection limit for tritium is at best 0.011 pCi/g by liquid scintillation counting, therefore quantification is difficult without enrichment. Alkaline electrolysis enrichment currently in use requires an aqueous electrolyte, generates explosive oxy-hydrogen gas and the electric current is limited by bubbles. New methodologies need to be developed to collect and enrich tritium reversibly and continuously without consumables or hazardous chemicals. This would permit improved field sampling enrichment and measurement capabilities greater than currently achievable. We believe that the DPT material work for depleting contaminant tritium from air streams will provide a pathway to tritium enrichment and subsequent volume reduction meeting NTS needs for improved environment sampling of tritium.

APPROACH

The primary technical objective was to evaluate the possibility, from a materials approach, of isotopically enriching HTO from bulk H_2O. An implicit requirement for this enrichment is that it must work at trace levels, because most methods for gas enrichment are limited to no less than 1–10% of analyte of interest whereas trace detection levels are 10–14%. Performance of tests previously conducted by DPT at SRNL impressively demonstrated chromatographic column functionality using a zeolite material for depleting tritium from an air stream. Initial modeling studies looking at impacts from water content, flow rate, and desorption mechanisms optimized for HTO/H_2O separation(s) from the perspective of enrichment verses depletion were performed to better understand the current process and extend the understanding from depletion to enrichment.

Recent research by Taguchi et al.[3] suggests the potential of mesoporous materials for T enrichment as well as a guide for the design of novel adsorbents, for example, the critical pore size or functionalizing of mesopores, for T enrichment. We intend to use the same technical approach with our advanced column material to investigate the possibility that saturated bulk water content in these materials could be lowered and therefore isolate the higher energy silanol sites for tritium retention.

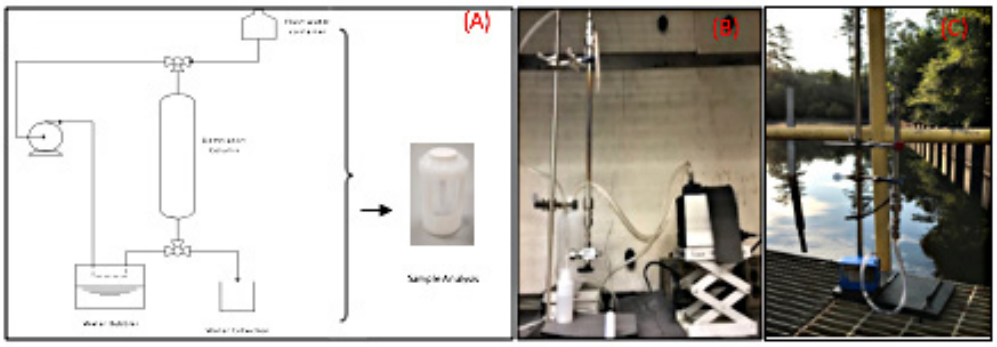

Figure 1. (A) Deuterium-spiked water bubbler system used for the capture and recovery of deuterium using catalytic column material. (B) Laboratory setup for HTO collection. (C) Deployable in-field system setup.

Figure 1 outlines our overall research plan, where we intend to perform the following objectives:

- Demonstration of optimized elution profiles of tritiated water from the zeolite column.
- Demonstrate collection of tritium from air.
- Investigated the effects of humidity and/or temperature.
- Demonstrated trace tritium analysis with low-level liquid scintillation counting (LSC).
- Verify column reuse cycles.
- Development of isotopic enriched separations of tritiated water (HTO) from air.
- Initial field work study to demonstrate the catalytic exchange zeolite's capabilities to capture tritium.

RESULTS/DECISION

H/D proof of concept experiments. Initial laboratory tests were conducted utilizing deuterium-spiked feed into a water bubbler system shown in **Figure 1 on previous page;** approximately 2.7% D/H. HTO fractions collected from sample air circulated through the bubbler, column, and pump were measured and analyzed for several different time intervals of exposure. Sample aliquots, 0.5 mL, were analyzed by a tunable-laser cavity ring-down spectroscopy instrument. Results are shown in **Figure 2 (A)** and **(B),** which demonstrate successful capture and removal of deuterium from the column with elution with water. A second set of experiments testing low-level deuterium using room air by exploiting the natural atmospheric moisture ~ 151 ppm D/H. Air was circulated throughout the column and pump system and vented back to the room. After a designated duration of time, water was added to the column and the eluted fractions were collected and measured. Initial experiments indicated lower levels of deuterium than the feed, which was suspected to be caused by flow rate from the syringe during the column flushings to be too high. Additional tests were performed with a gravity fed reservoir for fraction columns. Gravity feed proved the ability to enrich deuterium approximately 10% above the original feed level(s).

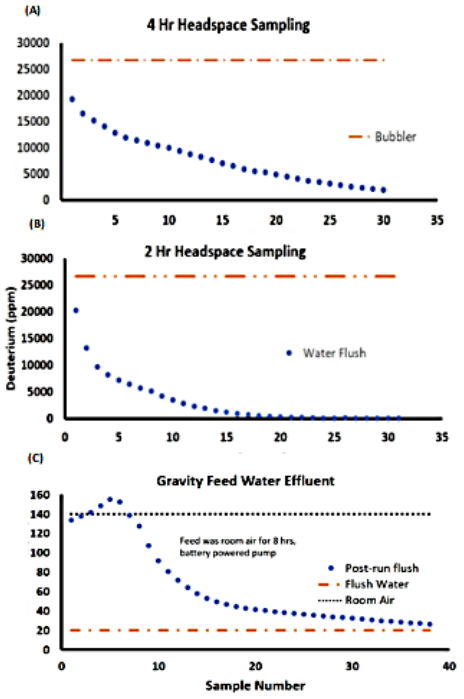

Figure 2. Catalytic exchange column for (A) and (B) deuterium removal and (C) deuterium enrichment.

Lab scale HTO signature collections. Similarities of deuterium and tritium directed the continued modeling for tritium using the catalytic zeolite column material in order to better understand the functionality for enriching tritium from an air stream. Experimental modeling considered impacts such as water content, flow rate, and optimized desorption mechanisms for HTO/H_2O separation. A zeolite packed column with a high affinity for T was prepared and setup in the laboratory as indicated in **Figure 1 (B)** and **Figure 3 (A).** Feed solutions were collected from the Mixed Waste Management Facility (MWMF) at SRS with an initial measured activity concentration of approximately 1,940 pCi/g; the activity concentration of a second collection of pond water collected for further T experiments was approximately 1,200 pCi/g. The zeolite sieve was dried for a minimum of 17 hours with a supply of dry air before and after experiments were conducted. The column was exposed to a headspace of the tritiated pond water, and head space gases were pushed through the column at a flow rate of 1.8 liters per minute for a designated time durations to include a range of 4 hours up to 24 hours. Small aliquots of HTO were collected from the column after introducing deionized water to the column and measured using ultra low-level liquid scintillation counting (LSC), Quantulus 1220. **Figure 3 (B)** depicts the initial results for ambient temperature breakthrough profiles for tritium, where the feed "stock" solutions were measured before and after each experiment. As proof of concept, similar retention and desorption capabilities were observed using the zeolite column; however, enrichment was not observed. This could be partly due column elutions being performed with pressure rather than gravimetrically. The longer collection time also proved to represent the most optimal collection time studied; however, high levels of moisture would build up causing cluster formations

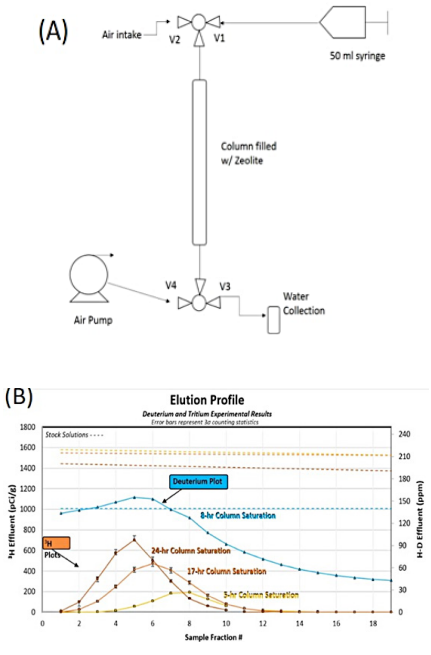

*Figure 3. (A) Catalytic column exchange bench-top setup; **(B)** HTO collections captured at variable room temperatures saturating the column with MWMF water vapor.*

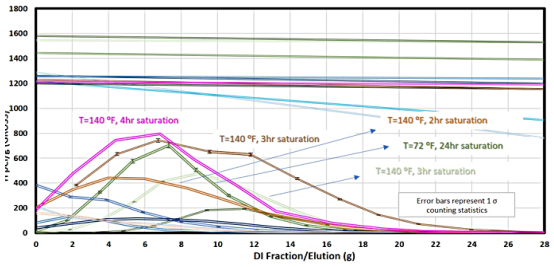

Figure 4. Breakthrough profiles for aliquots of HTO eluted from zeolite column captured in the laboratory for higher temperatures to simulate field conditions. Initial field tests are also demonstrated in the plot.

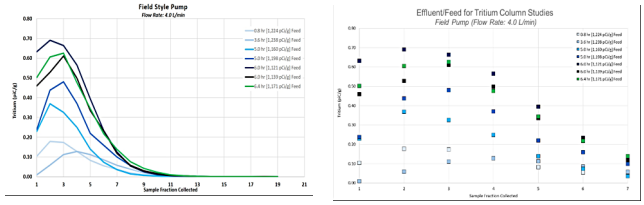

Figure 5. Effluent verses feed ratio profiles for repeated column studies with fixed 1.8 L/min flow rate.

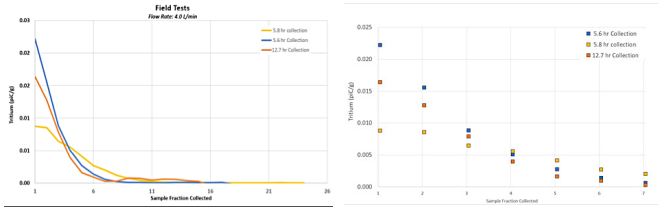

Figure 6. Effluent verses feed ratio profiles for repeated column studies with fixed 2 L/min flow rate for collections in the field.

with the zeolite material and creating a "popcorn effect" during longer column exposures, in addition to a strong back pressure within the column.

As expected, results indicated tritium adsorption in the sieve causes replacement of structural OH groups by OT groups found in HTO in the vapor phase, further evolving the understanding for behavior of tritium within the column. After successfully demonstrating collection and detection of low-level tritium in the laboratory, additional studies were performed at elevated temperatures to simulate field conditions. **Figure 4** shows the results from the high temperature studies in addition to preliminary in-field tests using a battery powered pump and returning the column to the laboratory for elution of collected tritium.

Ratios were calculated for activities of tritium measured in the effluent aliquots collected verses the average feed stock solution and demonstrated in **Figures 5 and 6.**

FUTURE DIRECTIONS

- Optimization of current laboratory setup.
  - Refined studies to optimize time on-line (column saturation)
  - Environmental tritium collection by water distillation column.
  - Enhance ultra-low-level tritium activity in distillate collections through variable time, temperature, and humidity studies.
- Field testing studies employing a battery powered experimental column setup.
  - Impact and efficacy of environmental sample collection under different temperature, humidity and weather conditions.
- Fundamental understanding of the transport mechanism and fate of environmental tritium in determined locations.

PUBLICATIONS/PRESENTATIONS

1. Initial stage planning for submission of a peer-reviewed journal and patent.

REFERENCES

1. T. Sugiyama, Y. Asakura, T. Uda, T. Shiozaki, Y. Enokida, I. Yamamoto, Fusion Eng. Des. 81 (2006) 833.
2. A. López-Galindo, P. Fenoll Hach-Alí, A.V. Pushkarev, A.S. Lytovchenko, J.H. Baker, R.A. Pushkarova. 2008. Applied Clay Science 39 (2008) 151–159.
3. A.Taguchi, , Y. Kato, Y. Torikai, M. Matsuyama, S. Uchida. Microporous and Mesoporous Materials ,179, (2013) 217–223.
4. S. Fukada, J. Nuc. Science and Technology, 41, (2004) 619-623.
5. Y.Miho, S. Fukada, T. Motomura, J. Mizutani, S. Hirano, M. Arimoto, T. Takeuchi, Fusion Science and Technology, 71, (2017), 326-332.
6. S. Fukada, Y.Miho, K. Katayama, Fusion Eng. Des., 133, (2018), 64-69.

ACRONYMS

SRS	Savannah River Site
MWMF	Mixed Waste Management Facility
HTO	Environmental Tritium in Water
DPT	Defend Programs Technology
NTS	Non-Proliferation Technology Section
LSC	Liquid Scintillation Counting
T	Tritium
H-D	Hydrogen-Deuterium
D/H	Hydrogen-Deuterium Ratios
D	Deuterium
O	Hydroxide
OT	Oxygenated tritium
E-HAP	Electronic hazards analysis package

INTELLECTUAL PROPERTY

This report has been reviewed by SRNL Legal Counsel for intellectual property considerations and is approved to be publicly published in its current form.

THERMOMECHANICAL MODELING OF HYDRIDE MATERIALS FOR TRITIUM STORAGE BEDS

PROJECT TEAM: K. J. Heroux (Primary), R. L. Rabun, J. A. Swegle, P. F. Cloessner

COLLABORATORS: P. Baxter (James Martin Center for Nonproliferation Studies)

THRUST AREA:
National Security

PROJECT START DATE:
October 1, 2018

PROJECT END DATE:
September 30, 2019

U.S. analysts currently have a very limited understanding of hydride materials potentially used by other nuclear weapon states for the storage and delivery of tritium and deuterium. The ability to model such hydride materials and their associated storage beds would provide a unique fundamental capability to SRNL in support of multiple programs in National Security. This capability will provide a competitive advantage relative to other DOE Laboratories and a collateral benefit for the SRNL Tritium processing mission. The modeling capability is of interest to many sponsors that SRNL is currently engaged with. This capability will leverage and expand upon a key core competency of the National Security Directorate.

FY 2018

Objectives

- Conduct extensive foreign database open literature search for hydride materials used for deuterium/tritium storage, particularly those engaged by Russian scientists, whom we assume would have the most to offer in terms of technical alternatives
- Leverage network analysis techniques to identify important connections within Russia's metal hydride research and development community – individual contributors, associated institutions, and funding agencies
- Identify candidate hydride material(s) of interest and begin collecting characterization data as the basis for a phenomenological model of its storage and delivery performance

Accomplishments

- Completed extensive open-source foreign database search using SRNL-generated criteria, focused on materials found in connection with "tritide" and "deuteride" search terms.
- Utilized multi-modal network analysis technique to gain valuable insight into the scientific network involved in metal hydride research and development in Russia.
- Determined that the "tritide" network is far less complex than the "deuteride" network, with a clear divide observed between those working with platinum and those focusing on other materials.
- Identified several materials of interest, including various vanadium and titanium alloys, as well as novel hydride storage and delivery concepts for further investigation and baseline modeling efforts.

INTRODUCTION

U.S. analysts, technologists, and programmatic decision makers currently have a very limited understanding of the hydride materials used in foreign systems for the storage and delivery of deuterium and tritium. The fundamental properties of hydride storage materials affect storage vessel/bed and weapon performance, associated maintenance intervals (decay and He-3 retention), required production capacity, and required tritium delivery pressures/rates. At elevated temperatures, hydrogen reacts with many transition metals to form hydrides. The lanthanides, actinides, members of the titanium and vanadium groups, scandium, and yttrium as well as their associated alloys are the most reactive toward hydrogen absorption.[1] The absorption/desorption behavior of metal hydrides is most commonly measured by isothermal pressure-composition response curves (isotherms), in which the material undergoes a phase transition (α→β or vice versa) as hydrogen is either absorbed or desorbed. The transition is demonstrated in the isotherm by the length and slope of the plateau region, which are indicative of the capacity and homogeneity of the hydride, respectively. A schematic of a typical two-phase isotherm is given in **Figure 1.**[2]

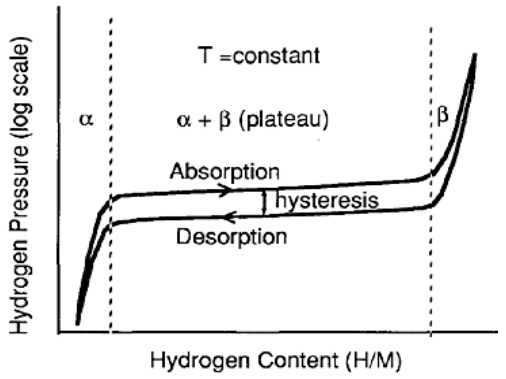

Figure 1. General absorption/desorption isotherm

The thermodynamic properties of metal hydride formation from gaseous hydrogen can determined by the collection of isotherms at various temperatures. The series of isotherms can be used to calculate the enthalpy (ΔH) and entropy (ΔS) for the absorption and desorption of the hydrogen using the equilibrium pressure and the van't Hoff equation:

$$ln\frac{P_{eq}}{P_{eq}^{0}} = \frac{\Delta H}{R} \times \frac{1}{T} - \frac{\Delta S}{R}$$

A schematic of hydrogen absorption and a general van't Hoff plot is shown in **Figure 2,** where the enthalpy (ΔH) and entropy (ΔS) of reaction are given by the slope and y-intercept of the line, respectively.

Alternate storage materials potentially used in other countries may perform better (in terms of absorption/desorption rates, storage capacity, He-3 retention, etc.) – or differently, in ways we should understand – than the current hydride materials used by the United States. Understanding hydride storage materials and their application to tritium storage and delivery is a core competency of SRNL and an area of recognized expertise for SRNL within the U.S. foreign technology analytical community (albeit, in competition with the nuclear design laboratories). Expanding our understanding of hydride materials used by other nuclear-weapon states will enhance an SRNL core competency and establish a strategic capability to assess new technology opportunities as well as the capabilities of other nations.

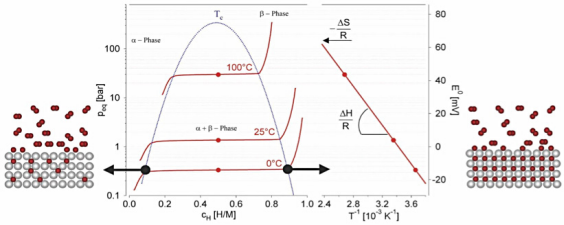

Figure 2. Schematic of hydrogen absorption and van't Hoff plot.

This project aims to develop a fundamental modeling capability suitable for the simulation and assessment of various hydride materials and their associated storage vessels and deuterium/tritium delivery methods. If successful, this work will:

- **Enhance** a core competency of SRNL by adding a unique capability to the tritium processing R&D efforts currently performed for NNSA Defense Programs
- **Optimize** the design and operation of future hydrogen storage technologies in anticipation of increased demands and the call for a robust, reliable, resilient, and responsive stockpile
- **Establish** SRNL as a valuable analytic resource for DOE and DoD decision makers and the foreign technology assessment community, which has already shown significant interest in developing such models to assess the likelihood and feasibility of alternative foreign gas (deuterium/tritium) storage and delivery systems that might provide new technical pathways for the U.S. and to determine the performance of alternative foreign systems

APPROACH

The primary objective of this work is to focus on the research of Russian scientists to identify alternative metal hydride storage materials of interest and to develop a phenomenological model to simulate the performance of these hydride materials and their associated storage system. The first step toward this goal was an extensive literature search of hydride storage materials involved in tritium research and development in Russia. After thorough review of historical data, conference proceedings, and standard open literature sources, SRNL compiled a comprehensive list of search terms, including field-specific technical terms as well as individual contributors and institutions of interest. The search criteria were then applied to foreign databases by an expert network data analyst at the James Martin Center for Nonproliferation Studies with access to and expertise in various foreign databases. Next, a multi-modal network analysis of the resulting dataset was performed to provide insight into the overall structure of Russia's tritium storage research network. In addition to revealing potential hydride materials of interest for further study, this approach also provided valuable information on the institutions, funding agencies, and individuals engaging such materials in applied tritium research in Russia.

The hydride materials of interest will then be synthesized or obtained for further characterization. Depending on the rarity of the material(s), much of their hydrogen storage and delivery properties may already be known in the literature. If not, pressure-composition-temperature (PCT) response curves will be measured using protium and deuterium on existing test manifolds at SRNL, designed specifically for generating such data. The absorption/desorption performance, thermodynamic properties, and He-3 retention capability of the materials can then be used to predict the vessel parameters (e.g., wall thickness, heat load, pressure rating, tritium desorption/generation rate) required for operation in an engineered storage system. Finally, the developed models simulating the performance of the hydride materials and their associated storage vessels can be integrated to assess the capabilities of possible foreign systems and their applications. This approach leverages SRNL expertise and capabilities in metal hydride chemistry, tritium processing and storage, and national security studies and various activities within the intelligence community.

RESULTS/DECISION

A thorough review of historical data, conference proceedings, open literature, and institutional knowledge was first performed to generate search criteria aimed at identifying potential alternatives to metal hydrides used at SRS. Field-specific terms (in both English and Russian) along with a list of individual researchers and institutions known for their work in this area were used as the basis for the initial foreign database bibliographic search. The broad scope of the initial search resulted in a dataset too large and noisy to draw any conclusions from. Thus, the search was narrowed down to focus on metals and/or materials in connection with either "tritide" or "deuteride" (and their Russian translations). This final iteration of the literature search resulted in a manageable dataset for further analysis.

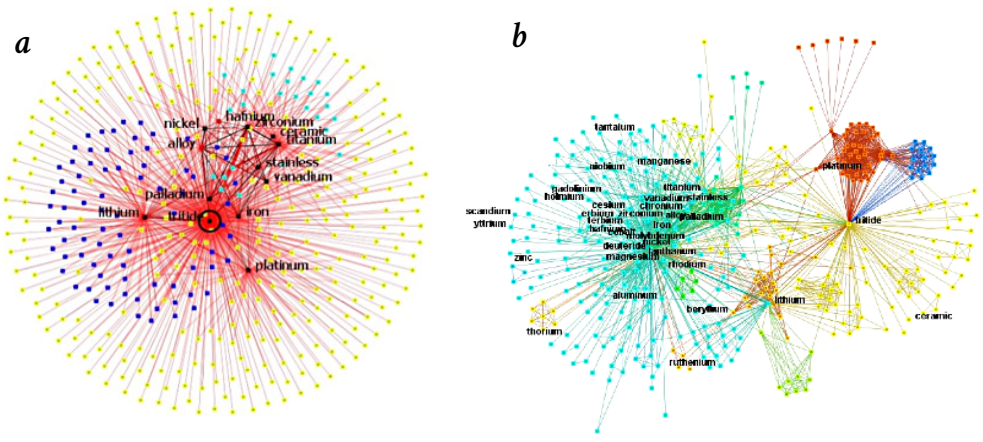

Figure 3. (a) "Tritide" 1st degree network with CONCOR grouping, which attempts to identify groups that are structurally similar. (b) Aggregate network with strong ties and Newman clustering, which attempts to identify local communities within a network.

Multi-modal network graphing techniques were then used to visualize the overall structure of the metal hydride research and development network in Russia, and highlight important connections between individual contributors, institutions, and funding agencies engaging materials of interest. Since there were no major surprises as far as the institutions, agencies, or individuals engaged in this field of research, the focus shifted toward the connection to specific metals and metal alloys being used. The large dataset revealed several materials of interest, including various vanadium (V) and titanium (Ti) alloys, for further investigation – some of which have been previously studied or are easily obtainable at SRNL. Of interest is Ti-Al6-V4, which is a powder alloy currently being used in SRNL's metal additive manufacturing (AM) machine. Pure titanium has been extensively studied at SRNL for its applications in long-term tritium storage,[3] but little is known about the tritium storage performance of its alloys. Work has begun to obtain materials of interest and collect hydrogen absorption/desorption data (if not known in the literature) to use as the basis for a phenomenological model of hydrogen storage and delivery performance.

In addition to revealing potential materials of interest, the network graphing also provided valuable insight into the "tritide" and "deuteride" research efforts in Russia. There was limited technical overlap observed between materials associated with "tritide" and "deuteride" research, which leads to other questions regarding the potential transition from fundamental to applied tritium research. The "tritide" network **(shown in Figure 3a on previous page)** was also found to include fewer material connections and be far less complex than the "deuteride" network. Moreover, a clear divide is observed in the "tritide" network between those working with platinum and those focusing on other materials, which is clearly delineated in the aggregate network shown in **Figure 3b on previous page.**

Other noteworthy items from this work include specific designs/materials for hydrogen storage vessels. For example, the details of a Russian "tritium generator" device (likely using uranium as the tritium storage medium) were found, which may provide insight into other tritium storage and delivery materials, container designs, and associated applications. Additionally, several papers on non-porous ceramic materials for induction heating were discovered, which may help support recent and ongoing R&D efforts at SRNL regarding the potential benefits and feasibility of induction heating of metal hydride vessels.

FUTURE DIRECTIONS

Material Characterization

- Obtain/fabricate/procure materials of interest (some already available at SRNL or commercially available) and collect known absorption/desorption data or measure PCT isotherms using protium and deuterium on existing hydride manifolds at SRNL.
- Develop/re-establish SRNL in-house capability to producemetal alloy and intermetallic hydride-forming material in research quantities.

Integrated Modeling

- Using the thermodynamic data, develop models to simulate the performance of hydride materials and their associated storage beds to predict vessel parameters, heat loads, and gas flow rates required for operation in an engineered storage system.
- Integrate storage component models (material performance and associated storage container) and run simulations to assess capabilities of possible foreign systems.

Data/Network Analysis

- Additional mining of bibliographic data is necessary to further parse out fields, researchers, papers, materials, groups, etc.
- Create a timeline of key term "hits" to determine surges and/or gaps in technical competencies or focus areas. This will effectively map the history of metal hydride research (associated with tritium storage and delivery) in Russia over last 70 years to investigate alignment with significant world events and predict current/future trends.
- Develop SRNL in-house capability for bibliographic network analysis to allow real-time interactive graphical analysis of networks.

REFERENCES

1. Züttel, "Materials for Hydrogen Storage," Materials Today, Vol. 6, pp. 24-33, 2003
2. L. K. Heung, "RTF Hydride Bed Technical Operating Guide", WSRC-TR-93-140, 1993
3. L. K. Heung, "Titanium for Long-Term Tritium Storage", WSRC-TR-94-0596, 1994

REFERENCES

Al	Aluminum
AM	Additive manufacturing
DOE	Department of Energy
ΔH	Enthalpy
H/M	Hydrogen-to-metal ratio
He-3	Helium-3
NNSA	National Nuclear Security Administration
PCT	Pressure-composition-temperature
P_{eq}	Pressure at equilibrium
R	Ideal gas constant
ΔS	Entropy
Ti	Titanium
V	Vanadium

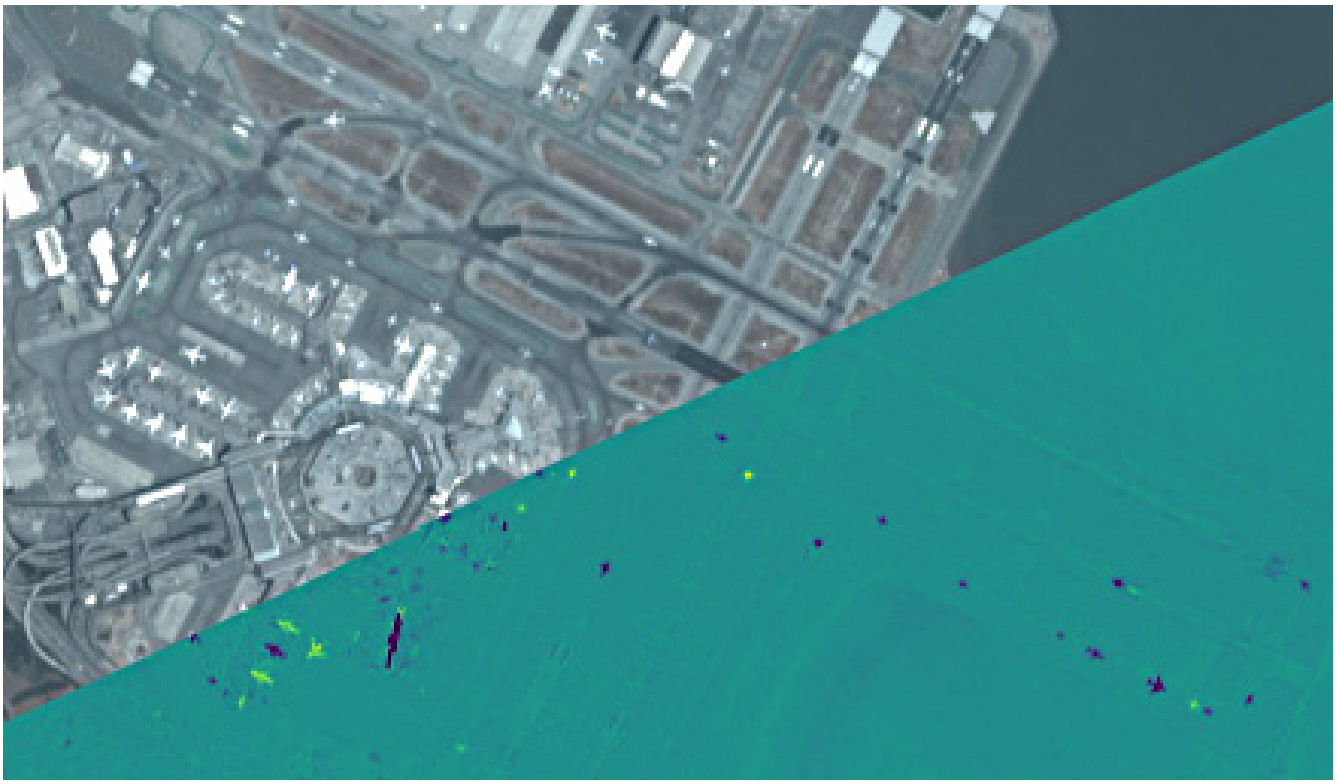

SEMI-AUTOMATED CHANGE DETECTION WORKFLOW FOR OVERHEAD IMAGERY

PROJECT TEAM:
K. N. Salvaggio (primary), B. Sellak, B. P. d'Entremont, T. C. McCarthy

THRUST AREA:
National Security

PROJECT START DATE:
October 1, 2018

PROJECT END DATE:
September 30, 2020

As satellite imagery becomes more prevalent, an unprecedented number of images of Earth are acquired daily, leading to an exploitation problem as there is more imagery to view than current analysts can handle. Applications such as broad area search, facility monitoring, construction chronology, transit activity monitoring, and land cover change can all benefit from the frequent revisit rates of current satellite platforms. However, manual searches conducted by an analyst can be cumbersome and time consuming. The objective of this project is to implement a semi-automated workflow that an analyst can use to highlight changes of interest in a sequence of imagery, where changes may be transient (e.g. aircraft movement) or persistent (e.g. construction). Multispectral imagery is used to highlight changes in multiple wavelength regions, some of which may not be visible to a human observer.

FY 2018

Objectives

- Acquire computing resources and necessary image exploitation software
- Identify change scenarios and acquire image data for initia development and testing
- Develop a methodology to register multiple images
- Implement an initial change detection methodology

FY 2018

Accomplishments

- Purchased two high-end computing workstations, where hardware specifications were based on image processing requirements
- Purchased/acquired commercial image processing software and open source software necessary for project development and installed on workstations
- Planet Labs Open California dataset was chosen for initial development purposes
- Acquired datasets for various types of change
- Successfully implemented open source image stitching and image registration algorithms that resulted in less than 0.3 pixels of error in each band
- Successfully implemented the IR-MAD change detection algorithm; preliminary results, while noisy, look promising and appear to direct an analyst's attention to areas of change

INTRODUCTION

The number of commercial earth-observing satellites has been rapidly increasing over the past several years, offering an unprecedented quantities of image acquisition over large areas of the earth. This has been driven not only by growth of the industry but also by new emphasis on high volume, low cost satellites such as the Planet Labs Flock constellations, which emphasize frequency and breath of coverage over image fidelity and robustness of each individual satellite. Planet Labs aims for daily coverage of the earth at 3-5 meter resolution which they currently obtain with over a hundred satellites in orbit. Using such data, it is possible to monitor daily activity over large swaths of land or large numbers of low-value targets. However, to extract value from this data it is necessary to filter the large volume of images to a smaller number of scenes in which locations of significant change can be highlighted for the analyst.

The objective of the project is to automate detection of change of objects on the ground. The challenge is to isolate change in the imaged scene since numerical values of the data also change due to factors such as satellite position, atmospheric condition, solar angle, and sensor calibration. Solutions to image registration (matching of the exact geometry of one image to another) and change detection (isolation of change in pixel values due to scene change rather than image conditions) exist in the open literature and the project aims to incorporate these into a workflow applicable numerous images possibly derived from different platforms in a manner useful to an analyst.

APPROACH

An analyst defines a region of interest and imagery that covers that region is returned to the analyst as the source of input to the workflow. The region is not guaranteed to be covered by a single image; in cases where multiple images are required to provide coverage of the region, the images are stitched together such that there is a single frame for the date/time of interest. Embedded geolocation data is used, in conjunction with an open source library (GDAL[1]), to stitch the images together while minimizing pixel error. Once image stitching is complete, images from different dates are registered together. This is accomplished by computing keypoints and descriptors for each image and matching them together. A keypoint descriptor characterizes the local image region in such a way that is invariant to changes in scale, orientation, and illumination, and generally partially invariant to affine transforms. Speeded Up Robust Features (SURF)[2] was chosen as the keypoint algorithm. A brute force matching algorithm is used to compute matches between sequential images using Euclidean distance as a metric. The matches are then used to compute a homography matrix, which describes the relationship between the two images. The homography matrix is then used to warp one image to another, thereby registering the images.

Once the images have been registered, a change detection algorithm is applied. Traditional change detection algorithms have historically been pixel-based, where changes are identified using pixel to pixel comparisons between images. More recently object-based algorithms have worked to group image segments into objects prior to looking for changes during further analysis. And finally, as the amount of available data grows, data mining and deep learning techniques are becoming more viable options. For the initial change detection implementation, a pixel-based change detection algorithm known as IR-MAD (iteratively reweighted multivariate alteration detection)[3,4] was chosen, due to its existing open source implementation. Additionally, because this project is considering multispectral imagery, any change detection techniques that are chosen must be compatible with the multi-band data. Implementing a preliminary change detection algorithm provided another method to verify that the image registration was working as expected. Future work will look to implement other change detection methods, and possibly use them in conjunction with one another in some sort of voting scheme.

RESULTS/DECISION

Preliminary results are shown in **Figure 1** for a natural disaster, ongoing construction, and airport traffic. Two different methods were used to display the change maps: in the first two cases, a binary map displaying changes is shown, and in the last case, a gray scale map is shown, where changes from light to dark (black) and dark to light (white) are indicated. In each case, changes of interest were accurately identified and highlighted. In the Big Sur example, the brightest area of change is the region in which the mudslide occurred and created new land in the ocean. In the San Jose example, there is a facility being built in the upper right corner of the scene which is highlighted nicely in the change map, in addition to some other areas of construction. It also appears that the change algorithm has brought out some of the land grading that was done, which is likely a result of using the multispectral imagery and taking advantage of data available in all the bands. Finally, in the San Francisco airport example, plane movement is highlighted in the change detection map as expected, but information can also be gained about the direction that flights were taking off based on the line of planes along the runway, which could also be indicative of wind speed.

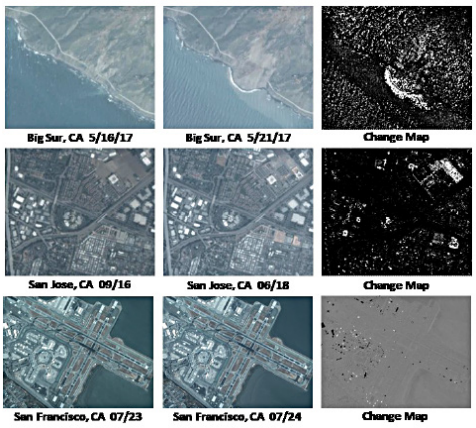

Figure 1. Preliminary change detection results using Planet Labs Imagery[5]: natural disaster, 2017 mudslide in Big Sur, CA; ongoing construction activities, San Jose, CA; airport traffic on consecutive days, San Francisco, CA. Open California Satellite Imagery © 2016 Planet Labs Inc. Licensed under CC BY-SA 4.0.

While the preliminary results from the IR-MAD change detection algorithm are promising, there is a moderate amount of noise in each case which could be distracting to an analyst. Future work will focus on reducing this noise by using several change detection algorithms to create multiple change maps that can then vote on the regions where change is most likely to have occurred. Results can be used to compute a probability of change that is then displayed to an analyst. Similarly, the current visualization techniques do not take advantage of the multispectral nature of the data. It is possible that changes in the near infrared band of the imagery are of more interest to an analyst than changes in other bands, and future visualization techniques will need to be flexible enough to be able to display what is of greatest value to the analyst. Finally, the examples presented here are for single image pairs, which is a necessary first step in the workflow development. Ultimately, the workflow seeks to present changes for sequences of imagery, which may result in adaptations to current workflows.

FUTURE DIRECTIONS

- Improve upon the results of the preliminary change detection implementation by reducing noise, mitigating the effects ofsolar angle and shadow movement, and returning a probability of change
- Create a flexible data visualization tool that will give analysts the ability to easily identify changes while also referencing the original imagery for context
- Expand the current results to a series of images that ultimately results in a timeline of transient and persistent changes
- Create a distributed workflow that will increase the computational speed to a reasonable time frame
- Broaden the workflow to other data sources, such as DigitalGlobe's WorldView or NASA's Landsat satellites
- A continuation to this LDRD has been awarded for FY 2019

REFERENCES

1. GDAL/OGR contributors, GDAL/OGR Geospatial Data Abstraction software Library. Open Source Geospatial Foundation. (2018) URL http://gdal.org
2. Bay, Herbert, et al. "Speeded-up robust features (SURF)." Computer vision and image understanding 110.3 (2008): 346-359.
3. Nielsen, Allan Aasbjerg. "The regularized iteratively reweighted MAD method for change detection in multi- and hyperspectral data." IEEE Transactions on Image processing 16.2 (2007): 463-478.
4. Canty, Morton J. and Nielsen, Allan A. "Automatic radiometric normalization of multitemporal satellite imagery with the iteratively re-weighted MAD transformation." Remote Sensing of Environment 112 (2008): 1025–1036.
5. Planet Team. Planet Application Program Interface: In Space for Life on Earth. (2017) San Francisco, CA. https://api.planet.com.

ACRONYMS

GDAL	Geospatial Data Abstraction Software Library
GEOINT	Geospatial Intelligence
IR-MAD	Iteratively Reweighted Multivariate Alteration Detection
SURF	Speeded Up Robust Features
USGIF	United States Geospatial Intelligence Foundation

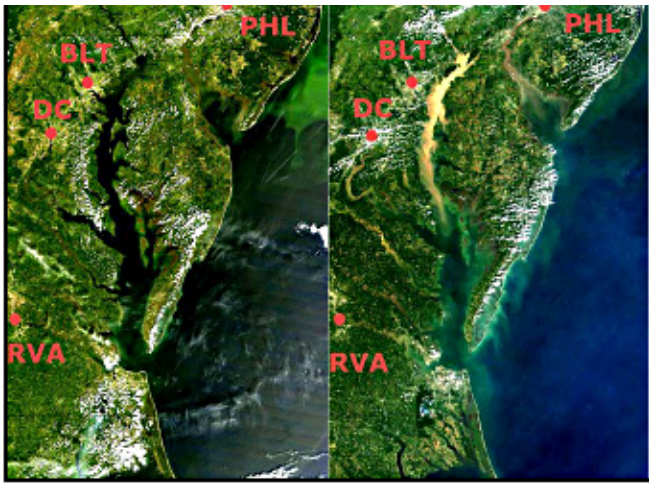

Figure 1. MODIS images of Chesapeake Bay August 23, 2011 and September 12, 2011. Major population centers are labeled.

DEVELOP SRNL'S ALGE3D CODE FOR USE AS NATIONAL RESPONSE ASSET

PROJECT TEAM:
GM Maze (Primary), S Aleman, A Garrett, R Buckley, E Viparelli

THRUST AREA:
National Security

PROJECT START DATE:
October 1, 2017

PROJECT END DATE:
September 30, 2018

Current national models employed by emergency response agencies have well developed models to simulate the effects of hazardous contaminants in riverine systems primarily driven by one-dimensional flows; however, there is a gap in the support for more complex systems. While many models exist, none are capable of quick deployment in emergency situations that could contain a variety of release situations including mixtures of both particulate and dissolved chemicals in a complex flow area. Adaptations of ALGE3D are planned to update and expand particulate tracer and sedimentation capabilities to allow for a more comprehensive model. Quick-deployment model inputs will also be developed for a few high impact areas to aide in the timeliness of emergency response in key locations. The final product of ALGE3D will allow for coupling of dissolved tracer concentrations, particulate tracer concentrations, and their associated sedimentation effects.

FY 2018

Objectives

- Define key locations
- Develop particulate tracer module for ALGE3D
- Develop sedimentation module for ALGE3D
- Verification, testing and publication

Accomplishments

- Developed bathymetric and identification grid for 2 locations and began development for 3 additional locations.
- Gathered oceanographic and meteorological verification data for 2 developed locations for 1 full year each.
- Identified 1-2 events for validation at each developed location and gathered oceanographic and meteorological data for each event.
- Modified code to include an unlimited number of sediment classes and particulate speciation. This includes sediment bed loading, deposition and resuspension, and adsorption/desorption of dissolved species.
- Verification of particulate and sediment modules was performed using a stagnant water column simulation

INTRODUCTION

On average North Americans live within ~3 km of a water body **[1]**. Of the top 10 most populated US cities from a 2015 US Census Bureau estimate, 7 of the cities are situated near the ocean, a bay, or on one of the Great Lakes **[2].** A contamination of the water ways in the United States could be devastating to the economy (through tourism and industries such as fishing), public health (from direct contact, or contaminated drinking water), and in some cases even infrastructure (water treatment plants). For example, **Figure 1 on previous page** shows two visible satellite images for Chesapeake Bay, the first on August 23, 2011 and the second on September 13, 2011. In the second image a large plume of suspended particles in the Bay can clearly be seen. In this case it was a sediment plume caused by a large storm system moving through, and the major impacts included mainly damage to the fishing and oyster industries that year along with beach and recreation area closures **[3, 4].** However, a similar plume containing radioactive or chemical material would have resulted in much costlier and wide spread consequences due to the associated human health impacts.

Current US emergency response capabilities for contamination to waterways, either from an accidental release or a planned attack, include the use of a one-dimensional transport model **[5, 6].** This works well for most riverine systems which have flow in primarily one (downstream) direction. However, in more complex systems, such as tidal estuaries, bays, or lakes, a more complex model is needed. SRNL will develop ALGE3D to fill this gap in technology for emergency response of multi-dimensional aqueous modeling of scales below the Rossby radius of deformation, where the forces associated with the rotation of the earth are negligible. A three-dimensional model with the capability to handle dissolved and particulate contaminants, model the associated sedimentation effects, and support quick-deployment will provide a unique capability that could support the US emergency response enterprise.

APPROACH

ALGE3D is a 3-D hydrodynamic code developed by SRNL which solves the momentum, mass, and energy conservation equations to predict the movement and dissipation of thermal or dissolved chemical plumes discharged into cooling lakes, rivers, and estuaries **[7].** The first portion of this project included data gathering for Chesapeake Bay and Lake Michigan, two high populated bodies of water with multiple potential sources of accidental release. Data was gathered for each location to provide input files for the model. While data gathering was being accomplished a pre-processor GUI was developed. The highly structured format of the required input files can be limiting and provide an endless source of frustration for users, so to facilitate use in an emergency response situation a program was developed. This program guides the user through the selection of necessary data and generates the necessary input files in the proper format and verifies all required files are present based on the user's selections.

Code modifications were made to include suspended sediment, particulate species, and dissolved species transport **(Figure 2)**. The dissolved species can be adsorbed onto or desorbed off of suspended sediment particles based on the chemical properties specified of the released material. Sedimentation effects, including erosion and deposition were also added into the code and will be verified in the second year of the project. In addition to the transport modules added, modifications were made to the code to reduce the amount of spin up time needed to obtain the physical properties (salinity and temperature) by adding an option to include an initial spatially varying field rather than one set initial value. This modification allows the code to be run in a more operational time frame.

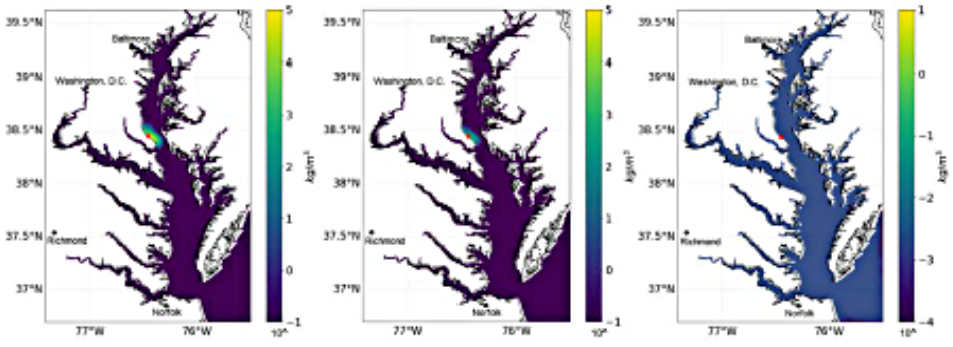

*Figure 2. Dissolved species **(Left)**, particulate species **(Middle)**, and suspended sediment concentrations 24 hours after a theoretical release from Calvert Cliffs Nuclear Power*

RESULTS/DECISION

Chesapeake Bay and Lake Michigan bathymetry data was gathered from 30 arcsecond topography horizontal topography with 1 m vertical resolution **[8]** and interpolated to 500 m and 1 km horizontal resolutions. River coordinates and stream flow data for each domain were gathered from USGS water data **[9].** Input files were developed to include bathymetry and grid identifications for each domain and at each scale. The pre-processing GUI allows for user selection of a release location from several different pre-set locations on each main domain, including nearby nuclear power plants. Tidal harmonics were gathered for Chesapeake Bay **[10]** (Lake Michigan is not tidally forced) and coded into the pre-processor allowing tidal forcing to be calculated based on the user's selection of date. Testing of the predicted tidal forcing was matched against the NOAA tidal forecast.

Code modifications to include suspended sediment, particulate species and dissolved species transport were tested using a stagnant column of water with suspended sediments introduced at the surface and settling through a layer of constantly discharged dissolved species, before settling into a layer with no dissolved or particulate concentration. Scenarios were run with three different classes of sediments with varying diameters, densities, and adsorption/desorption rates **(Figure 3).** As expected as the suspended sediment settles from the surface layer into the layer with dissolved concentration some of the material adsorbs onto the suspended sediments, moving onto the particulate species form. As the suspended sediments and particulate species settle further into the water column in the area with no concentration some of the material desorbs from the particulate species back into the dissolved species. The suspended sediment material and the particulate species settle into the bottom of the water column and accumulate into the bed, where some adsorption/desorption continues until an equilibrium is reached. This equilibrium is based on the user specific constants provided and are material dependent. Total mass balance was conserved showing there was no mass loss/gain in movement between species.

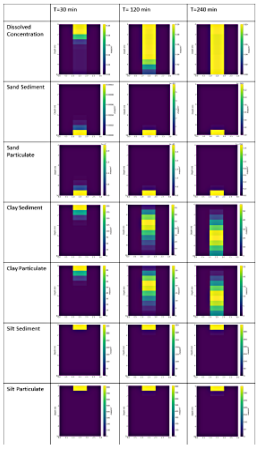

Figure 3. Concentration of dissolved species, suspended sediments, and particulate sediments 30 minutes, 120 minutes and 240 minutes after release.

FUTURE DIRECTIONS

- Refine pre- and post- processing GUI
- Configure code to allow GPU processing to significantly reduce model run time
- Validation and verification of simulations.
- Expand library of release locations
- Add library of potential release materials with the appropriate model inputs and critical values for analysis
- Inverse modeling
- Couple with atmospheric dispersion model for inputs of deposition over waterways.

PUBLICATIONS/PRESENTATIONS

1. Maze, Grace. (2017, December) *ALGE3D: A Three-Dimensional Transport Model,* Presented at the American Geophysical Union Fall Meeting, New Orleans, Louisiana.
2. Maze, Grace. (2018, February) *ALGE3D: A Three-Dimensional Transport Model,* Presented at Ocean Sciences Meeting, Portland, Oregon.
3. Maze, Grace. (2018, March) *ALGE3D: Development as an Aqueous Emergency Response Model,* Presented at the Palmetto Chapter of the American Meteorological Society Mini-Technical Conference, Columbia, South Carolina.
4. Submitted: Maze, Grace (2018, December) *Expanding ALGE3D as an aqueous emergency response model,* Submitted for Presentation at the American Geophysical Union Fall Meeting, Washington, D.C.
5. Submitted: Maze, Grace. (2019, January) *ALGE3D development as an aqueous emergency response model,* Submitted for Presentation at the 99th American Meteorological Society Annual Meeting, Phoenix, Arizona.

REFERENCES

1. M. Kummu, H. de Moel, P. J. Ward and O. Varis, "How close do we live to water? A global analysis of population distance to freshwater bodies," PloS ONE, vol. 6, no. 6, June 2011.
2. "US Census Bureau," [Online]. Available: https://factfinder.census.gov/faces/tableservices/jsf/pages/productview.xhtml?src=bkmk.
3. D. Strain, "A 2011 storm walloped the Bay with sediment, study says," Sea Grant Maryland, 30 **4.** R. M. Hirsch, "Flux of Nitrogen, Phosphorus, and suspended sediemnt from the Susquehanna River Basin to the Chesapeake Bay during Tropical Storm Lee, September 2011, as an indicator of the effects of reservoir sedimentation on water quality," U.S. Department of the Interior, U.S. Geological Survey, Reston, Virginia, 2012.
5. R. Bahadur and W. B. Samuels, "Modeling the fate and tansport of a chemical spill in the Elk River, West Virigina," J. Environ. Eng., vol. 141, no. 7, 2005.
6. W. B. Samuels and D. Ryan, "ICWater: Incident command tool for protecting drinking water," in ESRI Internation User Conference, 2005.
7. J. Blanton, A. Garrett, J. Bollinger, D. Hayes, L. Koffman and J. Amft, "Transport and Dispersion of a conservative tracer in coastal waters with large intertidal areas," Estuaries and Coasts, vol. 32, no. 3, 2009.
8. J. J. D. T. S. W. H. F. S. J. B. B. B. J. D. D. F. J. F. S. I. S.-H. K. R. L. K. M. S. N. A. P. R. T. J. V. R. G. W. P. W. Becker, "Global Bathymetry and Elevation Data," 2009.
9. USGS, "Current Water Data for the Nation," [Online]. Available: https://waterdata.usgs.gov/nwis/rt.
10. NOAA, "Tides and Currents," [Online]. Available: https://tidesandcurrents.noaa.gov/.

ACRONYMS

US	United States
USGS	United States Geological Survey
NOAA	National Oceanographic and Atmospheric Administration

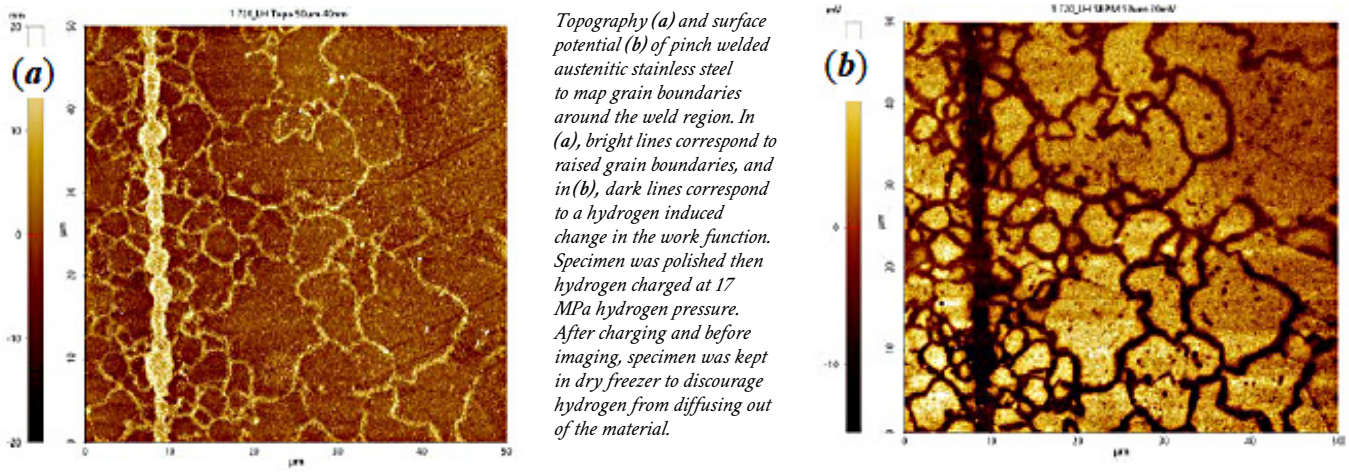

Topography (a) and surface potential (b) of pinch welded austenitic stainless steel to map grain boundaries around the weld region. In (a), bright lines correspond to raised grain boundaries, and in (b), dark lines correspond to a hydrogen induced change in the work function. Specimen was polished then hydrogen charged at 17 MPa hydrogen pressure. After charging and before imaging, specimen was kept in dry freezer to discourage hydrogen from diffusing out of the material.

KELVIN PROBE FORCE MICROSCOPY FOR HIGH-RESOLUTION IMAGING OF HYDROGEN IN STEEL ALLOYS

PROJECT TEAM:
A. J. Duncan,
J. D. McNamara (Co-PIs)

COLLABORATORS:
P. S. Korinko,
M. J. Morgan and R. J. Smith

THRUST AREA:
National Security

PROJECT START DATE:
October 1, 2017

PROJECT END DATE:
September 30, 2018

Kelvin probe force microscopy (KPFM) was used to directly image and co-locate the presence of hydrogen in stainless steel with various microstructures. Several specimens were investigated, including forged, welded, LENS® fabricated, and pinch welded materials. Each sample was examined either after being charged under hydrogen gas, or as received (i.e., uncharged) condition. H-charged forged and welded samples show an increase in the work function for regions of retained delta ferrite, and this is indicated by a decrease in the contact potential difference (CPD) voltage. LENS® fabricated samples show an increase in the CPD around the cellular regions. This is indicative of elemental variation which is confirmed by energy dispersive spectroscopy (EDS) data. Cleaned austenitic 316L fill stems were pinch welded under nitrogen using range of currents. The pinch welds were characterized by atomic force microscopy (AFM) and KPFM in the as-welded condition (with and without hydrogen) and post weld hydrogen charging. The results show the presence of hydrogen along grain boundaries in the welded region. Electron backscatter diffraction (EBSD) was used to analyze the grain size and orientation along the pinch welds.

FY 2018

Objectives

- KPFM development at SRNL and sample preparation optimization
- Develop inert nitrogen atmosphere for AFM enclosure
- Characterized microstructural differences between forged, welded, LENS®, and pinch welded SS specimens.
- Imaged hydrogen charged and uncharged samples, and confirmed hydrogen segregation to grain and cell boundaries.
- Compare with other scanning electron microscope and electron backscatter diffraction measurements.

Accomplishments

- Characterized microstructural differences between forged, welded, LENS®, and pinch welded SS specimens.
- Developed sample prep methodology, and nitrogen environment for AFM.
- Imaged hydrogen charged and uncharged samples; and confirmed hydrogen segregation to grain and cell boundaries.

INTRODUCTION

Understanding the mechanism of hydrogen interactions in metal alloys is continually a topic of interest for applications which involve the long-term storage of hydrogen.[1] Atomic hydrogen segregates to regions of extended defects, such as grain and phase boundaries, and can cause stress and premature cracking through a process known as hydrogen embrittlement.[2,3,4] Advanced microstructural imaging techniques, with minimal sample preparation needs, that are capable of resolving features down to the nanometer scale are needed. Current imaging and testing technologies for understanding the effects of hydrogen in metals involve low-resolution optical microscopy and fractography after mechanical testing. Hydrogen segregated at the surface and particularly at defect sites changes the local work function of the material and can be measured by KPFM, a variant of atomic force microscopy (AFM). [5] KPFM produces surface potential (i.e., voltage) images, and is capable of measuring the local change in work function of surfaces with very high spatial resolution compared to current methods of optically imaging the microstructures. The spatial and energy resolution of KPFM is approximately 5 nm and 10 mV, respectively. [6] By locating the presence of hydrogen and its relationship with extended defects at the surface using KPFM, it may be possible to predict the long-term storage properties of a container.

The mechanism of Kelvin probe microscopy is based on establishing an electrical equilibrium between the work function of a metallized probe and the work function of a surface when the two systems are placed in electrical connection.[6] During KPFM operation, an AFM is used to bring an oscillating metallized probe very close to the sample surface. A piezo actuator mechanically drives the probe close to its resonant frequency, and, due to Van der Waals forces between the tip and surface, the resonance frequency of the probe changes as it raster scans across the surface of the sample for a predetermined scan area. In this way, topological variations can be measured. Simultaneously, the second resonant frequency of the probe is monitored while applying an AC voltage to electrostatically resonate the probe.A potential difference will develop between the sample and the probe due to differing Fermi levels and will create an electrostatic force between the two materials. [6] Using a feedback loop, a specific DC voltage is also applied to the probe such that, at any given point on the surface, the electrostatic force between the tip and the sample is nullified. In the case of vanishing electrostatic force, the applied DC voltage will be equal to the surface potential. This value is called the contact potential difference (CPD) and is defined as the change in work function between the sample and the probe:[6]

$$CPD = \varphi tip - \varphi sample, \quad (1)$$

where φtip and φsample are the work functions of the tip and sample, respectively. The CPD is equal in magnitude, opposite in polarity, to the backing potential that is necessary to nullify the electrostatic force between the sample and the probe. **Figure 1** shows schematically how the vacuum levels of the sample and the probe become aligned as a DC voltage is applied, thereby allowing for the measurement of the CPD. **Figure 2** gives an example of the topography and microstructure of 304L austenitic stainless steel after it has been electropolished. The corresponding surface potential image shows how the work functions of the grains vary which could be due to different oxidation levels or grain orientation. Using the KPFM technique allows for very localized work functions to be measured and attributed to the corresponding defects. It is important to mention that crystallographic orientation[7] and compositional variation will change the local work function as well.

KPFM has been previously used to image hydrogen in palladium thin films, duplex stainless steel and aluminum alloys.[8,9,10,11,12] Duplex stainless steels were electrochemically charged with hydrogen and subsequently measured with KPFM. Since the

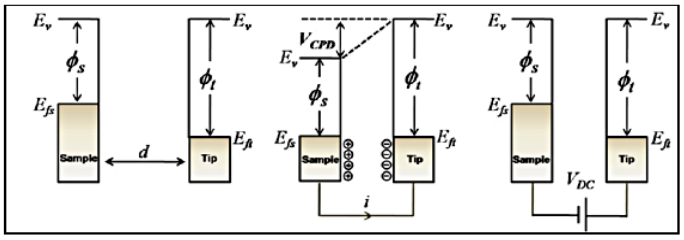

Figure 1. V_{CPD} is the difference in work function values of the sample and the tip. This value can be measured by applying a DC voltage to nullify the electrostatic force between the sample and the tip.

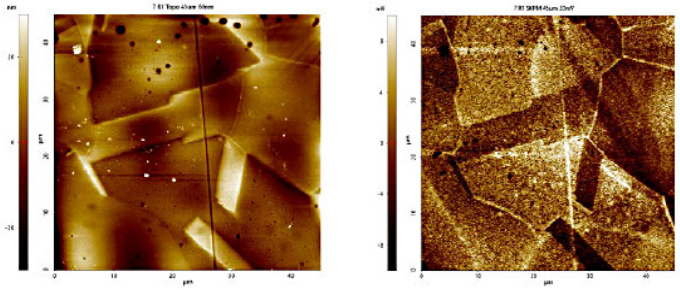

Figure 2. Left shows the height or topography information of electropolished stainless steel. Right shows the corresponding variation of the surface potential.

work function of the surface is the physical quantity being monitored during these measurements, it was possible to detect the diffusion of hydrogen to the surface as it changed the local work function. The ferrite phase showed a much more drastic change in work function compared to the austenite phase with increasing time of hydrogen loading. The change in work function was attributed to changes of the surface oxide band structure due to the presence of hydrogen.[9] Studying the behavior of hydrogen at the surface of duplex steels yields interesting results due to the vastly different diffusion rates of hydrogen in ferrite and austenite phases. Hydrogen segregation was also observed at deformation twin sites in twinning-induced plasticity (TWIP) steel, where the potential images showed a decrease in CPD in the region of the deformation twin sites. For most of the research reported in the literature, samples of stainless steel are coated with palladium to reduce topological effects, as well as to desorb the hydrogen. In these instances, the samples were electrochemically charged with hydrogen using various electrochemical solutions.

Additionally, it is important to characterize and understand the capabilities of additive manufactured (AM) stainless steel components being considered for hydrogen storage. Years of research and operational experience have demonstrated the effects of tritium on traditionally fabricated hydrogen service components, but the same cannot be said for AM components. KPFM studies of the microstructural behavior of hydrogen charged AM stainless steels can provide a technique to understand and predict the long-term effects of tritium and hydrogen embrittlement on its containers.

In this work, we discuss the results of KPFM imaging of various stainless-steel samples and compare it with complimentary techniques, such as scanning electron microscopy (SEM) and electron backscatter diffraction (EBSD) measurements to understand the behavior of hydrogen segregation in stainless steel.

APPROACH

Stainless steel samples which were forged, welded, pinch welded, and fabricated by the LENS® method[13] were investigated to understand their microstructures and the behavior of hydrogen within the material. Forged stainless steel samples, type 304L and welded stainless steels, with 21% Cr - 6%Ni - 9% Mn base metal, and 308L filler metal were hydrogen charged under 34 MPa hydrogen gas, at 350°C, for 2 weeks. Fill stems which were type 304L stainless steel, machined from forgings, gun drilled and crush ground and Oakite cleaned were obtained from Kansas National Security Campus and were pinch welded at varying currents (2900-4100 A) in nitrogen. Specific pinch weld samples were then hydrogen charged under the same conditions as above. Four type 304L stainless steel (SS) samples were prepared by the directed energy deposition method of laser engineered net shaping (LENS®) at Sandia National Laboratory and Los Alamos National Laboratory and are listed in **Table 1.** Hydrogen charging was performed on two of the samples (D and E) by pressurizing a chamber with 34 MPa of hydrogen gas at 350°C for approximately 2 weeks. All samples which were pressure charged by hydrogen are hereafter called "H-charged" samples. After charging, samples were stored at 0°C to prevent the unnecessary loss of hydrogen by diffusion. All samples were cut and mechanically polished for AFM imaging by standard metallographic practices. Samples were cleaned by rinsing with soap and de-ionized (DI) water, followed by rinsing with ethanol and drying with dry nitrogen or air. A light electrolytic etch was performed with 10% oxalic acid for 30s at 10V to reveal the microstructures for initial measurements. Once these initial measurements were performed, the samples were re-polished to return to the as-polished conditions for subsequent analysis. Before imaging, all samples were cleaned with supercritical CO_2 gas which acted to both dissolve organic contamination and release particulate material from the surface.

Imaging was performed using a Park Systems XE-70 AFM, in non-contact mode and the extended, electrostatic force microscopy mode coupled with a Stanford Research Systems lock-in amplifier for KPFM measurements. The AFM is contained within an environmental chamber to control the humidity levels, and dry nitrogen is flowing through the chamber during imaging. The relative humidity levels for the AFM measurements in this work are about 8%. Optical micrographs were taken on a Nikon MM-400 measuring microscope. SEM examination was conducted on a Hitachi SU823 SEM and energy dispersive spectroscopy (EDS) measurements were performed with the attached Oxford detector. EBSD measurements were performed as well. Since KPFM is a surface sensitive technique, only the behavior of hydrogen at the surface can be investigated. Additionally, imaging the samples while in a nitrogen environment reduces the thin water layer which develops on the surface of materials exposed to ambient conditions and acts as a screening potential, which is detrimental to surface potential measurements.

RESULTS/DECISION

Forged, Welded, and LENS® Fabricated Samples:

The surface morphology of the forged, welded and LENS® fabricated stainless-steel samples were characterized by an AFM to understand the microstructural characteristics. In order to image the fine cellular grains of the LENS® fabricated samples, the samples were given a quick electrolytic etch. **Figure 4** shows the microstructure for one of the LENS® samples. Typical microstructural patterns of these samples are large grain features on the order of 50 – 100 μm across, and small cellular-like regions which are on average less than 5 μm. The cells have either polygonal (sometimes circular) shapes or elongated skeletal structures and are contained within the large grains. The size of the structures is related to the heat input during melting and its corresponding solidification rate. Samples fabricated by LENS® undergo highly localized heating from the laser, followed by rapid cooling and solidification as the heat source advances.[14, 15] This process creates fusion zone type microstructures very similar to those of welded samples. Each layer of the sample is melted by the laser, solidified rapidly, and followed by successive deposition and solidification of more material. The melt pools are about 500 μm to 1 mm wide, and AFM image areas are no greater than 45 μm, which allows each image to be fully contained within one melt region. LENS® materials show very fine grains compared to forged steels and have directional anisotropy depending on the build parameters.

Surface potential measurements (KPFM), with their corresponding topography images, were performed on as-polished forged, welded and LENS® samples, both H-charged and uncharged, to image the changes in the local work function and are shown in **Figure 5.** All the samples in **Figure 5.** were hydrogen charged; however, the sign of the change in CPD was negative for the forged and welded samples, and positive for the LENS® samples. Uncharged samples, regardless of the growth conditions showed no noticeable variation in surface potential for our measurements. This leads us to conclude that the surface potential variation is a factor of elemental composition or phase variation. It is well known that welded samples have regions of retained delta ferrite which should have a different work function than the surrounding austenitic regions. For the LENS® samples, EDS data (**Figure 6**) show that the intercellular regions have a higher percentage of Cr content and a decrease in the Ni content. This is indicative of retained ferrite at the boundaries of the austenitic microstructures and is consistent with other studies on AM 316L stainless steel.[15] EDS measurements performed on one of the LENS® fabricated are shown in **Figure 6.** which is representative of the other LENS® samples. Both EDS line scans **[Figure 6(c) and 6(d)]** and maps (not shown) show an increase in the Cr content and a decrease in the Ni content at the cellular and grain boundaries. Other EDS data show that there is compositional variation in the same regions (e.g., grain boundaries)[14] which are posited to be concentrated in hydrogen. Since both charged and uncharged samples showed a change in surface potential, we must assume that the changes in the work function are due to crystallographic orientation or elemental variation for the LENS® samples.

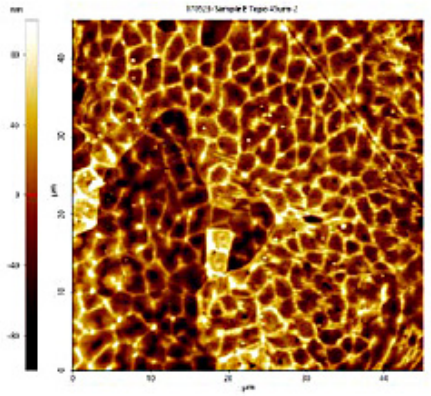

Figure 4. Topography as measured by the AFM for a LENS® fabricated sample after mechanical polishing a light oxalic acid etch.

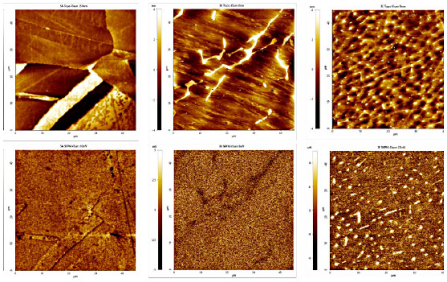

*Figure 5. **(Top)** topography images of forged **(Left)**, welded **(Center)**, and LENS® fabricated samples (right) with their corresponding surface potential maps **(Bottom)**.*

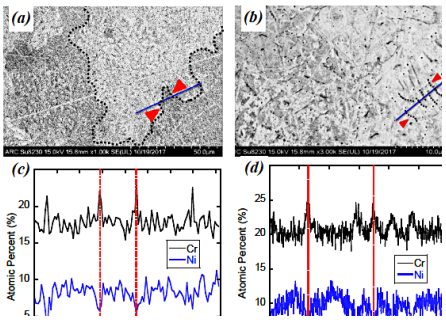

*Figure 6. SEM micrographs and EDS line scans of a LENS® sample. The red dotted lines in **(a)** highlight the edges of a grain, and the correlating EDS line scan **(c)** shows an increase in Cr and decrease in Ni content. Similarly, **(b)** and **(d)** show an increase in Cr and decrease in Ni content at the boundaries of the rice-like structures, which are similar to cellular structures in these LENS materials.*

Pinch Welded Samples:

The topography and KPFM images of 4 pinch welds are shown in **Figures 7 and 8** prepared with the weld in the longitudinal orientation. On the left, the samples were measured uncharged and, on the right, the samples were measured after hydrogen charging, for both **Figures 7 and 8**. For **Figure 7,** the pinch welds were welded at 2900 A, and the weld is clearly visible in the topography images. **Figure 8** shows samples that were welded at 4100 A, and the weld line is no longer visible due to continuous grain growth across the boundary.

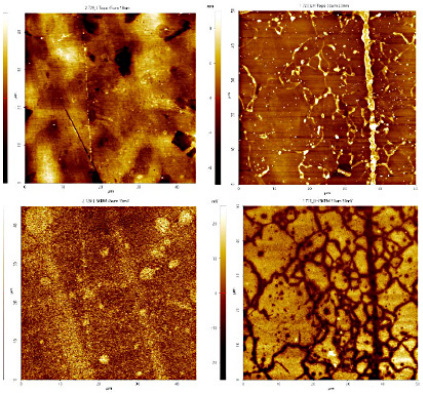

Figure 7. Two pinch weld samples with topography (top) and KPFM surface potential measurements (bottom) welded at 2900 A. The sample on the right was h-charged before imaging and shows clear surface potential variation around the weld line and surrounding grain boundaries.

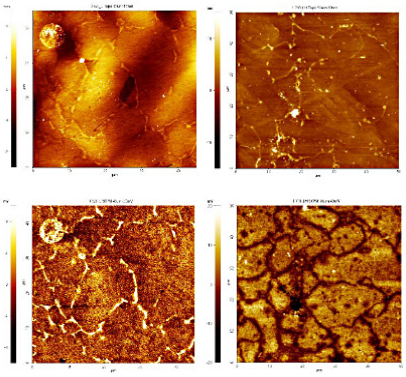

Figure 8. Two pinch weld samples welded at 4100 A with topography (top) and KPFM surface potential measurements (bottom). The weld line is not visible as the grains grew across the boundary during the pinch process. The sample on the right was h-charged before imaging and shows clear surface potential variation around the surrounding grain boundaries.

The surface potential images show drastic changes in the work function for the hydrogen charged samples (on the right in both **Figures 7 and 8).** The regions surrounding the grain boundaries and the weld line seem to indicate increased hydrogen content compared to the surrounding matrix. For the hydrogen charged pinch welds, care was taken to ensure that they were kept in a freezer between H-charging and imaging to inhibit hydrogen diffusion from the material.

Pinch welds performed at 2900 A and 4100 A were characterized using EBSD to investigate the grain size distributions and orientation with respect to the weld interface. These data are shown in **Figure 9.** Three types of maps were chosen to image the welds. Inverse pole figure (IPF) maps show various orientations of the grains and the many colors are representative of the grain orientation in respect to the Euler angles. The IPF maps are shown at the top of **Figure 9** with the weld oriented horizontally. Band contrast (BC) images use the average intensity of the Kikuchi bands in regard to the overall intensity of the map to highlight the grain boundaries (GB) and special boundaries (SB). The GB maps are defined based on misorientation angles, and the SB are specifically oriented <111> 60° Twin boundaries, with sigma 3. These BC+GB+SB maps are shown in the middle of **Figure 9.** Finally, grain size (GS) maps use a color scale to indicate the sizes of grains, and these maps are shown at the bottom of Fig. 9. For the sample that was welded at a relatively low current value of 2900 A (**Figure 9** left), the weld interface at the center propagating from the pinch point is clearly visible in all three maps. The IPF and GS distribution maps do not show any correlation with the growth of the grains at the weld interface. In contrast, the sample which was welded at a higher current (4100 A, **Figure 9** right) displays interesting features in the EBSD maps. The band contrast image shows grains which are grouping together in bands parallel to the weld line. The GS map shows that very small grains lie close to the weld interface in a band, as shown by the blue colored grains, and in another band about 250 μm above the weld line. This behavior was observed, previously.[17] Future measurements need to be performed to understand the nature of the grain growth in respect to grain size and distribution, and to understand the changing strain fields occurring in the samples. In this manner, we hope to shed light on the segregation of hydrogen at the surface of stainless steel.

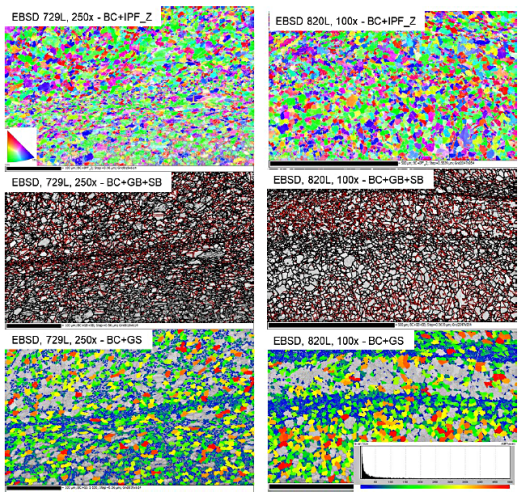

*Figure 9. EBSD maps of a pinch weld welded at 2900 A **(Left)** and one welded at 4100 A **(Right).** Weld interface is oriented horizontally. Inverse pole figures in respect to the z direction **(Top)** show the varying grain orientations along the weld; the band contrast together with grain boundaries and special boundaries **(Middle BC+GB+SB)** show the outline of the grains; the grain size distribution maps (bottom) show the distribution of grain sizes along the weld.*

FUTURE DIRECTIONS

- Incorporate electrochemical H-charging and time-resolved studies for H decay studies.
- Determine the role kinetics play in H-charging and redistribution after charging.
- Image specifically engineered defects and microstructures.
- Correlate direct imaging KPFM with indirect quantitative techniques for hydrogen studies.
- Parallel KPFM, TDS (thermal desorption spectroscopy), and magnetic force microscopy (MFM) studies.
- Develop system for deuterium/ tritium work.
- Understand isotopic effects of deuterium/ tritium.
- Improve sample preparation methods.
- Increase resolution of AFM and KPFM.

PUBLICATIONS

1. J. D. McNamara, A. J. Duncan, M. J. Morgan, and P. S. Korinko, "Imaging hydrogen in stainless steel alloys by Kelvin probe force microscopy" Proc. ASME 2018 Pressure Vessels and Piping Conference, PVP2018, July 15-20, 2018, Prague, Czech Republic.
2. M. J. Morgan, D. Hitchcock, T. Krentz, J. McNamara and A. Duncan, "2017 Accomplishments – Tritium Aging Studies on Stainless Steel Weldments and Heat-Affected Zones," SRNL-STI-2018-00036, January, 2018, Savannah River National Laboratory, Savannah River Nuclear Solutions, LLC, Aiken, SC 29808

PRESENTATIONS

1. J. D. McNamara, A. J. Duncan, M. J. Morgan, and P. S. Korinko, "Kelvin Probe Force Microscopy for Imaging Hydrogen in Steel Alloys", AVS 64th International Symposium and Exhibition, Tampa, FL, November 2, 2017.
2. P. S. Korinko, "SRNL Welding Joining Site Update," SRNL-STI-2018-00024, welding IMOG, WAM FE, Sandia National lab, Jan 22-23, 2018.
3. P. S. Korinko, SRNL-STI-2018-00237, SRNL welding and joining site update, Wire Additive Manufacturing Focused Exchange and Welding JOWOG, May 21-25, 2018, AWE, Reading, Berkshire, England
4. J. D. McNamara, A. J. Duncan, M. J. Morgan, and P. S. Korinko, "Imaging hydrogen in stainless steel alloys by Kelvin probe force microscopy" Proc. ASME 2018 Pressure Vessels and Piping Conference, PVP2018, July 15-20, 2018, Prague, Czech Republic.

REFERENCES

1. Caskey, Jr., G. R., Hirth, J. P., Oriani, R. W. and Smialowski, M., eds., Noyes Publication, Park Ridge, NJ, 1985, p. 822.
2. Koyama, M., Rohwerder, M., Tasan, C. C., Bashir, A., Akiyama, E., Takai, K., Raabe, D. and Tsuzaki, K. "Recent progress in microstructural hydrogen. mapping in steels: Quantification, kinetic analysis, and multi-scale characterisation," *Mater. Sci. Technol.* **33** (13), 1481 (2017).
3. Perng, T.-P. and Altstetter, C. J., "Hydrogen effects in austenitic stainless-steels," ***Mater. Sci. Eng.*** A, **129**(1), **99** (1990).
4. Wang, Y., Wang, X., Gong, J., Shen, L. and Dong, W., "Hydrogen embrittlement of catholically hydrogen-precharged 304L austenitic stainless steel: Effect of plastic prestrain," *International Journal of Hydrogen Energy,* **39**(25), 13909 (2014).
5. Melitz, W., Shen, J., Kummel, A. C. and Lee, S., "Kelvin Probe Force Microscopy and Its Application," *Surf. Sci. Rep.* **66,** 1 (2011).
6. Melitz, W., Shen, J., Kummel, A. C. and Lee, S., "Kelvin Probe Force Microscopy and Its Application," *Surf. Sci. Rep.* **66,** 1 (2011).
7. Hua, Z., An, B., Iijima, T., Gu, C. and Zheng, J. "The finding of crystallographic orientation dependence of hydrogen diffusion in austenitic stainless steel by scanning Kelvin probe force microscopy," *Scripta Mater.* **131,** 47 (2017).
8. Evers, S., Senoz, C. and Rohwerder, M., "Spatially resolved high sensitive measurement of hydrogen permeation by scanning Kelvin probe microscopy," *Electrochemica Acta* **110,** 534 (2013).
9. Senoz, C, Evers, S., Stratmann, M. and Rohwerder, M., "Scanning Kelvin Probe as a highly sensitive tool for detecting hydrogen permeation with high local resolution," *Electrochem. Commun.* **13,** 1542 (2011).
10. Evers, S., Senoz, C. and Rohwerder, M., "Hydrogen Detection in Metals: a Review and Introduction of a Kelvin Probe Approach," *Sci. Technol. Adv. Mater.* **14,** 014201 (2013).
11. Larignon, C., Alexis, J., Andrieu, E., Lacroix, L., Odemer, G. and Blanc, C., "Investigation of Kelvin Probe Force Microscopy Efficiency for the Detection of Hydrogen Ingress by Cathodic Charging in an Aluminium Alloy," *Script. Mater.* **68,** 479 (2013).
12. An, B., Hua, Z., Iijima, T., Gu, C., Zheng, J., Marchi, C. S., "Scanning Kelvin Probe Force Microsopy Study of Hydrogen Distribution and Evolution in Duplex Stainless Steel" *Proceedings from the ASME Pressure Vessels and Piping Conference,* Waikoloa, Hawaii, PVP2017-66121, (2017).
13. Korinko, P. S., Adams, T. M., Malene, S. H., Gill, D. and Smugeresky, J., "Laser Engineered Net Shaping® for Repair and Hydrogen Compatibility," *J. Welding*, **90,** 171 (2011).
14. Wang, Z., Palmer, T. A. and Beese, A. M., "Effect of processing parameters on microstructure and tensile properties of austenitic stainless steel 304L made by directed energy deposition additive manufacturing," *Acta Mater.* **110,** 226 (2016).
15. Ziętala, M., Durejko, T., Polański, M., Kunce, I. , Płociński, T., Zieliński, W., Łazińska, M., Stępniowski, W., Czujko, T., Kurzydłowski, K. J., Bojar, Z., "The microstructure, mechanical properties and corrosion resistance of 316 L stainless steel fabricated using laser engineered net shaping," *Mater. Sci. Eng. A,* 677, 1 (2010).
16. Wei, H. L., Mazumder, J. and DebRoy, T. "Evolution of solidification texture during additive manufacturing," *Sci. Rep.* **5,** 16446, (2015).
17. Korinko, P.S. and West, W.L. "Pinch Weld Evolution: A Phenomenological Model," WSRC-RP-2005-01762, September 2005, Savannah River National Laboratory, Aiken, SC 29808

ACRONYMS

AFM	Atomic Force Microscopy
AM	Additive Manufactured
CPD	Contact Potential Difference
EBSD	Electron Backscatter Diffraction
EDS	Energy Dispersive Spectroscopy
H	Hydrogen
KPFM	Kelvin Probe Force Microscopy
LENS®	Laser Engineered Net Shaping
MFM	Magnetic Force Microscopy
PW	Pinch Weld
SS	Stainless Steel
TDS	Thermal Desorption Spectroscopy
TWIP	Twinning-induced Plasticity

TOTAL NUMBER OF POST-DOCTORAL RESEARCHERS

1. J. D. McNamara was the technical lead on this project as a postdoctoral researcher.

ACKNOWLEDGEMENT

The authors would like to recognize T. Curtis and S. Crossland for their assistance with sample preparation, A. McWilliams for hydrogen charging and R. Wyrwas for assistance in electropolishing. The contributions of these individuals to this work are gratefully acknowledged.

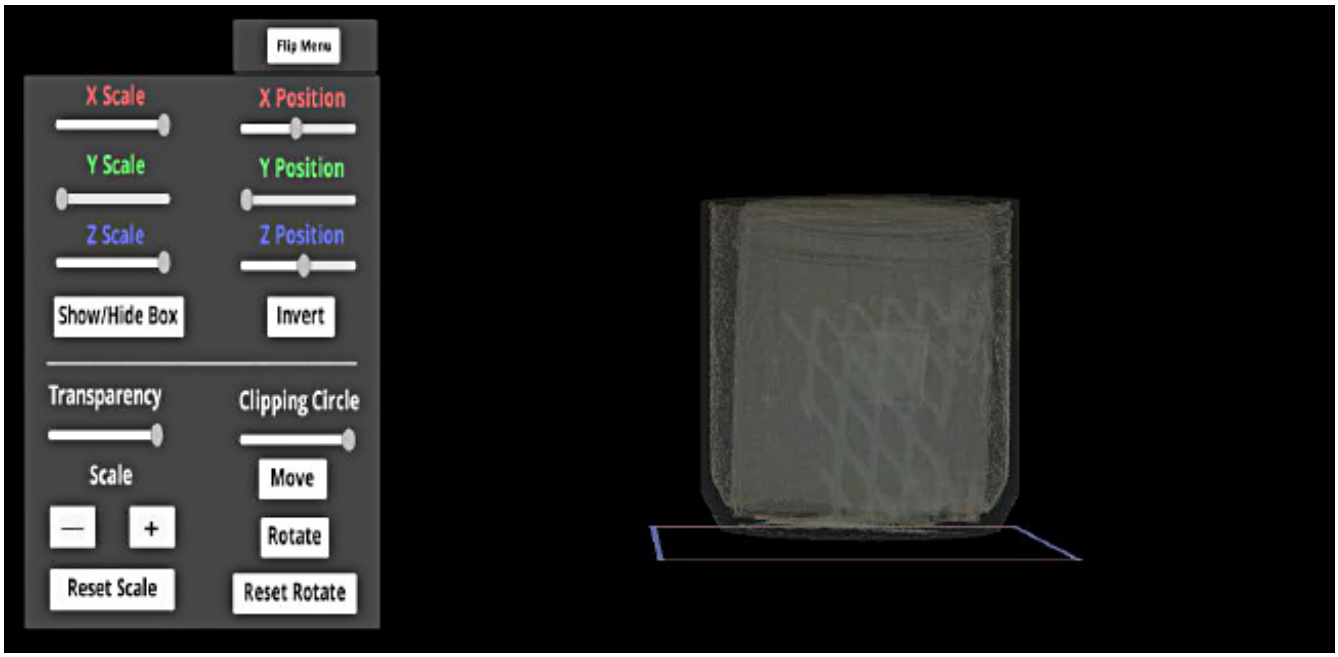

User interface that is superimposed on reality through the Augmented Reality glasses.

AUGMENTED REALITY RENDERING OF COMPUTED TOMOGRAPHY 3-D DENSITY DATA

PROJECT TEAM: Rick Poland, Derek Gobin, David Weir, Savannah Lawson

THRUST AREA:
National Security

PROJECT START DATE:
March 26, 2018

PROJECT END DATE:
September 30, 2018

While models of digitally scanned objects and virtual entities have been successfully rendered in virtual and augmented reality, these visualizations contain only surface data. This project seeks to develop a system that allows the user to interact with computed tomography (CT) data in an augmented reality (AR) environment for critical missions. By including the density data that is inherent in CT scanning, the contents of a structure can be rendered, not just the surface elements.

FY 2018

Objectives

- Purchase equipment and Software required to develop the technology.
- Import CT Data for viewing on an AR device.
- Develop the tools necessary to manipulate the data in AR.

Accomplishments

- CT data sets were imported into the HoloLens as surface data.
- The data was viewed and manipulated in AR.
- A presentation of the technology was given to the MPF team.

INTRODUCTION

Three-dimensional visualization techniques allow a wider range of observers to interact with data at once from many different angles. This project seeks to develop a tool that converts CT scans of equipment/containers into a 3D object that is viewable in AR. This is a useful tool for training workers here at SRNS and across the DOE complex. It would also be of use for workers of the Mobile Plutonium Facility (MPF) by allowing several workers to visualize the inside of containers before they must work on them. The capability can be of use in the medical field where data visualization is vital to medical professionals' ability to quickly and correctly diagnose patients. The education field can also benefit immensely from true 3D visualizations in collaborative environments.

APPROACH

Our general approach for this seedling was to identify the devices and software that are currently in use for data visualization and evaluate them for use in the project. After that we came up with a plan for the system we wished to design. We then took some actual CT data and displayed and manipulated it in AR.

RESULTS/DECISION

We have evaluated two different AR devices for use in the project and selected the one most likely to fit our needs. We were able to convert the CT data into an object viewable in AR but that did not include the density information. We also developed tools to manipulate the object.

Microsoft HoloLens

FUTURE DIRECTIONS

- Include density data.
- Create server/client architecture.
- Develop graphics processing shaders outside of the Unity Game Engine.
- View from multiple AR devices at once.
- Test other AR devices.

PUBLICATIONS/PRESENTATIONS

1. The work was presented to members of the MPF team.

ACRONYMS

AR	Augmented Reality
CT	Computed Tomography
MPF	Mobile Plutonium Facility

SECURE ENERGY MANUFACTURING

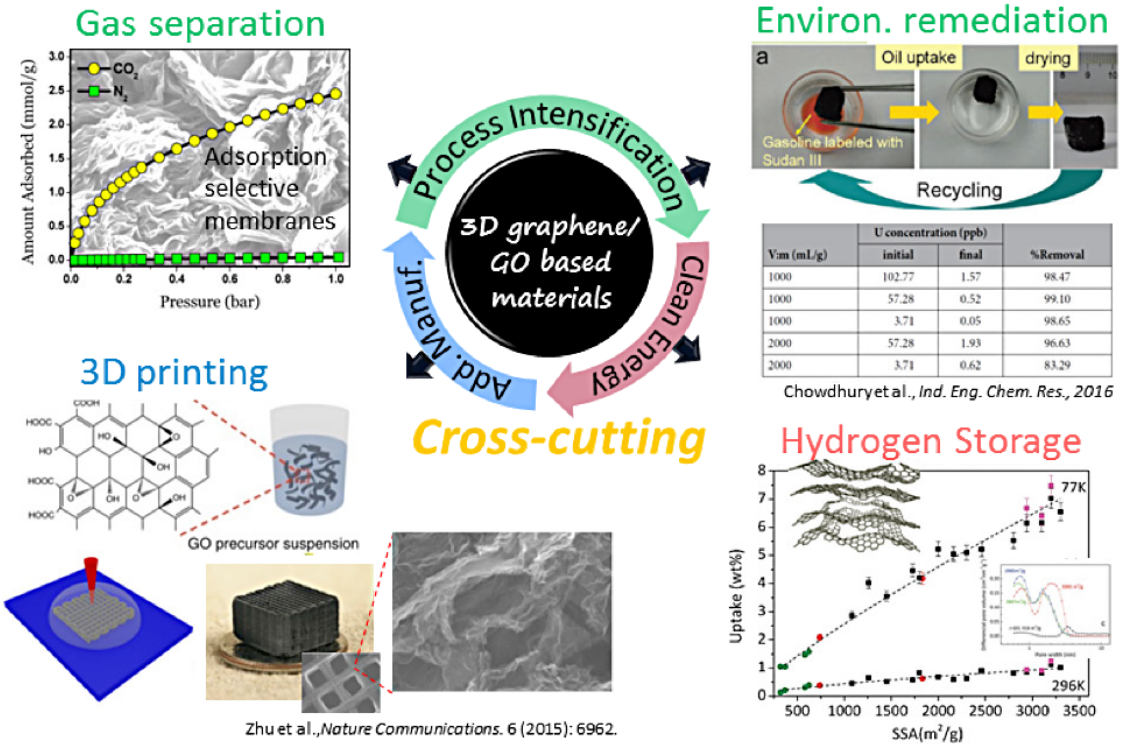

V:m (mL/g)	U concentration (ppb) initial	final	%Removal
1000	102.77	1.57	98.47
1000	57.28	0.52	99.10
1000	3.71	0.05	98.65
2000	57.28	1.93	96.63
2000	3.71	0.62	83.29

Figure 1. The need for 3D graphene optimization is ubiquitous across multiple applications.[1-4]

CROSS-CUTTING HIGH SURFACE AREA GRAPHENE-BASED FRAMEWORKS WITH CONTROLLED PORE STRUCTURE/DOPANTS

PROJECT TEAM: Jay Gaillard (primary), S. Tinkey, M. Elvington, L. Angelette, Steven Gardner, and Martin Sulic; R. Czerw (NanoTechLabs, Inc.); N. Li, Z. Wang, R. Baughman, (University of Texas at Dallas, NanoTech Insitute)

SUBCONTRACTOR:
University of Texas at Dallas
NanoTechLabs, Inc.

THRUST AREA:
Secure Energy Manufacturing

PROJECT START DATE:
October 1, 2017

PROJECT END DATE:
September 30, 2018

The proposed research seeks to enhance SRNL's materials innovation portfolio by developing novel 3D graphene-based frameworks that apply to applications in process intensification, advanced manufacturing, and secure energy manufacturing with a specific focus on hydrogen storage. The objective during FY18 was to enhance the hydrogen adsorption properties of graphene nanoribbons (GNR) by optimizing pore structure and increasing hydrogen binding energy at adsorption sites. Graphene oxide nanoribbons (GONRs) were produced by oxidative unzipping multi-walled carbon nanotubes (MWNTs) with small and large diameters (~30nm and ~150nm, respectively). The research focused on developing thermal exfoliation and activation techniques amenable to enhancing the structural and chemical properties of reduced GONRs and final activated structures to control pore structure and increase specific surface area (SSA). A blueprint for optimizing high SSAs was revealed were controlling the thermal exfoliation step prior to activation was found to be critical to reach SSAs above 3000 m^2/g.

FY 2018

Objectives

Produce rationally designed graphene nanoribbon framework hydrogen adsorbents.

- Synthesize GNRs with varied geometric architecture
- Develop methods for therma exfoliation of graphene nanoribbons that is activated by chemical (KOH) methods.
- Prepare 3D graphene frameworks with a high surface area (>3000 m^2/g) and > 7 wt% H_2 uptake.

Prepare High Surface Area GNRs doped with Heteroatoms

- Prepare high surface area (>3000 m2/g) GNRs with substitutional doping.
- Measure hydrogen uptake of high surface area activated GNRs.

Accomplishments

- Graphene nanoribbon adsorbents with BET SA of 2400 m^2/g have been prepared with H_2 uptake ranging from 4.5 to 5.0 wt%.
- Small diameter (30 nm) and large diameter (150 nm) CNTs were fully unzipped, thermally exfoliated, and KOH activated to obtain high SSA. The highest BET surface area was measured from the large-width GNRs to be 3007 m^2/g for partially activation.
- Hydrogen adsorbents (ZIF-8) have been incorporated into a unique geometric architecture, a biscrolled CNT/ZIF-8 yarn composite. Hydrogen uptake was found to perform similar to literature values and thermal conductivity was increased by an order of magnitude.
- During this LDRD performance period a DOE Advance Manufacturing Office proposal has been selected for FY19-FY21 funding ($4.35M total) based on using novel graphitic nanostructures.

INTRODUCTION

The need for 3D graphene optimization is widespread across multiple applications including fuel cell catalysts, gas adsorbents, supercapacitors batteries, ion (e.g., actinides) capture, gas separation, oil adsorption, and catalysis. DOE's Fuel Cell Technologies Office has set a goal to enable widespread commercialization of hydrogen, which requires adequate hydrogen storage media for onboard vehicles and portable power applications. SRNL is teaming with the University of Texas at Dallas (UTD) to use a facile rationally designed approach to enhance the hydrogen adsorption properties of high-aspect ratio graphene nanoribbons (GNRs). Although GNRs have been produced using scalable techniques, it remains challenging to construct these unique structures into macroscopic functional architectures, which impedes our effort in further exploring their practical applications. GNRs are a new sp^2 carbon allotrope that has the planar properties of graphene but high aspect ratio of carbon nanotubes. These smaller building blocks provide high graphene edge content with a significant advantage for edge functionalization over standard graphene structures in addition to easier access to the graphene planar surface. Little is known about the thermal exfoliation and activation of graphene nanoribbons after oxidative unzipped carbon nanotubes which motivates exploration of these new structures.

APPROACH

As a means to investigate the next generation of sp2 carbon nanomaterials for hydrogen storage, we are teaming with the University of Texas at Dallas (UTD) to use a multifaceted post-treatment approach to enhance the hydrogen adsorption properties of commercially scalable graphene nanoribbons (GNRs) via activation, heteroatom substitution, pore optimization, and edge decoration/functionalization.

The overarching goal of the proposed research is to produce rationally designed 3D graphene framework adsorbents with controlled reversible hydrogen storage characteristics at low pressure and commercially viable temperatures. The specific objective is to produce high surface area (>2500 m^2/g) 3D graphene and graphene nanoribbon frameworks with suitable pore structure and increased binding energy compared to typical Van der Waals interactions.

The innovation of the approach comes from first developing scientific principles for GNR base materials with: **1)** ribbons of various dimensions (i.e., widths and lengths controlled by MWNT starting material) where MWNTs are synthesized with incremental diameters by carefully controlling growth parameters, and **2)** controlling stacked (unzipped, but not fully exfoliated) and single layer architectures while understanding their role in hydrogen adsorption. The developed base materials were thermally exfoliated and perforated using recently improved KOH activation5 to significantly increase surface area near or above 3000 m^2/g.

RESULTS/DECISION

High surface area perforated graphene nanoribbons were prepared using the Tours6 method to form various morphologies of graphene oxide nanoribbons (GONRs), followed by optimized thermal exfoliation and KOH activation. FY2018 focus was on GNR based adsorbents, prepared from MWNTs with ~30 nm diameter and ~150 nm diameter. The initial unzipping and chemical oxidation of MWNTs was investigated to determine optimal oxidizer content and exposure time to the oxidant. $KMnO_4$ was varied between 300 wt% and 800 wt%, with varying oxidation times and analyzed by SEM and by XRD. Optimal oxidation occurs when unzipping is first complete with no further oxidation as seen in XRD near 26°. Once the MWNTs are fully unzipped, any additional oxidation results in more oxygen functionalities, more structural defects, and lower aspect ratios due to oxidative cleavage of ribbons at the defect sites. **Figure 2** shows SWGONRs produced using 300 wt% $KMnO_4$ and 500 wt% $KMnO_4$ at both 1 hr exposure time and 1 hr and 45 min of exposure time. At 300 wt% $KMnO_4$, the XRD data **(Figure 2d)** shows the presence of oxidation, however, the CNT peak at 26° remains indicating only partial unzipping. At 400 wt% $KMnO_4$, the CNT peak is greatly diminished and at 500 wt% $KMnO_4$ it is absent, indicating complete unzipping. Following unzipping, thermal exfoliation of the small-width GONRs was difficult regardless of structure while exfoliation of the LWGNRs is easily performed. Complete disappearance of the graphene oxide peak can be seen in the XRD data **(Figure 2c inset)** for LWGONRs.

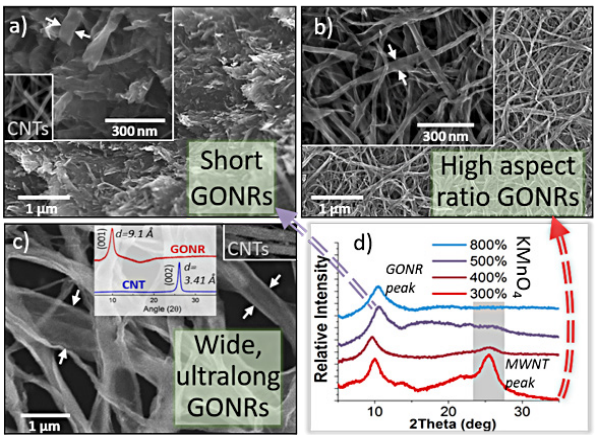

*Figure 2. GONRs are shown to scale. White arrows indicate GONR edges. **(a, b)** GONR structures were produced from small diameter MWNTs (~30nm) and **(d)** from large diameter MWNTs (~150nm). a) GONRs with complete disappearance of the CNT peak (XRD, seen in **d)**) tends to be short defective few-layer GONRs while b) high aspect ratio GONRs produced from lower oxidation still show a MWNT XRD peak (seen in d)). **d)** wide, ultralong (50 – 200 µm) GONRs produced from large diameter CNTs (150 nm) are shown here to have exceptional GONR structure with low defects.*

After thermal reduction/exfoliation, the GNR materials were activated at high temperature (800 °C) with KOH. KOH activation resulted in a significant increase in surface area as well as higher pore volume as expected. Following thermal exfoliation of the LWGONRs, SSAs of 510 m2/g were measured. Following KOH activation, an SSA of 2726 m^2/g was measured with a total pore volume of 2.07 ml/g **(Figure 3).** Sonication of the reduced LWGONRs during preparation for KOH activation was also investigated. This sample gave a slightly lower SSA of 2465 m^2/g with a lower total pore volume of 1.66 ml/g. Both samples showed a portion of the total pore volume below 1.3 nm, the optimal pore diameter for hydrogen storage. Both samples show a significant portion of the total pore volume in the mesopore range. KOH activation of the LWGNR material resulted in incomplete activation as shown by SEM **(Figure 4 on following page).**

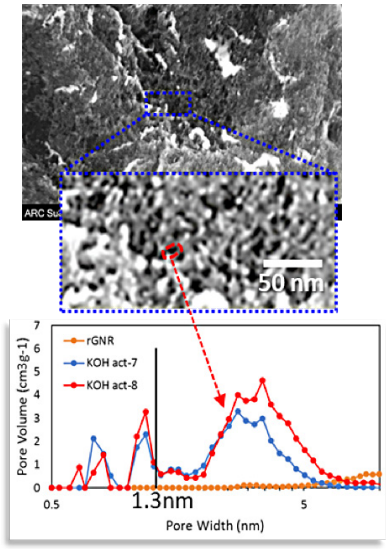

Figure 3. SEM showing porous structure of LWGNR following KOH activation (top). Pore volume/pore width and SSA measurements for the reduced LWGNRs (Bottom).

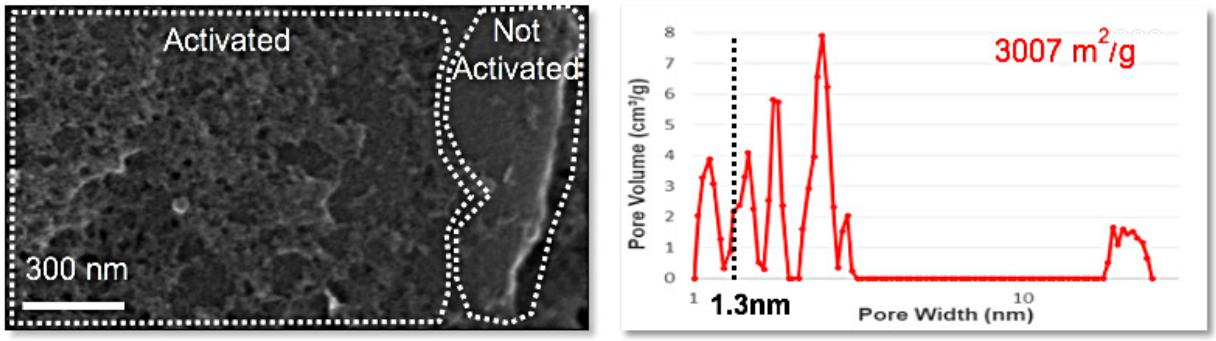

Figure 4. (Left) SEM of LWGNR showing the porous structure of a region that was KOH activated, and a region that was not activated. (Right) Pore volume/ pore width and SSA measurements for the KOH activated LWGNRs

Typically, K/C ratios of 1.7 are optimal for graphene-based materials, however this ratio may require optimization for certain GNR materials due to the higher aspect ratio and higher SSA of the thermally exfoliated samples. Despite incomplete activation, higher SSAs were found as shown in **Figure 4.** The SSA for the activated LWGNRs was measured to be 3007 m^2/g, with a total pore volume of 1.81 ml/g.

Hydrogen uptake was not performed before project end due to primary focus on physiochemical optimization to obtain the high SSA.

During FY18, UTD has focused on incorporating hydrogen adsorbents into biscrolled nanotube yarns with an eventual goal to incorporate the high SSA GNR structures. The biscrolled yarns retain high strength and elasticity from the nanotubes and are being investigated for twist-induced densification. Unfilled twisted yarns have principal direction anisotropic thermal conductivities[7] up to 400 W/m-K In addition to powder densification, twisted yarns are predicted here to impart high thermal conductivity following biscrolling.

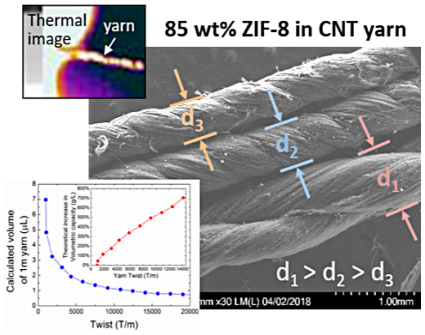

Figure 5. SSEM of a loose ZIF-8 biscrolled yarn twisted into smaller diameters. Image on lower left shows calculations of total volume reduction as a function of twist angle.

Calculating the composite thermal conductivity based on Rule-Of-Mixtures (ROM), a CNT/MOF yarn composite would have an approximate thermal conductivity of ~40 W/m-K assuming 10 vol% CNTs, 90% MOF and experimental values of 400 W/m-K and 0.5 W/m-K, respectively. Nanotube networks suffer from several factors that limit their known individual tube thermal conductivity (3000 W/m-K) and thus a ROM upper bounds of 300 W/m-K. These issues include thermal contact resistance and bundle size.

Thermal Contact Resistance - Thermal contact resistance is influence by the number of contact points and nanotube-to-nanotube distance. This issue is partially solved by compaction and long nanotube lengths.

Bundle Size - Thermal performance is reduced within large diameter yarns that comprise many overlapping bundles due to coupling between CNTs in bundles, where bundles restrict out-of-plane phonon vibrations and therefore suppress low lying optical modes that are known to contribute significantly to thermal conductivity at room temperatures.

Twisting a bundle of parallel fibers into a yarn causes the fibers on the outside of the bundle to apply compressive forces to the core of the yarn, since each fiber must follow a longer, helical path. If the bundle were held at constant length L during twisting, by inserting twist until the surface fibers are aligned at angle θ relative to the fiber axis, the fibers must stretch to a path length of L/cos(θ). This helical stretch causes compression. High stiffness and high strength of the yarn fibers are both important to maximize this effect, so that the highest compressive force can be applied to the yarn core without damaging the yarn. Carbon nanotube yarns are therefore an ideal material for this twist-induced compression that would increase thermal conductivity.

The twisting force can considerably increase the density of the yarn, increasing thermal contact between neighboring absorbent particles and the thermally-conductive CNT matrix. **Figure 5** shows an SEM image of a yarn that was biscrolled using ZIF-8 (1400 m2/g). The yarns were produced at a total weight of 100 mg and tested at SRNL for hydrogen adsorption. This preliminary result yielded an expected ~2.4 wt% H2 uptake (77K, 10 bar) that closely matches the ZIF-8 surface area. Encouragingly, preliminary results showed that this 88 wt% ZIF-8 filled yarn exhibits around 10 times the effective thermal conductivity (1.5 W/m·K) of that of ZIF-8 powders alone (0.16 W/m·K). Further optimization of yarn density would anticipate to significant thermal enhancement.

FUTURE DIRECTIONS

- Focus on pore structure, volumetric capacity, and increasing binding energy (increase uptake temperature).
- Develop techniques to fully activate GNRs and increase pore volume below 1.3 nm pore sizes.
- Publish work in collaboration with UTD. The work for the two different sized GNRs will be finished and published in FY18.

PUBLICATIONS/PRESENTATIONS

1. Jay B Gaillard, Héctor Colón-Mercado, M. Elvington, L. Angelette, S. Tinkey, A. d'Entremont, S.M. Serkiz , "Graphene-based nanomaterials for alternative future energy and nuclear security applications", The Southeastern Regional Meeting of the American Chemical Society Augusta, GA; October 31 – November 3, 2018, invited.

REFERENCES

1. *Ind. Eng. Chem. Res.,* 55 (29), pp 7906–7916 (2016).
2. *Scientific Reports 6,* Article number: 19367 (2016).
3. *Zhu et al., Nature Communications.* 6: 6962 (2015).
4. *Chem. Commun.,* 51, 15280 (2015).
5. *Klechikov* et al., *Chem. Commun.,* **51,** 15280 (2015).
6. *Kosynkin,* et al., *Nature,* 458, 872 (2009).
7. Aliev et al., Carbon 45, 2880–2888 (2007).

ACRONYMS

SRNL	Savannah River National Laboratory
UTD	University of Texas at Dallas
GNR	Graphene nanoribbon
GONR	Graphene oxide nanoribbons
CNT	Carbon nanotubes
MWNT	Multi-walled nanotubes
SWGONR	Small-width graphene oxide nanoribbons
LWGONR	Large-width graphene oxide nanoribbons

INTELLECTUAL PROPERTY

Ongoing efforts for results generated by this project not presented here are being pursued for publication and may include a patent application.

POWER HARDWARE-IN-THE-LOOP TESTING OF DISTRIBUTION SOLID STATE TRANSFORMERS

PROJECT TEAM: John McIntosh (Primary), Klaehn Burkes

SUBCONTRACTOR:
Resilient Power System, Clemson University

THRUST AREA:
Secure Energy Manufacturing

PROJECT START DATE:
October 1, 2018

PROJECT END DATE:
September 30, 2018

Savannah River National Laboratory and Resilient Power Systems have developed a utility grade solid state transformer (SST). The SST is the next generation solution to implementation of distributed energy resources such as solar and batteries. The SST can revolutionize current grid modernization initiatives by supplying grid support and building support services at the edge of the grid. This is not currently a function for traditional transformers. For this fiscal year a test plan for testing the SST capabilities was developed, along with the FPGA controls for the SST output ports. These controls will allow for any waveform to be produced by each port of the SST. Finally, a hybrid distribution SST was tested at the eGRID resulting in medium voltage testing experience for SRNL engineering team. DOE is currently engaged in future work building from this project.

FY 2018

Objectives

- Develop SST Test Bed and System
- Receive Distribution SST at eGRID
- Perform Load Profile Shaping at eGRID
- Develop Control Strategy for Lead Acid and Lithium Ion Dual Battery Systems
- Lease and test functionality of GridBridge Hybrid Transformer
- Develop Control Strategy for Lithium Ion Battery systems
- Perform SST Functionality Tests

Accomplishments

- Test procedure for function testing SST was developed in coordination with Clemson.
- FPGA control of SST was developed by SRNL to provide 12kHz control loop to provide point-on-wave control (*Allows for SRNL to dictate any waveform on SST secondary; Includes DC, Harmonics, AC, High frequency; Has been tested on prototype secondary system for limited cycles; System will allow SRNL to perform more advanced controls than other SST developers such as HEMP mitigation)*
- Tested hybrid distribution SST at eGRID (*Lessons learned in types of instrumentation: High voltage with high accuracy; and High voltage with low current)*
- Full 500kVA 12.47kV SST delivered to eGRID for future research applications

INTRODUCTION

The electric grid is changing rapidly through the integration distributed energy resources (DER) that consists of intermittent renewable energy sources, battery energy storage systems (BESS), and other advanced technologies. DERs require higher levels of control from power electronic inverters and rectifiers to convert the DC power consumed or produced into AC power to connect to the electric grid. To fully leverage DER penetration, passive elements such as a traditional transformers and passive inverters and rectifiers need to be replaced with equivalent active elements like a solid-state transformer (SST). With SSTs integrated into the electric grid more functionalities are becoming readily available at the grid edge to perform grid and building support functions such as control of power flow on multiple ports, reactive power support, power factor correction, integration of renewables and BESS on DC buses, fault isolation, advanced metering, load shaping, demand side management, and transactive control.

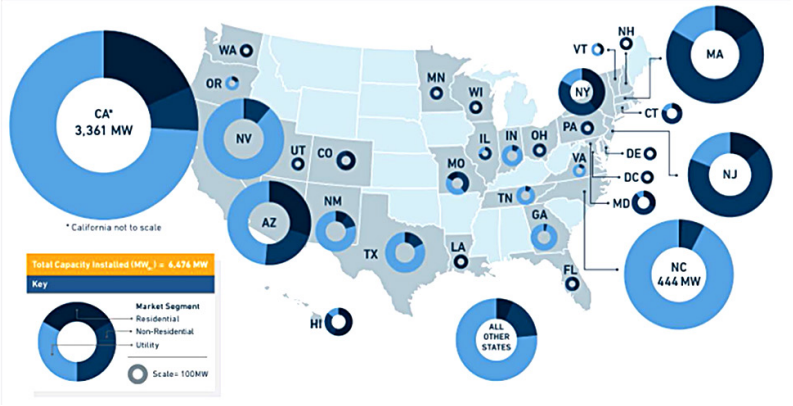

Figure 1. PV installations in the US by state in 2014 [1]

Renewable sources are being integrated into the electric grid at alarming amount and not only in the California region. North Carolina has the second highest integration of photovoltaic (PV) energy in the country see **Figure 1.** One problem seen by this large amount of PV integration is that generation peak and load peak don't occur at the same time. This is because the largest power demand is at the end of the day, when people are returning home from work. PV systems peak power supply is in the middle of the day. Since PV's supplied power is falling off when the load is increasing, high spinning reserves and fast ramp rate generators must be committed to supply power late in the day. This is a large amount of wasted money to support the loss of PV energy. This problem can be solved by integrating a BESS controlled by a distribution scale SST to absorb the PV energy during the peak and supplying it back into the system as PV energy lessens and load is ramping up.

APPROACH

SRNL worked with Resilient Power Systems to develop the solid-state transformer. Together SRNL and RPS determined the parameters for the SST, what type of functionality the SST can perform, how many ports the SST contains, and how the SST will operate above that of a traditional transformer. SRNL also worked with GridBridge a startup company developing hybrid transformers to test a utility deployed hybrid SST. GridBridge is owned by ERMCO a transformer manufacturer.

The solid-state transformer consists of power electronics that convert the AC power delivered by the electric grid to a high frequency AC power. This high frequency allows for a smaller transformer to be used to isolate the primary from the secondary. The high frequency transformer is a 1-to-1 transformer and only performs isolation. The power electronics on the secondary are configured in a way to which they drop the voltage down to the secondary voltage level. A block diagram of the system is shown in **Figure 2.** The primary and secondary power electronics are utilizing multiple modules that consist of active h-bridge architectures to control power flow bi-directionally. This allows for power to be routed through any port in the transformer in any direction. To increase power and voltage the modules are cascaded to reach desired levels, and the modules utilize silicon IGBTs and not wide band gap devices. This allows for reduced losses and costs because the power is being distributed throughout many modules, and the costs of wide band gap devices would make the system prohibitively expensive and not cost competitive with current installed technologies.

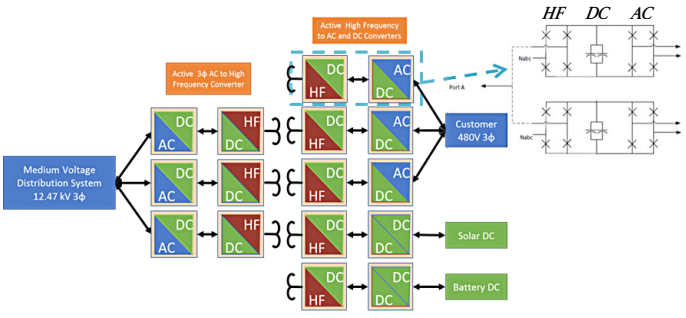

Figure 2. SST system block diagram

RESULTS/DECISION

SRNL developed control signatures to produce any type of waveform from each port on the SST. This includes DC, 60 Hz AC, higher frequency AC, and integration of harmonics. An example of the output waveforms is shown in Figure 3. This will allow for future emulation of any type of waveform and allow for the improvement of power quality for both primary and secondary sides of the transformer. The control works by sending a specific voltage point at a set time step to result in any arbitrary waveform. By performing this point-on-wave control with a 12kHz control loop, SRNL has high accuracy and fidelity in output wave forms that can replicate traditional power electronic systems.

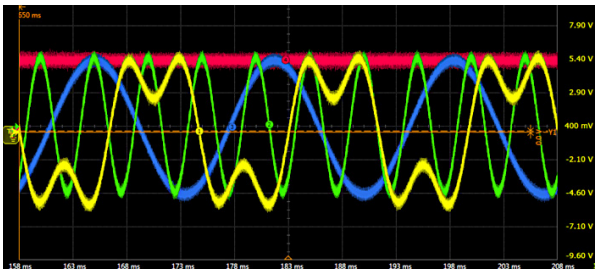

Figure 3. Waveform Output for controlling SST

SRNL also tested the hybrid distribution SST at the Clemson University eGRID. This gave SRNL experience in testing medium voltage distribution components and making accurate measurements at high voltage and low current. SRNL experimented with different types of sensors to improve the accuracy of the power measurement taken on the transformers. High voltage differential probes were required to reach the 7.2 kV voltage of the primary side of the transformer. A current shunt was ultimately used on the neutral return of the transformer to measure the primary current. This is because the voltage potential on the neutral is very low and it was safe to utilize low voltage probes. The instrumentation connections are shown in **Figure 4.** The transformer was driven by the PAUs from the eGRID and loaded with a RLC load bank shown in **Figure 5.**

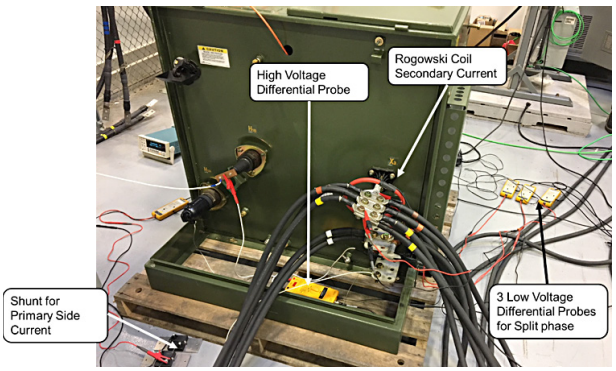

Figure 4. (Left) Instrumentation for hybrid distribution SST.

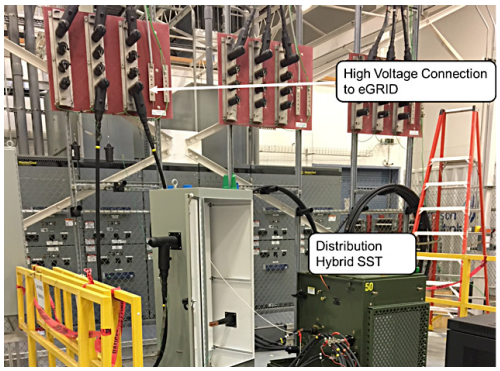

Figure 5. (Right) Connection to eGRID for distribution SST

FUTURE DIRECTIONS

SRNL is currently working with PNNL, GridBridge, ERMCO, and Clemson University to integrate distribution SSTs into transactive control of buildings and campuses. This work is being funded through Building Technology Office and scoping study is currently in process to develop a test plan for the next three years to full hardware in the loop transactive control utilizing demand response and distribution SSTs. Results from this work will feed into a new GMLC lab call proposal.

SRNL is also working with Resilient Power systems to develop solid state power substations that are hardened from high altitude electromagnetic pulses. The SST or hybrid SST can be used to reduce the amount of neutral current and core saturation caused by the E3 component of the HEMP electric field. By using the SST to remove or counter this, component damage can be mitigated.

PUBLICATIONS/PRESENTATIONS

1. "Solar Market Insight Report 2014 Q4" Solar Energy Industries Association, 2014. (Accessed 9/20/2017) https://www.seia.org/research-resources/solar-market-insight-report-2014-q4

ACRONYMS

AC	Alternating Current
BESS	Battery Energy Storage Systems
DC	Direct Current
DER	Distributed Energy Resources
eGRID	Electrical Grid Research Innovation and Development
GMLC	Grid Modernization Laboratory Consortium
HEMP	High-Altitude Electromagnetic Pulse
PV	Photovoltaic
PAU	Power Amplifier Unit
SST	Solid State Transformer

TOTAL NUMBER OF POST-DOCTORAL RESEARCHERS

Two post-doctoral researches worked on the project through Clemson University.

EMBEDDED HARDWARE SOLUTION FOR CYBERSECURITY IN INDUSTRIAL CONTROL SYSTEMS (ICS)

PROJECT TEAM:
Robert Blair Barnett, Richard Poland, Ryan Cruz (Intern)

THRUST AREA:
Secure Energy Manufacturing

PROJECT START DATE:
October 1, 2017

PROJECT END DATE:
September 30, 2018

Manufacturing and Utility companies utilize industrial controls systems (ICS) to automate their plants as a means of increasing efficiency and productivity. These environments consist of older ICS devices that have been networked, although they were never intended to have this functionality. To identify appropriate defensive characteristics needed to contribute to defense-in-depth of cyber-physical systems, we performed a survey of ICS environments and devices. A unique level of concern for ICS are levels one and zero (L1/L0). Devices at these levels are conducting physical activities (and thus considered cyber-physical systems). Our focus are gateway controllers which exist as the interface for L1/L0 devices to higher network controllers. Our strategy is to develop an authentication method using TLS without encryption enabled thus providing an authenticated channel of communication to a gateway device.

FY 2018

Objectives

- Categorize Vulnerability Concerns in ICS
  - Review ICS Architectures, Common Devices, and Protocols
  - Identify general or common weaknesses and vulnerabilities
- Stand Up ICS Testbed
  - Design a robust and flexible testing environment for ICS
- Develop Concept for mitigation of vulnerability at L1/L0
  - Leverage lessons learned from task 1 to devise a strategy for mitigating vulnerability that can be developed into a prototype for testing within the testbed environment

Accomplishments

- Identified a critical problem affecting a class of devices – gateway controllers - at the low level on ICS networks in general
- Developed criteria to establish a working environment for ICS that will be used for this project but can be leveraged towards others and external customers
- Devised design specifications for a hardware device that can implement a security solution for the gateway controllers identified as suffering from critical security concerns.
- Established relationships with Fort Gordon and Florida International University
  - Project utilized a Cybersecurity graduate student from Florida International University via the DOE-Fellowship program

INTRODUCTION

Manufacturing and Utility companies utilize industrial controls systems (ICS) to automate their plants as a means of increasing efficiency and productivity. These environments consist of older ICS devices that have been networked, although they were never intended to have this functionality. More modern Industrial Internet of Things (IIOT) devices, that are rapidly developed with full suites of communication and intelligence features but not security, are also being deployed in these environments. This new interconnectedness on the production floor is being used to connect facilities across the internet to command and control centers. This state of highly interconnected computing capability leaves these systems vulnerable where once a true air-gap existed. In an unfortunate inability to learn from the general history of the internet the networking technologies for these environments are largely being developed on a model of trust. While this attitude is changing, improving ICS security it is a very slow process. The lifecycle for ICS devices can be 10-20 years in time making ICS enticing targets for adversaries looking to impact critical infrastructure **[1].**

A common topology of ICS networks is generalized by breaking the network into five standard levels. It starts with a Business/Enterprise center at the top (level 5) and ends with sensor or actuator devices at the bottom (level 0). Supervisory Control and Data Acquisition systems (SCADA) show up typically at level 3 in the model. It is this point in the model that communication technology transitions from Information Technology (IT) to Operations Technology (OT). With the shift in technology type comes changes in hardware and communication protocol usage. This shift in technology means there must also be changes in how security is conducted for OT systems as compared to standard IT security that accounts for the different nature of the OT environments and devices **[2].**

A unique level of concern for ICS are levels one and zero (L1/L0). Devices at these levels are conducting physical activities (and thus considered cyber-physical systems). These two levels are also the most different from IT in terms of behavior and considerations and suffer the most in terms of security. In order to raise the bar for security of these end devices, we have reviewed network architectures and device types, and engaged with industry to identify weaknesses and vulnerabilities which would benefit from tailored security for L1/L0 cyber-physical systems. Using this information, we have developed a plan for an ICS testbed, and the outline of a prototype device which will be developed in the second year to test security concepts for cyber-physical systems.

APPROACH

To identify appropriate defensive characteristics needed to contribute to defense-in-depth of cyber-physical systems, it was necessary to begin with a survey of ICS environments and devices. Engagement with the ICS community via conferences and workshops, as well as utilization of white papers provided by SANS and E-ISACs, and conversations with Fort Gordon cyber protection team personnel were used to discover contemporary issues with control systems. The results of this discovery phase were used to develop a plan for the development of an ICS-specific cybersecurity testbed, as well as development of specifications for a device that would allow implementation of security features at this low level.

Protocol usage for L1/L0 devices can vary greatly and any added security to existing systems must avoid interfering with this communication. Deep packet inspection is one established layer of security at this low level and anything added to defense-in-depth must compliment this technique. One initial constraint in our approach is to not use encryption as a means of security as to not interrupt this capability. To achieve this, novel forms of authentication were explored as a way of validating the communications without obscuring the traffic between points. The full development of this method is left for 2019.

RESULTS/DECISION

We had three main objectives for this year: identify vulnerabilities in the ICS environment, develop a testbed that will allow us to conduct cybersecurity research on a range of ICS environments, and develop specifications for a prototype to address one of the identified vulnerabilities. We determined that a very common vulnerability in ICS systems is a lack of authentication. This exists at many levels, but our focus will be at the gateway controller level. This narrowed our focus to developing an authentication method using TLS without encryption enabled thus providing an authenticated channel of communication to a gateway device. For the end of the first-year goals, we thus began developing a lab environment and a prototype device that would allow us to test this method of defense. The continuation of this will be discussed in the Future Directions section.

Initially we intended to produce a report classifying the vulnerabilities in ICS but the sheer volume proved overwhelming and ultimately distracting from the scope of this project (**[3]** as an example of the depth of this rabbit hole). The most discussed problem in person and at conferences was around gateway controllers and their lack of authentication **[4] [5] [6].** More specifically, the conversation is about their inadequate authentication. Many of the devices that were explored by others contained some form of authentication – but with such poor implementation or easily accessed backdoors they were near useless. Many responses from vendors to this problem was to suggest disabling the security altogether. These devices typically control communication between L1/L0 devices and HMIs or RTUs at a higher level. This placed them at the level of interest, but also as a critical component to the security at the level of interest for us which made them prime candidates to be addressed by this project.

FUTURE DIRECTIONS

- Design and Develop Embedded Hardware
  - Apply specifications from FY18 to develop prototype hardware
  - Develop and Test an authentication method for the security hardware
- Test and Validate Authentication Method on ICS Testbed
  - Finish leftover tasks for completing the testbed construction
  - Deploy mock ICS network with security solution authenticating at the gateway controller
  - Verify the hardware provides tangible security benefit on the system

REFERENCES

1. L. Obregon, "Secure Architecture for Industrial Control Systems," 23 September 2015. [Online]. Available: https://www.sans.org/reading-room/whitepapers/ICS/secure-architecture-industrial-control-systems-36327. [Accessed 2018].
2. G. Aydell, "The Perfect ICS Storm," 15 May 2015. [Online]. Available: https://www.giac.org/paper/gcia/10551/perfect-ics-storm/141222. [Accessed 2018].
3. J. Z. Andrei Costin, "IoT Malware: Comprehensive Survey, Analysis Framerwork and Case Studies," 2018. [Online]. Available: http://i.blackhat.com/us-18/Thu-August-9/us-18-Costin-Zaddach-IoT-Malware-Comprehensive-Survey-Analysis-Framework-and-Case-Studies-wp.pdf. [Accessed 2018].
4. T. Roth, "Breaking the IIOT: Hacking Industrial Control Gateways," in Blackhat USA 2018, Las Vegas, 2018.
5. J. Shattuck, "Snooping on Cellular Gateways and Their Critical Role in ICS," in BlackHat USA 2018, Las Vegas, 2018.
6. M. P. J. S. Daniel Crowley, "Outsmarting the Smart City," August 2018. [Online]. Available: http://i.blackhat.com/us-18/Thu-August-9/us-18-Crowley-Outsmarting-The-Smart-City-wp.pdf. [Accessed 2018].

ACRONYMS

HMI	Human Machine Interface
ICS	Industrial Control System
IIOT	Industrial Internet of Things, category of industrial devices designed to allow control over either local or internet network connections
IT	Information Technology
L1/L0	Level 1 and Level 0 of the Purdue ICS network model, lowest level where computer devices are performing physical activities.
OT	Operations Technology
RTU	Remote Terminal Unit
SCADA	Supervisory Control and Data Acquisition

HYBRID THERMOCHEMICAL HYDROGEN PRODUCTION

PROJECT TEAM: R H. Colon-Mercado, M. Gorensek, A. Thompson (SRC), M. Elvington (USC), J. Weidner, J. Weiss, B. Meekins, B. Tavakoli

SUBCONTRACTORS:
University of South Carolina (USC), Savannah River Consulting (SRC)

THRUST AREA:
Secure Energy Manufacturing

PROJECT START DATE:
October 1, 2017

PROJECT END DATE:
September 30, 2018

The Hybrid Sulfur (HyS) process is a promising thermochemical water-splitting cycle with global scale hydrogen production potential. The SO2- depolarized electrolyzer (SDE) is a critical component of the cycle. At the core of the SDE is the membrane-electrode assembly (MEA), which consists of a polymer electrolyte membrane (PEM) sandwiched between two electrocatalyst layers. New electrocatalyst and membrane materials are being developed with the goals of improving the electrolyzer performance and extending the lifetime of the MEA. A high-throughput methodology is being developed to screen potential candidates based on Pt and Au thin films prepared through physical vapor deposition. SO_2 oxidation reaction kinetics are being analyzed for the novel catalysts and compared to the state-of-the-art, Pt/C. In addition, advanced polymer electrolyte membranes of polybenzimidazole (PBI) will be utilized, which have shown superior performance in comparison to the state-of-the-art, Nafion®. These catalysts and membranes will be combined to produce high performance MEAs.

FY 2018

Objectives

- Electrocatalyst Development
  - Develop High-throughput catalyst screening methodology
  - Develop carbon-supported catalysts
- Membrane Development
  - Develop optimized membranes
  - Membrane testing
- Electrolyzer Performance Evaluation
  - Membrane electrode assembly fabrication
  - Modification of test station

vEvaluate material performance in electrolyzer

Accomplishments

- **Goal:** Find better catalysts and membranes for the Hybrid Sulfur (HyS) process for hydrogen production from water
- **Approach:** Improve catalyst activity, improve membrane ionic conductivity, and improve catalyst/membrane stability for operation at higher temperature and higher acid concentration (faster kinetics and efficiency)
- **Progress:** Found promising new mixed-metal catalysts and better membranes for further exploration, developed new capabilities/techniques for high-throughput catalyst synthesis/testing, established new partnerships and external funding

INTRODUCTION

There exists a significant and growing need for clean, efficient, and large-scale hydrogen production. Using high temperature heat, thermochemical cycles can provide an energy-efficient route for hydrogen production. The HyS process is a promising thermochemical water-splitting cycle with significant scalability. The HyS process, one of the most researched thermochemical cycles, is a sulfur-based water-splitting cycle which contains a low temperature electrolysis step, and thus can be considered an electrochemical and thermochemical hybrid process. In the HyS process, H_2SO_4 is thermally decomposed at high temperature (> 600 °C), producing SO_2 **[r1].** SO_2 and H_2O enter the SDE where SO_2 is oxidized to form H_2SO_4 and H+ at the anode **[r2],** while at the cathode, H+ is reduced to form H2 **[r3].** The overall electrochemical reaction consists of the production of H_2SO_4 and H_2 **[r4],** while the entire cycle produces H_2 and O_2 from H_2O with no side products **[r5].**

Figure 1 shows a simplified schematic of the overall process and the main chemical reactions taking place.

$H_2SO_4 \rightarrow SO_2 + ½O_2 + H_2O$ Thermochemical Step **[r1]**

$SO_2 + 2H_2O \rightarrow H_2SO_4 + 2H^+ + 2e-$ Anode Electrochemical Step **[r2]**

$2H^+ + 2e- \rightarrow H2$ Cathode Electrochemical Step **[r3]**

$SO_2 + 2H_2O \rightarrow H_2SO_4 + H_2$ Overall Electrochemical Step **[r4]**

$2H_2O \rightarrow 2H_2 + O_2$ Cycle Process Reaction **[r5]**

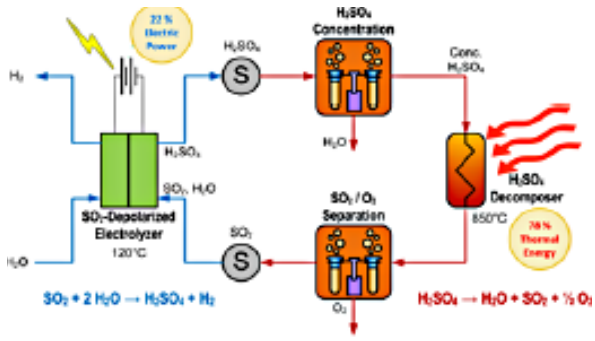

Figure 1. Simplified schematic of the HyS

The electrolysis step must be maintained at the highest possible conversion fraction to minimize unreacted SO_2 and obtain high H_2SO_4 concentration. Unreacted SO_2 must be recycled, and water must be removed prior to the high temperature decomposition step. Both of these are energy intensive steps and must be minimized to keep process efficiency high. Operation of the electrolyzer at the target conditions, however, is unfeasible using the current state-of-the-art materials. Therefore, new materials will be required to achieve the electrolysis performance goals. This project is focused on the development of new electrocatalysts and membranes and their effect on process efficiency, with the goals of improving the electrolyzer performance and extending the lifetime of the MEA.

APPROACH

A collaborative effort between SRNL and USC was initiated to develop novel materials designed to operate under the HyS process conditions with superior performance compared to the state-of-the-art. SRNL is utilizing its expertise in catalyst development and screening, along with USC's expertise in membrane development and gas anolyte stream HyS operation, in order to achieve improvements in the HyS and meet DOE-EERE's hydrogen production goals. The work is being carried out in three main tasks.

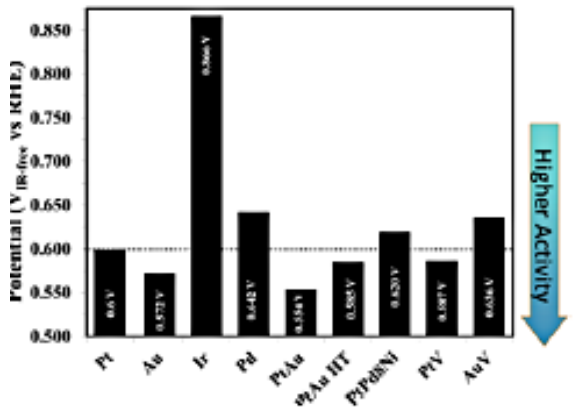

Figure 2. Initial catalyst screening results for the [r2]. Chronopotentiometry test performed in 30 wt% $H2_sO_4$ saturated with SO_2

Task 1-Catalyst Development: Pt black and Pt/C have long been the state-of-the-art catalysts for PEM electrolyzers. Recently, as demonstrated in **Figure 2,** advances in catalyst design have demonstrated that Pt-M (M: V, Co, Fe, etc.), Au, and Au-based catalysts have improved kinetics for the SO_2 oxidation reaction [r2]. In order to design a catalyst for the conditions of the HyS, a high-throughput combinatorial methodology is under development that will aid in the catalyst selection. Once a catalyst composition has been identified, electrocatalyst materials will be produced in order to test them in-situ.

Task 2-Membrane Development: Nafion® has long been the PEM solid electrolyte material of choice due to its stability in highly corrosive solutions (30 wt% H_2SO_4 saturated with SO_2) and at high operating temperature (80 °C), while maintaining practical ionic conductivity. However, to meet H2 cost targets, membrane materials capable of operating at higher temperatures and acid concentrations are needed. At higher temperatures (>80 °C) and acid concentrations, Nafio[n®] and many other solid electrolyte membranes become dehydrated and consequently become more resistive to ion transport. Benicewicz and Weidner's research groups at USC are currently developing membrane materials specific for the HyS process. Not only are the membranes able to operate at higher temperatures than Nafion®, they can also operate at higher acid concentrations as they do not rely on water content for their H+ conductivity. Membranes developed at USC will be evaluated at SRNL and combined with newly developed catalysts to meet HyS operational targets.

Task 3-Electrolyzer Performance Evaluation: SRNL modified its existing pressurized button cell test facility to evaluate the performance of new catalysts and s-PBI membranes. MEAs are being fabricated and tested for activity and stability according to SRNL's developed protocols.

RESULTS/DECISION

Combinatorial Catalyst Development

An order with an external company was established in FY18 to produce combinatorial trimetallic catalyst films of Pt, Au, and V. The metals will be deposited by sputtering a range of compositions onto glassy carbon plates. These catalysts will be characterized by X-ray diffraction (XRD) and texture analysis via pole figure measurements. Literature research and discussions with partner universities are currently underway to develop an appropriate technique. XRD pole figure analysis will provide insight on whether the catalyst crystallites have a preferred orientation, how the orientation changes with composition, and how it affects reactivity.

The catalyst films will be mapped by scanning electrochemical microscopy (SECM) in order to determine the most active catalyst composition. In order to develop this method, a SECM was set up and tested under various conditions. Cyclic voltammetry and approach curves were obtained for the ferrocyanide/ferricyanide redox couple in two different electrolytes **(Figure 3),** and were consistent with expected trends and literature data.[1] A catalyst mapping experiment was also performed on the same anolyte in KCl electrolyte with a gold electrode and showed catalyst activity that varied across the surface. This demonstrates that SECM can be used as a sensitive probe of surface reactivity, but experimental conditions need to be further optimized to eliminate streaks in the scanning direction. In addition to standard SECM techniques, a scanning droplet system (SDS) has been procured, which will be more suitable for studying irreversible reactions such as SO_2 oxidation.[2]

SDS-SECM system requires specific material surface properties for the system to scan the surface. Several tests were carried out to validate the materials that will be used in the high-throughput catalyst screening and compared to results using standard characterization techniques. The performance of metal nanoparticles supported on carbon black and that of metal thin films on glassy carbon was evaluated in two different electrolytes. As shown in **Figure 4,** a comparison between model solutions and SO_2 saturated sulfuric acid solutions yielded similar results for metal-doped carbon electrocatalysts and thin metal films, respectively. As confirmed by both tests, gold catalysts show higher performance than the state of the art catalysts, platinum on carbon.

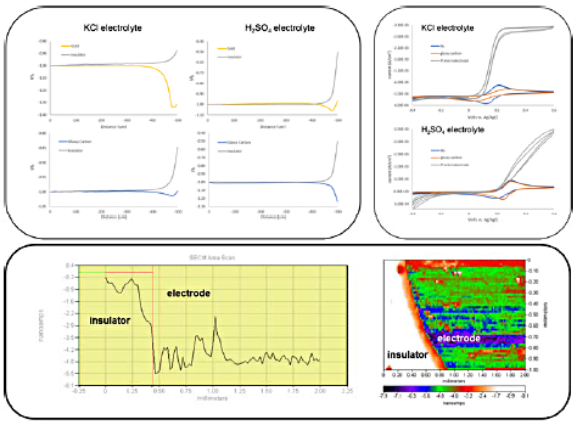

Figure 3. SECM approach curves (top left) and cyclic voltammograms (top right) for 5 mM $[Fe(CN)_6]^{3-/4-}$ in 0.1 M electrolyte on gold and glassy carbon electrodes; line scan and surface map of a gold electrode in 5 mM $[Fe(CN)_6]^{3-/4-}$ anolyte and 0.1 M electrolyte

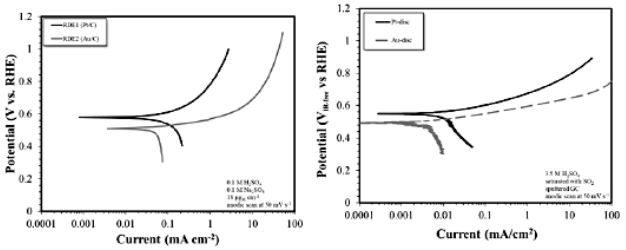

Figure 4. The use of model solutions (left) for the implementation in high throughput screening shows similar behavior to thin films tested in SO_2 saturated sulfuric acid solutions (right). As observed by our initial screening, Au/C shows better performance than Pt/C.

Electrolysis test station modification and validation

The MEA button cell test facility has been modified for gas-phase SO_2 testing. Various improvements were made during modification, such as elimination of dead volume and leak points, making the system more efficient and increasing throughput. The new gas-phase system has been successfully set up and tested. **Figure 5** shows that the performance is comparable to liquid-phase at low current densities. At higher current densities, a discrepancy is observed, attributed to low pressure operation.

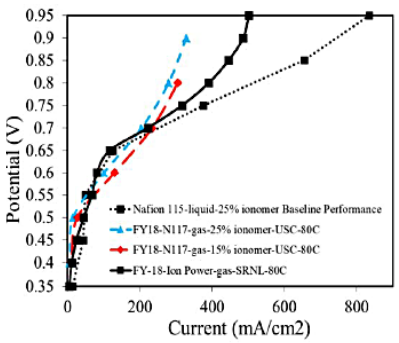

Figure 5. Performance curves for the operation of the gas fed button cell test facility compared to the liquid fed test results.

FUTURE DIRECTIONS

- Initiate high throughput catalyst screening
- Develop, characterize and test metal supported on carbon anode catalysts
- Test sulfonated polybenzimidazole membrane electrode assemblies

REFERENCES

1. Rock, P.A. J. Phys. Chem. **1966,** 70, 576-580
2. Gorensek, M.B. Int. J. Hydrogen Energy **2009**, 34, 6089-6095

ACRONYMS

DOE-EERE	Department of Energy-Office of Energy Efficiency and Renewable Energy
HyS	Hybrid Sulfur
MEA	membrane electrode assembly
PBI	polybenzimidazole
PEM	polymer electrolyte membrane
SDE	SO_2-depolarized electrolyzer
SDS	Scanning droplet system
SECM	Scanning electrochemical microscopy
SRC	Savannah River Consulting
SRNL	Savannah River National Laboratory
USC	University of South Carolina

TOTAL NUMBER OF POST-DOCTORAL RESEARCHERS

J. Weiss (under-graduate, USC)
B. Tavakoli (Post-doctoral Student, USC)
M. Elvington (Post-doctoral Student, SRC)

SURFACE PLASMON ASSISTED CATALYSIS FOR METHANE CONVERSION AND HYDROGEN PRODUCTION

PROJECT TEAM:
Patrick Ward, Simona Murph, Anthony Thompson, Steve Xiao, Ragaiy Zidan

SUBCONTRACTORS:
Joseph Teprovich
(California State University Northridge)

THRUST AREA:
Secure Energy Manufacturing

PROJECT START DATE:
October 1, 2017

PROJECT END DATE:
September 30, 2018

The excitation of localized surface plasmon resonances in noble metal nanoparticles generate electrons with energies well above the fermi energy of electrons for the material. These hot electrons can be transferred into the conduction band of adjacent semiconductors and utilized to drive chemical reactions. Furthermore, these electrons can be ejected with energies on the order of 1-15 eV which can ionize gas molecules leading to additional chemical reaction pathways. It is well known that higher energy hot electrons and electric fields can be generated at edges and points on plasmonic nanoparticles. Herein, we develop high edge and point content nanoparticles attached to photoactive semiconductors and dye molecules to broaden the spectrum of light which can be absorbed and increase the catalytic activity of these composites.

FY 2018

Objectives

- Synthesize high edge and point content nanoparticles
- Characterize high edge and point content nanoparticles
- Produce high edge and point content nanoparticles on photoactive semiconductor substrates
- Utilize synthetic methods to attach porphyrin molecule to high edge and point plasmonic nanoparticles to broaden the absorption spectrum of these materials for better solar spectrum utilization
- Demonstrate water splitting capabilities of these plasmonic nanomaterial composites
- Demonstrate methane conversion capabilities o these plasmonic nanomaterial composites

Accomplishments

- Synthesized high edge and point content nanoparticles
- Characterized nanomaterial composites
- Attached porphyrin molecules to plasmonic nanoparticles to enhance solar absorption spectrum
- Synthesized high edge and point content nanoparticles embedded into photoactive semiconductor substrates
- Developed methodology to determine the direction of electron transfer of hot electrons within plasmonic nanocomposite systems
- Developed technique to probe the mechanism of water splittin in plasmonic nanoparticle systems

INTRODUCTION

Methods to efficiently convert water into hydrogen and oxygen in a cost-effective manner are critical to the realization of the hydrogen economy. Furthermore, technologies which enable the conversion of methane into an easily transportable liquid commodity can allow for the utilization of flare gas and provide pathways to generate value added chemicals from currently abundant methane resources. Leveraging solar energy to drive these chemical reactions provides the opportunity to carry out chemical reactions (such as methane conversion) in remote areas and utilize a free and abundant source of energy. Advances in photocatalytic methods provide a potential pathway for the realization of low-cost chemical conversion technologies for energy applications. In particular, chemical reactions induced by surface plasmon resonances have not been studied in significant detail and provide a mechanism to generate energetic electrons on the surface of a material which can be used to drive chemical reactions.

APPROACH

Localized surface plasmon resonances in metallic nanoparticles are well-known to produce hot electrons (electrons above the Fermi level)[1] which can be ejected from the surface with substantial kinetic energies[2] or donated into the conduction band of other materials. The energy of ejected electrons from metallic nanoparticles is a function of the shape, size, and composition of the nanoparticle. By tuning the shape and size of Au and Ag nanoparticles the kinetic energy of ejected electrons can be tuned to match the ionization energy of the desired reactant (i.e. methane or water) to invoke chemical reactions. In addition, ejected electrons can be accelerated by the localized electric field produced by localized surface plasmon resonances to reach kinetic energies on the order of several tens of eV.[3] Kinetic energies of this magnitude are more than sufficient for ionization of molecules such as methane, which has an ionization energy of 12-14 eV.[4] Furthermore, hot electrons can be donated into the conduction band of an appropriate co-catalysts or capping ligand to drive chemical reactions. Previous studies have demonstrated that the presence of noble metal nanoparticles on a semi-conductor surface helps stabilize charge carrier separation and prevent efficiency losses from recombination. [5] These phenomena provide novel pathways for light driven chemical reactions. The predicted nanoparticles of interest lie in smaller nanoparticles with high edge and point content. This is due to the higher energy "hot electrons" (electrons with energies above the Fermi level) present in corners and edges versus flat or curved surfaces. At higher temperatures, the conduction band of the co-catalyst will have a higher population of electrons and there is a small decrease in the ionization energy of gases at elevated temperatures.

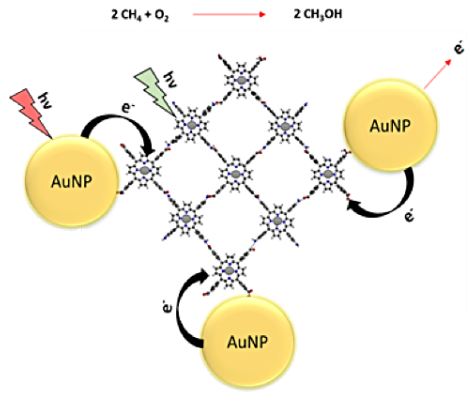

Figure 1. Illustration of nanoparticle embedded porphyrin framework.

Figure 2. Illustration of nanoparticle embedded porphyrin framework.

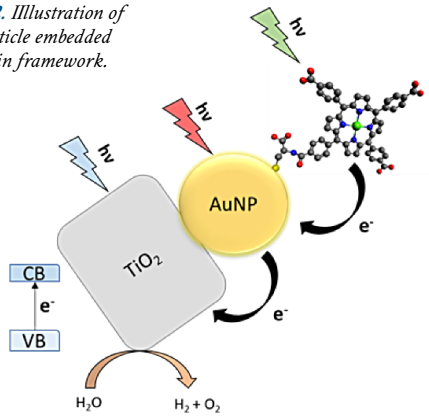

To provide a larger catalytic surface for reactions to take place, a covalently attached network of nanoparticles can be created based on porphyrin 2 dimensional frameworks. In this case, electrons can be donated to the framework to drive chemical reactions over a larger surface area as shown in **Figure 1.** In another approach, porphyrin "tagged" nanoparticles can be attached to a semiconductor surface to provide a catalytic nanocomposite. **Figure 2** illustrates the potential electron transfer pathway utilizing a broad spectrum of light to drive the chemical reaction. In this case, the semiconductor would have a band excitation in the ultraviolet, the nanoparticle in the red, and the porphyrin in the green.

RESULTS/DECISION

Gold nanoparticles of various shapes and sizes were synthesized and characterized. Of particular interest were nanoparticles with high edge and point content. To maximize edge and point content, "nano-stars" were synthesized of various sizes as shown in **Figure 3** starting from spherical "seed" nanoparticles. Figure 4 on the following page displays the characteristic red-shift of the surface plasmon resonance (SPR) with increasing size of the nano-stars grown from different size seed nanoparticles.

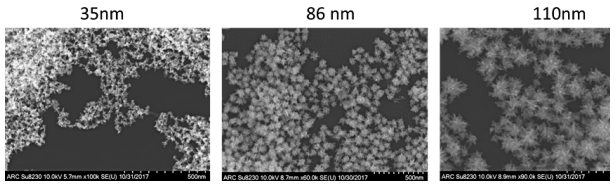

Figure 3. SEM images of nano-stars of various sizes

To ensure appropriate electrical contact between the semiconductor substrate and the Au nanoparticle (AuNP), the "seed" nanoparticles used to produce the star nanoparticles were grown directly on TiO_2 nanoparticle substrates. From there, the nano-stars could be grown on

semiconductor substrates with increased electrical contact. Adequate electrical contact is an essential factor for efficient electron transfer processes. SEM/EDS mapping images confirm the presence of Au nano-stars grown from TiO_2 nanoparticle substrates as shown in **Figures 5 and 6.**

To develop further insight into the underlying reaction mechanism which takes placed during and Electron Paramagnetic Resonance (EPR) reaction cell was fabricated which allows the introduction of a gas and light during an EPR measurement. By the addition of spin trap molecules which stabilize short lived free radicals, these species can be monitored during photocatalytic reactions. Preliminary results suggest the formation of •OH radicals during water splitting reactions involving Au nanoparticles decorated TiO_2. To enable photocatalytic reaction studies, a high power pulsed optical parametric oscillator (OPO) with pump laser was acquired with a wavelength range from the UV to the IR. **(Figure 7)** A specially designed cell to analyze products produced by laser illumination was also produced. This allows for the confirmation of SPR induced catalysis by observing reaction only during surface plasmon excitation, but not when off resonance. Extensive laser acquisition times prevented material catalytic activities studies during the funding period of this project.

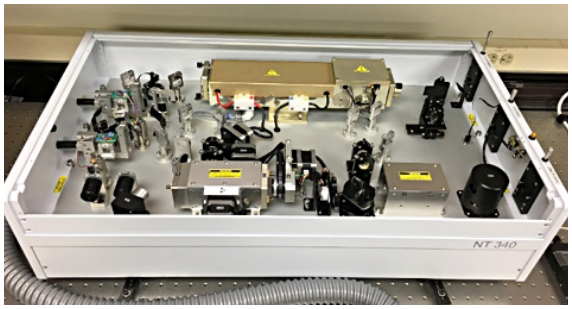

Figure 7. Integrated Nd:YAG pump laser with OPO system

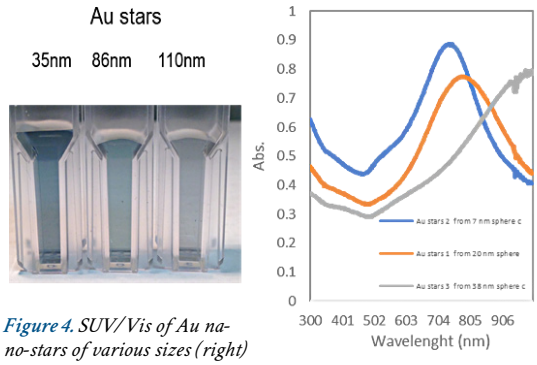

Figure 4. SUV/Vis of Au nano-stars of various sizes (right) and suspension of the different size nano-stars in water.

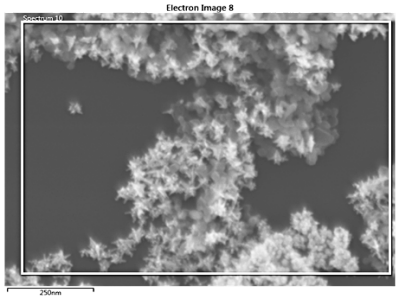

Figure 5. SSEM image of Au nano-stars on TiO2

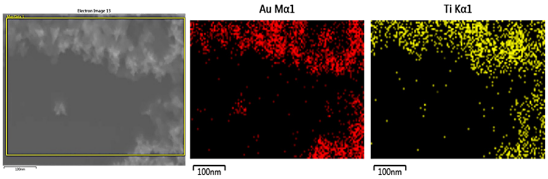

Figure 6. SSEM image of Au nano-stars on TiO2

FUTURE DIRECTIONS

- Investigate the catalytic activity of newly developed plasmonic nanoparticle composite materials for water splitting and methane conversion
- Spectroscopically determine the direction of electron transfer in the initial stages of hot electron excitation
- Determine mechanism of catalytic reactions in order to understand and develop pathways towards producing a practical solar plasmonic photo catalyst system
- Leverage novel materials for alternative photocatalysis applications

PRESENTATIONS

1. Murph, Simona "Nanotechnology Innovations at SRNL" – 256th ACS National Meeting

REFERENCES

1. Marchuk, K.; Willets, K. A. Chem. Phys. 2014, 445, 95-104.
2. Jouin, H.; Raynaud, M.; Duchateau, G.; Geoffroy, G.; Sadou, A.; Martin, P. Phys. Rev. B 2014, 89, 195136.
3. Nagel, P. M.; Robinson, J. S.; Harteneck, B. D.; Pfeifer, T.; Abel, M. J.; Prell, J. S. et. al. Chem. Phys. 2013, 414, 106-111.
4. Stano, M.; Matejcik, S.; Skalny, J. D.; Mark, T. D. J. Phys. B: At. Mol. Opt. Phys., **2003,** 36, 261.
5. Kamat, P. V. J. Phys. Chem. B **2002,** 106, 7729-7744.

ACRONYMS

SPR	Surface Plasmon Resonance
AuNP	Gold nanoparticle
SEM	Scanning Electron Microscopy
EDS	Energy Dispersive X-ray Spectroscopy
EPR	Electron Paramagnetic Resonance
OPO	Optical Parametric Oscillator

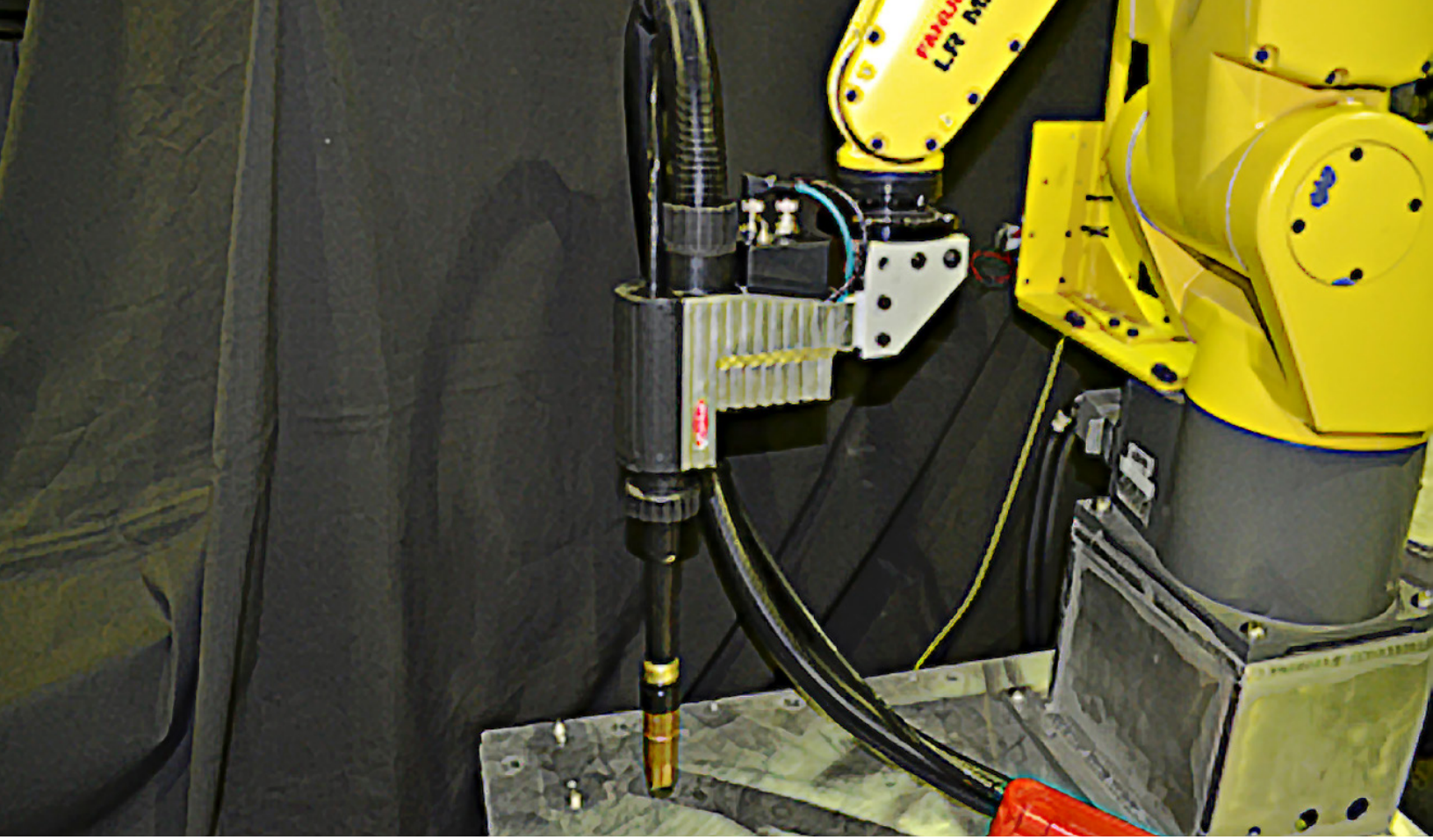

Wire Arc Additive Manufacturing setup with a Fronius Cold Metal Transfer Torch mounted on a Fanuc robot arm.

WIRE ARC ADDITIVE MANUFACTURING

PROJECT TEAM:
A. J. Duncan, P. S. Korinko (Co-PIs)

COLLABORATORS:
P. S. Lam, A. L. d'Entremont,
J. T. Bobbitt, D. Gobin,
M. Folsom W. Housley, E. Kriikku

THRUST AREA:
Secure Energy Manufacturing
Advanced Manufacturing

PROJECT START DATE:
October 1, 2016

PROJECT END DATE:
September 30, 2018

This project develops and deploys a wire arc additive manufacturing (WAAM) capability for SRNL. To better understand and predict Process-Structure-Property-Performance interrelationships, modeling was conducted a-priori with results that were consistent with the trends for cooling rate and secondary dendrite arm spacing. Two aluminum alloys, Al 2219 and Al 4043 were deposited using either a cold wire gas tungsten arc welding (GTAW) process or cold metal transfer mode of gas metal arc welding. This project positions SRNL as a technical leader in WAAM. This project redeploys a Fanuc robot arm with a state of the art aluminum welder, develops the software needed to drive the robot and weld system, and develops microstructure, thermal, and residual stress predictive tools to enable SRNL and USC to improve/optimize the manufacturing processes.

FY 2018

Objectives

- Integrate CMT with Fanuc robot
- Conduct scoping studies to determine appropriate wire arc additive manufacturing space for future experiments
- Conduct statistically designed experiments to optimize microstructure and deposit shape
- Complete developing scripts to predict cooling rate and microstructure from Abaqus Weld Interface models
- Conduct instrumented experiments to facilitate correlating experimental data with models

FY 2018

Accomplishments

- Integrated Fanuc robot with Fronius welder to enable arc start and motion for simple geometries. Prior to this development, SRNL did not have the capability for robotic welding in more than two dimensions.
- Completed scoping studies that resulted in a significant improvement in process conditions to virtually eliminate porosity in the CMT GMAW WAAM deposits.
- Fabricated and tested a gas cover showerhead using polymer additive manufacturing to improve shielding to reduce deposit porosity. Conducted a DoEx and determined the effects of travel speed, wire feed, gas cover, and arc distance at two levels.
- Completed an experiment to determine the temperature and cooling rate as a function of position from the WAAM deposit and as a function of 1 to 4 layers in the presence and absence of additional cover gas.
- Completed DoEx for optimizing a square deposit using cold wire GTAW to maximize the material usage on a layer to layer basis. Developed an ImageJ script for image analysis to automate the data capture and analysis.
- Demonstrated that the predicted cooling rate from the weld modeling and the measured secondary dendrite arm spacing data had consistent trends.

INTRODUCTION

Additive Manufacturing has the capability to make components of almost infinite complexity using one of several different technologies. These technologies include directed energy approaches such as laser engineered net shape (LENS) or powder bed laser or electron beam processes. The powder processes work well and have dimensional limits of about 75 μm. However, the build rate is slow due to layer thicknesses of about 50 μm each, requiring over 4000 layers to build a 200 mm tall component over a time of approximately 45 hours with a single heat source. The size of the article for powder bed processes is further limited by the size of the process bed and ability of the heat source to uniformly reach the entire work area. Finally, the powder processes also have a potential fire concern, especially for reactive metals like aluminum and fine titanium. The fire hazard may be mitigated by using passivated powders, thus reducing their pyrophoric nature by slightly oxidizing the surfaces or by adding other reaction products, but this treatment degrades the powder purity which will compromise the material performance of the finished part. The reaction products could also prevent melting and inhibit the incorporation of the particles into an integral part of the component. Alternative AM methods such as the currently proposed Wire Arc Additive Manufacturing (WAAM) can alleviate these anticipated concerns.

Wire Additive Manufacturing (WAM) uses a wire feedstock and an appropriate heat source (arc, laser, or electron beam) to melt the wire and deposit the material in a programmed consistent manner. Wire Arc Additive Manufacturing (WAAM) uses either cold or hot wire feed Gas Tungsten Arc Welding (GTAW), Plasma Arc Welding (PAW), or Gas Metal Arc Welding (GMAW) technology to deposit metal layer by layer. The use of wire as the source material enables significantly higher build rates, e.g., 1 kg/h for WAAM vs. 0.2 kg/h for powder bed processes, reported for titanium alloys **(1).** In contrast to fine unpassivated powders **(2),** wires are generally not considered pyrophoric. As a result, WAAM eliminates the fire hazard without introducing impurities (e.g., oxides) into the product. Finally, WAAM reduces the material costs, since it costs less to make wire than powder.

WAAM is being rediscovered as an approach for freeform fabrication or three-dimensional printing for large net shape components. Unlike many of the powder-based processes that produce net or near net shapes, WAAM is generally considered an additive manufacturing process that can be coupled directly with a subtractive process. The subtractive element is required due to the higher volume deposition rate and coarse deposit scale that requires machining of the excess material to meet final dimensions. This allows WAAM to produce complex parts with machined surfaces. Despite the need for subtractive manufacturing, WAAM provides tremendous cost and material savings over conventional subtractive processes. For example, the "buy-to-fly" ratio, i.e., the material required to make a component, like an airplane wing spar **(Figure 1),**

Figure 1. Material size and scale for (a) WAAM wingspar.

vs. the material remaining after final machining, can be 10:1 for conventional processing of titanium alloys while the buy-to-fly for WAAM can be as low as 1.2:1. WAAM does have the shortcoming that parts must be slightly oversized to accommodate the machining allowance; this gives rise to new design terminologies such as total wall width (TWW) and effective wall width (EWW) where TWW includes the weld bead scallops on the surface which need to be machined away and EWW is the final dimension of the post-machining wall. The difference in TWW and EWW gives rise to the buy-to-fly ratio that is attributed to WAAM. Finally, the WAAM structures can be forged to obtain improved properties over the as-fabricated microstructure.

APPROACH

This project has two primary drivers: first, establishing a WAAM capability and, second, establishing a modeling capability based on commercial software evolution. WAAM has been established as a viable technology for titanium-based alloys **(3, 4, & 5)** and has been suggested as a feasible technology for aluminum as well **(3).** Aluminum is best deposited using GMAW and either spray or dip transfer modes. The benefit of using dip transfer is that it minimizes the spatter associated with spray transfer for GMAW and the total heat input **(Figure 2).** The software and hardware will be integrated with open source code and open architecture to allow both simple and more complex 3D shapes to be printed using GMAW torch mounted to a Fanuc Robot arm.

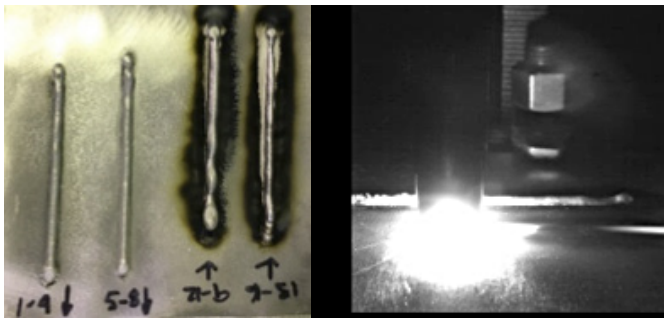

Figure 2. WAAM A4043 beads deposited on Al6061 and the CMT GMAW deposition.

One major hurdle for AM is to close the gap between the as-designed and the as-manufactured configurations. For WAAM, this includes minimizing the difference between TWW and EWW **(Figure 3)** as well as controlling distortion and residual stresses in the printed part. This optimization can be facilitated by computer modeling or simulation of the WAAM process. Therefore, in parallel to fabricating the SRNL WAAM system, coupled microstructural, thermal, and stress modeling was conducted. The following three-step approach is proposed. **Step 1** – Simulate WAAM by predicting the as-manufactured part based on the as-designed specifications. The multi-purpose commercial finite element code Abaqus, available at SRNL, was utilized along with its welding-interface plugin. The 2017 Abaqus Welding Interface (AWI), which SRNL currently has access to in beta version, has the capability to account for gradual addition of material to the workpiece over the course of the simulation (vital for simulation of WAAM), coupled with a heat source model well-established for representing welding heat inputs. The AWI also enables specification of weld geometric features, temperature-dependent material properties, bead/chunk specification, multiple weld passes, and thermal and structural boundary conditions. The final shape of the product, distortion, and residual stress will be calculated both before and after "unclamping" of the mechanical constraints, fracture and damage can be assessed, and optimization of the WAAM process will be conducted by varying the operating parameters and the material properties. **Step 2** – To close the gap between as-designed and as-manufactured configurations, it may be necessary to capture the material properties using samples with a variety of dimensions since the AM process impacts the material properties. Important metal phase transformations occur during melting and re-solidification that affect tensile strength and fracture toughness, but most currently available property data corresponds to temperatures well below the solidus temperature. This can be resolved by benchmarking the test data, or by acquiring multiscale computer software for materials modeling. **Step 3** – Conduct optimization of process parameters to match the as-manufactured to the as-designed configurations (or minimize the gap between TWW and EWW, **Figure 3**). The process-specific considerations include deposition path data, heat source characteristics, multi-scale scope, and the model size.

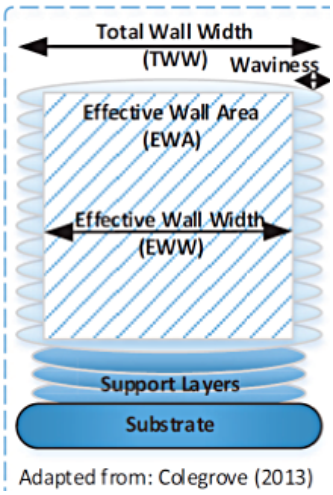

Figure 3. Definitions for TWW and EWW for WAAM processes showing the required overbuild.

RESULTS/DECISION

Weld microstructures were improved from significantly porous structures to near full density by modifying the appropriate weld parameters. Scoping studies, **Figure 5,** were used to define the initial parameter space and were optimized using statistically designed experiments. One concern for the build-up of the deposits is the incorporation of air and presence of oxides on the weld wire, but the wire could not be cleaned either prior to loading in the welder or while it was being consumed by the welder. To minimize the effects of local atmosphere on the deposit microstructure, an additively manufactured gas showerhead was produced to displace the air with argon during welding. The level of soot that was deposited on the surface of the substrate decreased in the presence of the gas showerhead, but not consistently. An unfortunate condition occurred when using the Fanuc robot in that the controller did not produce a smooth movement. This characteristic manifested itself as waves in the WAAM deposit with a periodicity of about 8 mm and a height that depended on the weld current.

A two-level, four-variable design of experiments was conducted to determine the process window for pore-free deposits. The wire feed, torch speed, use or omission of the gas showerhead, and cup-to-plate height variables were tested. The parameter set selected did not fully eliminate the porosity, although the porosity was reduced and concentrated near the top of the weld as opposed to throughout the weld, as shown in **Figure 5a.** The presence and absence of soot on the plate was not a good indicator of porosity. High wire feed rates significantly affected porosity, while the other three variables had small or no discernable effect **(Figure 6).** Torch speed and wire feed affected the weld bead deposit size with high torch speed producing a smaller deposit and high wire feed producing a larger deposit. There was no discernable effect of cup height and shield gas on the response variables.

Figure 4. As-printed surface condition from a full factorial DoEx conducted at USC.

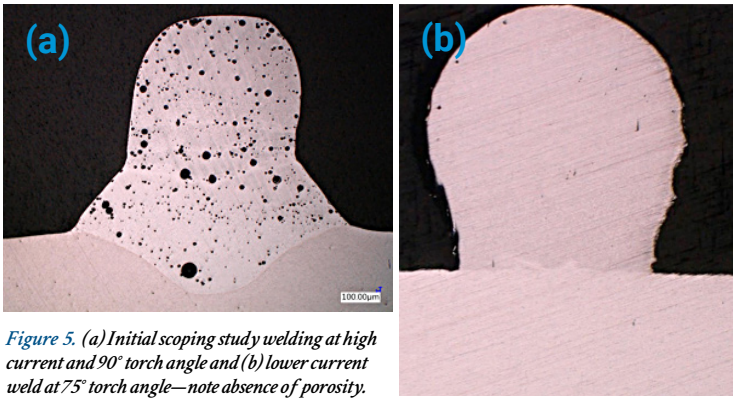

Figure 5. (a) Initial scoping study welding at high current and 90° torch angle and (b) lower current weld at 75° torch angle—note absence of porosity.

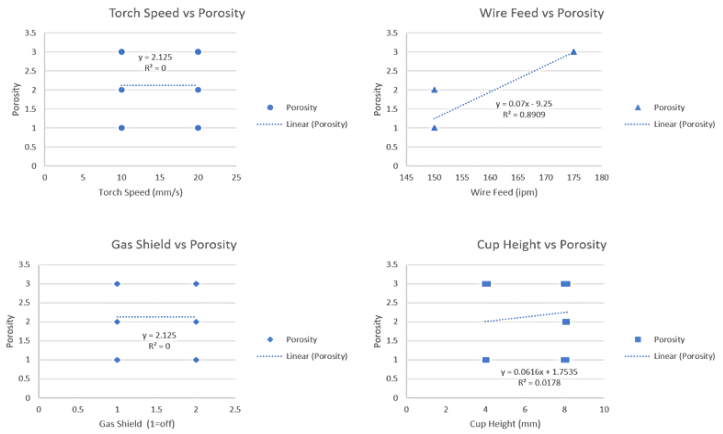

Figure 6. Effect of the variables tested, torch speed, wire feed, gas shield, and cup height on the response variable "porosity".

The robotic control of the welder was not optimized but the WAAM system was used to fabricate a 3-D layup that consisted of four layers, using non-optimized parameters, in the shape of a rectangle, **Figure 7.** The control system was not optimized for stops and starts so craters and bulges were present. In addition to the rectangle, a single bead wide "blade" eight layers thick was also deposited as can be seen in **Figure 7.**

Experiments were conducted that demonstrated the ability to generate relatively square cross-sections of weld deposit, **Figure 4 on previous page.** These samples were subsequently evaluated for secondary dendrite arm spacing (SDAS). The SDAS coupled with weld modeling is used to correlate cooling rates to weld parameters. These data can then be utilized for estimating deposition strengths based on literature correlations.

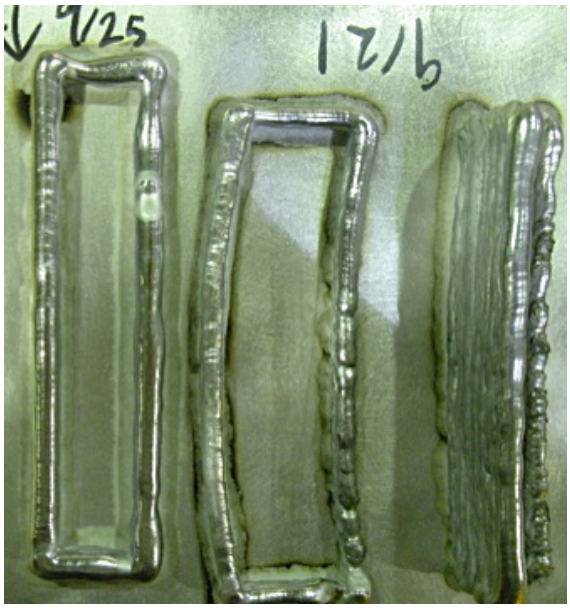

Figure 7. 3-D WAAM deposits using programmed torch paths to create a four-layer rectangle and an eight-layer "blade".

FUTURE DIRECTIONS

- Obtain future funding to enable additional capabilities of the WAAM based on having a capability at SRNL.
- Incorporate additional sensors and data analytics for smart manufacturing using thermal and optical sensors for process sensors and defect detection and prevention.

PRESENTATIONS/PUBLICATIONS

1. SRNL-STI-2017-00594, Development and Deployment of a Wire Arc Additive Manufacturing Capability, Anna d'Entremont, Andrew Duncan, Poh-Sang Lam, John Bobbitt, Eric Kriikku, Derek Gobin, Matthew Folsom, Paul Korinko, Anthony Reynolds (USC), presented at MS&T17, Oct. 8-12, 2017 Pittsburgh, PA.

2. SRNL-STI-2017-00688, Development of a Wire Arc Additive Manufacturing System, Paul Korinko, Andrew Duncan, J. Bobbitt, E. Kriikku, D. Gobin, PS Lam, A. d'Entremont, M. Folsom, W. Housley, & A. Reynolds* (*USC), Additive Manufacturing IMOG, Kansas City National Security Campus, Nov. 7&8, 2017

3. SRNL-STI-2018-00025, SRNL Additive Manufacturing Site Update, Paul Korinko, Welding IMOG / WAM FE, Sandia National Laboratory, Livermore, CA, Jan. 22-23, 2018

4. 2018-SRNL-STI-00167, Savannah River National Laboratory Additive Manufacturing and Metallurgy, Paul Korinko, Georgia Southern University, April 13, 2018, Statesboro, GA

5. SRNL-STI-2018-00234, Wire Arc Additive Manufacturing at SRNL, Paul Korinko, Andrew Duncan, J. Bobbitt, E. Kriikku, D. Gobin, PS Lam, A. d'Entremont, M. Folsom, W. Housley, & A. Reynolds* (*USC), Wire Additive Manufacturing Focused Exchange and Welding JOWOG, May 21-25, 2018, AWE, Reading, Berkshire, England.

6. SRNL-STI-2018-00236, SRNL Additive Manufacturing Update, Paul S. Korinko, Wire Additive Manufacturing Focused Exchange and Welding JOWOG, AWE, Reading, Berkshire, England, May 21-25, 2018

7. SRNL-STI-2018-00237, SRNL Welding and Joining Site Update, Paul Korinko, Wire Additive Manufacturing Focused Exchange and Welding JOWOG, AWE, Reading, Berkshire, England, May 21-25, 2018

8. SRNL-STI-2018-00339, Prediction of local microstructure for wire-arc additive manufacturing of aluminum alloys, Andrew Duncan, Anna d'Entremont, Poh-Sang Lam, Paul Korinko, ASME 2018 Pressure Vessels and Piping Conference, July 15-20, 2018.

9. SRNL-STI-2018-00130, Deposition of Aluminum 4043 during Wire Arc Additive Manufacturing, Paul Korinko, Eric Kriikku, William Housley, John Bobbitt, Andrew Duncan, Anna d'Entremont, Matthew Folsom, and Matthew Van Swol, to be presented at MS&T18, Oct. 15-21, 2018, Columbus, OH.

REFERENCES

1. Busachi, A., et. al, "Designing a WAAM Based Manufacturing System for Defence Applications", Procedia CIRP (2015), 48-53.

2. Kwon, Y.S. et. al, "Passivation process for superfine aluminum powders obtained by electrical explosion of wires", Applied Surface Science 211 (2003) 57–67.

3. Williams, S.W, et. al "Wire + Arc Additive Manufacturing", Materials Science and Technology, 32:7, 641-647, DOI:10.1179/1743284715Y.0000000073

4. Szost, B.A., et. al, "A comparative study of additive manufacturing techniques: Residual stress and microstructural analysis of CLAD and WAAM printed Ti–6Al–4V components, Materials and Design 89 (2016) 559–567.

5. Berminham, M.J., et. al, "Controlling the Microstructure and Properties of Wire Arc Additive Manufactured Ti-6Al-4V with Trace Boron Additions", Acta Materialia 91 (2015) 289-303.

ACRONYMS

Al	Aluminum
Al4043	Aluminum welding alloy 4043
Al6061	Aluminum alloy 6061
AWE	Atomic Weapons Establishment
AWI	Abaqus Welding Interface
CMT	Cold Metal Transfer
DoEx	Design of Experiments
EWW	Effective Wall Width
GMAW	Gas Metal Arc Welding
GTAW	Gas Tungsten Arc Welding
MS&T	Materials Science and Technology
SDAS	Secondary Dendrite Arm Spacing
SRNL	Savannah River National Laboratory
USC	University of South Carolina
TWW	Total Wall Width
WAAM	Wire Arc Additive Manufacturing

TOTAL NUMBER OF POST-DOCTORAL RESEARCHERS

One MS student was supported through a subcontract with University of South Carolina

Savannah River
National Laboratory™

OPERATED BY SAVANNAH RIVER NUCLEAR SOLUTIONS